A Comparison of Rheological Drag Reduction in Wall Turbulence Using Different Additives

by

Lucas Nicholas Warwaruk

A thesis submitted in partial fulfillment of the requirements for the degree of

Doctor of Philosophy

Department of Mechanical Engineering
University of Alberta

Abstract

It is well known that long-chain polymers and surfactants can significantly reduce the skin-friction drag of turbulent liquid flows; a phenomenon often referred to as rheological drag reduction. However, it is unclear if the mechanism for drag reduction is common among different types of polymers and surfactants. In the present dissertation the rheology and drag-reducing capabilities of three different additives are compared, including a flexible polymer, a rigid polymer and a cationic surfactant. Educated predictions regarding each additives mechanism for drag reduction are made.

Aqueous solutions of flexible polymers exhibit viscoelastic non-Newtonian rheology, and a good ability to reduce drag in turbulent channel and boundary layer flows. Measurements of steady shear rheology indicate that drag-reducing flexible polymer solutions are only marginally shear thinning. That being said, the same solutions have an appreciable extensional relaxation time, as demonstrated by extensional rheology measurements using a capillary break up extensional rheometer (CaBER) and dripping onto substrate (DoS) rheometer. In a turbulent channel flow with a Reynolds number Re of approximately 30 000, flexible polymer solutions achieve drag reduction (DR) percentages as large as 70% and a mean velocity profile that straddles the maximum drag reduction (MDR) limit. A turbulent boundary layer comprised of flexible polymers with low amounts of DR, indicate that skin-friction drag is reduced from a near-wall attenuation of vorticity and extensional flow motions – particular biaxial extension. As a result, the polymer-laden boundary layer exhibits more two-dimensional and shear-dominate flow within the conventional limits of the buffer layer, indicative of an expansion in the viscous sublayer and flow parobolization.

Similar to flexible polymers, solutions of rigid polymers can exhibit large amounts of DR in a turbulent channel flow; however, the mechanism for reducing drag in rigid polymers is seemingly different. A rigid polymer solution that is capable of imparting the same amount of DR as a flexible polymer solution in a turbulent channel flow tends to have a larger overall shear viscosity, more shear thinning, but no measurable extensional relaxation time using CaBER and DoS. Therefore, drag reduction using rigid polymers is largely

driven by the shear thinning rheology of the solution. Gradients in the mean velocity coupled with the solutions shear thinning rheology generate an effective slip within the buffer layer and a reduction in skin friction drag.

Unlike the polymeric solutions, drag-reducing solutions of cationic surfactants do not have a shear thinning viscosity, nor do they have a measurable extensional relaxation time from CaBER and DoS rheometry. Instead, surfactant solutions have a shear and extensional rheology similar to water, despite their ability to achieve a large DR of 70% in a turbulent channel flow. To discern the non-Newtonian qualities of the surfactant solution, the laminar flow of the drag-reducing fluids were compared in a periodically constricted tube (PCT), where the tube walls vary sinusoidally with respect to the streamwise direction. Although the PCT flow is not rheometric, it is also not as complex as wall turbulence and provides a comparison among the polymeric and surfactant fluids in a nontrivial flow with mixed kinematics. Above an Re of 100 within the PCT, certain surfactant solutions exhibit a similar inertioelastic flow pattern as flexible polymers. Due to the sudden onset of inertioelastic flow with increasing Re, evidence is provided that flow-induced structures develop within the surfactant solutions. These flow-induced structures produce similar rheological features as flexible polymers, and most likely, a common means for reducing drag.

Preface

The content in Chapters 5 and 6 of the current thesis were published in the *Journal of Fluid Mechanics*:

> **Warwaruk, L.** & Ghaemi, S. 2023 Polymer and surfactant flows through a periodically constricted tube. *J. Fluid . Mech.* 960, A19.

Chapter 7 contains content published in a separate article, but also in the *Journal of Fluid Mechanics*:

> **Warwaruk, L.** & Ghaemi, S. 2021 A direct comparison of turbulent in drag-reduced flows of polymers and surfactants. *J. Fluid . Mech.* 917, A7.

Cambridge University Press is the copyright holder of the two previously listed documents. The work presented in Chapters 5, 6 and 7 are reproduced with permission from the publisher.

The content presented in Chapter 8 was published in *Physical Review Fluids*:

> **Warwaruk, L.** & Ghaemi, S. 2022 Near-wall lubricating layer in drag-reduced flows of rigid polymers. *Phys. Rev. Fluids* 7(6), 064605.

The American Physical Society holds the copyright permission on the article listed above. The content presented in Chapter 8 is reproduced with permission from the publisher.

The content in Chapter 9 has been submitted for publication in the *Journal of Fluid Mechanics*.

I am responsible for generating all of the content contained within this thesis. In creating this work I performed an extensive review of the relevant literature, formulated the project objectives and methodology, designed the necessary facilities and experiments, collected and processed the experimental data, and assembled the content into a manuscript for journal publication. My PhD supervisor, Dr. Sina Ghaemi, provided guidance and was co-author on all of the previously listed publications.

Dedicated to Dr. Joseph Warwaruk P.Eng, PhD, Professor Emeritus

Acknowledgements

The work presented in this thesis would have not have been possible with out the support and guidance of my doctoral supervisor, Professor Sina Ghaemi. I am forever grateful for the opportunities Dr. Ghaemi has afforded me during my tenure as a graduate student. I am also very appreciative for the input from the committee members of my candicacy and final examinations including, Professors Carlos Lange, Marc Secanell, Mark Loewen, Patricio Mendez, and Robert Poole. Lastly, I would like to acknowledge the support of Dr. R. Sean Sanders, who provided me with access to a torsional rheometer that was used in several of the works presented in this thesis.

To the many colleagues I have made at University of Alberta, much of the work in this thesis was made easier from our conversations, your guidance and our time-spent helping one another in the lab. In particular, Bayode Owolabi helped teach and train me on rheology. Bradley Gibeau was very instrumental in helping me prepare for my candidacy and final examinations (including providing me with a formatting template for this thesis). Sen Wang and Prashant Das were both helpful when it came to setting up my measurement equipment. Wagih Abu Rowin provided me with the initial code, which I then adapted, for processing the Lagrangian velocity measurments of my first work.

During my time as a graduate student, the help and encouragement from my parents, Dave and Corinne Warwaruk, has been consistent. I am truly privileged to have grown up in such a loving home with two incredibly talented and caring people.

Contents

List of Tables

List of Figures

List of Symbols

$\langle \cdots \rangle$	Ensemble average of a quantity
$\overline{\cdots}$	Average along streamwise $x-$direction in the PCT
$\vert\vert \cdots \vert\vert$	L2-norm of a vector
$\mathcal{R}(\cdots)$	standard deviation of a quantity
A	Fitting coefficient for EC thinning regime
a	Fitting coefficient for CY viscosity model
B	Logarithmic law of the wall intercept
C_f	Skin-friction coefficient
$C_{f,N}$	Newtonian skin-friction coefficient
$C_{f,NN}$	non-Newtonian skin-friction coefficient
c	Additive concentration
D_0	Nozzle diameter of the DoS rheomter
D_h	Hydraulic diameter
D_{mid}	Mid-point diameter measured using CaBER
D_{min}	Minimum diameters measured using DoS
$\mathbf{D}$	Rate of deformation tensor
d_p	Seeding particle diameter
$\mathbf{d}$	Fluctuating rate of deformation tensor
De	Deborah number
DR	Drag reduction
DR_1	Drag reduction based on pressure drop
DR_2	Drag reduction based on fit of linear viscous sublayer
F_γ	Strain coefficient
F_τ	Stress coefficient
f	Focal length
$\boldsymbol{f}$	Body force vector
Fr	Froude number
G	Elastic modulus
G'	Gain modulus
G''	Loss modulus
G^*	Complex modulus
H	Full channel height

h	Half channel height
h_{dg}	Average gap width of double gap geometry
h_{pp}	Gap height between parallel plates
I	Single gap cylinder moment of inertia
I_{max}	Maximum image intensity
$\mathcal{K}$	Kinematical vorticity number
k	Shear thinning flow index
L_{sg}	Immersion height of single gap geometry
L_{dg}	Immersion height of double gap geometry
$\mathbf{L}$	Velocity gradient tensor
M	Shear thinning consistency
$\dot{m}$	Mass flow rate
N	Total number of samples
Oh	Ohnesorge number
P	Static pressure
P_D	First invariant of the rate of deformation tensor
P_D	First invariant of the velocity gradient tensor
Q	Volumetric flow rate
Q_D	Second invariant of the rate of deformation tensor
Q_L	Second invariant of the velocity gradient tensor
Q_W	Second invariant of the rate of rotation tensor
R	Average radius of the PCT wall
R_1	Inside radius of fixed double gap cylinder
R_2	Outside radius of fixed double gap cylinder
R_3	Inside radius of rotating double gap cylinder
R_4	Outside radius of fixed double gap cylinder
R_D	Third invariant of the rate of deformation tensor
R_L	Third invariant of the velocity gradient tensor
R_i	Minimum radius of the PCT geometry
R_{max}	Maximum radius of the single gap geometry
R_{min}	Minimum radius of the single gap geometry
R_o	Maximum radius of the PCT geometry
R_{pp}	Radius of the parallel plates
R_{uu}	Two-point correlation of velocity fluctuations
R_w	Wall radius of the PCT
$R_{\mu'\mu'}$	Two-point correlation of viscosity fluctuations
Re	Reynolds number of the PCT
Re_H	Reynolds number based on full channel height

Re_b	Reynolds number based on hydraulic diameter
Re_d	Reynolds number of entrance region to PCT
Re_{pp}	Reynolds number of the parallel plate geometry
Re_ϕ	Reynolds number based on momentum thickness
Re_τ	Friction Reynolds number
r	Radial direction
SF	Velocity profile shape factor
St	Stokes number
T	Rheometer torque
Ta	Taylor number
Tr	Trouton ratio
$\mathcal{T}$	Large eddy turnover time
$\boldsymbol{T}$	Non-Newtonian torque
t	Time
t_b	Filament break up time
t_e	Elastic relaxation time
t_f	Flow time scale
t_p	Particle response time
t_v	Viscous time scale
t_R	Rayleigh time
U	Instantaneous streamwise velocity
U_0	Centreline velocity
U_∞	Free-stream velocity
U_H	Velocity of upper moving plate
U_b	Bulk velocity
U_r	Radial velocity component
U_x	Streamwise velocity component
U_θ	Angular velocity component
$\boldsymbol{U}$	Instantaneous velocity vector
u	Fluctuating streamwise velocity
u_f	Representative flow velocity
u_p	Particle settling velocity
u_τ	Friction velocity
$\boldsymbol{u}$	Fluctuating velocity vector
V	Instantaneous wall-normal velocity
VA	Vorticity advection
VSD	Vorticity solvent diffusion
v	Fluctuating wall-normal velocity
W	Instantaneous spanwise velocity or channel width
w	Fluctuating spanwise velocity

$\mathbf{W}$	Rate of rotation tensor
Wi	Weissenberg number
x	Streamwise coordinate
$\boldsymbol{x}$	Position vector
y	Wall-normal coordinate
y_v	Thickness of the linear viscous sublayer
z	Spanwise coordinate
α	Multiplicative pre-factor in equation for IC thinning
Γ	Eigenvalues of the rate of deformation tensor
γ	Shear strain
γ_0	Shear strain amplitude
$\dot{\gamma}$	Shear strain rate
$\dot{\gamma}_w$	Wall shear rate
$\dot{\gamma}$	Strain rate based on invariants in the rate of deformation tensor
Δ	Discriminant of the velocity gradient tensor
Δ_D	Discriminant of the rate of deformation tensor
δ	Boundary layer thickness
δ^*	Displacement thickness
δ_v	Viscous length scale of turbulent wall flow
ϵ	Amplitude of the PCT walls
$\dot{\varepsilon}$	Extensional strain rate
ζ	Indicator function
θ	Angular position
κ	Von Kármán constant for the logarithmic law of the wall
Λ	Eigenvalues of the velocity gradient tensor
λ	Wavelength of the PCT wall
μ	Dynamic viscosity
μ'	Dynamic viscosity fluctuations
$\tilde{\mu}$	Pseudo-viscosity
μ_0	Zero-shear-rate viscosity
μ_∞	Infinite-shear-rate viscosity
μ_E	Extensional viscosity
μ_s	Solvent viscosity
μ_w	Dynamic viscosity at the wall
ν	Kinematic viscosity
ν_w	Kinematic viscosity at the wall
ξ	Divergence error
ρ	Density
ρ_p	Density of tracer particles
σ	Surface tension

τ	Shear stress
τ_0	Shear stress amplitude
τ_0'	In-phase shear stress amplitude
τ_0''	Out-of-phase shear stress amplitude
τ_R	Reynolds shear stress
τ_v	Viscous shear stress
τ_v'	Fluctuating viscous shear stress
τ_w	Shear stress at the wall
$\tau_{w,1}$	Shear stress at the wall based on pressure drop
$\tau_{w,2}$	Shear stress at the wall based on fit of linear viscous sublayer
$\boldsymbol{\tau}$	Stress tensor
$\boldsymbol{\tau_{nn}}$	Non-Newtonian stress tensor
$\boldsymbol{\tau_s}$	Solvent stress tensor
τ_w	Shear stress at the wall
ϕ	Momentum thickness
ψ	Phase offset between G' and G''
Ω	Angular velocity of steady shear viscosity measurements
ω	Angular frequency of dynamic shear viscosity measurements
$\boldsymbol{\omega}$	Vorticity vector

List of Abbreviations

2D	Two-dimensional
3D	Three-dimensional
CaBER	Capillary break-up extensional rheometer
C14	Trimethyl Tetradecyl Ammonium Chloride
CY	Carreau-Yasuda model
DG	Double gap geometry
DNS	Direct numerical simulation
DOF	Depth of focus
DoS	Dripping onto substrate
DRA	Drag-reducing additive
EC	Elastocapillary
EIT	Elastoinertial turbulence
FOV	Field of view
GN	Generalized Newtonian
HDR	High drag reduction
IC	Inertiocapillary
IW	Interrogation window
JPDF	Joint probability density function
LDR	Low drag reduction
LVE	Linear viscoelastic
MDR	Maximum drag reduction
PAM	Polyacrylamide
PCT	Periodically constricted tube
PDF	Probability density function
PIV	Particle image velocimetry
PP	Parallel plate geometry
PSV	Particle shadow velocimetry
PTU	Programmable timing unit
PTV	Particle tracking velocimetry

SI	Sisko model
SIS	Shear-induced structure
STB	Shake the box
TBL	Turbulent boundary layer
VGT	Velocity gradient tensor
VOI	Volume of interest
XG	Xanthan gum

Part I

Background

Chapter 1

Introduction

1.1 Motivation

Turbulence is a flow state characterized by a chaotic velocity field that varies in both time and space (Davidson, 2015). The chaos and disorder that is associated with turbulence promotes enhanced energy dissipation, mixing, heat transfer, and drag. Turbulent flows are ubiquitous in engineering applications, many of which involve flows that are bounded by one or more solid surfaces. In some instances, turbulence can be undesirable. For example, the efficiency of fluid transport in thermofluid systems is encumbered by the additional drag needed to sustain turbulence in pipes and ducts. In other circumstances, turbulence can be advantageous; turbulence has been known to prevent stall on aircraft wings and enhance heat transfer in heat exchangers. Turbulence control techniques seek to improve the desired outcomes of these engineering applications by amplifying or attenuating the turbulent motions within the flow.

Turbulence control techniques can be categorized as active or passive (Ghaemi, 2020). Active flow control methods include sensors and actuators that detect and respond to disturbances within the flow (Cattafesta III & Sheplak, 2011). On the other hand, passive techniques are more simple. Many passive techniques involve modifications to the geometry of the solid boundary. For example, the dimples on a golf ball promote the formation of a turbulent boundary layer that delays flow separation, shrinks the size of the wake, and decreases pressure drag (Quintavalla *et al.*, 2013). Other passive control techniques involve modifications to the fluid. Dissolving trace amounts of polymers or surfactants into liquid wall-bounded flows has been a common method for attenuating turbulence and reducing skin friction drag (Qi & Zakin, 2002; White & Mungal, 2008). Dissolving these additives into a compatible liquid solvent produces a complex fluid with non-Newtonian rheology. Therefore, this passive flow control method is often referred to as rheological drag reduction (Graham, 2014).

Discovered in the late 1940s, rheological drag reduction is arguably one of the most successful, yet poorly understood passive flow control strategies (Toms, 1948; Mysels, 1949; Graham, 2014). A variety of industries have largely benefited from the use of polymers and surfactants for drag reduction or enhanced mass flow. For example, the Trans Alaska Pipeline System used polymers to increase their daily oil delivery by 300,000 barrels per day – a 20% improvement to their daily throughput (Burger *et al.*, 1980). Japan has adopted the use of surfactants in over 180 district heating and cooling facilities, some of which have demonstrated a 60% reduction in their total energy demands (Saeki, 2014). Despite its utilization in several industry applications, key aspects of rheological drag reduction remain unknown. Generally, researchers have yet to determine the mechanism by which polymers and surfactants attenuate turbulence and reduce skin friction drag.

There are incentives to better understanding the mechanism of rheological drag reduction. From an engineering perspective, this would help develop design tools and methods for better predicting the performance of drag-reducing additives (DRAs) in various industry applications. From a scientific perspective, understanding how non-Newtonian rheology interacts with turbulence can provide insights into the physics of fluid turbulence, of which much is still unknown (White & Mungal, 2008). Motivated by the possibility of improving the efficiency of thermofluid applications and better understanding the physics of rheology, fluid turbulence and turbulence control, the present research attempts to determine the traits and mechanism of rheological drag reduction for different DRAs. The remainder of this chapter summarizes existing knowledge of polymer and surfactant DRA rheology and theories regarding their rheological mechanism for drag reduction. Lastly, the objective for the current thesis is presented, followed by an overview of the thesis layout.

1.2 Rheology of polymer drag-reducers

Polymer drag-reducers are classified as having either a flexible or a rigid molecular structure (Virk & Wagger, 1990). When dissolved in a Newtonian solvent, both flexible and rigid polymers form a solution that is generally shear thinning (Escudier *et al.*, 1999; Pereira *et al.*, 2013). However, the rheological traits that are typically attributed to drag reduction are extensional viscosity and viscoelasticity (Lumley, 1973; de Gennes, 1990). For solutions of flexible polyacrylamide polymers, Owolabi *et al.* (2017) demonstrated a correlation between the amount of drag reduction in various turbulent duct flows and a characteristic relaxation time. The latter feature was obtained based on measurements of extensional stress growth in a small liquid filament contained between two rapidly displaced parallel plates using a device known as a capillary breakup extensional rheometer (CaBER). However, such a relaxation time has not been reported for samples of rigid polymer solutions. The filament of the rigid polymer solutions tends to break up rapidly upon extension using the standard CaBER systems, owing to its significantly lower extensional viscosity (Pereira *et al.*, 2013; Mohammadtabar *et al.*, 2020). With regards to viscoelasticity, a correlation between the elastic moduli of polymer solutions and drag reduction has yet to be confirmed experimentally (Pereira *et al.*, 2013; Mohammadtabar *et al.*, 2020). Therefore, a common rheological property among flexible and rigid polymer solutions that correlates with their ability to reduce drag has not been determined.

1.3 Rheology of surfactant drag-reducers

Drag-reducing solutions of surfactants can exhibit various rheological characteristics depending on the type of surfactant and the canonical flow. Qi & Zakin (2002) summarized the three qualities of dilute surfactant solutions that are of significance to drag reduction: shear-induced structures (SISs), viscoelasticity and a large extensional viscosity. The latter two properties share similarities with polymeric solutions, while SISs allude to a structural transformation of the surfactant molecules caused by deformation of the fluid. Shear-induced structures are best demonstrated in steady shear viscosity measurements. At sufficiently low shear rates the shear viscosity is Newtonian, but above a critical shear rate the viscosity increases (i.e., shear thickening). After increasing the shear rate further, the viscosity begins to decrease, becoming shear thinning. While certain surfactant solutions exhibit SISs, viscoelasticity and a large extensional viscosity, some surfactant solutions only show one, or occasionally none of these rheological traits. Lin (2000) observed that several dilute surfactant solutions had a Newtonian shear viscosity (i.e., no SISs or shear thinning), no elasticity and a Newtonian resistance to uniaxial extension. Yet, the same dilute solutions could produce large amounts of drag reduction in a turbulent pipe flow – around 70%. Therefore, a rheological property of surfactant solutions that correlates with their ability to reduce drag remains unknown.

1.4 Non-Newtonian rheology and turbulence

Understanding how non-Newtonian rheology interacts with turbulence is critical to unravelling the mechanism of rheological drag reduction. Although experimental investigations have correlated drag reduction with certain rheological features of the solution (Owolabi *et al.*, 2017), a particular interaction between the non-Newtonian rheology and the coherent patterns within the turbulent flow has yet to be determined. For example, drag-reducing flexible polymer solutions were shown to have an appreciable extensional viscosity, but it is unclear how this large extensional viscosity can reduce drag in a turbulent wall flow. It is counter-intuitive that a solution with a larger viscosity than its solvent would have less skin friction drag. Two classical theories attempt to reconcile how flexible polymers interact with turbulence and reduce drag (Lumley, 1973; de Gennes, 1990). The *viscous* theory of Lumley (1973) asserts that the large extensional viscosity of polymer solutions strongly inhibits turbulent fluctuations just outside the viscous sublayer, causing the buffer layer to expand and wall friction to reduce (Lumley, 1973; White & Mungal, 2008). In a channel flow simulation that utilized a simplified constitutive model of polymer stresses – the retarded-motion expansion (Bird *et al.*, 1987) – Roy *et al.* (2006) demonstrated that the non-Newtonian extensional viscosity opposed flow in both uniaxial and biaxial flow regions, which mitigated the strength and formation of quasi-streamwise vortices and reduced drag. On the other hand, the *elastic* theory of de Gennes (1990) speculates that polymers are not sufficiently stretched within a turbulent flow to produce a large local enhancement in extensional viscosity. Rather, drag reduction occurs when turbulent kinetic energy becomes comparable to the elastic energy of the flexible polymers. Each theory has their own merit (Roy *et al.*, 2006; Min *et al.*, 2003*a*,*b*); however, evidence that one is more valid than the other has not been established (White & Mungal, 2008; Xi, 2019). Furthermore, the viscous and elastic theories are only considered applicable for flexible polymers and not rigid polymers or surfactants; although, de Gennes (1990) conjectured that the viscous theory could apply to rigid polymers. It is therefore unclear whether the mechanism for drag reduction is similar among these different additives.

1.5 Objective and methods

The overarching objective of the present dissertation is to compare the rheology and drag-reducing capabilities of different DRAs – namely a flexible polymer, rigid polymer and surfactant. Prior evidence suggests that their respective mechanisms for drag reduction are unique, given their different chemical composition and rheological features. Therefore, it is expected that the fluids will respond differently within a turbulent environment. The DRA solutions are evaluated using the following methods.

1. The rheology of the three DRA solutions are compared at similar concentrations.

2. One-point and two-point ensemble statistics are measured and contrasted for the three DRA solutions in a turbulent channel flow with similar amounts of drag reduction.

3. Coherent flow patterns are identified within a polymer drag-reduced turbulent boundary layer. The influence of non-Newtonian rheology on the topology of the turbulent flow is determined.

Surprisingly, it is found that different DRA solutions, with unique rheology, can produce similar velocity statistics within a turbulent wall flow. Assertions are made regarding each DRAs respective mechanism for drag reduction.

1.6 Thesis overview

This thesis is separated into five parts: Background, Rheology, Turbulent channel flow, Turbulent boundary layer, and Closing. A description of the chapters contained with each part are detailed below.

Part I: Background

- Chapter 1: Introduction

  This chapter describes the motivation for investigating DRAs, the existing understanding of the mechanism for drag reduction, and the objectives and overview of the current thesis.

- Chapter 2: Complex fluids and rheology

  Rheological traits and principles, common in drag-reducing solutions, are derived and discussed. These traits include shear viscosity, linear viscoelasticity and extensional viscosity.

- Chapter 3: Wall-bounded turbulence

  An overview of wall-bounded turbulence is presented. Details regarding the canonical Newtonian turbulent channel and boundary layer flows are provided, followed by brief discussions of drag-reduced wall flows. Background information is also provided about identifying flow topology and turbulent coherent patterns utilizing a method known as the Δ-*criterion*.

- Chapter 4: Experimental methods

  A description of the experimental facilities and measurements are provided. These include rheological measurements (steady shear, dynamics shear and extensional), wall-bounded turbulent flow facilities (channel and boundary layer flows), and the flow measurements used to analyze the wall-bounded turbulent flows.

Part II: Rheology

- Chapter 5: Shear and extensional rheology

  Steady shear, dynamic shear and extensional rheology of DRA solutions, including a flexible polymer, rigid polymer and a cationic surfactant solution, are documented and compared.

- Chapter 6: Nontrivial rheology

  Conventional rheology done in Chapter 5, does not yield a non-Newtonian response for certain DRA solutions. To discern the non-Newtonian features of these fluids, the flow through nontrivial apparatus, a periodically constricted tube, is considered.

Part III: Turbulent channel flows

- Chapter 7: Comparing drag-reduced channel flows of polymer and surfactants

  One-point and two-point ensemble velocity statistics are compared among the drag-reduced flows of flexible polymers, rigid polymer and suractants. Flows are compared at a common drag reduction percentage.

- Chapter 8: Lubricating layer in drag-reduced flow of rigid polymers

  Assuming the rigid polymer solution is inelastic, a generalized Newtonian constitutive model is used to comment on the rheological features of the rigid polymer solution within the turbulent flow. A near-wall lubricating layer, with a lower viscosity than the channel core is found.

Part IV: Turbulent boundary layer

- Chapter 9: Local flow topology of a polymer-laden boundary layer

  High spatial resolution velocity measurements in a thick boundary layer are used to derive velocity gradients within the turbulent and drag-reduced wall flows. Velocity gradients and the Δ-*criterion* are used to establish the distribution of fine scale motions within a turbulent drag-reduced flow. The effect of non-Newtonian rheology on the flow topology is presented.

Part V: Closing

- Chapter 10: Conclusions

  The conclusions of the thesis are presented and potential future works are suggested.

- Appendix A: Uncertainty analysis

  Supplemental discussions on measurement uncertainty for the respective investigations in chapters 6, 7, 8 and 9 are presented.

Chapter 2

Complex fluids and rheology

With the advancement of the chemical industry at the turn of the 20th century, the production of synthetic plastics produced a number of unique materials with unconventional flow behaviours (Macosko, 1994). These complex materials sparked a wave of investigations and research that was eventually organized into a new field of study, *rheology*. The concept of rheology was developed by Dr. Eugene C. Binham in 1920 at Lehigh University; it refers to the study of the deformation and flow of matter (Barnes *et al.*, 1989). Rheology encompasses several topics including those related to fluid dynamics (also, aeronautics, hydrodynamics, hydraulics), and solid mechanics. More specifically, rheology involves determining the constitutive equations that describe the relationship between force and deformation in materials. A rheologist (i.e., someone who studies rheology) attempts to derive constitutive relations by investigating material behaviours in very simple deformation (Macosko, 1994). On the other hand, a mechanicist applies the constitutive relations developed by the rheologist to study the forces of materials in complex deformations. This philosophy is central to the present dissertation, particularly when investigating unique materials in highly complex turbulent flows.

Under simple shear deformation, the most basic relation between force and deformation in solid mechanics is Hooke's law,

$$\tau_{xy} = G\gamma_{xy} \tag{2.1}$$

where τ_{xy} is the shear stress (force per unit area), γ_{xy} is the change in length relative to the initial configuration, and G is an intrinsic property of the material known as the elastic modulus. At the other end of the spectrum, the simplest constitutive relation for fluids is Newton's law of viscosity,

$$\tau_{xy} = \mu\dot{\gamma}_{xy} \tag{2.2}$$

where $\dot{\gamma_{xy}} = d\gamma_{xy}/dt$ is the rate of shear straining and μ is the shear viscosity of the material. There are a number of ideal elastic solids or Hookean solids, such as metals and ceramics, that obey equation (2.1) (Macosko, 1994). Similarly, gases and most small molecule liquids, such as water and oils, are Newtonian fluids and obey equation (2.2). However, many materials – including blood, polymers and foods – have properties that fall somewhere between an ideal Hookean solid and Newtonian fluid. The focus of the present dissertation is on liquid-like non-Newtonian materials with a propensity to reduce drag in a turbulent flow regime. These include dilute aqueous solutions of polymers and surfactants. The following section will review the common rheological traits (shear viscosity, linear viscoelasticity, and extensional viscosity) of non-Newtonian drag-reducing liquids. Three different types of simplified flow deformations or rheometric flows (steady shear, dynamic shear, and uniaxial extension) that help discern these rheological traits will be considered. Before discussing these traits, the conservation equations of a moving fluid are defined.

Conservation of mass and momentum are represented by the following equations,

$$\nabla \cdot \boldsymbol{U} = -\frac{1}{\rho}\frac{D\rho}{Dt}, \tag{2.3a}$$

$$\rho\frac{D\boldsymbol{U}}{Dt} = -\nabla P + \nabla \cdot \boldsymbol{\tau} + \boldsymbol{f}, \tag{2.3b}$$

where ρ is the fluid density, $\boldsymbol{U}$ is the velocity vector, P is the static pressure, $\boldsymbol{\tau}$ is the symmetric deviatoric stress tensor, and $\boldsymbol{f}$ is the body force vector. Here, the total or material derivative of $\boldsymbol{U}$ is represented as $D\boldsymbol{U}/Dt = \partial\boldsymbol{U}/\partial t + \boldsymbol{U} \cdot \nabla\boldsymbol{U}$. Liquids are generally incompressible with ρ that is constant; therefore, $D\rho/Dt = 0$ and equation (2.3*a*) simplifies to $\nabla \cdot \boldsymbol{U} = 0$. The velocity gradient tensor (VGT) $\mathbf{L} = \nabla\boldsymbol{U}$ describes the relative rate of separation between neighbouring points within a material. The VGT can be decomposed into a symmetric rate of deformation tensor $\mathbf{D} = (\nabla\boldsymbol{U} + \nabla\boldsymbol{U}^{\dagger})/2$ and antisymmetric rate of rotation tensor $\mathbf{W} = (\nabla\boldsymbol{U} - \nabla\boldsymbol{U}^{\dagger})/2$, where $\mathbf{L} = \mathbf{D} + \mathbf{W}$ and $\dagger$ is the transpose operation. The constitutive equation is the relationship between the deviatoric stress tensor $\boldsymbol{\tau}$ and the rate of deformation tensor $\mathbf{D}$, which describes the rate of stretching and straining. For a Newtonian fluid, the constitutive equation in full tensor notation is $\boldsymbol{\tau} = 2\mu\mathbf{D}$, and equation (2.3*b*) reduces to the well-known Navier-Stokes equation.

2.1 Shear viscosity

A schematic of Couette flow, the most simple steady shear flow, is shown in figure 2.1. Here, fluid is contained between two parallel surfaces separated by a distance H along y, where x, y and z are the streamwise, wall-normal and spanwise directions respectively. The upper surface moves tangentially relative to the lower surface at a constant speed of U_H along x. The fluid velocity is homogeneous (no velocity gradients) along the x and z directions. Fluid velocity along the streamwise, wall-normal and spanwise directions are U, V and W respectively. Due to no-slip boundary conditions, the fluid velocity at the lower surface is zero, while the velocity of the fluid at the upper surface is U_H.

Fluid velocity for Couette flow is listed as follows,

$$U = \dot{\gamma}y, \quad V = 0, \quad W = 0.$$

where $\dot{\gamma} = \partial U/\partial y = U_H/H$ is the shear rate. Therefore, the VGT for steady shear flow is,

$$\mathbf{L} = \begin{bmatrix} 0 & \dot{\gamma} & 0 \\ 0 & 0 & 0 \\ 0 & 0 & 0 \end{bmatrix} \tag{2.4}$$

the rate of deformation tensor is,

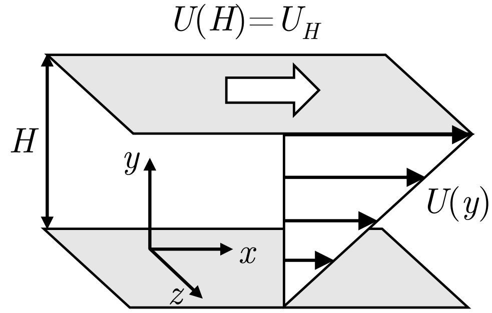

Figure 2.1: Schematic of steady simple shear flow or Couette flow. The shaded grey surfaces represent solid walls.

$$\mathbf{D} = \begin{bmatrix} 0 & \dot{\gamma}/2 & 0 \\ \dot{\gamma}/2 & 0 & 0 \\ 0 & 0 & 0 \end{bmatrix} \tag{2.5}$$

and the rate of rotation tensor is,

$$\mathbf{W} = \begin{bmatrix} 0 & \dot{\gamma}/2 & 0 \\ -\dot{\gamma}/2 & 0 & 0 \\ 0 & 0 & 0 \end{bmatrix} \tag{2.6}$$

For a Newtonian fluids, the deviatoric stress is proportional to the rate of deformation $\boldsymbol{\tau} = 2\mu\mathbf{D}$; therefore, the only nonzero components of $\boldsymbol{\tau}$ is $\tau_{xy} = \tau_{yx} = \mu\dot{\gamma}$. Note that τ is usually presented as the shear stress, and hence going forward, it should be assumed that $\tau = \tau_{xy}$. Therefore, the viscosity can be derived according to $\mu = \tau/\dot{\gamma}$. For simplicity, the shear strain and shear rate are also represented as $\gamma_{xy} = \gamma$ and $\dot{\gamma}_{xy}$, respectively.

In various non-Newtonian fluids μ has a strong dependence on the shear rate, $\dot{\gamma}$. Generalized Newtonian fluids have a shear-rate dependent stress and viscosity. The most simple example of a shear-rate dependent fluid is a power-law fluid with a shear stress and viscosity of the form

$$\tau = M\dot{\gamma}^k, \quad \text{and} \quad \mu = M\dot{\gamma}^{k-1}. \tag{2.7}$$

where M and k are constants called the consistency and flow index. Non-Newtonian materials with $k < 1$ exhibit shear thinning where μ decreases with increasing $\dot{\gamma}$. This is arguably the most commonly observed non-Newtonian feature of drag-reducing fluids comprising polymers (Escudier *et al.*, 1999, 2009; Mitishita *et al.*, 2023); however, it is unclear if shear thinning is necessary for drag reduction. Boger fluids are an example of a fluid that exhibits no shear thinning, but is viscoelastic and proven to reduce drag (James, 2009; Min *et al.*, 2003*a*,*b*).

2.2 Linear viscoelasticity

The term "viscoelastic" implies the simultaneous existence of viscous and elastic properties within a material (Barnes *et al.*, 1989). Linear viscoelasticity relies on the notion that the differential equation that relates stress and strain are linear. Mechanical models or spring and dashpot diagrams provide analogs or visual depictions of linear viscoelastic materials. Hookean deformation is represented by a spring with an elastic modulus of G, similar to (2.1). While Newtonian flow is represented using a dashpot with a viscosity of μ, similar to (2.2). A Maxwell material consists of a spring and dashpot in series, as shown in figure 2.2. When the spring and dashpot are in series, the strain or strain-rates are additive. Therefore, the linear ordinary differential equation that describes the deformation within the Maxwell element is,

$$\frac{1}{G}\dot{\tau} + \frac{1}{\mu}\tau = \dot{\gamma},$$

where $\dot{\tau} = d\tau/dt$. A relaxation time can be derived according to $t_e = \mu/G$, and the previous equation can be rearranged to,

$$t_e\dot{\tau} + \tau = \mu\dot{\gamma}. \tag{2.8}$$

This is one example of a linear viscoelastic model. Other examples include the Kelvin model (a spring and dashpot in parallel) and the Jeffrey model (a dashpot in series with a spring-dashpot in parallel) (Barnes *et al.*, 1989). Two different types of methods are used to measure linear viscoelastic behaviour, including static and dynamic methods. Static methods include creep and relaxation tests where a step change in the shear stress or strain is applied to a material and temporal development in the strain or stress is observed. Dynamic tests involve the application of a harmonically varying shear stress or strain, and are often called small amplitude oscillatory shear measurements. In more liquid-like materials, static tests do not produce a very obvious viscoelastic response; therefore, dynamic viscoelastic tests are prioritized.

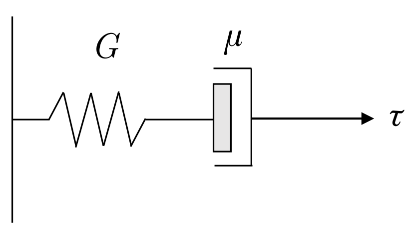

Figure 2.2: Mechanical model or spring and dashpot diagram of a Maxwell material.

Small amplitude oscillatory shear measurements involve deforming a sample with a sinusoidally varying shear strain γ in time t. A viscoelastic material will respond with a shear stress τ that oscillates with the same frequency as γ, but with a phase offset ψ between 0° and 90°. Here, the strain and stress are represented as,

$$\gamma = \gamma_0 \sin(\omega t), \tag{2.9a}$$

$$\tau = \tau_0 \sin(\omega t + \psi), \tag{2.9b}$$

where ω is the oscillation frequency in rad s^{-1}, γ_0 is the amplitude of the strain wave, and τ_0 is the amplitude of the stress response. In this type of deformation γ can be applied in the same configuration as figure 2.1, where a fluid sample is contained between two parallel surfaces and the upper surfaces oscillates such that the strain rate within the sample is,

$$\dot{\gamma} = \frac{d\gamma}{dt} = \omega\gamma_0 \cos(\omega t).$$

Recall that the velocity of the upper surface can be similarly represented as $U_H = H\dot{\gamma}$.

From trigonometric identities, it can be shown that the shear stress τ can be decomposed into a component that is in-phase with γ, i.e., $\tau_0' = \tau_0 \cos(\psi)$, and another that is 90° out-of-phase with γ, i.e., $\tau_0'' = \tau_0 \sin(\psi)$. In other words, τ can represented according to,

$$\tau = \tau_0' \sin(\omega t) + \tau_0'' \cos(\omega t).$$

Using each of these amplitudes, an in-phase and out-of-phase elastic moduli can be derived,

$$G' = \frac{\tau_0'}{\gamma_0}, \tag{2.10a}$$

$$G'' = \frac{\tau_0''}{\gamma_0}, \tag{2.10b}$$

where G' is also referred to as a gain modulus and G'' is a loss modulus. The phase offset ψ, can be determined according to,

$$\tan(\psi) = \frac{G''}{G'}, \tag{2.11}$$

For a Hookean solid G' is finite, $G'' = 0$ and $\psi = 0°$. While for a Newtonian fluid $G' = 0$, G'' is finite and $\psi = 90°$. For a Maxwell material of figure 2.2 and (2.8), with mixed contributions of elastic and viscous features, the gain and loss moduli are,

$$G' = \frac{\mu t_e \omega^2}{1 + \omega^2 t_e^2}, \tag{2.12a}$$

$$G'' = \frac{\mu\omega}{1 + \omega^2 t_e^2}, \tag{2.12b}$$

and the phase offset between the strain and stress signals is,

$$\tan(\psi) = \frac{1}{t_e \omega}.$$

Small amplitude shear viscosity or dynamic shear viscosity measurements are a useful method for discerning the non-Newtonian properties, namely the linear viscoelasticity, of a complex material. Although better than static viscoelastic measurements, dynamic shear viscosity measurements have their limitations, particularly when evaluating dilute aqueous solutions with low shear viscosities. Therefore, this analysis is used less often in the present dissertation than steady shear and extensional rheology. However, elasticity is believed by many to be a key rheological feature of drag reduction (Tabor & de Gennes, 1986; de Gennes, 1990). As such, dynamic shear viscosity measurements are performed when possible.

2.3 Extensional viscosity

Non-Newtonian elastic liquids generally exhibit significantly different extensional or elongational flow features than Newtonian fluids. Lumley (1973) and Roy *et al.* (2006) argued that the nonmontonic trend in the so-called extensional viscosity with strain rate in dilute liquid-like polymer solutions is the rheological property responsible for turbulent drag reduction. Therefore, quantifying the extensional properties of the drag-reducing liquids is important. Three of the most simple types of steady extensional flows are uniaxial, biaxial and planar extension (Barnes *et al.*, 1989). For bevity, only uniaxial extensional flow is reviewed.

Steady uniaxial extension consists of a velocity of the form,

$$U = \dot{\varepsilon}x, \quad V = -\dot{\varepsilon}y/2, \quad W = -\dot{\varepsilon}z/2.$$

where $\dot{\varepsilon}$ is the extension rate. Therefore, the VGT and rate of deformation tensor for the steady uniaxial extensional flow is,

$$\mathbf{L} = \mathbf{D} = \begin{bmatrix} \dot{\varepsilon} & 0 & 0 \\ 0 & -\dot{\varepsilon}/2 & 0 \\ 0 & 0 & -\dot{\varepsilon}/2 \end{bmatrix}, \tag{2.13}$$

while the rate of rotation tensor is $\mathbf{W} = 0$. The uniaxial extensional viscosity μ_E can be represented as,

$$\tau_{xx} - \tau_{yy} = \dot{\varepsilon}\mu_E. \tag{2.14}$$

For a Newtonian fluid,

$$\tau_{xx} - \tau_{yy} = 3\mu\dot{\varepsilon}.$$

The Trouton ratio $Tr = \mu_E/\mu$ defines the ratio between the extensional and shear viscosity. For a Newtonian fluid under uniaxial deformation, the Trouton ratio is identically 3. Elastic polymer solutions with a shear thinning viscosity are known to exhibit large Tr greater than 3 (Barnes *et al.*, 1989). Contrary to shear thinning, the extensional viscosity of viscoelastic polymer solutions μ_E tends to increase dramatically with increasing $\dot{\varepsilon}$, a trend known as tension thickening. Measuring μ_E is difficult, considering imposing uniaxial deformation (or biaxial and planar extension) of the form of (2.13) at a constant strain rate $\dot{\varepsilon}$ and without any shear deformation is challenging. That being said, some recent techniques have been developed (Rodd *et al.*, 2005; Dinic *et al.*, 2015), some of which are utilized in the current dissertation and detailed in §4.1.

Chapter 3

Wall-bounded turbulence

Many turbulent flows encountered in engineering systems are bounded by one or more solid surfaces. When fluid flows over a solid wall a boundary layer profile develops due to viscous shear stresses and the no-slip boundary condition. For internal duct flows, e.g., pipe flows, the boundary layers develop along all walls of the conduit and their thickness increases along the flow direction. With increasing streamwise distance, the flow eventually becomes fully developed and the profiles merge, occupying the complete duct cross-section. External flows, e.g, the boundary layer along the surface of a vehicle, develop freely and continuously along the flow direction. They also consists of a turbulent/non-turbulent interface, where the turbulent boundary layer meets the uniform free stream. An internal channel flow and external boundary layer are considered in the present dissertation. The current chapter provides details regarding the canonical turbulent channel and boundary layer flows, respectively. Background information about polymer and surfactant drag-reduced channel and boundary layer flows are also provided. The final section of this chapter discusses the concept of flow topology and the utilization of the $\Delta-$*criterion* for identifying coherent patterns within turbulent flows.

3.1 General equations and definitions

The conservation of mass and momentum was defined previously in §2. Equations (2.3) are valid for both laminar and turbulent flows. In a turbulent regime, a Reynolds decomposition can be used to segregate the velocity and pressure into a time average and fluctuating component. The Reynolds decomposed velocity components are as follows:

$$U = \langle U \rangle + u, \tag{3.1a}$$

$$V = \langle V \rangle + v, \tag{3.1b}$$

$$W = \langle W \rangle + w \tag{3.1c}$$

where $\boldsymbol{u}$ is the fluctuating velocity vector with components u, v, w. The angle brackets $\langle \cdots \rangle$ represent the Reynolds time average. For the streamwise velocity, the Reynolds time average is defined according to,

$$\langle U \rangle = \lim_{T \to \infty} \frac{1}{T} \int_0^T U(x, y, z, t) dt.$$

For a Newtonian fluid, the deviatoric stress tensor is represented as, $\boldsymbol{\tau} = 2\mu\mathbf{D}$. When the terms in equation (3.1) are substituted into (2.3) and the resulting equation is time averaged, the mean mass and momentum equations for an incompressible Newtonian fluid are,

$$\nabla \cdot \langle \boldsymbol{U} \rangle = 0, \tag{3.2a}$$

$$\rho\langle \boldsymbol{U} \rangle \cdot \nabla\langle \boldsymbol{U} \rangle = -\nabla\langle P \rangle + \mu\nabla^2\langle \boldsymbol{U} \rangle - \rho\nabla \cdot \langle \boldsymbol{uu} \rangle, \tag{3.2b}$$

where $\langle \boldsymbol{uu} \rangle$ is the Reynolds stress tensor and is representative of turbulent velocity fluctuations. Equation (3.2) describes the mean balance of momentum within a Newtonian, turbulent flow and is more commonly known as the Reynolds averaged Navier-Stokes equations.

3.2 Channel flows

A depiction of a fully-developed two-dimensional (2D) channel flow is shown in figure 3.1. Fluid is contained between two parallel walls separated by height H and propelled along the positive $x-$direction by a favourable pressure gradient $\partial\langle P \rangle/\partial x < 0$. At the walls ($y = 0$, and $y = H$) there is a no-slip boundary condition, $U = W = 0$, and a non-permeable boundary condition, $V = 0$. Along the centreline of the channel, where $y = h = H/2$, mean streamwise velocity $\langle U \rangle$ is at a maximum. Fluid is also bound along the $z-$direction between two side walls that are into and out of the plane of the page with reference to figure 3.1. Flow within the channel is considered two-dimensional if the width is significantly larger than H. Dean (1978) prescribed that an aspect ratio larger than 7 produces approximately two-dimensional flow. Similarly, the flow is fully-developed if the length of the channel is significantly longer than H. Fully-developed, two-dimensional flow implies that the ensemble velocity statistics, such as $\langle U \rangle$, do not vary along x or z and the mean spanwise velocity $\langle W \rangle$ equals zero. From mass conservation (3.2*a*) it can also be shown that $\langle V \rangle = 0$.

The Reynolds number defines the ratio of inertial to viscous forces within the flow. A bulk Reynolds number Re_H is defined according to,

$$Re_H = \frac{\rho U_b H}{\mu} \tag{3.3}$$

where U_b is the bulk or average velocity across y,

$$U_b = \frac{1}{h}\int_0^h \langle U \rangle dy.$$

Above an Re_H of 5772, flow within the channel is linearly unstable and turbulent (Orszag, 1971). Hence, velocity fluctuations or Reynolds stresses are present.

Simplifying (3.2*b*), the mean streamwise momentum balance of the turbulent channel flow is,

$$0 = -\frac{\partial\langle P \rangle}{\partial x} + \mu\frac{\partial^2\langle U \rangle}{\partial y^2} - \rho\frac{\partial\langle uv \rangle}{\partial y}.$$

Integrating the above equation produces the mean streamwise stress balance,

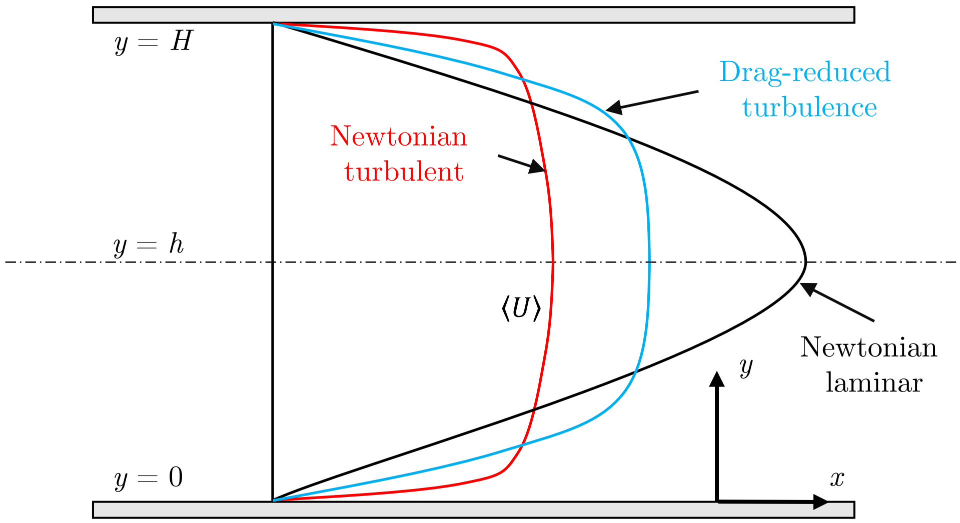

Figure 3.1: Schematic of a two-dimensional channel flow. Representative mean velocity profiles $\langle U \rangle$ are drawn for Newtonian turbulent, Newtonian laminar and non-Newtonian drag-reduced turbulence at a similar U_b. Grey shaded regions are the channel walls.

$$\tau(y) = \tau_v + \tau_R = \mu \frac{d\langle U \rangle}{dy} - \rho \langle uv \rangle, \tag{3.4}$$

where τ is the total mean stress, τ_v is the viscous stress, and τ_R is the Reynolds shear stress (Pope, 2000). In the case of a channel flow, the streamwise pressure gradient and wall-normal gradient of shear stress are constant and equal. Therefore, the wall shear stress can be defined according to,

$$\tau_w = -h \frac{\Delta \langle P \rangle}{\Delta x}, \tag{3.5}$$

and,

$$\tau(y) = \tau_w \left(1 - \frac{y}{h}\right), \tag{3.6}$$

In equation (3.4), τ_R becomes zero close to the wall due to the no-slip boundary condition. Therefore, τ_w can be similarly represented as,

$$\tau_w = \mu \frac{\partial \langle U \rangle}{\partial y}\bigg|_{y=0}. \tag{3.7}$$

A non-dimensional wall shear stress or skin friction coefficient is defined according to,

$$C_f = \frac{\tau_w}{\frac{1}{2}\rho U_b^2}. \tag{3.8}$$

Dean (1978) found that C_f varied with respect to Re_H according to,

$$C_f = 0.073 Re_H^{-0.25} \tag{3.9}$$

based on an empirical fit of various experimental measurements of C_f and Re in Newtonian channel flows.

Near the wall, Reynolds stresses approach zero, due to the no-slip boundary condition and viscous stresses are more significant. The so-called *viscous scales* are used to define the appropriate velocity and legnthscales for which these viscous effects are important. These include the friction velocity,

$$u_\tau = \sqrt{\frac{\tau_w}{\rho}}, \tag{3.10}$$

and viscous lengthscale,

$$\delta_\nu = \frac{\nu}{u_\tau}, \tag{3.11}$$

where $\nu = \mu/\rho$ is the kinematic viscosity. The friction Reynolds number Re_τ, is used to define the separation between the viscous and geometric length scales according to,

$$Re_\tau = \frac{u_\tau h}{\nu} = \frac{h}{\delta_\nu}. \tag{3.12}$$

As Re_τ increases, δ_ν decreases, and so does the thickness of the viscous wall region. The friction and bulk Reynolds numbers can be approximately related with one another according to, $Re_\tau \approx 0.09 Re_H^{0.88}$ (Pope, 2000).

The velocity and wall-normal distance normalized by the viscous scales are defined as $\langle U \rangle^+ = \langle U \rangle / u_\tau$ and $y^+ = y/\delta_\nu$. Derived from various scaling arguments, i.e., *the law of the wall*, the velocity profile within a Newtonian turbulent channel flow takes on a piece-wise function of the form,

$$\langle U \rangle^+ = \begin{cases} y^+, & y^+ \leq 5, \\ (1/\kappa)\ln(y^+) + B, & y^+ > 30, \quad y/h < 0.3. \end{cases} \tag{3.13}$$

where κ is the Von Kármán coefficient, and B is a constant. The flow region defined by $y^+ < 5$ is referred to as the viscous sublayer, while the region with $y^+ > 30$ is denoted the logarithmic layer. Between the viscous sublayer and log layer $5 < y^+ < 30$, is referred to as the buffer layer. Another profile of $\langle U \rangle^+$ exists for y/h greater than 0.3, which is derived from the velocity defect law (Pope, 2000). However, this profile does not differ significantly from the log layer and is omitted in (3.13) for brevity. The approximate values for the Von Kármán coefficient and log layer intercept are, $\kappa = 0.41$ and $B = 5.2$ (Pope, 2000). Figure 3.2(*a*) demonstrates that the distributions of (3.13) show good agreements and overlap with the profiles of $\langle U \rangle^+$ derived from direct numerical simulation (DNS) of a Newtonian turbulent channel flow by Lee & Moser (2015) at an Re_τ of 550. When not normalized by the viscous scales, the velocity profile $\langle U \rangle$ takes on a distribution similar to that shown schematically in figure 3.1, where velocity gradients are much larger near the wall than closer to the channel centreline. At a similar bulk or average velocity U_b, the turbulent profile of $\langle U \rangle$ is more "flat" or blunted near the channel core compared to the parabolic laminar velocity profile shown in red.

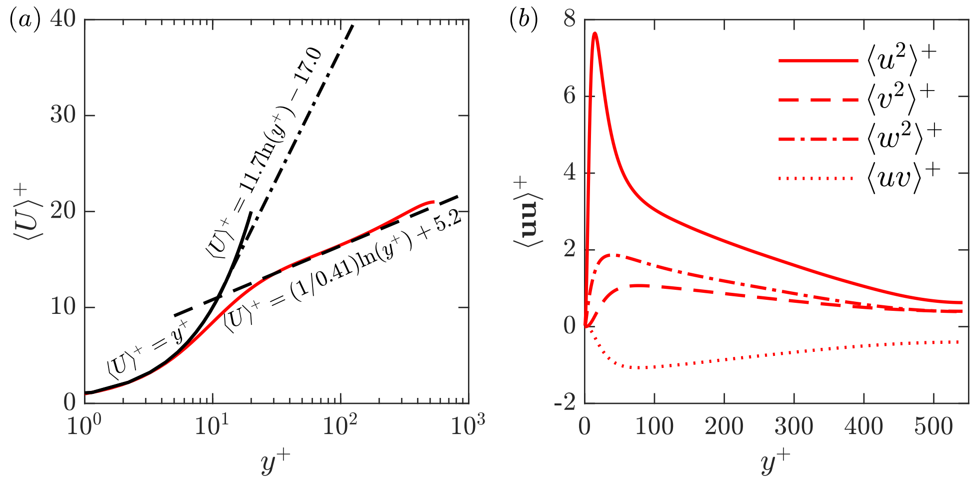

Figure 3.2: Profiles of (*a*) mean velocity and (*b*) Reynolds stresses for the Newtonian turbulent channel flow DNS by Lee & Moser (2015) at a $Re_\tau = 550$. In (*a*) the solid red line is the $\langle U\rangle^+$ versus y^+ profiles from Lee & Moser (2015), the solid black line is the linear viscous sublayer and the dashed black line is the log layer profile of (3.12). The dash-dotted black line in (*a*) is the MDR ultimate profile of (3.16).

Drag-reduced flows of polymers and surfactants have a lower skin friction coefficient C_f relative to Newtonian turbulent channel flows at a similar Re_H. A drag reduction percentage is defined according to,

$$DR = \left(1 - \frac{C_{f,NN}}{C_{f,N}}\right) \times 100\% \tag{3.14}$$

where $C_{f,NN}$ is the skin friction coefficient of the non-Newtonian drag-reduced flow, and $C_{f,N}$ is the skin friction coefficient of the turbulent Newtonian flow at a similar Re_H. For generally all types of drag-reducing additives, polymers or surfactants, DR increases monotonically with the additive concentration c. Eventually, the DR saturates and no longer increases with further enhancements of c (Virk *et al.*, 1970). The limit at which DR saturates is the maximum drag reduction (MDR) asymptote, represented by the distribution

$$\frac{1}{\sqrt{C_f}} = 19.0 \log_{10}(Re_H\sqrt{C_f}) - 32.4. \tag{3.15}$$

The DR that corresponds to the MDR asymptote is generally around 60-80% depending on Re_H.

One of the most noticeable effects of polymer and surfactant drag-reducers is the modification to $\langle U\rangle$ relative to the Newtonian profile. The elastic sublayer model of Virk (1971) described drag-reduced flows with intermediate DR as having three layers: a viscous sublayer, a buffer layer — that was re-termed the elastic sublayer — and a logarithmic layer that was referred to as the Newtonian plug layer. Relative to Newtonian flows, the viscous and elastic sublayers of a polymer drag-reduced flow are thicker. The Newtonian plug layer possesses a similar slope $1/\kappa$ as the logarithmic layer of a Newtonian flow, but a larger intercept B due to the thickened buffer or elastic sublayer. When the flow attains MDR, the Newtonian plug layer is eradicated and the elastic sublayer demonstrates an ultimate profile (Virk *et al.*, 1970), represented as

$$\langle U\rangle^+ = 11.7\ln(y^+) - 17.0, \tag{3.16}$$

and shown by the black dash-dotted line in figure 3.2(*a*). Drag-reduced flows not at MDR will have a $\langle U\rangle^+$ profile that falls between the Newtonian log layer of (3.13) and the ultimate profile of (3.16). The elastic sublayer model and ultimate MDR velocity profile have been observed in a number of experimental and numerical investigations (Warholic *et al.*, 1999*b*; Ptasinski *et al.*, 2001, 2003; Min *et al.*, 2003*b*). When not normalized by the viscous scales, the velocity profile $\langle U\rangle$ for a polymer or surfactant drag-reduced channel flow takes on a distribution similar to that shown schematically in figure 3.1. At a similar U_b, the drag-reduced flow lies somewhere between the laminar and turbulent distributions. Note, that if the viscosity μ of the drag-reduced flow is similar to the Newtonian fluid, flows with an identical U_b also constitutes a matching Re_H as per (3.3). Even at MDR, drag-reduced flows are not laminar. Instead, a drag-reduced flow has velocity fluctuations that are significantly attenuated relative to Newtonian turbulence.

Reynolds stress profiles demonstrate the significance of velocity fluctuations within the turbulent flow. Plots of the non-zero components of the Reynolds stress tensor $\langle \boldsymbol{uu}\rangle$ are shown in figure 3.2(*b*) for the Newtonian turbulent channel flow DNS of Lee & Moser (2015) at a Re_τ of 550. Here, the Reynolds stresses are normalized by u_τ^2, e.g., $\langle u^2\rangle^+ = \langle u^2\rangle/u_\tau^2$. Based on figure 3.2(*b*), the largest Reynolds stress component is $\langle u^2\rangle^+$, followed by $\langle w^2\rangle^+$, and then $\langle v^2\rangle^+$. The Reynolds shear stress $\tau_R = -\langle uv\rangle^+$, is the negative distribution shown in figure 3.2(*b*). The most energetic turbulence activity occurs within the buffer layer of the flow, where the large peak in $\langle u^2\rangle^+$ is situated.

Several experimental investigations have documented the modification to the Reynolds stresses caused by polymers and surfactants (Ptasinski *et al.*, 2001; Escudier *et al.*, 2009; Mohammadtabar *et al.*, 2017). Warholic *et al.* (1999*b*) showed that polymer drag-reduced flows have different inner-normalized Reynolds stress profiles depending on whether DR was "low" or "high". The transition between these two states, coined low drag reduction (LDR) and high drag reduction (HDR), occurred at a DR of approximately 40% (Warholic *et al.*, 1999*b*). The main distinction in the Reynolds stresses of LDR and HDR flows was the change in the peak value of the Reynolds stresses (Warholic *et al.*, 1999*b*; Escudier *et al.*, 2009). For polymer drag-reduced flows at LDR, an increase in DR was accompanied by an increase in the peak streamwise Reynolds stress, $\langle u^2\rangle^+$, and an attenuation in the wall-normal, $\langle v^2\rangle^+$, and spanwise Reynolds stresses, $\langle w^2\rangle^+$. In contrast, HDR flows showed a decrease in all Reynolds stresses with increasing DR. The Reynolds shear stress, $\langle uv\rangle^+$, of a polymer drag-reduced flow decreased monotonically with increasing DR in both LDR and HDR regimes. Warholic *et al.* (1999*b*) found that the profile of $\langle uv\rangle^+$ for drag-reduced flows close to MDR was approximately zero for all y^+. Contrary to the findings of Warholic *et al.* (1999*b*), other experiments and simulations have suggested a $\langle uv\rangle^+$ profile equal to zero is not a necessary condition for MDR (Ptasinski *et al.*, 2003). The discrepancy still remains unexplained, but it is generally accepted that flows near MDR have a significantly attenuated Reynolds shear stress profile (White & Mungal, 2008).

3.3 Boundary layers

A schematic of a boundary layer flow over a smooth flat surface is shown in figure 3.3. The boundary layer is formed when a uniform laminar free-stream, with a streamwise velocity U_∞, flows over a flate plate. Compared to the channel flow of figure 3.1, the boundary layer flow has a thickness along y that is unconfined. Instead, the boundary layer thickness δ increases with x, shown in figure 3.3. The statistics are therefore, dependent both on y and x. That being said, statistics are still independent of the spanwise direction, assuming the boundary layer is not bounded along z. Fluid at the wall $y = 0$ satisfies the no-slip ($U = W = 0$) and non-permeable boundary conditions ($V = 0$). At the outer region of the flow there is a turbulent/non-turbulent interface where the boundary layer meets the uniform free-stream or $y = \delta$.

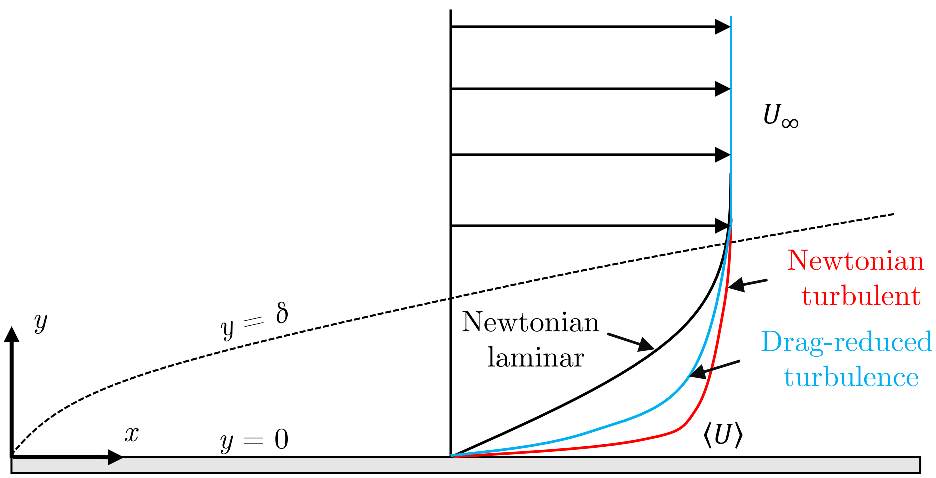

Figure 3.3: Schematic of a boundary layer flow. Representative mean velocity profiles $\langle U \rangle$ are drawn for Newtonian turbulent, Newtonian laminar and non-Newtonian drag-reduced turbulence at a similar U_∞. The grey shaded region is the wall.

The boundary layer thickness δ is defined as the value of y where $\langle U \rangle$ is equal to 99% of U_∞. Other length scales that define the boundary layer flow include the displacement thickness,

$$\delta^* = \int_0^\infty \left(1 - \frac{\langle U \rangle}{U_\infty}\right) dy, \tag{3.17}$$

and the momentum thickness,

$$\phi = \int_0^\infty \frac{\langle U \rangle}{U_\infty}\left(1 - \frac{\langle U \rangle}{U_\infty}\right) dy. \tag{3.18}$$

In the present dissertation, two Reynolds numbers are used to uniquely define the boundary layer flows. They include the friction Reynolds number,

$$Re_\tau = \frac{u_\tau \delta}{\nu}, \tag{3.19}$$

and momentum thickness Reynolds number,

$$Re_\phi = \frac{U_\infty \phi}{\nu}, \tag{3.20}$$

Utilizing Bernoulli's equation in the free-stream of the flow, it can be demonstrated that the streamwise pressure gradient can be represented as,

$$-\frac{dP_\infty}{dx} = \rho U_\infty \frac{dU_\infty}{dx}, \tag{3.21}$$

where P_∞ is the pressure within the free-stream. Applying dimensionless scaling arguments to simplify the mean mass and momentum equation (3.2*b*), yields the Newtonian boundary layer equations,

$$\frac{\partial \langle U \rangle}{\partial x} + \frac{\partial \langle V \rangle}{\partial y} = 0, \tag{3.22a}$$

$$\langle U \rangle \frac{\partial \langle U \rangle}{\partial x} + \langle V \rangle \frac{\partial \langle U \rangle}{\partial y} = -\frac{1}{\rho}\frac{\partial \langle P \rangle}{\partial x} + \nu \frac{\partial^2 \langle U \rangle}{\partial y^2} - \frac{\partial \langle uv \rangle}{\partial y}, \tag{3.22b}$$

$$0 = -\frac{1}{\rho}\frac{\partial \langle P \rangle}{\partial y} - \frac{\partial \langle v^2 \rangle}{\partial y} \tag{3.22c}$$

From (3.22*c*) it follows that the $\langle P \rangle$ is constant with respect to y, considering $\langle v^2 \rangle = 0$ at $y = 0$ and $y = \delta$ due to the no-slip boundary condition and the laminar flow conditions within the free-stream. Therefore, the following equality holds, $\partial \langle P \rangle / \partial x = dP_\infty / dx$. Utilizing (3.21), equation (3.22*b*) can be re-written as,

$$\langle U \rangle \frac{\partial \langle U \rangle}{\partial x} + \langle V \rangle \frac{\partial \langle U \rangle}{\partial y} = \frac{1}{\rho}\frac{\partial \tau}{\partial y} + U_\infty \frac{dU_\infty}{dx}, \tag{3.23}$$

where the total shear stress τ is defined as,

$$\tau(x, y) = \tau_\nu + \tau_R = \mu \frac{\partial \langle U \rangle}{\partial y} - \rho \langle uv \rangle, \tag{3.24}$$

Unlike the channel flow, the total stress τ is not a linear function of y and the streamwise pressure gradient (3.6) due to the convective terms on the left hand side of (3.23). That being said, (3.24) demonstrates that the flow still exhibits a balance between viscous and Reynolds stresses. Therefore, many of the properties defined for the channel flow are still "locally" applicable; locally meaning at a particular location along x. For example, definitions of τ_w, u_τ and δ_ν from (3.7), (3.10), and (3.11) are still valid; however, they change with respect to x. A new skin friction coefficient is defined utilizing the free-stream velocity,

$$C_f = \frac{\tau_w}{\frac{1}{2}\rho U_\infty^2}. \tag{3.25}$$

Compared to the streamwise velocity profile of a Newtonian laminar boundary, the mean velocity profile of the turbulent boundary layer is more flat and blunted, depicted in figure 3.3 and similar to that of the channel flows detailed previously in §3.2. Velocity profiles, normalized by the viscous scales also follow the law of the wall (3.13) for the turbulent boundary layer flow. Boundary layer DNS by Jiménez *et al.* (2010) at an Re_ϕ of 1551 and Re_τ of 578 is shown in figure 3.4(*a*) alongside the profiles of (3.13). The DNS profile shows good agreements with the linear viscous sublayer and log layer within their respective y^+

ranges. Reynolds stress profiles for the Newtonian DNS of Jiménez *et al.* (2010) are also visually similar to those of the channel flow. The most energetic turbulence activity within the boundary layer flow is contained within the buffer layer, where the large peak in $\langle u^2 \rangle^+$ is situated.

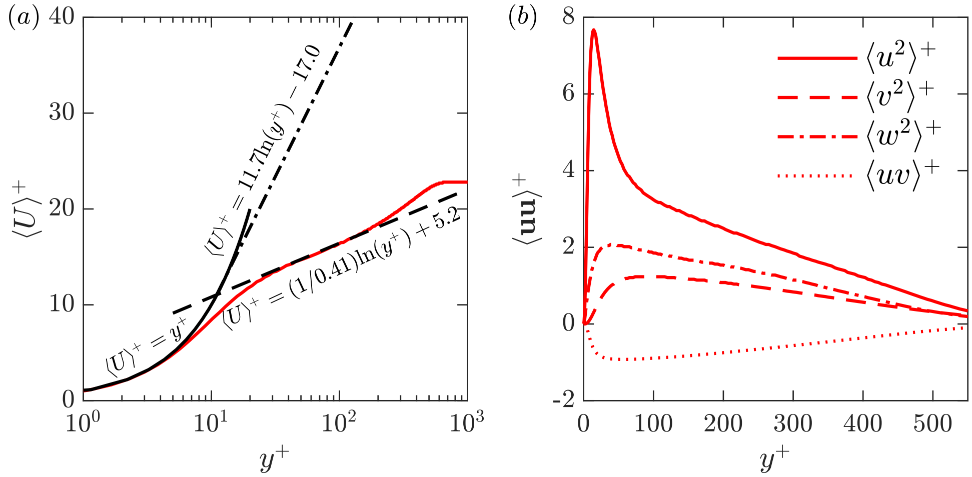

Figure 3.4: Profiles of (*a*) mean velocity and (*b*) Reynolds stresses for the Newtonian boundary layer flow DNS by Jiménez *et al.* (2010) at $Re_\phi = 1551$ and $Re_\tau = 578$. In (*a*) the solid red line is the $\langle U \rangle^+$ versus y^+ profiles from Jiménez *et al.* (2010), the solid black line is the linear viscous sublayer and the dashed black line is the log layer profile of (3.12). The dash-dotted black line in (*a*) is the MDR ultimate profile of (3.16).

Polymer and surfactant drag-reduced boundary layers can be produced using two approaches. The first involves injecting a concentrated polymer or surfactant solution into the turbulent boundary layer from a slot cut into the wall. The second involves mixing a large homogeneous solution (often called a polymer ocean) and pumping the fluid over the flat plate similar to the Newtonian solvent. Both methods have been shown to produce large quantities of DR, where DR is defined similarly to the channel flow (3.14); however, $C_{f,N}$ is defined as a Newtonian flow with a similar Re_ϕ (White *et al.*, 2004; Tamano *et al.*, 2011; Elbing *et al.*, 2013; Tamano *et al.*, 2018; Farsiani *et al.*, 2020). Modifications to the mean velocity profile are also similar to the channel flow. With increasing DR, the buffer layer expands and the intercept of the log layer B increases (Tamano *et al.*, 2018; Farsiani *et al.*, 2020). At a large enough concentration, the distribution $\langle U \rangle^+$ overlaps with the MDR ultimate profile of (3.16). Assuming the change in δ is the same between the drag-reduced and Newtonian flows, and both flows have the same U_∞, profiles of $\langle U \rangle$ appear as shown in figure 3.3. For the drag-reduced boundary layer wall shear stress is lower than the Newtonian turbulent flow. Therefore, shear near the wall is greatly diminished and the profile of $\langle U \rangle$ for the drag-reduced flow falls somewhere between the Newtonian laminar and turbulent distributions, depending on DR. Reynolds stresses within the boundary layer flow are also modified similar to that of the channel flow. White *et al.* (2004) and Tamano *et al.* (2011) demonstrated that profiles of $\langle u^2 \rangle^+$ are enhanced, while distributions of $\langle v^2 \rangle^+$, $\langle w^2 \rangle^+$ and $\langle uv \rangle^+$ are attenuated with increasing DR.

3.4 Flow topology

Turbulent flows consist of various coherent patterns that persist in both time and space (Graham & Floryan, 2021). There are a number of different types of coherent flow motions; in wall-bounded turbulence, examples of coherent flow patterns include quasi-streamwise and hairpin vortices. Together, these elemental vortical structures are believed to account for the measured ensemble statistics (e.g., mean velocity and Reynolds stresses) within the different canonical turbulent flows. Therefore, understanding the distribution and dynamics of these coherent flow patterns is crucial to comprehending the nature of turbulence and unravelling methods on how it can be controlled or manipulated. There are several methods for identifying coherent flow patterns. The present work utilizes that of Chong *et al.* (1990), where the eigenvalues and invariants of the velocity gradient tensor (VGT) are used to identify the local topology and streamline patterns about critical points within the flow.

The method established by Chong *et al.* (1990), herein referred to as the Δ-*criterion*, groups the flow into regions that are focal (vortical) and dissipative (saddle points), depending on the sign convention of the invariants and the real/complex nature of the eigenvalues. Here, Δ is defined as the discriminant of the characteristic equation of the VGT. Although the Δ-*criterion* can be applied to both compressible and incompressible fluid flows, the focus of the present work is only on incompressible flows, which narrows down the number of flow classifications. Using the Δ-*criterion*, various works have demonstrated that quasi-streamwise and hairpin vortices can be visualized in numerical simulations and flow measurements of Newtonian wall-bounded turbulence. Furthermore, the joint probability density function (JPDF) of the invariants in the VGT ear-drop or pear-shaped distribution. This tear-drop pattern in the JPDF of the VGT invariants is not only found in wall-bounded turbulence, but also turbulent mixing layers, jets and isotropic turbulence, implying a universal distribution of topologies exists among different types of Newtonian turbulence (Soria *et al.*, 1994; Chong *et al.*, 1998; Ooi *et al.*, 1999; da Silva & Pereira, 2008).

The following section will serve to summarize the Δ-*criterion* of Chong *et al.* (1990). Recall from §2 that the VGT is $\mathbf{L} = \nabla \boldsymbol{U}$, and $\boldsymbol{U}$ is the velocity vector. The characteristic equation for the tensor $\mathbf{L}$ is,

$$\Lambda^3 + P_L\Lambda^2 + Q_L\Lambda + R_L = 0, \tag{3.26}$$

where P_L, Q_L, and R_L are the invariants of $\mathbf{L}$. The eigenvalues are the roots to (3.26), and are defined as Λ_1, Λ_2 and Λ_3 in descending order of magnitude. In an incompressible flow, the first invariant $P_L = -\mathrm{tr}(\mathbf{L})$ is equal to zero, while Q_L and R_L are the only non-zero invariants of $\mathbf{L}$ and can be expressed as,

$$Q_L = -\frac{1}{2}\mathrm{tr}(\mathbf{L}^2), \tag{3.27a}$$

$$R_L = -\det(\mathbf{L}). \tag{3.27b}$$

Here, $\mathrm{tr}(\dots)$ represents the trace operator on a square matrix, and $\det(\dots)$ the determinant. The nature of the eigenvalues of $\mathbf{L}$ are dictated by the sign convention of the discriminant Δ of (2.1),

$$\Delta = \frac{27}{4}R_L^2 + Q_L^3, \tag{3.28}$$

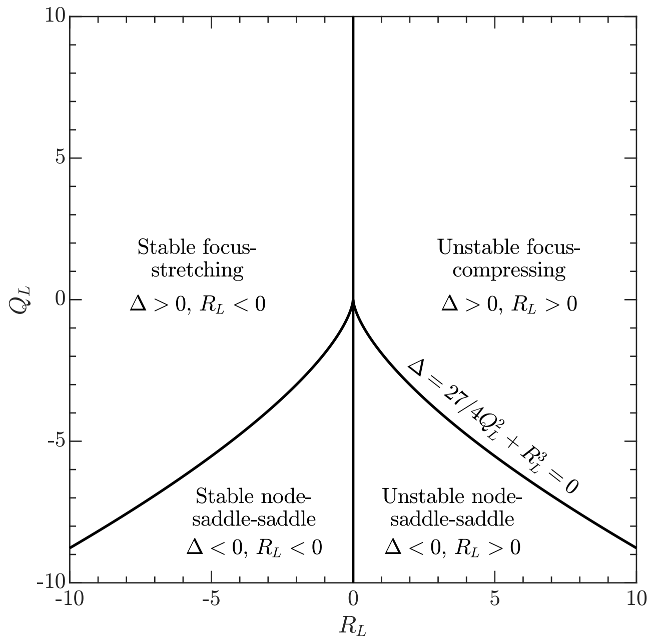

Figure 3.5: Local topologies for different R_L and Q_L in an incompressible flow with $P_L = 0$.

where $\Delta > 0$ produces one real and two complex eigenvalues, and $\Delta \leq 0$ produces three real eigenvalues. Figure 3.5 describes the different possible local flow topologies that depend on the sign convention of Δ and R_L. The lines corresponding to $\Delta = 0$, and shown in figure 3.5, are referred to as the Vieillefosse tail's. Here, ($\Delta = 0$, $R_L < 0$) is the left-Vieillefosse tail and ($\Delta = 0$, $R_L > 0$) is the right-Vieillefosse tail. Flow conditions above the Vieillefosse tail's with $\Delta > 0$, consist of motions that are focal and primarily vortical. Regions of the flow with $\Delta \leq 0$ take on a node/saddle/saddle streamline pattern. Flow topology is also divided about the $R_L = 0$ axis, where flows with $R_L < 0$ are stable (stretching) and $R_L > 0$ are unstable (compressing). JPDFs of Q_L and R_L in various Newtonian turbulent flows take on a tear-drop pattern (Soria *et al.*, 1994; Blackburn *et al.*, 1996; Chong *et al.*, 1998; Ooi *et al.*, 1999; da Silva & Pereira, 2008). The point or tip of the tear-drop falls on the right-Vieillefosse tail ($\Delta = 0$, $R_L > 0$), while the bulb of the tear-drop is situated in the quadrant of stable focus-stretching ($\Delta > 0$, $R_L < 0$).

Similar to $\mathbf{L}$, the tensors $\mathbf{D}$ and $\mathbf{W}$ have their own characteristic equation. For the tensor $\mathbf{D}$, the characteristic equation is

$$\Gamma^3 + P_D\Gamma^2 + Q_D\Gamma + R_D = 0, \tag{3.29}$$

where $P_D = -\mathrm{tr}(\mathbf{D}) = 0$, and the non-zero invariants are defined according to,

$$Q_D = -\frac{1}{2}\mathrm{tr}(\mathbf{D}^2), \tag{3.30a}$$

$$R_D = -\det(\mathbf{D}) = -\frac{1}{3}\mathrm{tr}(\mathbf{D}^3). \tag{3.30b}$$

The roots of (3.29) are the eigenvalues of $\mathbf{D}$ and are defined as Γ_1, Γ_2 and Γ_3 in descending order of magnitude. Similar to (3.28) for $\mathbf{L}$, the discriminant of (3.30) for $\mathbf{D}$ is,

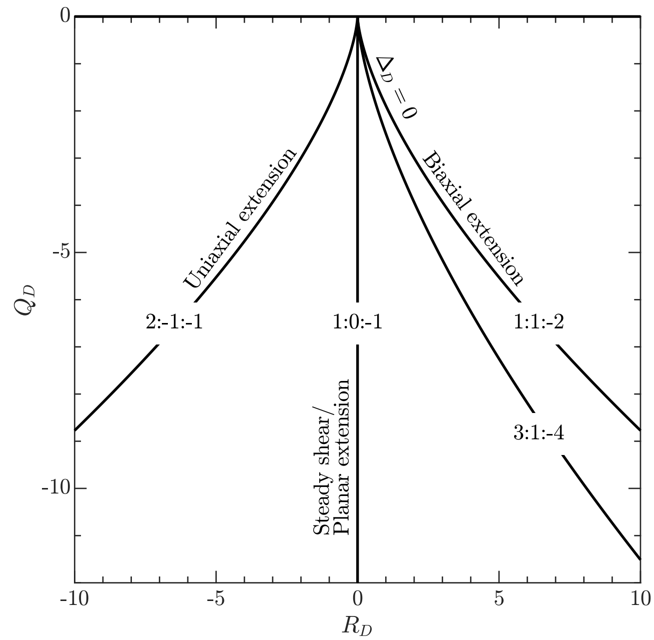

Figure 3.6: Ratios of eigenvalues for different R_D and Q_D for an incompressible flow with $P_D = 0$. The eigenvalues are listed in the descending order of $\Gamma_1{:}\Gamma_2{:}\Gamma_3$.

$$\Delta_D = \frac{27}{4} R_D^2 + Q_D^3. \tag{3.31}$$

Because $\mathbf{D}$ is a real and symmetric tensor, its eigenvalues will always be real and $\Delta_D \leq 0$. A plot of Q_D, R_D space is shown in figure 3.6, where black solid lines represent curves with the same ratio of principal strain rates or eigenvalue of $\mathbf{D}$, defined as $\Gamma_1{:}\Gamma_2{:}\Gamma_3$ (Blackburn *et al.*, 1996). The different eigenvalue ratios are commonly associated with unique straining motions.

Unlike tensors $\mathbf{L}$ and $\mathbf{D}$, the rate of rotation tensor has only one non-zero invariant for an incompressible flow, that being

$$Q_W = -\frac{1}{2}\mathrm{tr}(\mathbf{W}^2). \tag{3.32}$$

Note that the second invariant of $\mathbf{L}$ can be equally represented as $Q = Q_D + Q_W$. Values of Q_D are always negative, while values of Q_D are always positive. Truesdell (1954) established a kinematical vorticity number

$$\mathcal{K} = \left(\frac{Q_W}{-Q_D}\right)^{1/2}, \tag{3.33}$$

which defines the local strength of rotation relative to stretching (Ooi *et al.*, 1999). The change in $\mathcal{K}$ is shown schematically in figure 3.7 for different Q_D and Q_W, similar to the diagram provided in Soria *et al.* (1994). Regions of the flow with small Q_W and $\mathcal{K} \approx 0$ are more irrotational and dominated by dissipative motions, while flow regions with negligible Q_D and large values of $\mathcal{K}$ that approach ∞ experience solid body rotation. Regions with large enstrophy density and dissipation fall on the line with $\mathcal{K} = 1$, where

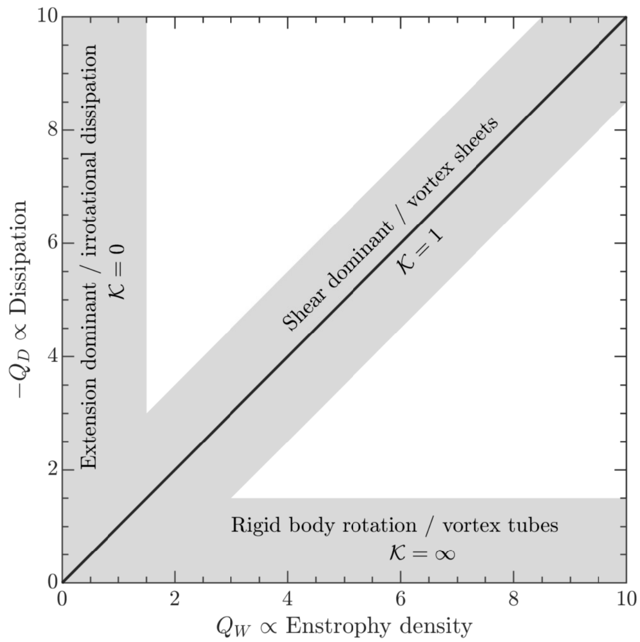

Figure 3.7: Schematic of the different flow types in Q_W, Q_D space and for different kinematic vorticity numbers $\mathcal{K}$.

$Q_W = -Q_D$. From simulations of an incompressible mixing layer, Soria *et al.* (1994) described how flow motions with $\mathcal{K} = 1$ consist of vortex sheets. From a rheological perspective, the values of $\mathcal{K}$ also translate to the different elementary rheometric flows, i.e., extension, shear and rotation.

The rheology of viscoelastic fluids depends heavily on whether the flow is dominated by extension or shear. Therefore, concerted efforts have been made within the rheology community to establish methods for distinguishing extensional flow motions from shear (Astarita, 1967, 1979). Many of these methods utilize the invariants in the VGT (more so $\mathbf{D}$ and $\mathbf{W}$), and were established long before the Δ-*criterion* was documented by Chong *et al.* (1990).

Consider the elementary rheometric flows, i.e., steady shear, extension and rigid body rotation. Note that steady extensional flows can be further divided into uniaxial, biaxial and planar extension. A review of these basic rheometric flows is not presented, however deriving their respective invariants in $\mathbf{D}$ and $\mathbf{W}$ is trivial – see e.g., page 73–75 of Macosko (1994). In the R_D, Q_D space, the ratio of principal strains also correspond to the limits of possible rheometric flows. The different rheological flows are labelled on the schematic of R_D, Q_D space of figure 3.6. Uniaxial and biaxial extension correspond to $\Delta_D = 0$ and the limits of R_D, Q_D space. Uniaxial extension flows have an eigenvalue ratio of Γ_1:Γ_2:Γ_3 = 2:-1:-1 (i.e., negative R_D), while biaxial extensional flows have an eigenvalue ratio of Γ_1:Γ_2:Γ_3 = 1:1:-2 (positive R_D). Shear and planar extension both exist on the $R_D = 0$ axis and are two-dimensional flows, with an eigenvalue ratio of Γ_1:Γ_2:Γ_3 = 1:0:-1. Comparing the invariants Q_W and Q_D is also commonly used to distinguish rheometric flows. Astarita (1979) derived a criteria that was adapted from the work of Astarita (1967), for distinguishing steady shear, extension and solid body rotation in non-Newtonian flows and served functionally the same as the kinematical vorticity number $\mathcal{K}$. Flow regions that are extension dominant ($\mathcal{K} = 0$), shear dominant ($\mathcal{K} = 1$) or in rigid body rotation ($\mathcal{K} = \infty$) are annotated on the schematic of Q_D, Q_W space shown in figure 3.7. Dimensionless indicators similar to $\mathcal{K}$ are generally referred to as a "flow-type" and can be commonly found in a variety of works involving non-Newtonian flows (Haward *et al.*, 2016, 2018*b*; Walkama *et al.*, 2020; Ekanem *et al.*, 2020; Kumar *et al.*, 2022).

Chapter 4

Experimental methods

Experimental measurements were performed using a consistent approach across all projects in this dissertation. Experiments of the turbulent flow of non-Newtonian fluids were performed in a large scale flow facility (e.g., channel flow or water flume). Samples of the fluid were extracted from the flow facility and their shear and extensional rheology is measured. The following chapter reviews the rheological methods in §4.1, followed by the large scale turbulent flow facilities in §§4.2 and 4.3, as well as the utilized flow measurements in §4.4.

4.1 Rheometric measurements

4.1.1 Steady shear rheology

The steady and dynamic shear viscosity of the Newtonian and non-Newtonian fluids were measured using a single-head stress-controlled torsional rheometer (HR-2, TA Instruments). The spindle head of the torsional rheometer is shown schematically in figure 4.1. The rheometer consists of a shaft that is driven by a drag cup alternating current (AC) motor. A torque T is applied to the shaft via the drag cup motor and the resulting angular velocity Ω or displacement is measured using an optical encoder. An air bearing helps support the spindle shaft and mitigate friction between the shaft and spindle head assembly. A geometry is fastened to the end of the spindle head; in figure 4.1 a single gap concentric cylinder geometry is depicted. Fluid is loaded between the upper geometry and a compatible and immovable lower fixture. The applied torque T of the drag cup motor can be converted into a stress τ imposed on the fluid sample, depending on the geometry. The shear strain γ and shear rate $\dot{\gamma}$ within the fluid sample can be established based on the measurements of the angular displacement and velocity Ω, again, depending on the geometry. The HR-2 single-head rheometer from TA Instruments has a minimum and maximum torque T of 10 nN m and 200 mN m. The maximum measurable angular velocity Ω is 300 rad s^{-1}. The biggest limitation of the single head rheometer, particularly for dynamic shear viscosity measurements, is the need to overcome the inertia of the spindle shaft. Three different types of geometries were used for measurements of the steady and dynamic shear viscosity. Limitations from low torque and inertia are discussed for the different geometries and the types of measurements.

Three different types of geometries were used for measurements of steady shear viscosity. An illustration

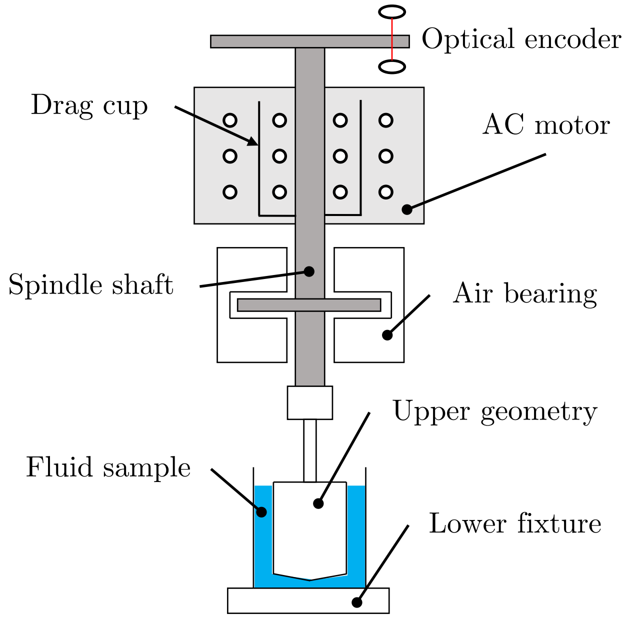

Figure 4.1: Schematic of single-head stress-controlled torsional rheometer.

of the geometries is shown in figure 4.2. A cylindrical coordinate system is shown alongside each geometry, where r is the radial direction, θ is the angular component and x is the axial component. The single gap concentric cylinder geometry is depicted in figure 4.2(a). A fluid sample is loaded between an inner cylinder of radius R_{min} = 14 mm and an outer fixed cylinder of radius R_{max} of 15.2 mm, with an immersion height of L_{sg} of 42.04 mm. The inner cylinder is fastened to the end of spindle shaft depicted in figure 4.1 and rotates due to the balance between the torque T applied from the drag cup and a counter-torque caused by the viscous skin friction of the sample. The flow between the cylinders is homogeneous Taylor-Couette flow with a constant shear rate $\dot{\gamma}$ between the gaps of the cylinders. This configuration emulates the simple shear Couette flow depicted in §2.1, but in cylindrical coordinates.

Figure 4.2(b) illustrates a double gap concentric cylinder geometry. The fixed cylinder has an inner cylinder of R_1 = 15.1 mm and outer radius of R_2 = 18.5 mm. The rotating cylinder fastened to the spindle head consists of an inner radius of R_3 = 16.0 mm and outer radius of R_4 = 17.5. Fluid is contained between two gaps from R_1 to R_3, and R_2 to R_4, at an immersion height of L_{dg} = 53.0 mm. Similar to the single gap concentric cylinder of figure 4.2(a), the double gap concentric cylinder imposes a homogeneous Taylor-Couette flow. The advantage of the double gap configuration over the single gap setup is the larger contact area between the fluid and the geometry. A larger contact area permits for lower measurements of Ω, and hence measurements of μ at much lower shear rates $\dot{\gamma}$.

Lastly, a parallel plate geometry is depicted in figure 4.2(c). Fluid is contained between a rotating circular plate or disk with a radius R_{pp} = 30 mm and another parallel fixed plate of larger radius. The gap h_{pp} between the fixed and rotating parallel plates is 0.2 mm. Unlike the Taylor-Couette flows of the single gap and double gap concentric cylinders of figure 4.2(a, b), the parallel plate geometry is not homogeneous and does not impose a constant shear rate $\dot{\gamma}$ within the sample. Instead, the shear rate is taken to be largest shear

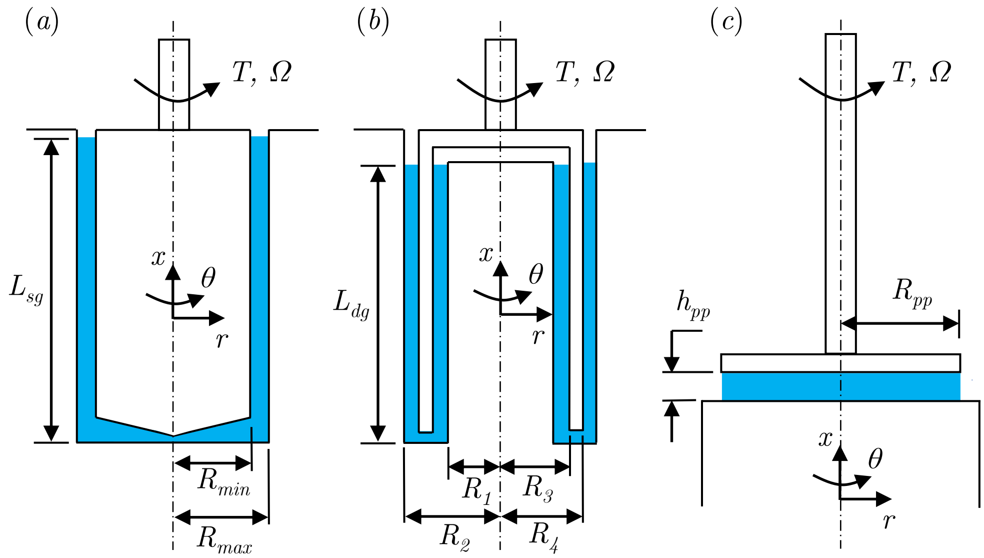

Figure 4.2: The geometries used in the torsional rheometer including (a) single gap concentric cylinders, (b) double gap concentric cylinder, and (c) parallel plates. The blue shaded area depicts the liquid samples contained within each geometry. Gravity is down or along the negative $x-$direction.

rate within the sample, which is shear rate at the edge or rim of the parralel plate. The advantage of the parallel plate geometry is that it allows for measurements of μ at very large Ω and $\dot{\gamma}$, when hpp is small. However, this can be accompanied with some additional challenges and measurement errors. These errors are discussed in §8.3 when the measurements using the parallel plate are presented.

The rotational velocity Ω, in rad s^{-1}, can be converted to $\dot{\gamma}$, using $\dot{\gamma} = F_\gamma \Omega$, where F_γ is the strain coefficient for the particular geometry. Similarly, the torque, T, can be converted to stress, τ, using $\tau = F_\tau T$, where F_τ is the stress coefficient of the geometry. After which, the shear viscosity can be derived based on, $\mu = \tau/\dot{\gamma} = (F_\tau/F_\gamma)(T/\Omega)$ (Barnes *et al.*, 1989; Ewoldt *et al.*, 2015). Each geometry has their own strain and stress coefficients, the values of which are listed in table 4.1 (Barnes *et al.*, 1989; Macosko, 1994).

Geometry	F_γ	F_τ
Single gap concentric cylinder	$\frac{R_{max}}{R_{max}-R_{min}}$	$\frac{1}{2\pi R_{max}^2 L_{sg}}$
Double gap concentric cylinder	$\frac{R_1^2}{R_3^2-R_1^2}+\frac{R_2^2}{R_2^2-R_4^2}$	$\frac{1}{2\pi(R_3^2+R_4^2)L_{dg}}$
Parallel plates	$\frac{R_{pp}}{h_{pp}}$	$\frac{2}{\pi R_{pp}^3}$

Table 4.1: Strain and stress coefficients for geometries used in the torsional rheometer.

The maximum shear rate limit of the steady shear viscosity measurements corresponds to the onset of inertial instabilities and turbulence. For the Taylor-Couette viscometers depicted in figure 4.2(*a, b*), this generally occurs when the Taylor number Ta, exceeds 1700 (Ewoldt *et al.*, 2015). For the single gap configuration $Ta = \rho^2\Omega^2(R_{max} - R_{min})^3 R_{min}/\mu^2$. While for the double gap geometry, $Ta = \rho^2(R_3 + R_4)h_{dg}^3\Omega^2/2\mu^2$, where $h_{dg} = [(R_3 - R_1) + (R_4 - R_2)]/2$ (Pereira *et al.*, 2013). For the parallel plate geometry, secondary instabilities corrupt the viscosity measurements when $Re_{pp} = \rho\Omega R_{pp}h_{pp}/\mu$ is greater than 100 (Davies & Stokes, 2008).

4.1.2 Dynamic shear rheology

Two types of dynamic shear viscosity or small amplitude oscillatory shear measurements were performed, in accordance with §2.2. The first was a sweep of stress amplitude τ_0 with a constant oscillation frequency ω. These experiments were used to establish the limit of linear viscoelasticity (LVE); for large τ_0, the relationship between stress and strain no longer follows a linear differential equation similar to (2.8) (Mezger, 2020). The second set of dynamic shear viscosity measurements was a sweep of ω using a sufficiently small value of τ_0 that is within the LVE regime. Trios software (TA Instruments) was used to determine the phase offset, ψ, using a cross-correlation of the sinusoidal stress, $\tau(t)$, and the measured strain, $\gamma(t)$ signals. The complex stress modulus was derived from the quotient of the stress and strain amplitudes, $G^* = \tau_0/\gamma_0$, where γ_0 is the measured strain amplitude. After determining the complex stress modulus and the phase offset, the gain modulus, G', and loss modulus, G'', could be determined using, $G^{*2} = {G'}^2 + {G''}^2$, and $\tan(\psi) = G''/G'$, (2.11). Distributions of G' and G'' for the non-Newtonian solutions were then used to comment on the linear viscoelasticity of the complex fluids.

Unlike steady shear viscosity measurements, dynamic shear viscosity measurements are much more constrained by the torque and inertia limitations of the device – especially when using a single head torsional rheometer (Läuger & Stettin, 2016). Correcting the torque measurements to compensate for the inertia of the spindle head and geometry can be effective, but not always perfect (Ewoldt *et al.*, 2015; Läuger & Stettin, 2016). Ewoldt *et al.* (2015) recommended ensuring that the torque imposed by the material exceed the torque required to overcome the inertia of the geometry. They derived a limitation on the shear moduli,

$$G > \frac{IF_\tau}{F_\gamma\omega^2}, \tag{4.1}$$

where G can be either G' or G'', and I is the moment of inertia of the geometry. Of the three geometries depicted in figure 4.2, the single gap concentric cylinder has the lowest geometry inertia, I, which was approximately equal to 4.3×10^{-6} kg m^2. Therefore, only the single gap concentric cylinder was used for the dynamic shear viscosity measurements. Measurements of G' and G'' that fall below the inertia limitation were disregarded.

4.1.3 Extensional rheology

The extensional rheology of the non-Newtonian fluids were evaluated using two types of devices. The first was a bespoke dripping onto substrate (DoS) apparatus, depicted in figure 4.3(*a*). In this measurement technique, a small droplet was discharged from a blunt-end nozzle with a diameter D_0 of 1.27 mm. A syringe pump (Legacy 200, KD Scientific Inc.) was used to expel the droplet from the nozzle at a rate of 0.02 ml min^{-1}. Pumping was terminated once the droplet made contact with a glass substrate that was situated $3D_0$ or 3.81 mm below the blunt-end of the nozzle outlet. An apparatus with similar features was used in Dinic *et al.* (2015), Dinic *et al.* (2017) and Zhang & Calabrese (2022). After the droplet made contact with the substrate, a liquid bridge was formed between the nozzle outlet and the substrate. The diameter of the liquid bridge D_{min} decayed rapidly due to capillary forces. Images of the liquid bridge were collected using a high-speed camera (v611, Vision Research) and back-lit illumination from a light emitting diode. Figure 4.3(b) shows a sample image of the liquid bridge for an aqueous solution of polyacrylamide with a concentration of 500 ppm. The camera had a 1280×800 pixel complementary metal oxide semiconductor sensor with pixels that were 20×20 µm^2 in size and had a bit-depth of 12 bit. A zoom lens was used to achieve a magnification of 3.8 and a scale of 5.16 µm pixel^{-1}. Images were collected at an acquisition rate of 2 kHz. The minimum diameter D_{min} of the liquid bridge was determined using a script developed in MATLAB (Mathworks Inc.).

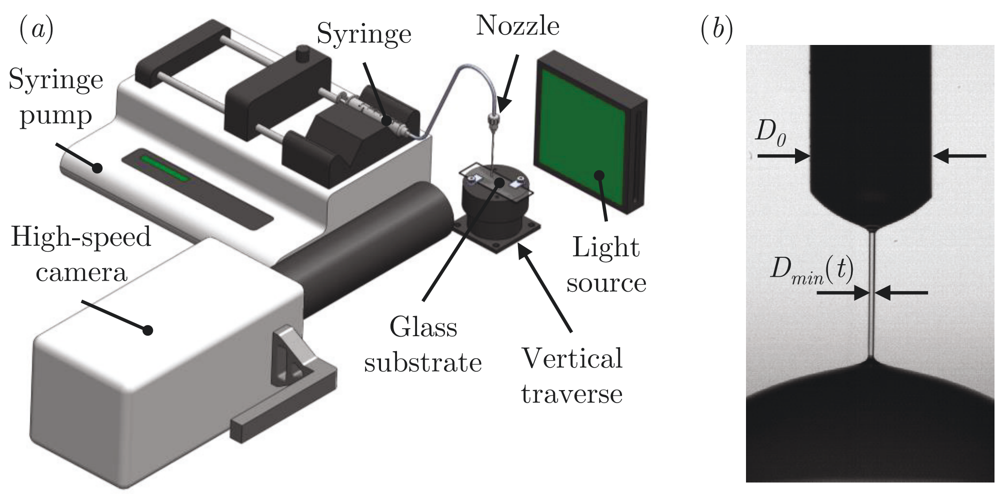

Figure 4.3: (a) Isometric view of a 3D model depicting the DoS setup. (b) A sample image taken for an aqueous solution of polyacrylamide with a concentration of 500 ppm in elastocapillary thinning.

The pinch-off dynamics of the liquid bridge in the DoS apparatus depends on forces attributed to inertia, surface tension, viscosity and elasticity (Dinic *et al.*, 2017). The Ohnesorge number $Oh = t_v/t_R$ relates the time scale associated with viscous forces to the Rayleigh time t_R, which pertains to surface tension and inertial forces. Here $t_v = \mu D_0/2\sigma$ is the characteristic timescale of viscocapillary thinning, $t_R = (\rho D_0^3/8\sigma)^{1/2}$, and σ is the surface tension. Low viscosity fluids typically have $Oh < 1$ and a necking process dominated by inertial and capillary forces. In this regime, inertiocapillary (IC) thinning is described by a 2/3 power law,

$$\frac{D_{min}(t)}{D_0} = \alpha\left(\frac{t_b - t}{t_R}\right)^{2/3}, \tag{4.2}$$

where t_b is the filament break-up time, and α is a multiplicative pre-factor between 0.4 and 1 (Zhang & Calabrese, 2022). If $Oh > 1$, viscous forces are significant, and the evolution of D_{min} is described by viscocapillary thinning, $D_{min}(t)/D_0 = 0.0709(t_b - t)/t_v$ (McKinley & Tripathi, 2000). For elastic fluids, the Deborah number $De = t_e/t_R$ describes the ratio of the extensional relaxation time t_e and the Rayleigh time (Tirtaatmadja *et al.*, 2006). If $De > 1$, the necking process is dominated by elastic and capillary forces. This elastocapillary (EC) regime is described by,

$$\frac{D_{min}(t)}{D_0} = A \exp\left(-\frac{t}{3t_e}\right), \tag{4.3}$$

where $A = (GD_0/2\sigma)^{1/3}$. Generally, the fluids measured using the DoS apparatus exhibited thinning in an IC ($Oh < 1$) or EC regime ($De > 1$). Nonlinear least square regression was used to establish t_e for fluids that exhibited EC thinning using measurements of D_{min} and equation 4.3. Values of t_e are listed in table 5.1.

The second extensional rheometer was a commercial piece of equipment called a capillary break-up extensional rheometer (CaBER) from Thermo Scientific. Similar to the DoS apparatus, the CaBER device relies on capillary forces to induce elastocapillary thinning in a fluid sample. Unlike the DoS apparatus, however, the CaBER device applies an initial step strain to the fluid that then triggers the break-up of the fluid filament.

Within the CaBER apparatus, a small sample is loaded between two 6 mm diameter circular plates that are parallel and separated 3mm apart from one another. After loading the sample, the top plate was then rapidly displaced causing the solution to stretch in uniaxial extension, similar to §2.3. The final gap between the plates was 9 mm and the strike time to attain the final position was 50 ms. A laser micrometer was used to measure the midpoint diameter D_{mid} as a function of time t. The extensional relaxation time t_e was then derived utilizing (4.3), but substituting D_{mid} for D_{min}.

4.2 Turbulent channel flow

A recirculating flow loop with an in-line channel section, as shown in figure 4.4, was used for measurements of a turbulent channel flow. The channel section had a rectangular cross-section with a height, H, of 15 mm and width, W, of 120 mm. It also consisted of four sub-sections connected with flanges as seen in figure 4.4. The third section from the channel inlet was made with glass walls for optical measurements. The measurements were carried out at the middle of this third section which was situated $107H$ downstream from the inlet of the channel section. This ensured a fully developed turbulent channel flow. The walls of the channel sections immediately upstream and downstream of the measurement section were cast acrylic. Transition fittings, 30 cm in length, were used to convert the cross-section from circular to rectangular, and *vice versa*. The complete length of the channel section was $168H$. Figure 4.5 demonstrates the cross-section of the measurement section and the coordinate system used here. Position along the streamwise direction is denoted as x, while y is the wall-normal direction and z is the spanwise direction. The coordinate system is centred at the mid-span of the lower channel wall.

Fluid was driven using a centrifugal pump (LCC-M 50-230, GIW Industries Inc.) controlled by a variable frequency drive. A thermocouple (Type K) and a double pipe heat exchanger were used to measure and maintain a constant temperature. The mass flow rate, $\dot{m}$, was measured using a Coriolis flow meter (Micro Motion F-series, Emerson Process Management) with an accuracy of ±0.2%. A proportional integral

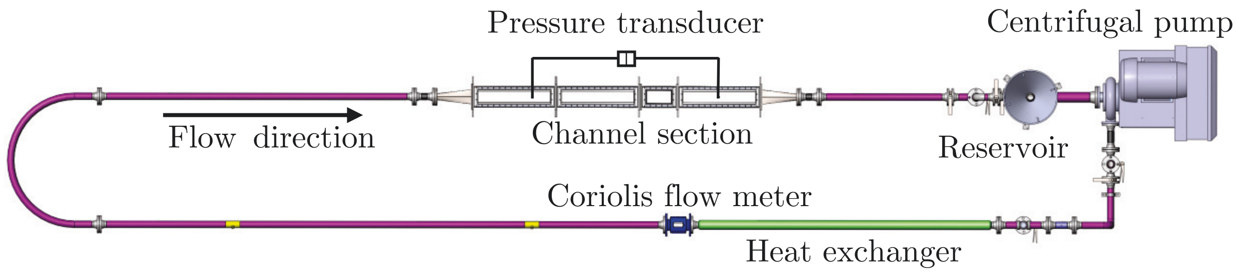

Figure 4.4: Annotated top view of experimental flow facility showing the pipe loop connected to the channel section.

derivative controller was used to maintain a constant $\dot{m}$ by controlling the input frequency to the pump. Static pressure loss along the channel was measured using a differential pressure transducer (DP-15, Validyne). Ports for the pressure transducer were separated $109H$, with the upstream port being $34H$ from the channel inlet.

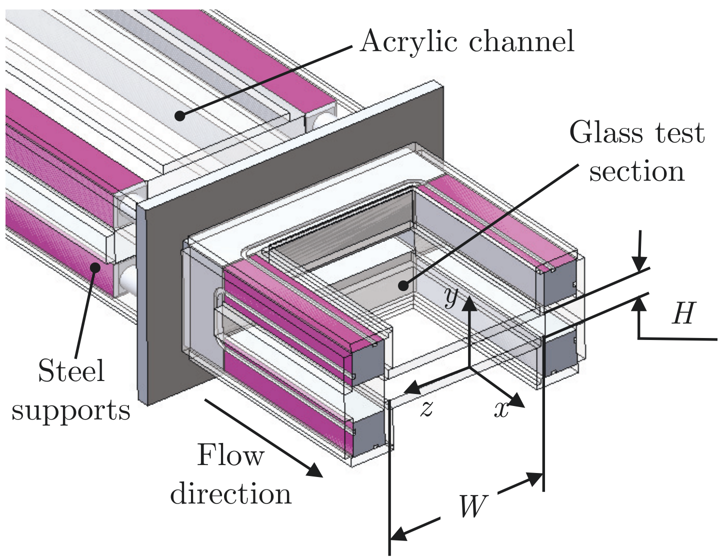

Figure 4.5: Cross-section of the channel flow test section.

4.3 Turbulent boundary layer

Turbulent boundary layers were formed along the floor of a closed-loop water flume illustrated in figure 4.6(a). The flume consists of a 5 m long channel that bridges two cubic reservoirs. The channel was 0.68 m in width W. The free surface was situated at a height H that was 0.2 m above the bottom floor of the channel. The channel cross-section with respect to the Cartesian coordinate system is shown in figure 4.6(b). The total volume of liquid within the flume was 3500 l. The walls of the channel consist of 12.7 mm thick glass panels. Two centrifugal pumps (Deming 4011 4S, Crane Pumps and Systems) in a parallel configuration were used to circulate the fluid within the flume. Variable frequency drives enabled control of the rotational speed of each pump. In all boundary layer experiments within the flume both pumps were operated at the same rotational speed. Measurements of the turbulent boundary layer of water were collected for pump speeds between 300 rpm and 1000 rpm, which corresponds to free-stream velocities U_∞ between 0.124 and 0.430 m s^{-1}. A series of mesh screens within the upstream reservoir of the water flume ensured that the turbulence intensity of the free-stream was less than 2%. Fluid temperature was monitored using a K-type thermocouple and a data logger (HH506, Omega Engineering).

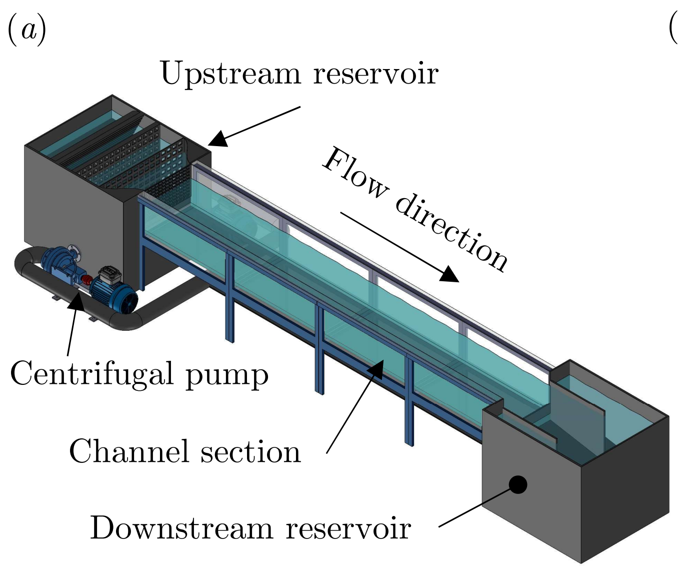

Figure 4.6: (*a*) Isometric view of a model that depicts the water flume facility, and (*b*) a cross-section of the open channel section.

4.4 Flow measurements

Particle image velocimetry (PIV) is a non-intrusive technique used to measure the local displacement ($\Delta\boldsymbol{x}$) of fluid elements over a short time interval (Δt) (Adrian, 1984). The technique infers the velocity field based on the broad movement of tracer particles that are evenly dispersed within the moving fluid. Tracer particle are illuminated using a light source – which in the case of planar PIV is a thin laser sheet, that is typically 1-2 mm in thickness. Light scatted by the particles are then recorded by a camera that is synchronized with the light source. Illumination is provided as a short pulse that "freezes" the motion of the tracers in one image. More advanced three-dimensional (3D) methods, such as tomographic PIV, utilize multiple cameras at different perspectives to measure the velocity of the fluid in all three spatial directions (Elsinga *et al.*, 2006). Particles are typically illuminated using a laser volume. Concurrent images are captured with a short intermittent time delay Δt, such that the motion of the tracer particles between subsequent images can be recorded. Images are then divided into interrogation windows. In planar PIV, the displacement of the tracers has two components, $\Delta \boldsymbol{x} = (\Delta x, \Delta y)$. The two-dimensional velocity vector is then inferred according to,

$$\boldsymbol{U} = \frac{\Delta \boldsymbol{x}}{\Delta t} \tag{4.4}$$

The displacement $\Delta \boldsymbol{x}$ within each interrogation window is determined using a cross-correlation technique. The cross-correlation operator is applied to the 2D light intensity signal recorded within each interrogation window.

Particle tracking velocimetry (PTV) is a Lagrangian approach that tracks individual particles as they travel through the measurement domain. The PTV setup consists of the same equipment used for PIV. A laser is used to illuminate tracers in the flow, and cameras are used to record the light scattered from the particles over several instances of time. Traditionally, PTV required lower seeding densities than PIV, in order to locate individual particles and track their position across different time instances without interference from neighbouring particles. An algorithm called Shake-The-Box (STB) was established for 3D-PTV measurements that permits higher seeding densities and a larger number of measured particle trajectories within the measurement domain (Schanz *et al.*, 2016).

The PIV and PTV measurement techniques rely on the assumption that tracer particle faithfully follow the fluid flow. Two criteria are used to convey the validity of this assumption (Bewley *et al.*, 2008). The first criteria utilizes the Stokes number,

$$St = t_p / t_f, \tag{4.5}$$

where $t_p = \rho_p d_p^2 / 18\mu$ is the particle response, t_f is a representative time scale of the flow, ρ_p is the density of the particles and d_p the diameter. If St is less than 0.1, tracer particles follow the flow well (Bewley *et al.*, 2008). The second criteria utilizes the Froude number,

$$Fr = u_p / u_f, \tag{4.6}$$

where the particle settling velocity is $u_p = (\rho_p - \rho) d_p^2 g / 18\mu$, g is the gravitational acceleration, and u_f is a representative velocity of the flow. If Fr is less than 1, the influence of particle settling caused by gravity is negligible. Each investigation that utilizes PIV and PTV, including §§6, 7, 8 and 9, provides a depiction of the measurement setup, a description of the equipment and a discussion fo measurement uncertainty. In the discussion of measurement uncertainty, the values of St and Fr are provided.

Part II

Rheology

Chapter 5

Shear and extensional rheology

Before investigating the drag-reducing capabilities of different non-Newtonian solutions, a review of their rheological features is first presented. The present chapter compares measurements of steady shear viscosity, dynamic shear viscosity and extensional rheology for aqueous solutions comprised of three different types of drag-reducing additives and using the methods detailed in §4.1. All of the additives are known to induce drag reduction in turbulent wall flows (Escudier *et al.*, 1999; Qi & Zakin, 2002).

5.1 Non-Newtonian fluids

The three additives included a flexible polymer, a rigid biopolymer and a cationic surfactant. Additives in their solid powder form were weighed using a digital scale (Explorer Analytical, OHAUS Corporation) with a 1 mg resolution. Solid powders were then gradually added to 15 l of distilled water and agitated for 8 h using a stand mixer equipped with a 100 mm diameter impeller (Model 1750, Arrow Engineering Mixing Products). After mixing, the aqueous non-Newtonian solutions were left to rest for 16 h. Fluid samples were then collected for rheology measurements.

The flexible polymer was polyacrylamide (PAM) from a sample batch contributed by SNF Floerger (6030S, molecular weight of 30-35 Mg mol^{-1}). The rigid biopolymer was xanthan gum (XG) (43708, MilliporeSigma). Both polymers, PAM and XG, have been readily used in various experimental investigations involving rheology and turbulent drag reduction (Escudier *et al.*, 1999; Mohammadtabar *et al.*, 2020; Warwaruk & Ghaemi, 2021). Cationic surfactants are quarternary ammomium salts of the form $C_nH_{2n+1}N^+(CH_3)^3Cl$, where n is an integer, generally between 12 and 18 (Qi & Zakin, 2002). When paired with a counterion, such as sodium salicylate (NaSal), the molecules combine to form complex molecular agglomerates known as micelles (Bewersdorff & Ohlendorf, 1988; Zhang *et al.*, 2005). For the present measurements, Trimethyl Tetradecyl Ammonium Chloride (n = 14) (T0926, Tokyo Chemical Industry Co., Ltd.) combined with NaSal (71945, MilliporeSigma) at a molar ratio of 1:2 was used, as this was combination was shown to produce considerable amounts of drag reduction in other studies (Bewersdorff & Ohlendorf, 1988; Warwaruk & Ghaemi, 2021). Going forward, the surfactant solution is referred to as C14. A parametric sweep of five concentrations were considered for each additive (i.e. PAM, XG, and C14). The concentrations, c, were the same for all additives: 100ppm, 200ppm, 300ppm, 400ppm, and 500ppm.

5.2 Steady shear viscosity

Shear rheology measurements were performed using the controlled-stress single-head torsional rheometer detailed in §4.1.1 and shown schematically in figure 4.1. The single gap concentric cylinder detailed in figure 4.2(a) was used for all viscosity measurements in the current chapter. Steady shear viscosity measurements involved a logarithmic sweep in the shear rate $\dot{\gamma}$ from 0.1 s^{-1} to 1000 s^{-1} with 10 data points per decade, and the corresponding stress τ was monitored. Recall from §4.1 that the rheometer has a lower torque limit of 10 nN m, or $\tau = 0.2$ mPa, according to the manufacturer, TA Instruments. In practice, it was found that the lower limit for steady shear viscosity measurements was higher, $T = 100$ nN m, or $\tau = 2$ mPa. A power-law model was fit to shear rheograms for fluids that exhibited shear thinning tendencies. The power law was defined according to $\mu = M\dot{\gamma}^{k-1}$ or equation (2.7), where M is the consistency and k is the flow index. Fits were performed on profiles of $\mu(\dot{\gamma})$ with $\tau > 2$ mPa and $Ta < 1700$, using nonlinear least square regression.

Figure 5.1 displays measurements of μ as a function of $\dot{\gamma}$ for the Newtonian and non-Newtonian fluids. Shear viscosity distributions of distilled water are shown in figure 5.1(a). Measurements of μ for water are constant with respect to $\dot{\gamma}$ provided $\tau > 2$ mPa and $Ta < 1700$. For $\tau < 2$ mPa, measurements of μ for water are noisy and scattered. When $Ta > 1700$, measurements of μ for water increase abruptly and are no longer constant with respect to $\dot{\gamma}$; Taylor vortices have corrupted the measurements of μ. The average viscosity of water for $\tau > 2$ mPa and $Ta < 1700$ is 0.97 mPa s. This is 3% lower than the theoretical shear viscosity of water at 20.1°C, 1.00 mPa s.

Figure 5.1(b) shows profiles of μ for the five PAM solutions. All five concentrations of PAM exhibit larger values of μ than water. They also exhibit shear thinning, where μ decreases monotonically with increasing $\dot{\gamma}$. At the higher values of $\dot{\gamma}$, μ appears to increase sharply for $\dot{\gamma}$ with a Ta less than 1700. Nonetheless, the trend by which μ reduces with respect to $\dot{\gamma}$ is well represented by the power law model (equation 2.7) for measurements with $\dot{\gamma} > 0.1$ s^{-1}, and $\dot{\gamma} < 100$ s^{-1} – sufficiently below the shear rate that μ increases abruptly. Values of the consistency, M, and flow index, k, for PAM are provided in table 5.1.

c (ppm)	M (Pa s^{n-1})	k	t_e (ms)
100	3.0×10^{-3}	0.92	2.2
200	6.0×10^{-3}	0.86	6.3
300	9.9×10^{-3}	0.82	16.3
400	32.8×10^{-3}	0.62	32.2
500	40.5×10^{-3}	0.62	48.6

Table 5.1: Rheological parameters of PAM from steady shear rheology and DoS.

Figure 5.1(c) demonstrates profiles of μ for the five XG solutions. Similar to PAM all concentrations of XG exhibit larger values of μ than water and prevalent shear thinning. Unlike PAM, μ appears to increase sharply for $\dot{\gamma}$ with a Ta equal to 1700. The shear thinning trend is well represented by the power law model

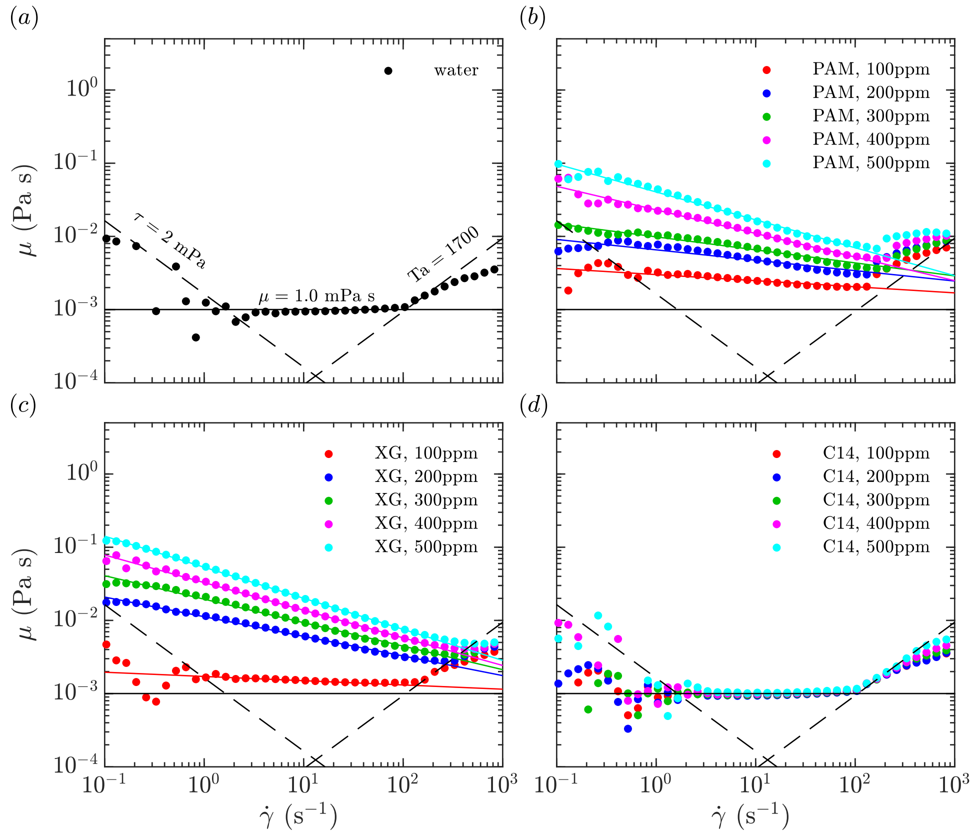

Figure 5.1: Steady shear viscosity distributions for (*a*) the baseline Newtonian fluids, (*b*) flexible polymer solution PAM, (*c*) rigid biopolymer solution XG, and (*d*) cationic surfactant solution C14. The horizontal black solid line is μ for water determined from the empirical correlation of Cheng (2008). Dashed black lines indicate the lower torque limit ($\tau < 2$ mPa) and the onset of Taylor vortices ($Ta > 1700$). In (*b*) and (*c*) solid coloured lines represent the power-law fits for shear thinning fluids given by equation (2.7) and with values provided in tables 5.1 and 5.2.

(equation 2.7) for measurements with $\dot{\gamma} > 0.1$ s^{-1}, and $Ta < 1700$. Values of the consistency, M, and flow index, k, for XG are provided in table 5.2.

Lastly, figure 5.1(*d*) demonstrates shear rheograms for the five C14 solutions. Interestingly, all five C14 solutions have values of μ similar to water (around 1.00 mPa s) and independent of $\dot{\gamma}$. Unlike PAM and XG, C14 does not augment the viscosity of the solvent.

5.3 Dynamic shear viscosity

Measurements of linear viscoelasticity are shown in figure 5.2 for high concentration solutions of PAM and XG. Details regarding the dynamic shear viscosity measurements are provided in §4.1.2. Figure 5.2(*a*) demonstrates sweeps of stress amplitudes τ_0 for PAM solutions, and figure 5.2(*b*) demonstrates the same stress amplitude sweep for the XG solutions. Both amplitude sweeps are conducted at a consant ω of 0.625 rad s^{-1}. Stress amplitude sweeps for PAM with c = 400ppm and 500ppm, shown in figure 5.2(*a*), have G' and G'' values greater than the inertia limit of (4.1). Lower concentration solutions, with $c \leq 300$ppm, are

c (ppm)	M (Pa s^{n-1})	k
100	1.7×10^{-3}	0.94
200	11.2×10^{-3}	0.73
300	19.5×10^{-3}	0.68
400	32.8×10^{-3}	0.62
500	53.3×10^{-3}	0.58

Table 5.2: Power law model parameters according to equation (2.7) for XG.

not shown as their G' and G'' measurements fall below the inertia limit of (4.1). Both PAM solutions with c = 400ppm and 500ppm, have $G'' > G'$ for all values of τ_0, implying the solutions are viscous dominant when $\omega = 0.628$ rad s^{-1}. The difference between G'' and G' diminishes as c increases, i.e. the solution becomes more elastic as c grows. Values of G' and G'' are constant for $\tau_0 < 10^{-2}$ Pa. Therefore, the LVE regime is confined to stress amplitudes less than 10 mPa for PAM. Stress amplitude sweeps for XG solutions, shown in figure 5.2(b), are similar to PAM. All XG solutions are viscous dominant for $\omega = 0.628$ rad s^{-1}. The disparity between G'' and G' decreases as the concentration of XG grows. Values of G' and G'' are constant with respect to τ_0 for $\tau_0 < 4$ mPa.

Sweeps of ω are shown in figure 5.2(c) for PAM and figure 5.2(d) for XG at a constant τ_0 of 3.3 mPa, which is within the LVE regime. PAM solutions have finite values of G' and G'' for ω between 0.1 and 10 rad s^{-1}. For both c = 400ppm and 500ppm, the solutions are viscous dominant, $G'' > G'$. As ω increases the elastic and viscous moduli become more similar in magnitude, implying the cross-over frequency where $G' = G''$ is slightly greater than 10 rad s^{-1}. Similar to PAM, XG also demonstrates finite G' that are lower in magnitude than G'', i.e., viscous dominant. As c increase, G' becomes more similar in magnitude to G''. Unlike PAM, XG with c = 300ppm and 400ppm have profiles of G' and G'' that are parallel. In other words, the difference between G' and G'' is not changing with respect to ω. When the concentration is increased to 500ppm, profiles of G' and G'' appear to begin converging towards one another, implying that the cross-over frequency becomes lower as c increases. Nonetheless, it is likely that the cross-over frequency is well above 10 rad s^{-1} for the XG solutions. Overall, both PAM and XG demonstrate characteristics of uncrosslinked polymer solutions with predominantly viscous behaviour. Solutions of C14 had no measurable G' or G'' values for the same reason the viscous moduli of water could not be measured; dynamic oscillation tests were overcome by the inertia of the geometry for 0.1 s$^{-1} < \omega <$ 10 s^{-1}.

5.4 Extensional rheology

Measurements of D_{min}/D_0 using the dripping onto substrate (DoS) apparatus are shown in figure 5.3 for the PAM solutions – the only solutions that demonstrated EC thinning. Details regarding the DoS setup are provided in §4.1.3. For t less than the inertial break up time t_b, the evolution of D_{min} is in an IC regime

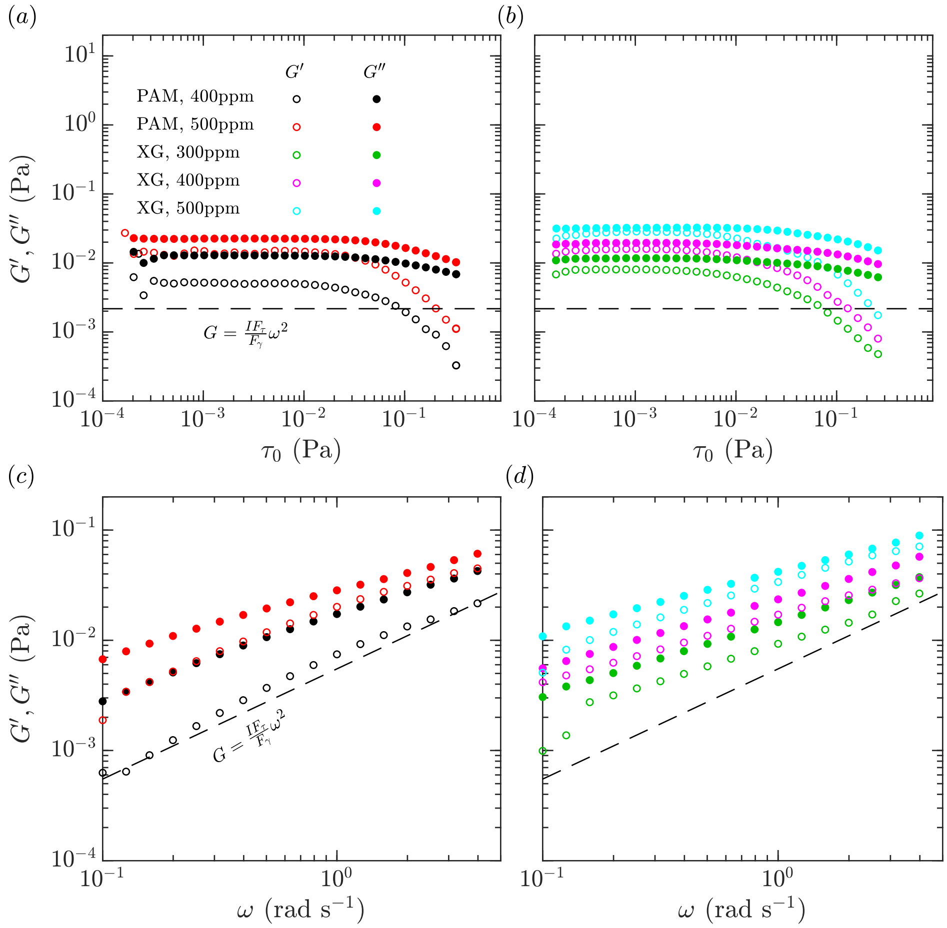

Figure 5.2: Dynamic shear viscosity distributions for PAM and XG. Plots (*a*) and (*b*) are the amplitude sweeps at a fixed ω of 0.628 rad s^{-1}. Plots (*c*) and (*d*) are frequency sweeps at a fixed τ_0 of 3.3 mPa. Hollow symbols are G' and filled symbols are G''. The dashed black line represents the geometric inertia limitation (4.1) for the measurements Ewoldt *et al.* (2015).

and well described by equation (4.2). The inertial break-up time t_b was not significantly different among the PAM solutions of different c and was approximately 7.2 ms ± 0.6 ms. Measurements of $D_{\min}/D_0$ for PAM with c = 100ppm, are shown in the inset axes of figure 5.3. The IC thinning represented by equation (4.2), and shown by the black solid line in the inset axes of figure 5.3, has $\alpha = 0.5$ and $t_R = 1.9$ ms. This value of α is between 0.4 and 1, which is within the margin of experimental expectations (Zhang & Calabrese, 2022). The theoretical Rayleigh time $t_R = (\rho D_0^3/8\sigma)^{1/2}$ should be 1.89 ms (assuming $\sigma \approx 72$ mN m^{-1}) – not significantly different than t_R derived from fitting equation (4.2) onto measurements of $D_{\min}/D_0$ in the IC regime. Recall that the Ohnesorge number is defined as $Oh = t_v/t_R$, where $t_v = \mu D_0/2\sigma$. If μ in the equation for t_v is taken to be the largest measured viscosity in figure 5.3 (about 0.1 mPa s for PAM with c = 500ppm), then $t_v \approx 0.9$ ms, and the largest Oh is about 0.5.

For $t > t_b$, all PAM solutions demonstrate EC thinning, well represented by equation (4.3) and the coloured lines shown in figure 5.3. As the concentration grows, the extensional relaxation time t_e increases. Values of t_e are provided in table 5.1. If it is assumed that $t_R = 1.89$ ms for all PAM solutions, De was between 1.2 and 25.7 depending on c. For the high concentration PAM solutions, the 2 kHz image acquisition rate coupled with the spatial resolution of the camera results in repetitive measurements of $D_{\min}/D_0$ over several time instances (i.e., the small horizontal lines).

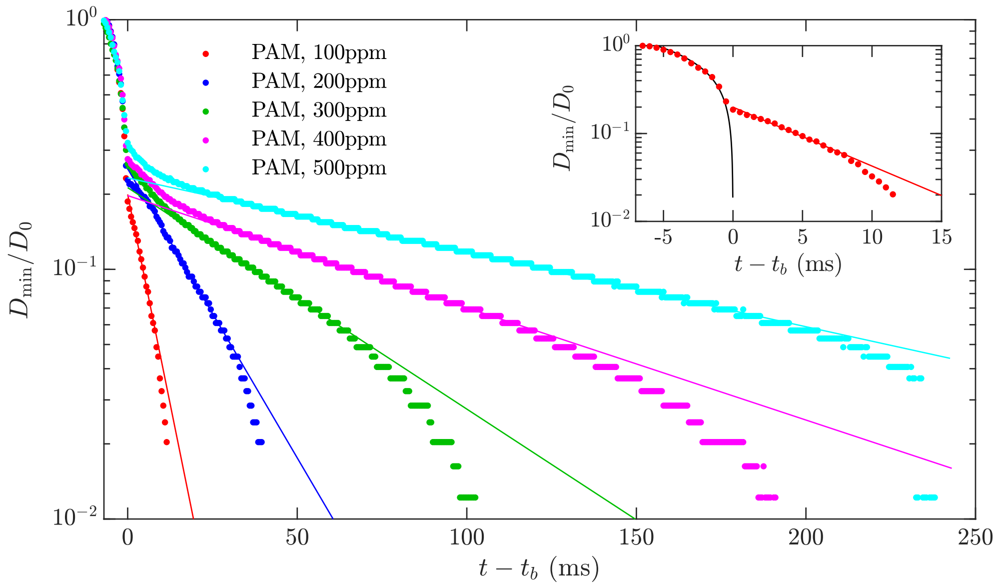

Figure 5.3: Normalized minimum filament diameter with respect to time for the PAM solutions, as determined from the DoS system. The inset figure demonstrates a zoomed in distribution along time for PAM with c = 100ppm. Coloured solid lines indicate the fits of the EC regime using equation (4.3). The solid black line in the inset denotes the fit of the IC regime using equation (4.2).

Solutions of C14 and XG do not demonstrate EC thinning, and therefore, $De < 1$. A lack of EC thinning is either a result of a low t_e or a large t_R, by definition of the Deborah number $De = t_e/t_R$. It is well known that surfactant solutions have a much lower σ than the solvent and hence, a large t_R (Zhang *et al.*, 2005). It is possible that the lack of EC thinning in C14 could be attributed to low surface tension. Surface tension σ is generally 40% lower for large concentration solutions of cationic surfactants relative to water (i.e., 35-45 mN m^{-1}). This would mean that t_R could be approximately 30% larger for surfactants. However, it is suspected that a 30% increase in t_R is not sufficient enough to explain the lack of EC thinning for C14. The present investigation does not measure σ, hence no definitive conclusion can be made in this regard. That being said, it is expected that the lack of EC thinning is attributed to low t_e at the conditions imposed from the DoS rheometer. This is another example of how difficult it is to measure t_e using capillary-driven extensional rheometers for drag-reducing surfactant solutions, as previously seen in Warwaruk & Ghaemi (2021) and Fukushima *et al.* (2022). It also highlights a need to develop other techniques for measuring extensional features of non-Newtonian solutions, as done in Wunderlich & James (1987). Ultimately, PAM solutions have relatively large t_e that could be derived from the DoS rheometer, while C14 and XG solutions have t_e that could not measured using the DoS apparatus.

Chapter 6

Nontrivial rheology

To better understand the features of dilute non-Newtonian solutions, there is merit in considering flows of moderate complexity – those that are not trivial enough to be considered viscometric, but not overly complex such as turbulence. Bird & Wiest (1995) referred to these flows as "nontrivial flows," as they involved the laminar flow of non-Newtonian fluids through complex geometries. Some of these geometries include an abrupt contraction, periodically constricted tube, porous media, and undulating surfaces (Deiber & Schowalter, 1979; Pilitsis *et al.*, 1991; Poole *et al.*, 2005; Page & Zaki, 2016). Bird & Wiest (1995) referred to a few of these nontrivial flows as benchmark experiments, that could aid in the development of numerical methods for modelling the flow of non-Newtonian fluids. The features and phenomena observed from these nontrivial flows, particularly those involving dilute polymer solutions, are also believed by some to be of significance to polymer drag reduction or related to the onset of the self-sustaining chaotic state known as elasto-inertial-turbulence (EIT) (Joseph, 1990; Haward *et al.*, 2018*a*). Experiments of dilute polymer solutions, at relatively low Reynolds numbers, in pressure-driven contraction and periodic contraction-expansion channels demonstrated an increased streamwise pressure gradient, near-wall velocity overshoots, and an augmented vorticity, not observed for Newtonian fluids (Poole *et al.*, 2005; Ober *et al.*, 2013; Haward *et al.*, 2018*a*). Few experiments have considered dilute surfactant solutions in these nontrivial flows geometries. Based on the viscometric flows detailed in §5, dilute surfactant solutions had no apparent non-Newtonian features. The investigation in the present chapter seeks to unravel the non-Newtonian traits of the dilute surfactant solution by considering its flow in a nontrivial geometry, that being a periodically constricted tube (PCT). The same three types of non-Newtonian additives used in §5 are investigated within the PCT flow. Five concentrations are considered for each non-Newtonian fluid (15 solutions in total). A flow measurement technique known as particle shadow velocimetry (Santiago *et al.*, 1998; Estevadeordal & Goss, 2006; Khodaparast *et al.*, 2013) is used to directly measure the velocity of each fluid in the PCT at five different flow rates.

6.1 Periodically constricted tube

Figure 6.1(*a*) demonstrates a 2D cross-section of the flow setup used for the experiments. The flow consists of several stages. Each stage is detailed starting from the farthest upstream location on the left hand side of figure 6.1(*a*) and moving downstream or to the right. The entrance region was of radius, R_o = 1.07 mm, and was $68R_o$ in length – a sufficient length to ensure fully developed Poiseuille flow entered the sections to follow. Farther downstream of the entrance, the flow entered the PCT, where the radius of the tube wall, R_w, varied sinusoidally along the streamwise direction, x, according to,

$$R_w = R_o + \epsilon\left(\cos\left(\frac{2\pi x}{\lambda}\right) - 1\right), \tag{6.1}$$

where the sinusoidal amplitude of wall radius was, $\epsilon = 0.14$ mm, and the wavelength, λ, was 4.7 mm. The maximum radius of the PCT was R_o, the minimum radius R_i was 0.79 mm and the average radius R was 0.93 mm. The length of the PCT section was 7λ. Figure 6.1(b) demonstrates a magnified depiction of the PCT portion of the test section. The cylindrical coordinate system is shown for reference on figure 6.1(b). The streamwise, radial and azimuthal directions are denoted as x, r, and θ, respectively. The radius of the tube downstream of the PCT returned to R_o for a length of $28R_o$. The radius then gradually increased to 5.5 mm via a 3-degree axisymmetric conical expansion farther downstream from the PCT.

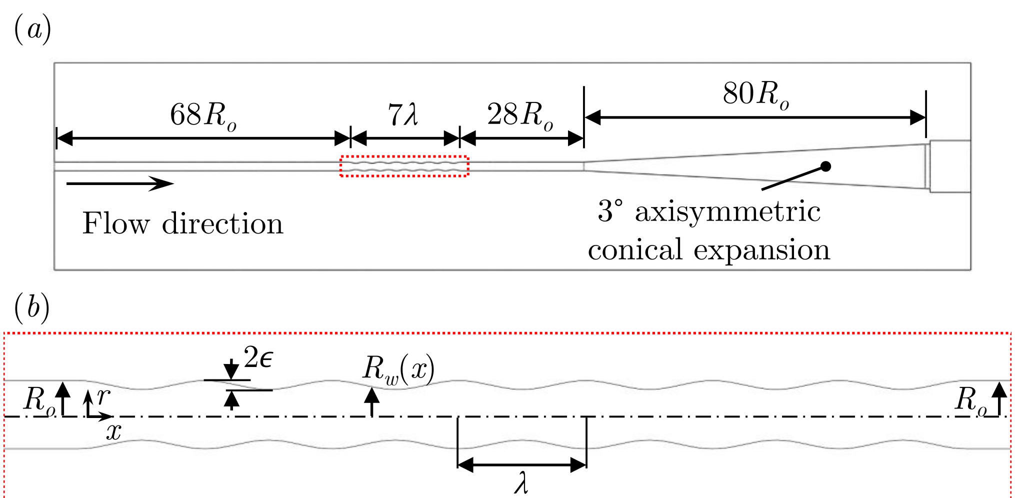

Figure 6.1: Two-dimensional schematic of the (a) complete acrylic test section, and (b) the periodically constricted tube.

The 3D axisymmetric tube was built from two halves of 12.7 mm thick acrylic. The radial profile shown in figure 6.1 was cut into the two acrylic halves using a computer numerical control router with a precision ball nose end mill. The scallop height – the height of the surface imperfections caused by the curvature and step length of the ball nose tool – was less than 1 µm or 0.1% of R_i. The two halves were pressed together to form the 3D axisymmetric tube without using any adhesive. Custom milled steel flanges with lag bolts and nuts were used to apply sufficient compression to the two halves, such that fluid did not expel out the sides of the test section.

Fluid entered the test section from a straight, 1.2 m long stainless-steel tube with an inner radius of R_o, that was face-sealed to the left hand side of the test section shown in figure 6.1(a). Fluid that exited the test section entered a 0.3 m long stainless-steel tube with an inner radius of 5.5 mm that was joined to the downstream portion of the test section. Fluid temperature was monitored using a K-type thermocouple and a data logger (HH506, Omega Engineering). The average fluid temperature of all experiments was

20.1°C ± 0.2°C. A syringe pump (Legacy 200, KD Scientific Inc.) with an accuracy of ± 1% was used to propel fluid through the flow facility. Glass syringes (Micro-Mate, Popper & Sons Inc.) with 10 ml and 30 ml volumes were equipped in the syringe pump; the choice in the syringe volume depended on the required volumetric flow rate Q. Flexible PVC tube with an inner radius of 3.18 mm connected the syringe to the 1.2 m long stainless steel tube. Five flow rates were considered for each Newtonian and non-Newtonian fluid: 1, 3, 6, 9 and 12 ml min^{-1}.

The Reynolds number was defined based on, $Re = 2\bar{U}_0 R/\nu_w$, where, $\nu_w = \mu_w/\rho$, is the kinematic wall viscosity, μ_w is the dynamic wall viscosity and ρ is the density. This definition of Re is similar to that used in Ahrens *et al.* (1987), where the flow of viscoelastic fluids was simulated through a wavy-walled tube. Within the PCT, the centreline velocity U_0 oscillates with respect to x. As such, the average centreline velocity $\bar{U}_0$ along x was determined from flow measurements in the PCT. Here, the overbar is used to denote spatial averaging along the x direction. Within the PCT, the fluid is subjected to a combination of shear and extensional deformation. A characteristic near-wall shear rate within the PCT was defined similar to the straight-walled section as $\dot{\gamma}_w = 2\bar{U}_0/R$. A characteristic extensional strain rate $\dot{\varepsilon}$ was defined as the range in U_0 (maximum subtracted by minimum) divided by $\lambda/2$. In the present investigation, $\dot{\gamma}_w$ was between 13 and 300 s^{-1} and $\dot{\varepsilon}$ was between 2 and 58 s^{-1} depending on the fluid and Re. The dynamic wall viscosity μ_w was derived from shear rheograms shown in figure 5.1 for non-Newtonian fluids and using $\dot{\gamma} = \dot{\gamma}_w$ in equation (2.7), as discussed in §5.2. For water, $\mu_w = \mu_s$, where μ_s is the viscosity of the solvent and was considered to be 1.00 mPa s according to Cheng (2008).

6.2 Particle shadow velocimetry

Particle image velocimetry (PIV) with backlight illumination, denoted as particle shadow velocimetry (PSV), was used to measure the velocity of the fluid within the test section. In PSV, the thickness of the measurement domain is driven largely by the depth of focus (DOF) of the imaging system. Provided a sufficient magnification and lens aperture, images can be acquired with a thin focal plan that enables 2D planar flow measurements along a select and narrow region of interest (Santiago *et al.*, 1998; Estevadeordal & Goss, 2006; Khodaparast *et al.*, 2013).

The PSV system consisted of a digital camera (Imager Pro X, LaVision GmbH) with a 2048 × 2048 pixel charged-coupled device sensor. Each pixel was $7.4 \times 7.4\,\mu\text{m}^2$ in size and had a 14-bit digital resolution. A Nikon lens with a focal length of $f = 105$ mm was equipped to the camera with an aperture diameter of $f/2.8$. The camera focus was adjusted such that images were focused on the radial mid-span of the test section. Two fields of view (FOVs) were considered, as shown in figure 6.2(a). The first FOV, i.e. FOV1, considered the entrance or development region immediately upstream of the PCT, as demonstrated in the left hand side of figure 6.2(a). The FOV1 captured the complete tube radius, R_o, and approximately 3λ along the x direction and immediately upstream of the first oscillation in the PCT. Only the Newtonian flow of water was considered in FOV1. The objective was to determine if the flow entering the PCT was fully-developed laminar Poiseuille flow. Experimental results for FOV1 were presented separately in Appendix A.1. The second field of view, FOV2, measured the velocity between the second to fifth oscillation of the PCT, that is from $x \approx 2\lambda$ to 5λ. For FOV2, flows of the three non-Newtonian fluids through the PCT were measured.

Both FOVs were approximately the same size, $(\Delta x, \Delta r) = 3.24 \times 14.1\ \text{mm}^2$, with a scale of 6.88 µm pixel^{-1} after the sensor was cropped to remove unnecessary data for $r/R_o > 1$. The magnification was 1.07 and the DOF was 87 µm, which was approximately 10% the minimum radius in the PCT, R_i.

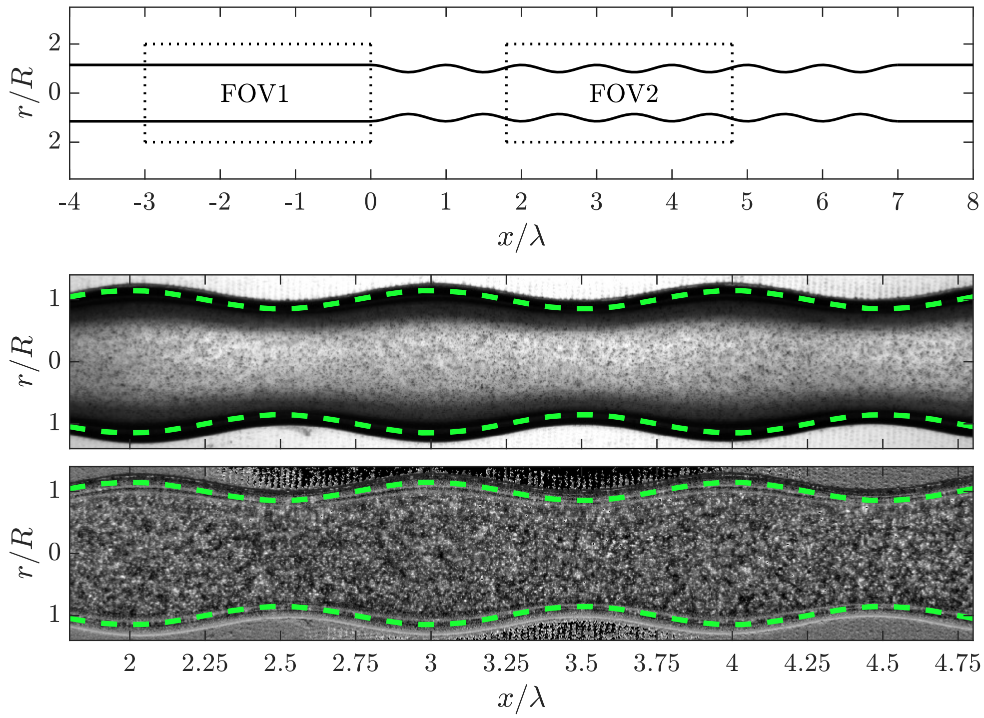

Figure 6.2: (*a*) A two-dimensional schematic showing the different PSV fields of view. (*b*) Sample PSV image (C14 at c = 400ppm) for FOV2. (*c*) An enhanced version of the sample image (*b*) for C14 at c = 400ppm and FOV2.

Backlight illumination of the PIV recordings was achieved using a 15 mJ pulse^{-1} Nd:YAG laser (Solo I-15, New Wave Research Inc.) equipped with a diffuser. A diffuser expanded the laser beam, made the incident light incoherent and changed the wavelength to 610 nm using fluorescent disks. A programmable timing unit (PTU-9, LaVision GmbH) and DaVis 8.4 software (LaVision GmbH) were used to synchronize the camera and laser. Silver coated hollow glass spheres with diameter, d_p = 10 µm, were used as tracer particles in the flow (S-HGS-10, Dantec Dynamics). These particles were opaque, which was ideal for projecting a shadow on the camera in backlight illumination. The density of the particles, ρ_p, was 1400 kg m^{-3}. As a result the particle response time, $t_p = \rho_p d_p^2/18\mu_s$, and particle settling velocity, $u_p = (\rho_p - \rho)d_p^2 g/18\mu_s$, could be established. Here, g is the gravitational acceleration. The particle response time, t_p, was 7.8 µs and the particle settling velocity, u_p, was 21.8 µm s^{-1}. The Stokes number is estimated to be, $St = t_p\dot{\gamma}_w$, and the Froude number to be, $Fr = 2u_p/U_0$. The largest St was 0.003 and the largest Fr was 0.005, depending on Q. Both the Stokes and Froude number are small (less than 0.1) and errors attributed to particle inertia and particle settling are negligible.

For FOV1, five sets of measurements were performed for water, each for the different values of Q that were previously listed in §6.1. The results for FOV1 are presented in Appendix A.1. The measurements of velocity within the entrance region show good agreement with the theoretical expectations for all values of

Q, providing good confidence in PSV to produce reasonable measurements. For FOV2, measurements were performed for three different non-Newtonian fluids, each having five different concentrations, and five flow rates Q (75 data sets in total). As well, five measurements were performed for distilled water at FOV2 for each value of Q. Each data set consisted of 600 pairs of double-frame images recorded at an acquisition frequency of 7.3 Hz. A sample image of the first frame for C14 at a mass concentration of 400ppm is shown in figure 6.2(b). The time delay, Δt, between image frames was between 500 and 7000 µs depending on the value of Q, such that the maximum particle displacement between the image frames was no greater than 15 pixel.

Image processing was performed using DaVis 8.4 software (LaVision Gmbh). First, the images were inverted; the intensity signal at each pixel was subtracted from a constant intensity value. Next, the minimum intensity within each pixel and along the complete image ensemble was determined and subtracted from all images in each data set. Third, the intensity signals at each pixel were normalized by the average intensity of the ensemble. A sample image (C14 at a concentration of 400ppm) after performing the previously detailed processing steps can be seen in figure 6.2(c). Compared to the native image, seen in figure 6.2(b), the processed image has more clearly defined bright particles for all values of r.

Vector fields were established using the ensemble-of-correlation method with an initial interrogation window (IW) size of 64×64 pixel (0.44×0.44 mm^2 or $0.41R \times 0.41R$) and a final IW size of 16×16 pixel (0.11×0.11 mm^2 or $0.10R \times 0.10R$) with 75% overlap between neighboring IWs (Meinhart *et al.*, 2000). The velocity vector was denoted as $\boldsymbol{U}$, with components in cylindrical coordinates being, U_r, U_θ, U_x, and corresponding to the velocity along the r, θ, x directions respectively. The flow is laminar and steady, with presumabely no swirl, i.e. $U_\theta = 0$, given the geometric dimensions of the PCT and the Reynolds numbers of the flows in the present investigation (Deiber & Schowalter, 1979). Evidence of secondary flow re-circulations, turbulence or swirl is not observed. An evaluation of the uncertainty in measurements of U is provided in Appendix A.1. Throughout this chapter, error bars are used to convey the uncertainty in the results.

6.3 Flow field analysis

Simplifying equation (2.3), the steady flow of complex and Newtonian fluids in the PCT are governed by the following equations for mass and momentum conservation,

$$\left.\begin{aligned} \nabla \cdot \boldsymbol{U} &= 0, \\ \rho \boldsymbol{U} \cdot \nabla \boldsymbol{U} &= -\nabla P + \nabla \cdot \boldsymbol{\tau}, \end{aligned}\right\} \tag{6.2}$$

where P is the indeterminate component of the Cauchy stress tensor, and $\boldsymbol{\tau}$ is the deviatoric stress tensor. The nonzero components of the rate of deformation tensor D, and rate of rotation tensor W are listed,

$$\left.\begin{gathered} D_{rr} = \frac{\partial U_r}{\partial r}, \quad D_{\theta\theta} = \frac{U_r}{r}, \quad D_{xx} = \frac{\partial U_x}{\partial x}, \\ D_{rx} = D_{xr} = \frac{1}{2}\left(\frac{\partial U_r}{\partial x} + \frac{\partial U_x}{\partial r}\right), \end{gathered}\right\} \tag{6.3}$$

$$\omega_\theta = -2W_{xr} = \frac{\partial U_r}{\partial x} - \frac{\partial U_x}{\partial r}, \tag{6.4}$$

where $\boldsymbol{\omega}$ is the vorticity vector, whose only non-zero component is ω_θ. Equations (6.1) reduces to the Navier-Stokes equation for Newtonian fluids when the deviatoric stress tensor is represented by the constitutive equation, $\boldsymbol{\tau} = 2\mu_s\mathbf{D}$. For non-Newtonian fluids, the constitutive relation is much more complex and can be a partial differential equation with nonlinear terms (e.g. Phan-Thien-Tanner and Giesekus models). For most non-Newtonian constitutive models, it is common to segregate the deviatoric stress tensor into a solvent and non-Newtonian stress, i.e. $\boldsymbol{\tau} = \boldsymbol{\tau_s} + \boldsymbol{\tau_{nn}}$ (Alves *et al.*, 2020). Here, $\boldsymbol{\tau_s} = 2\mu_s\mathbf{D}$, is the solvent stress, and $\boldsymbol{\tau_{nn}}$ is the non-Newtonian stress introduced from the polymers or micelles. Note that if $\boldsymbol{\tau_{nn}} = 0$, then $\boldsymbol{\tau} = \boldsymbol{\tau_s}$ and the constitutive equation is Newtonian. When substituted into equation (6.2), the divergence of the non-Newtonian stress, $\nabla \cdot \boldsymbol{\tau_{nn}}$, acts as an additional forcing term and for polymeric flows is often referred to as a "polymer force" (Kim *et al.*, 2007).

Equations (6.3) and (6.4) can be explicitly evaluated using the measured U_x and U_r. To circumvent the need for pressure, P, the vorticity transport equation is considered, from taking the curl of the momentum transport equation shown in (6.2). The only non-zero component of the vorticity in the PCT flow is ω_θ; therefore, the vorticity transport equation is only considered along the azimuthal direction,

$$\underbrace{U_r\frac{\partial \omega_\theta}{\partial r} + U_x\frac{\partial \omega_\theta}{\partial x} - \frac{U_r\omega_\theta}{r}}_{VA} = \underbrace{\nu_s\left(\frac{\partial^2\omega_\theta}{\partial r^2} + \frac{1}{r}\frac{\partial \omega_\theta}{\partial r} + \frac{\partial^2\omega_\theta}{\partial x^2} - \frac{\omega_\theta}{r^2}\right)}_{VSD} + T_\theta. \tag{6.5}$$

The additional term on the right hand side of equation (6.5) is the azimuthal component of the non-Newtonian torque, $\boldsymbol{T} = (\nabla \times \nabla \cdot \boldsymbol{\tau_{nn}})/\rho$. The non-Newtonian torque is a vector, whose only non-zero component in the PCT is T_θ. Previous numerical investigations have denoted $\boldsymbol{T}$ the "polymer torque" as it can be represented as the curl of the polymer force (Kim *et al.*, 2007, 2008; Kim & Sureshkumar, 2013; Page & Zaki, 2015, 2016; Biancofiore *et al.*, 2017; Lee & Zaki, 2017). Its simplified units are s^{-2} – when multiplied by moment of inertia, the units are force times unit distance, consistent with the true torque definition. The under-braces shown in equation (6.5) isolate the different combinations of terms within the vorticity transport equation. On the left hand side of equation (6.5), VA denotes the azimuthal vorticity advection. The first term on the right hand side of equation (6.5), VSD, represents vorticity solvent diffusion, where $\nu_s = \mu_s/\rho$. For each flow, the azimuthal non-Newtonian torque was calculated based on the deficit between VA and VSD, i.e. $T_\theta = VA - VSD$.

To establish the first-order spatial gradients of velocity, a moving second-order polynomial surface was fit on profiles of U_x and U_r. The size of the second-order polynomial filter was 20×20 pixels, $138 \times 138\,\mu m^2$, or $0.15R \times 0.15R$. Coefficients of the polynomial surface were used to establish first-order spatial derivatives of U_x and U_r. Azimuthal vorticity, ω_θ was then established using equation (6.4). To determine the higher order spatial gradients in the flow, a moving third-order polynomial surface was fit on profiles of U_x and U_r. The size of the cubic polynomial filter was 76×76 pixels, $522 \times 522\,\mu m^2$, or $0.56R \times 0.56R$. Coefficients of the third-order polynomial were used to the determine the second- and third-order spatial derivatives of U_x and U_r. Three orders of differentiation in $\boldsymbol{U}$ are required due to the VSD term in equation (6.5). These higher-order derivatives were then used to calculate the azimuthal non-Newtonian torque T_θ

using equation (6.5). Polynomial filters that overlapped with the PCT wall were neglected, and results of ω_θ and T_θ were not considered close to the wall.

All parameters including $\boldsymbol{U}$, ω_θ, and T_θ exhibited symmetry about $r = 0$. Therefore, $\boldsymbol{U}$, ω_θ, and T_θ on the lower half of the domain ($r < 0$) were averaged with the upper half ($r > 0$). When comparing $\boldsymbol{U}$, ω_θ, and T_θ in one oscillation to prior or subsequent oscillations, the parameters are not dramatically different for all flow conditions and fluids. Therefore, $\boldsymbol{U}$, ω_θ, and T_θ were periodically averaged over three oscillations, i.e. for x-coordinates that share the same wall radius, R_w.

The volumetric flow rate, Q can be determined from flow measurements based on a volume integration of U_x, i.e. $Q = 2\pi \int_0^{R_w} U_x r dr$. The bulk velocity can be defined according to, $U = Q/(\pi R_w^2)$. Because of mass conservation and the variation of R_w along x, the bulk velocity U_b changes along the streamwise x direction. Therefore an average value of U_b along x was determined, and an overbar was used to denote the spatial averaging along the x direction, i.e., $\bar{U}_b$. Recall from §6.1, that the same overbar was used to define the average centreline velocity along x, $\bar{U}_0$. An average shape factor can be determined from the ratio of centreline to bulk velocity, $\bar{U}_0/\bar{U}_b$. For Poiseuille flow in a straight-walled tube, $SF = 2$. Lastly, distributions of $\boldsymbol{U}$, ω_θ and T_θ for flows within the PCT (i.e., FOV2) were normalized by $\bar{U}_0$, $\dot{\gamma}_w$ and $\dot{\gamma}_w^2$, respectively. Spatial variables x and r were normalized by λ and R, respectively.

6.4 Flows in the periodically constricted tube

6.4.1 Water

Figure 6.3 demonstrates contours of the velocity magnitude $||\boldsymbol{U}|| = (U_x^2 + U_r^2)^{0.5}$ along with streamlines, for the flow of water at five different Re within the PCT. All flows with unique Re have a centreline velocity U_0 that attains a maximum value around $x/\lambda = 0.5$. When $x/\lambda = 0.5$ the wall radius of the PCT, R_w, is at its smallest value, $R_w = R_i$. For the lowest Re flow (i.e., $Re = 15.7$), the centreline velocity at $x/\lambda = 0.5$ attains $1.25\bar{U}_0$. The lowest magnitude in U_0 occurs when $x/\lambda = 0$ and 1, and is approximately equal to $0.7\bar{U}_0$ for $Re = 15.7$. At larger Re, the centreline velocity at $x/\lambda = 0.5$, is smaller in magnitude – around $1.1\bar{U}_0$. Values of U_0 are also slightly larger for the high Re cases when $x/\lambda = 0$ and 1 compared to the case with $Re = 15.7$ – approximately equal to $0.8\bar{U}_0$. Therefore, when Re increases, the normalized centreline velocity decreases. In all flow conditions, streamlines at large r/R tend to follow the sinusoidal profile of the wall. Near the core, streamlines are more parallel with respect to the streamwise x direction.

Profiles of $U_x/\bar{U}_0$ with respect to r/R at different points of x/λ are shown in figure 6.4(a) for water at $Re = 15.7$, 106 and 203. Sample error bars are shown for the flow condition with Re of 15.7 and at $x/\lambda = 0.5$. Relative errors were conservatively estimated to be $0.042\bar{U}_0$ near the centreline of PCT and $0.108\bar{U}_0$ near the wall at $x/\lambda = 0.5$, as discussed in Appendix A.1. As noted in the discussion pertaining to figure 6.3, the low Re flow of 15.7 has a large variation in U_0. When $x/\lambda = 0$, U_0 becomes $0.75\bar{U}_0$ and when $x/\lambda = 0.5$, U_0 equals $1.25\bar{U}_0$. Newtonian flows with larger Re of 106 and 203 have a centreline velocity of approximately $0.81\bar{U}_0$ when $x/\lambda = 0$ and $1.1\bar{U}_0$ when $x/\lambda = 0.5$. Within the PCT contractions and expansions (i.e., $x/\lambda = 0.25$ and 0.75 respectively), radial profiles of $U_x/\bar{U}_0$ are approximately the same. In other words, the velocity is symmetric about $x/\lambda = 0.5$. Figure 6.4(b) demonstrates that the streamlines

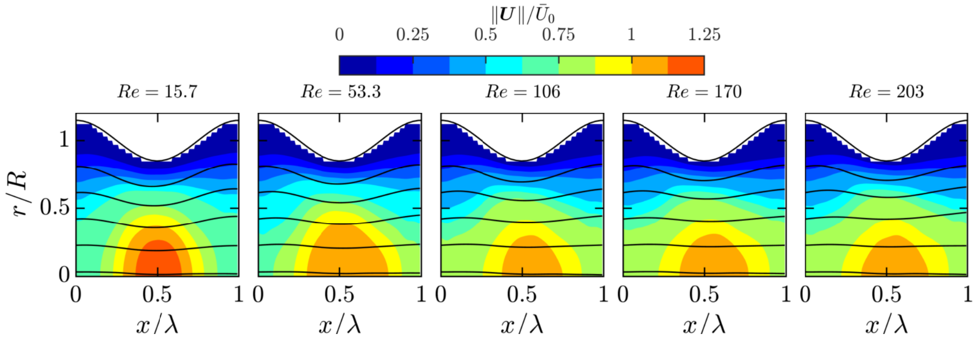

Figure 6.3: Velocity magnitude normalized by the average centreline velocity $\bar{U}_0$ for different Re of water. Solid black lines overlaid on filled contours are streamlines. The solid black line at the limit of the filled contour is the sinusoidal wall profile.

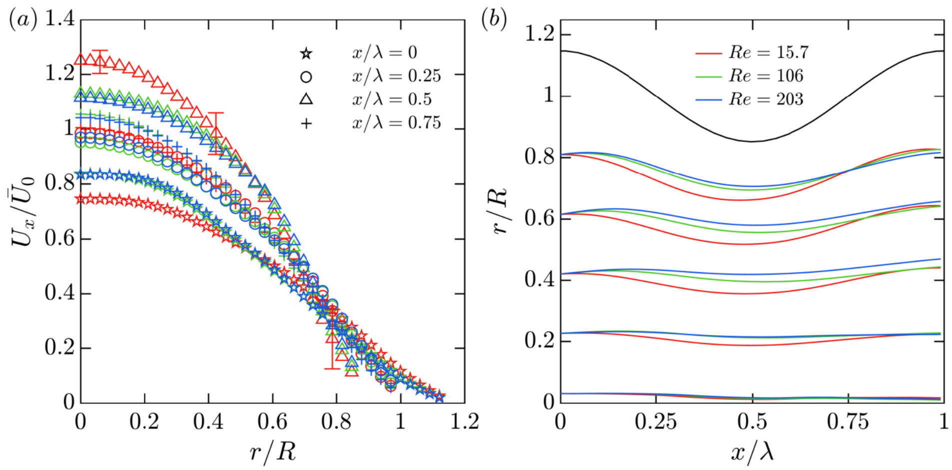

Figure 6.4: (a) Velocity profiles of water at $Re = 15.7, 106$ and 203 at different x locations along the PCT. Down sampled error bars are shown for the flow of water at $Re = 15.7$ and $x/\lambda = 0.5$. (b) Overlaid streamlines of the water flows at different Re. The black line in (b) indicates the wall profile R_w. Symbol colours in (a) correspond to the different Re as indicated in (b).

of the Newtonian flows also depend on Re. When Re is low, streamlines are more curved and their radial position is closer to the PCT centreline at $x/\lambda = 0.5$.

As noted in regards to figure 6.4(a), the velocity in the PCT for water demonstrates a dependence on Re most notable by the differences in the amplitude of the centreline velocity U_0. The standard deviation in the centreline velocity $\mathcal{R}(U_0)$ was computed for each Re and normalized by their respective average centreline velocities $\bar{U}_0$. Values of $\bar{U}_0$ and $\mathcal{R}(U_0)/\bar{U}_0$ are listed in table 6.1 for the different water flow. The inverse proportionality between the amplitude of U_0 and Re is clearly demonstrated by the decreasing trend in $\mathcal{R}(U_0)/\bar{U}_0$ as Re grows. In addition to centreline velocity, table 6.1 also lists the average bulk velocity $\bar{U}_b$ and shape factor $SF = \bar{U}_0/\bar{U}_b$ for the flows of water in the PCT. For Newtonian Poiseuille flow in a straight-walled pipe, SF equals 2. Although the PCT is not straight-walled, values of SF for all water flows are around 2.1 and not too different from the theoretical SF for straight-walled Poiseuille pipe flow.

Re	$\bar{U}_0$ mm s^{-1}	$\mathcal{R}(U_0)/\bar{U}_0$	$\bar{U}_b$ mm s^{-1}	SF
15.7	8.4	0.18	4.0	2.1
53.3	28.6	0.14	13.5	2.1
105.6	56.8	0.10	26.5	2.1
170.5	91.7	0.08	42.1	2.2
202.7	109.0	0.09	51.1	2.1

Table 6.1: Bulk and centreline velocity statistics for the flow of water within the PCT at different Re.

Contours of azimuthal vorticity, $\omega_\theta/\dot{\gamma}_w$ are shown in figure 6.5 for water within the PCT. Near the centreline, $\omega_\theta/\dot{\gamma}_w$ is approximately equal to zero. For all radial and streamwise coordinates, ω_θ is positive. The maximum $\omega_\theta/\dot{\gamma}_w$ is situated near the wall and at $x/\lambda = 0.5$ for all Re. Recall from §6.3 that measurements of $\omega_\theta/\dot{\gamma}_w$ within close proximity (15% of R_w) of the wall were not calculated. This is because the differentiation filter conflicted with the wall.

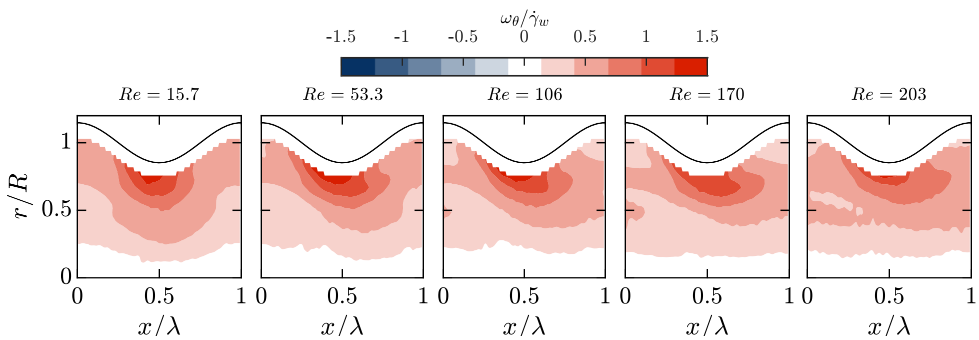

Figure 6.5: Vorticity normalized by average wall shear rate $\dot{\gamma}_w$ for different Re of water. The solid black line is the sinusoidal wall profile.

6.4.2 Xanthan gum solutions

Velocity contours and streamlines are shown in figure 6.6 for XG solutions at different Re. For brevity, only the results of two concentrations, c = 200ppm and 500ppm are shown. Similar to water, both of the XG solutions with c = 200ppm and 500ppm have magnitudes of $||\boldsymbol{U}||/\bar{U}_0$ that are lowest when $x/\lambda = 0$ and 1, and largest when $x/\lambda = 0.5$. Compared to Newtonian water flows seen in figure 6.3, the zone with larger values of $||\boldsymbol{U}||/\bar{U}_0$ is extended farther towards the tube wall. As c increases from 200ppm to 500ppm, $||\boldsymbol{U}||/\bar{U}_0$ also increases at $r/R > 0$ locations. Streamlines at large r/R take on a similar sinusoidal profile as the wall pattern. Similar to the water flows, the streamlines for XG at c = 200ppm and 500ppm are approximately symmetric with respect to $x/\lambda = 0.5$.

Streamwise velocity profiles $U_x/\bar{U}_0$ at different x/λ coordinates are shown in figure 6.7(a) for XG with c = 500ppm and at $Re = 10.2$. For comparison, the profiles of water at a similar Re are presented alongside XG. Relative to water at the same x/λ coordinates, XG has larger $U_x/\bar{U}_0$ values. The distributions of $U_x/\bar{U}_0$

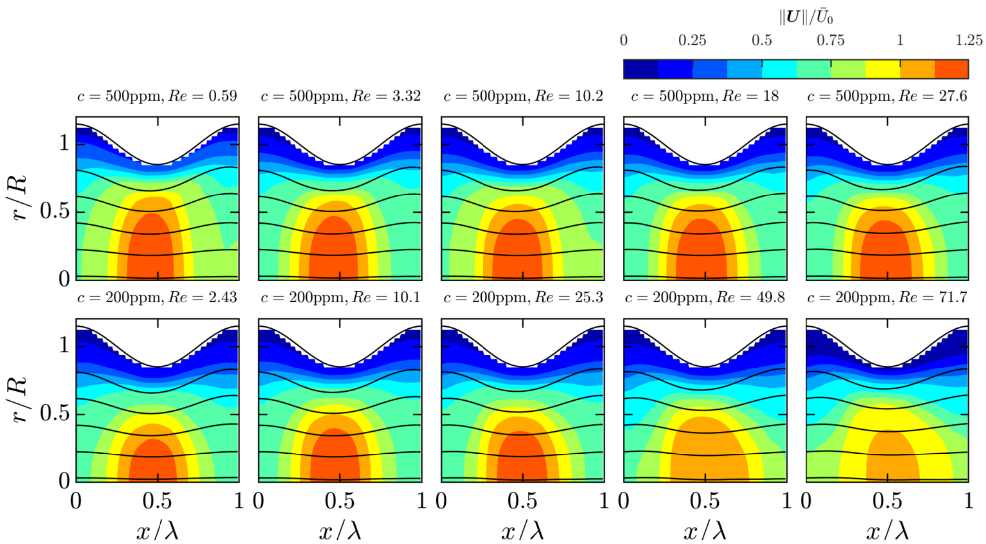

Figure 6.6: Velocity magnitude normalized by the average centreline velocity $\bar{U}_0$ for different c and Re of XG. Solid black lines overlaid on filled contours are streamlines. The solid black line at the limit of the filled contour is the sinusoidal wall profile.

are more flat in the PCT centre; a blunted profile that is common in shear thinning fluids (Bird *et al.*, 2007). Despite the different shaped velocity profile, the range of U_0 appears to be similar among water and XG. For the XG flow, $U_0 = 0.75\bar{U}_0$ at $x/\lambda = 0$, and $U_0 = 1.25\bar{U}_0$ at $x/\lambda = 0.5$ – the same as water. Lastly, figure 6.7(*b*) compares the streamlines of the same flows of XG and water seen in figure 6.7(*a*). Despite having different velocity profiles with respect to r/R, the streamlines for water and XG are approximately the same.

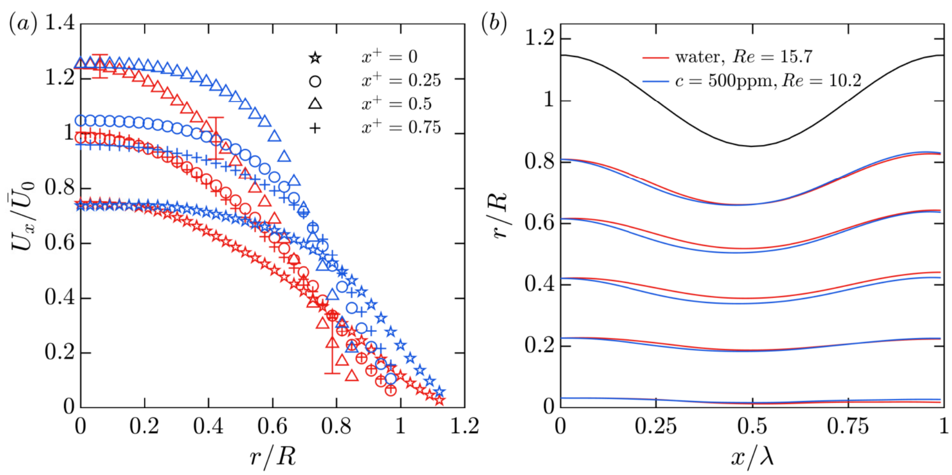

Figure 6.7: (*a*) Velocity profiles along different x locations for XG with c = 500ppm at Re = 10.2, and water at Re = 15.7. Down sampled error bars are shown for the flow of water at Re = 15.7 and x/λ = 0.5. (*b*) Overlaid streamlines of XG and water. The black line in (*b*) indicates the wall profile R_w. Red symbols in (*a*) correspond to the water flow with Re = 15.7, while blue symbols represent the XG flow with c = 500ppm and Re = 10.2.

Based on figure 6.7(*a*), it was shown that the shape of $U_x/\bar{U}_0$ profiles with respect to r/R were different, but the relative variations in U_0 were the same among the flows of water and XG at similar Re. Figure 6.8(a) demonstrates the standard deviation in U_0 normalized by the average centreline velocity, $\mathcal{R}(U_0)/\bar{U}_0$, for XG and water. Low concentration solutions of XG (c < 300ppm) appear to have $\mathcal{R}(U_0)/\bar{U}_0$ values that overlap with water at high Re. However, for $Re < 20$ and high XG concentrations, the values of $\mathcal{R}(U_0)/\bar{U}_0$ appear to be independent of the Reynolds number and relatively constant. The larger concentration XG solutions of 400ppm and 500ppm appear to have subtly larger values of $\mathcal{R}(U_0)/\bar{U}_0$ than water and the other XG solutions; however the difference is not substantial. Generally, $\mathcal{R}(U_0)/\bar{U}_0$ for XG appears to be independent of concentration, and similar to water at higher Re values. Figure 6.8(b) presents the average shape factor $SF = \bar{U}_0/\bar{U}_b$ for water and XG at different Re and c within the PCT. Relative to water, XG flows at all c and Re have lower SF values. As the c of XG increases, SF decreases. The reducing trend in SF, aptly summarizes how shear thinning makes the profile more blunt as the concentration of XG increases.

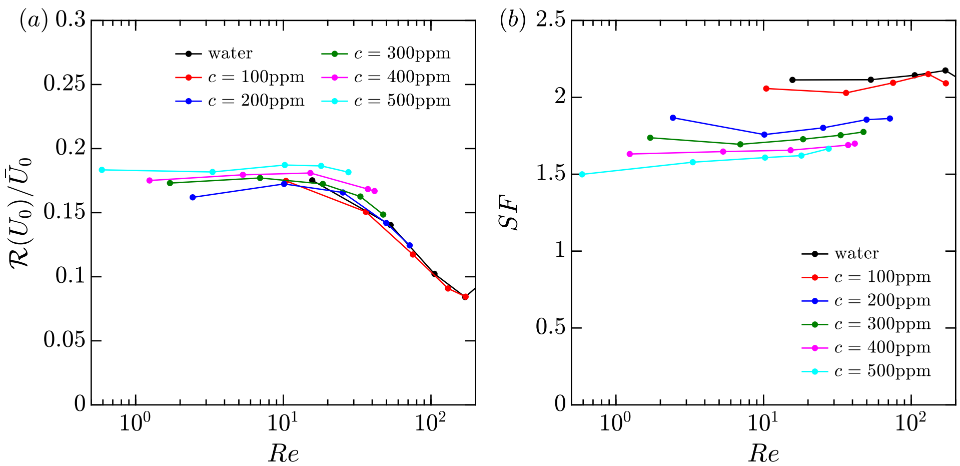

Figure 6.8: (a) The standard deviation in the centreline velocity divided by the mean centreline velocity, and (b) the shape factor with respect to different Re for XG solutions and water.

Vorticity contours for the XG flows with c = 200ppm and 500ppm are shown in figure 6.9. Similar to the flows of water in the PCT, $\omega_\theta/\dot{\gamma}_w$ attains a maximum value near the wall and at $x/\lambda = 0.5$. Both the XG flows with c = 200ppm and 500ppm have a noticeably attenuated $\omega_\theta/\dot{\gamma}_w$ in regions farther from the tube centreline. In other words, the thickness (along r/R) of the region near the pipe centreline with $\omega_\theta/\dot{\gamma}_w = 0$ is larger for XG relative to water. The thickness also grows with increasing c. The attenuated $\omega_\theta/\dot{\gamma}_w$ is attributed to the more uniform profiles of $U_x//\bar{U}_0$ caused by shear thinning.

6.4.3 Polyacrylamide solutions

Relative to water and XG, different patterns in the velocity are encountered for the flow of PAM within the PCT. Figure 6.10 demonstrates contours of $||U||/\bar{U}_0$ for PAM at different c and Re. In this figure, c increases from bottom to top, and Re increases from left to right. Despite the low Re flows showing some visual resemblance to the results for water, flows at high c and large Re are asymmetric about $x/\lambda = 0.5$. For these cases, the large velocity contours takes on a triangular or half chevron appearance leaning towards the upstream direction. Therefore, within the contraction regions (i.e. from $x/\lambda = 0$ to 0.5) the maximum

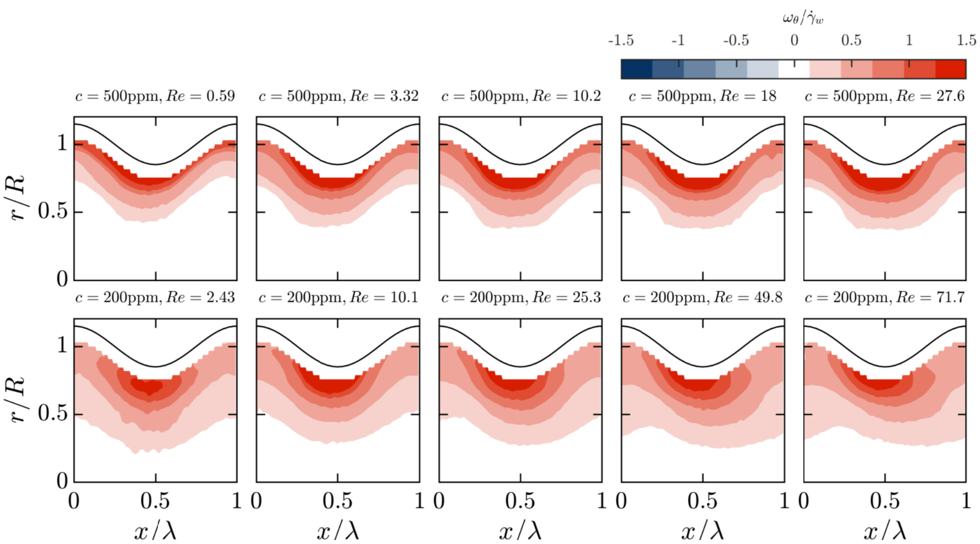

Figure 6.9: Vorticity normalized by the average wall shear rate $\dot{\gamma}_w$ for different c and Re of XG. The solid black line is the sinusoidal wall profile.

velocity is not necessarily situated at the centreline of the PCT. Within the tail of the chevron, streamlines appear to be tilted farther towards the centreline and non-conforming to the sinusoidal profile of the walls. Despite the PAM solutions having seemingly comparable steady shear rheology as the XG solutions (figure 5.1), the flow of PAM within the PCT produces an entirely different velocity distribution. It is clear that another rheological property, not present in XG, is causing the chevron pattern in the flows of PAM through the PCT.

Streamwise velocity profiles $U_x/\bar{U}_0$ along different x/λ values are shown in figure 6.11(a) for PAM with $c = 300$ppm. Two different Re are compared to contrast the change in the velocity from when the contours transition to the half chevron seen in figure 6.10. For the low Reynolds number case of $Re = 3.02$ (red symbols), profiles of $U_x/\bar{U}_0$ are similar to water or XG. The shape of the $U_x/\bar{U}_0$ profiles appear to be subtly more blunted than the parabolic Poisueille profile, and the variations in U_0 are slightly larger than the values encountered for water at $Re = 15.7$ seen in figure 6.3(a). Similar to XG, the more blunted velocity profile for PAM at low Re can likely be explained by shear thinning. Recall that PAM with $c = 300$ppm has a lower power-law index than XG with $c = 500$ppm, as seen in tables 5.1 and 5.2. Therefore, it is expected that $U_x/\bar{U}_0$ profiles are not to be parabolic, but also not as blunted as the higher concentration XG solutions. Although the low Re flow reflects some similarities to previous findings for XG, the higher Re flow of PAM (blue symbols) exhibits entirely unique distributions in $U_x/\bar{U}_0$. At $x/\lambda = 0$ the $U_x/\bar{U}_0$ profile has two local maxima – one at the centreline, the other at $r/R = 0.9$. Within the contraction, where $x/\lambda = 0.25$, the maximum value of $U_x/\bar{U}_0$ is no longer situated at the centreline, but at $r/R = 0.6$. Prior works have observed large velocity overshoot near the wall in gradual planar contraction flows of PAM solutions (Poole *et al.*, 2005) and numerical investigations that utilized various viscoelastic constitutive models (Afonso & Pinho, 2006; Poole *et al.*, 2007; Alves & Poole, 2007; Poole & Alves, 2009). Poole *et al.* (2005) referred to these velocity overshoots as “cat’s ears” given their appearance.

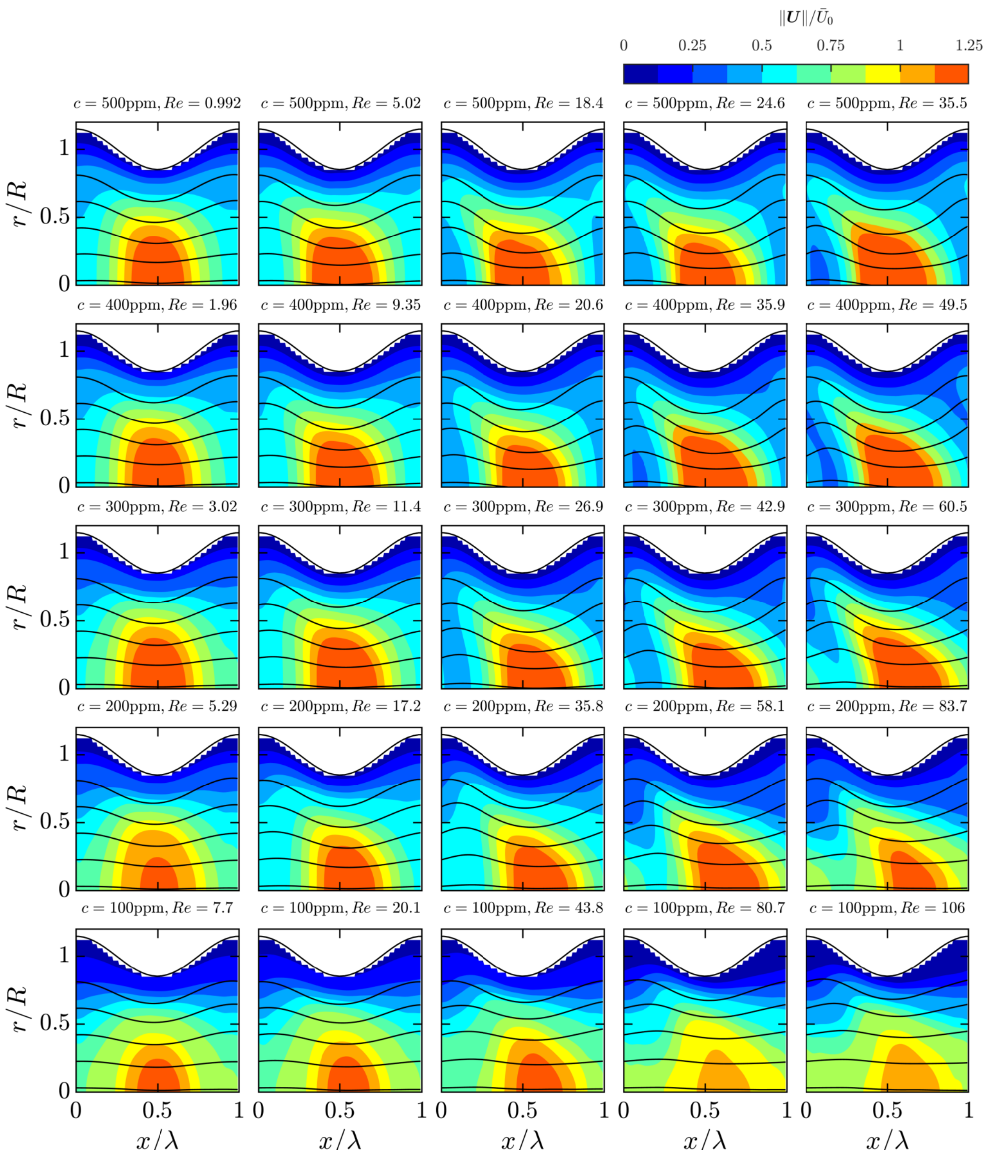

Figure 6.10: Velocity magnitude normalized by the average centreline velocity $\bar{U}_0$ for different c and Re of PAM. Solid black lines overlaid on filled contours are streamlines. The solid black line at the limit of the filled contour is the sinusoidal wall profile.

Coupled with the near-wall velocity overshoots are highly curved streamlines, as shown in figure 6.11(*b*). At sufficiently large Re, PAM with $c = 300$ppm has streamlines that are directed away from the PCT core and more towards the tube wall for $x/\lambda = 0$ to 0.5. The works by Cable & Boger (1978*a*,*b*, 1979) referred to the state of these curved streamlines as "divergent flow." In general, solutions of PAM with $c \geq 200$ppm and sufficiently large Re are subjected to near-wall velocity overshoots and divergent flow within the contracting portions of the PCT (i.e. $0 < x/\lambda < 0.5$), as seen in figure 6.10.

The pattern of $U_x/\bar{U}_0$ for PAM is clearly dependent on Re and c, as observed in figure 6.10. Compared to water, it can be observed that variations in U_0 are larger for PAM at large c and Re based on figure 6.11(*a*). Figure 6.12(*a*) demonstrates $\mathcal{R}(U_0)/\bar{U}_0$ as a function of Re for different c of PAM. When the concentration

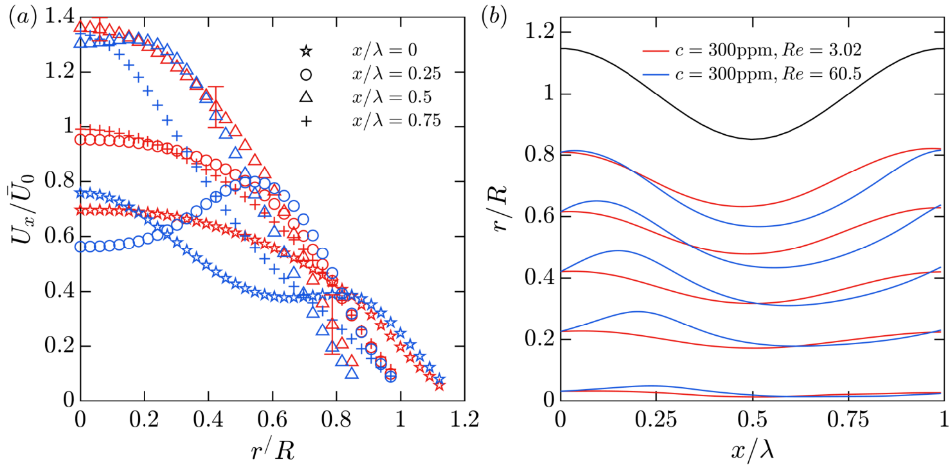

Figure 6.11: (*a*) Velocity profiles along different x locations for PAM with c = 300ppm at Re = 3.02, and Re = 60.5. Red symbols show Re = 3.02 and blue symbols show Re = 60.5. Down sampled error bars are shown for the flow of PAM with c = 300ppm and Re = 3.02 at x/λ = 0.5. (*b*) Overlaid streamlines of PAM at different Re. The black line in (*b*) indicates the wall profile R_w.

of PAM is low (c = 100ppm), values of $\mathcal{R}(U_0)/\bar{U}_0$ are similar to water. This is expected; contours of velocity for PAM with c = 100ppm do not exhibit a prevalent asymmetric half chevron pattern in figure 6.10. At large concentrations, PAM enhances the variations in U_0. For more moderate PAM concentrations of c = 200ppm and 300ppm, $\mathcal{R}(U_0)/\bar{U}_0$ increases up until an Re of about 35, before decreasing with further growth in Re. At large concentrations of c = 400ppm and 500ppm, values of $\mathcal{R}(U_0)/\bar{U}_0$ are similar.

Rheological measurements of PAM solutions demonstrated that the solutions are viscoelastic – see figures 5.2 and 5.3. Therefore, values of $\mathcal{R}(U_0)/\bar{U}_0$ are also contrasted with elastic properties of the flow. A Deborah number within the PCT was defined as $De = t_e/t_f$, where $t_f = \lambda/\bar{U}_0$ is the timescale of the flow along the PCT centreline. Figure 6.14(*b*) shows values of $\mathcal{R}(U_0)/\bar{U}_0$ with respect to De for different concentrations of PAM. For all flows of PAM with c = 100ppm, the values of De are less than 0.1, and corresponding values of $\mathcal{R}(U_0)/\bar{U}_0$ are less than 0.2. Larger concentration PAM solutions with $De > 0.1$ have large values of $\mathcal{R}(U_0)/\bar{U}_0$ that are greater than 0.2 and tend to increase with growing De – that is, up until the point where Re has attained 35, with reference to figure 6.12(*a*). Based on the trend in $\mathcal{R}(U_0)/\bar{U}_0$ versus Re for water, a decreasing $\mathcal{R}(U_0)/\bar{U}_0$ is likely attributed to inertial effects – perhaps producing more stagnant flow or small, unseen recirculations in the expansion regions with adverse pressure gradients and where $R_w = R_o$ (Deiber & Schowalter, 1981). On the other hand, elasticity acts to augment $\mathcal{R}(U_0)/\bar{U}_0$. The increasing-decreasing trend in $\mathcal{R}(U_0)/\bar{U}_0$ is most likely a result of the competing effects of elasticity and inertia. When c is sufficiently large, elasticity dominates and the trend in $\mathcal{R}(U_0)/\bar{U}_0$ as function of De show better overlap for different c. Cases with $De > 0.1$ also tend to have a pronounced half chevron velocity pattern in figure 6.10.

Lastly, contours of vorticity $\omega_\theta/\dot{\gamma}_w$ are shown for the flows of PAM in the PCT in figure 6.13. At low c and Re, $\omega_\theta/\dot{\gamma}_w$ is everywhere positive, similar to water and XG. However, PAM with sufficiently large c and Re exhibits negative values of $\omega_\theta/\dot{\gamma}_w$ within the PCT contractions. In certain cases, e.g. c = 300ppm

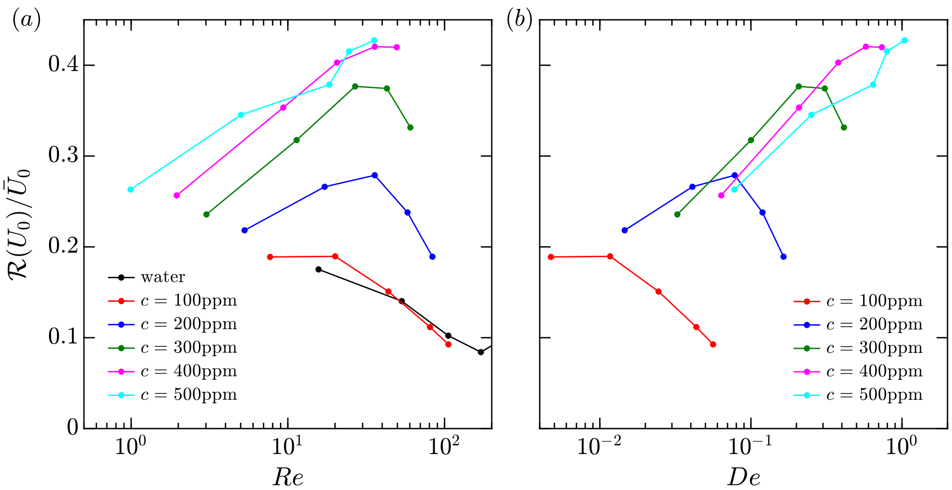

Figure 6.12: The standard deviation in the centreline velocity divided by the mean centreline velocity with respect to (*a*) different Re and (*b*) different Deborah number De for various PAM solutions.

and $Re = 60.5$, there is a strong contrast between the tilted negative contour of $\omega_\theta/\dot{\gamma}_w$ and the surrounding positive $\omega_\theta/\dot{\gamma}_w$ values.

6.4.4 Surfactant solutions

Velocity contours are shown for the C14 solutions in figure 6.14. At the lowest concentration of $c = 100$ppm and 200ppm, the contours are similar to water. Half chevron patterns that are similar to the those of PAM appear for all c greater than 300ppm and Re that exceed 115. The chevrons result in curved streamlines that are asymmetric with respect to $x/\lambda = 0.5$. Despite a water-like shear rheogram, shown in figure 5.1, C14 demonstrates a complex, non-Newtonian response within the PCT that is similar to flexible polymers and unlike rigid polymers. Therefore, the current measurements show that the rheological trait responsible for the asymmetric chevron pattern in PAM is clearly also inherent in C14.

Profiles of $U_x/\bar{U}_0$ with respect to r/R and at different x/λ are shown in figure 6.15(*a*) for C14 with $c = 500$ppm and $Re = 119$ and compared with PAM at $c = 200$ppm and $Re = 83.1$ – the closest possible Re. The near-wall velocity overshoots encountered for the PAM flows, are also present in the C14 solution. Within the contraction, from $x/\lambda = 0$ to 0.25, distributions of $U_x/\bar{U}_0$ can be described by a higher-order polynomial with two local peaks along r/R. Streamlines are also compared for C14 and PAM in figure 6.15(*b*). Both solutions demonstrate divergent flow patterns within the PCT contraction (Cable & Boger, 1978*a*,*b*, 1979). Streamlines for PAM are projected farther towards the wall relative to C14. This is despite PAM having slightly lower near-wall velocity overshoots. In general, there is good qualitative agreement between the velocity field of PAM and C14 – cat's ears and divergent flow.

Distributions of $\mathcal{R}(U_0)/\bar{U}_0$ as a function of Re are shown in figure 6.16 for C14 solutions of different c. Solutions that do not exhibit asymmetric velocity patterns, namely C14 with $c = 100$ppm and 200ppm, have values of $\mathcal{R}(U_0)/\bar{U}_0$ that overlap with water and demonstrate the same decreasing trend in $\mathcal{R}(U_0)/\bar{U}_0$ with increasing Re. For more concentrated solutions of C14, such as $c = 300$ppm and 400ppm, values of $\mathcal{R}(U_0)/\bar{U}_0$ overlap with measurements for water at low Re. As Re is increased further, values of $\mathcal{R}(U_0)/\bar{U}_0$

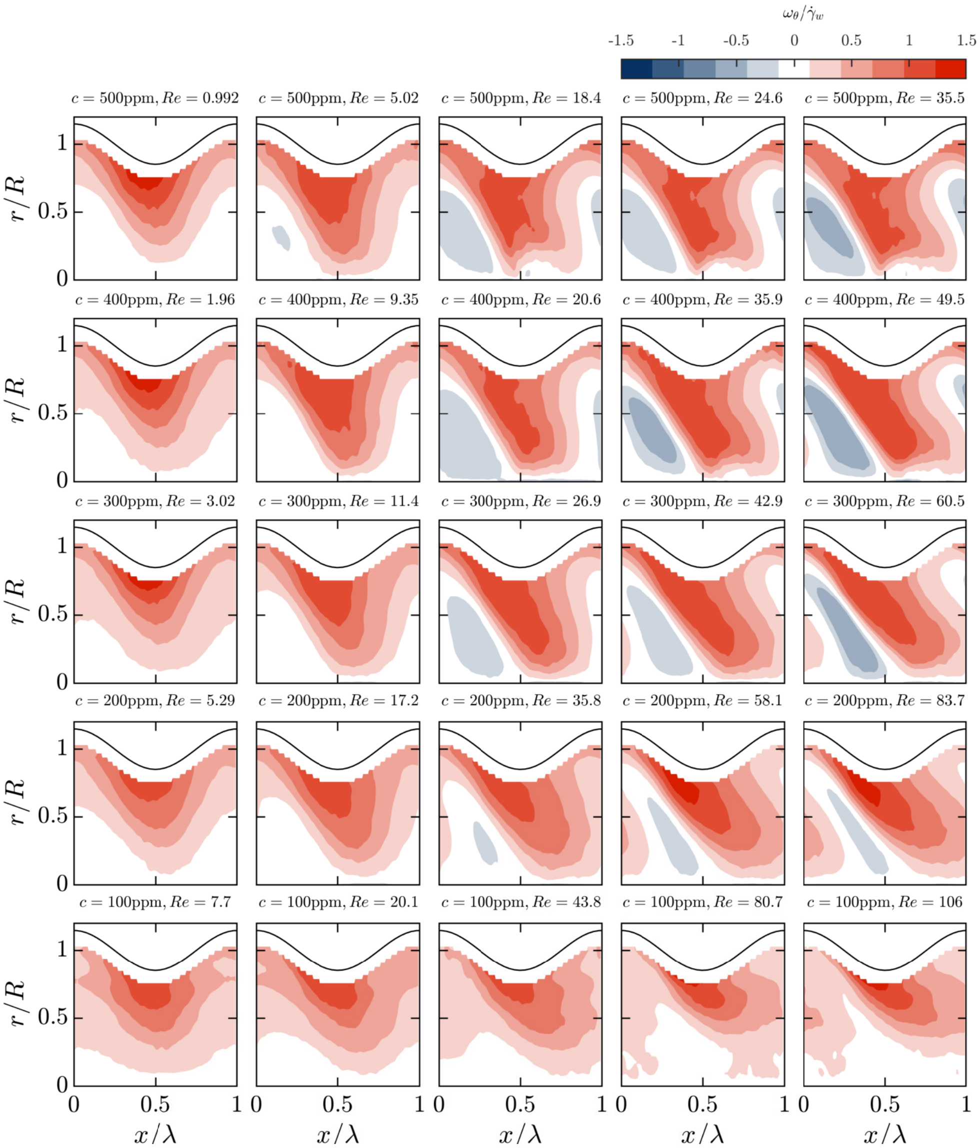

Figure 6.13: Vorticity normalized by $\dot{\gamma}_w$ for different c and Re of PAM. The solid black line is the sinusoidal wall profile.

abruptly increase. This is different than the monotonic increase in $\mathcal{R}(U_0)/\bar{U}_0$ with growing Re observed for PAM in figure 6.12(a). The Re at which $\mathcal{R}(U_0)/\bar{U}_0$ abruptly increases appears to be sensitive to small discrepancies in Re. It appears as though transition to large $\mathcal{R}(U_0)/\bar{U}_0$ occurs earlier for the c = 400ppm C14 solution compared to the c = 300ppm solution. However, the Re at which $\mathcal{R}(U_0)/\bar{U}_0$ increases for c = 300ppm is subtly larger than the Re of the c = 400ppm solution at a comparable flow rate. Evidently, the resolution of Re is too sparse to capture the sudden augmentation in $\mathcal{R}(U_0)/\bar{U}_0$. Ultimately, the trend in the velocity pattern, namely $\mathcal{R}(U_0)/\bar{U}_0$ as a function of Re, is different for C14 compared to PAM. Beyond a critical Re, the asymmetric velocity patterns that are formed by the C14 solution exhibit qualitatively the same pattern as PAM, with values of $\mathcal{R}(U_0)/\bar{U}_0$ that are also larger than the Newtonian and XG flows.

Figure 6.17 presents contours of $\omega_\theta/\dot{\gamma}_w$ for the C14 solutions at different c and Re. Similar to the PAM

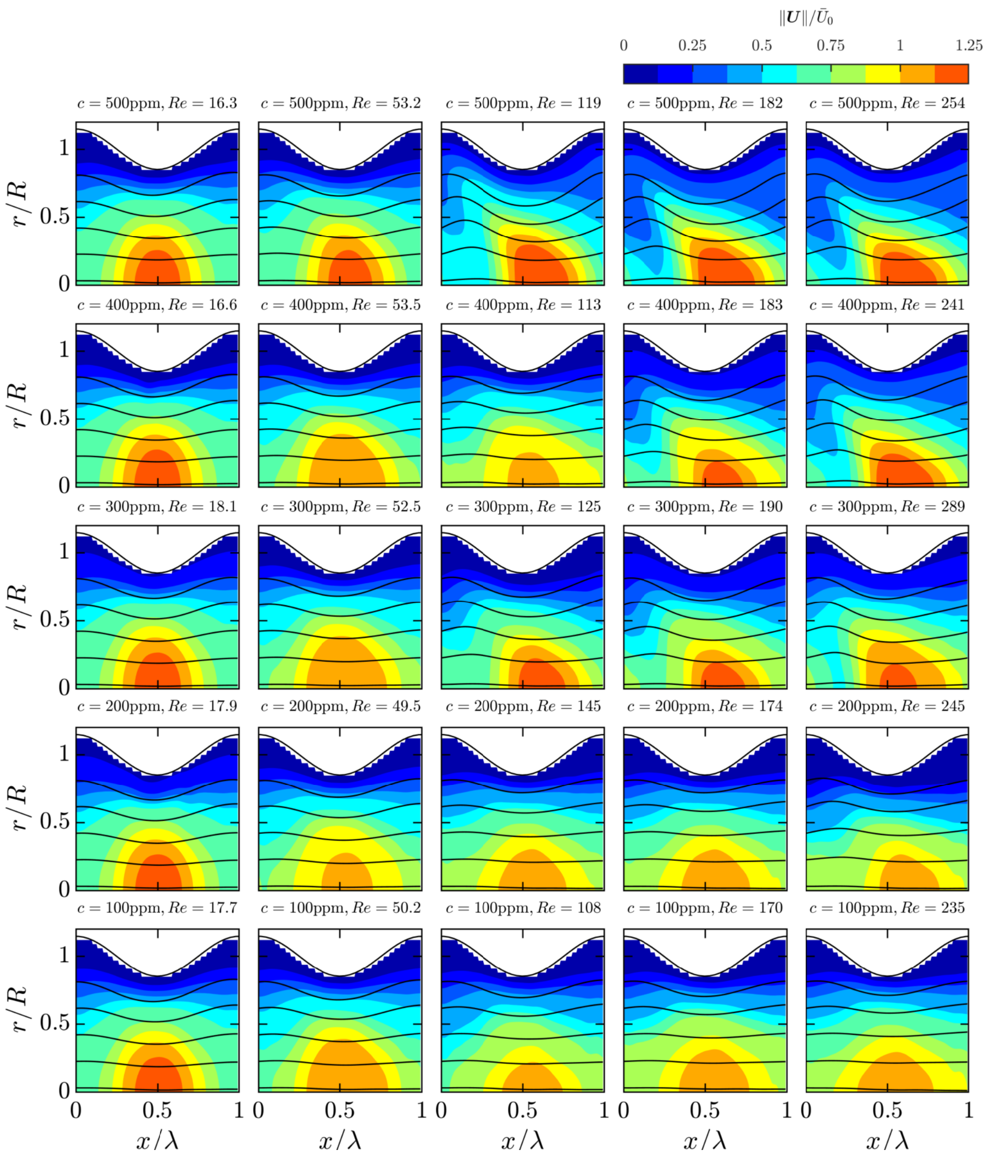

Figure 6.14: Velocity magnitude normalized by the average centreline velocity $\bar{U}_0$ for different c and Re of C14. Solid black lines overlaid on filled contours are streamlines. The solid black line at the limit of the filled contour is the sinusoidal wall profile.

solutions, the flows of C14 with sufficiently large c and Re demonstrate negative values of $\omega_\theta/\dot{\gamma}_w$ within the contractions of the PCT ($0 < x/\lambda < 0.5$). As expected, the conditions where half chevrons appear in velocity contours also reflect negative values in $\omega_\theta/\dot{\gamma}_w$. The c = 100ppm and 200ppm C14 solution have $\omega_\theta/\dot{\gamma}_w$ distributions that are seemingly identical to water, seen in figure 6.5. At large c and Re, negative contours of $\omega_\theta/\dot{\gamma}_w$ begin to appear. It is notable that the C14 solutions exhibit water-like rheology, yet they respond in a manner similar to PAM within the PCT at larger c and Re conditions.

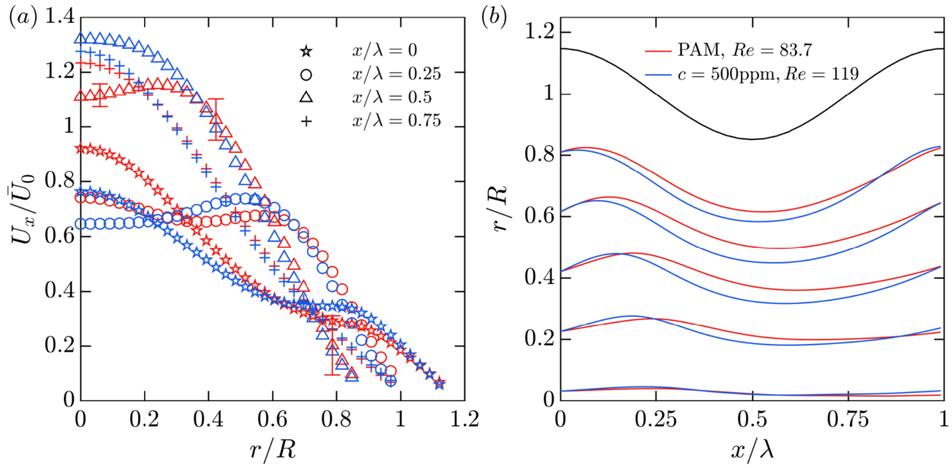

Figure 6.15: (*a*) Velocity profiles along different x locations for C14 with c = 500ppm at Re = 119, shown by the red symbols, and PAM with c = 200ppm at Re = 83.7, shown with blue symbols. Down sampled error bars are shown for the flow of PAM with c = 200ppm and Re = 83.7 at x/λ = 0.5. (*b*) Overlaid streamlines of C14 and PAM.

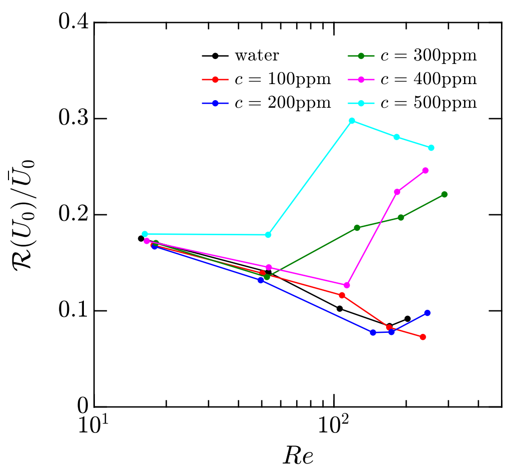

Figure 6.16: The standard deviation in the centreline velocity divided by the mean centreline velocity as a function of Re, for the various C14 solutions.

6.4.5 Non-Newtonian torque

The non-Newtonian torque was established based on the deficit between the advection of vorticity (VA) and the vorticity solvent diffusion (VSD) – see equation (6.5). The normalized azimuthal component of the non-Newtonian torque is $T_\theta/\dot{\gamma}_w^2$. The distributions of $T_\theta/\dot{\gamma}_w^2$ are presented in figure 6.18, 6.19 and 6.20 for water, XG, PAM and C14. In these figures, the open contours show $T_\theta/\dot{\gamma}_w^2$ and are overlaid on filled contours of $\omega_\theta/\dot{\gamma}_w$. Contour levels for $T_\theta/\dot{\gamma}_w^2$ are from -0.4 to +0.4 in steps of 0.2. Contours greater than or equal to zero are solid lines and negative contours are dotted lines. Values of $T_\theta/\dot{\gamma}_w^2$ were not computed or shown near the wall (within 42% of R_w) due to difficulties in computing spatial gradients within this region, as discussed in §6.3.

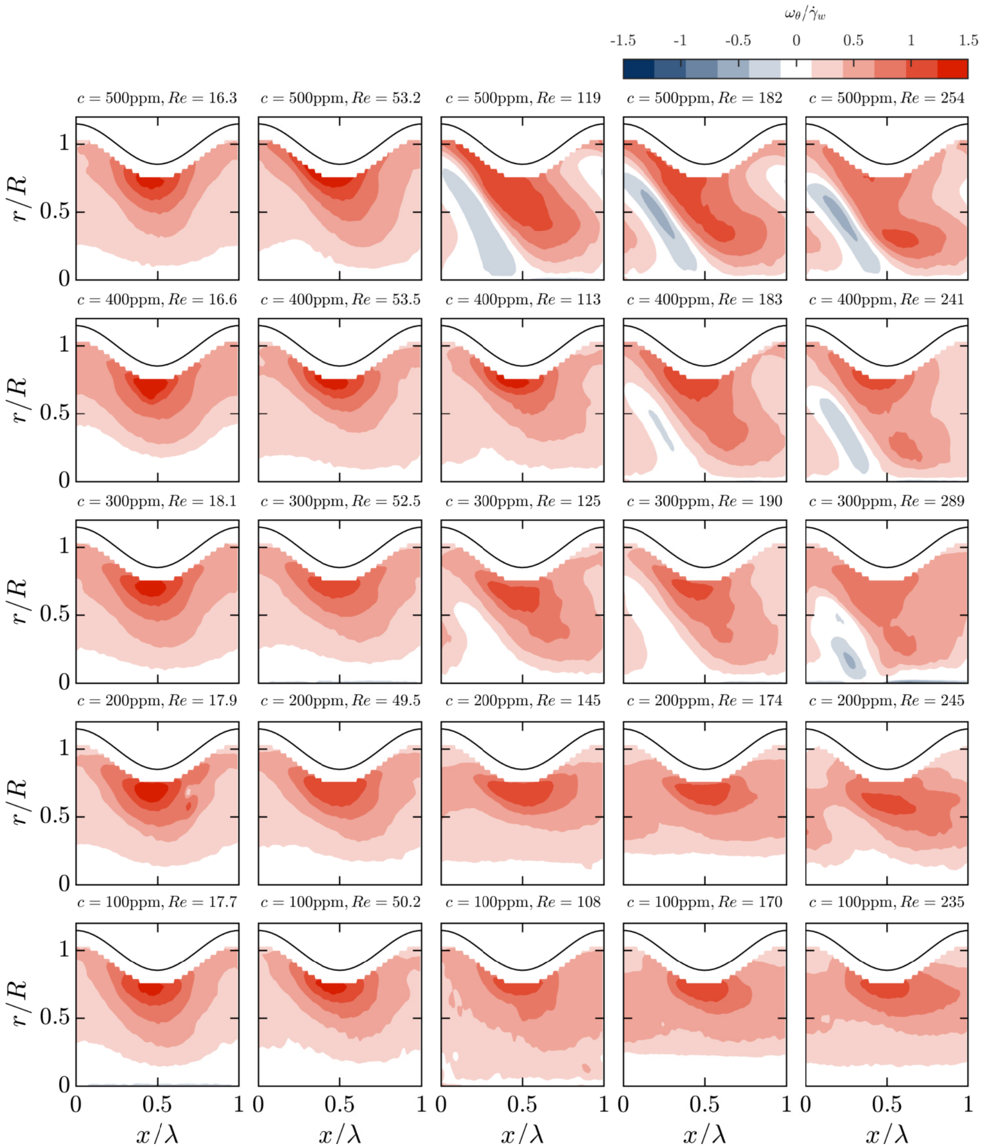

Figure 6.17: Vorticity normalized by $\dot{\gamma}_w$ for different c and Re of C14. The solid black line is the sinusoidal wall profile.

Based on equation (6.5), $T_\theta/\dot{\gamma}_w^2$ should be equal to zero in the flow of water. In other word, the dynamics of vorticity should be entirely described by vorticity advection (VA) and diffusion (VSD). Figure 6.18(a) presents contours of $\omega_\theta/\dot{\gamma}_w$ and $T_\theta/\dot{\gamma}_w^2$ for water at $Re = 170$. Contours of $T_\theta/\dot{\gamma}_w^2$ are relatively low in magnitude and noisy. Although XG is a non-Newtonian flow, with evidently large amounts of shear thinning and linear viscoelasticity (see figure 5.2), it too does not have contours of $T_\theta/\dot{\gamma}_w^2$ with large magnitude, as seen in figure 6.18(b). Generally, the plug-like flow of XG within the PCT has a larger region where $\omega_\theta/\dot{\gamma}_w$ and $T_\theta/\dot{\gamma}_w^2$ are equal to 0.

Contours of $\omega_\theta/\dot{\gamma}_w$ and $T_\theta/\dot{\gamma}_w^2$ for PAM with c = 300ppm and Re = 60.5 are shown in figure 6.19(a). A zone of large $T_\theta/\dot{\gamma}_w^2$ values is interspersed between regions of negative and positive $\omega_\theta/\dot{\gamma}_w$ within the PCT contraction. This $T_\theta/\dot{\gamma}_w^2$ zone appears in areas where values of $\omega_\theta/\dot{\gamma}_w$ significantly vary in space. The

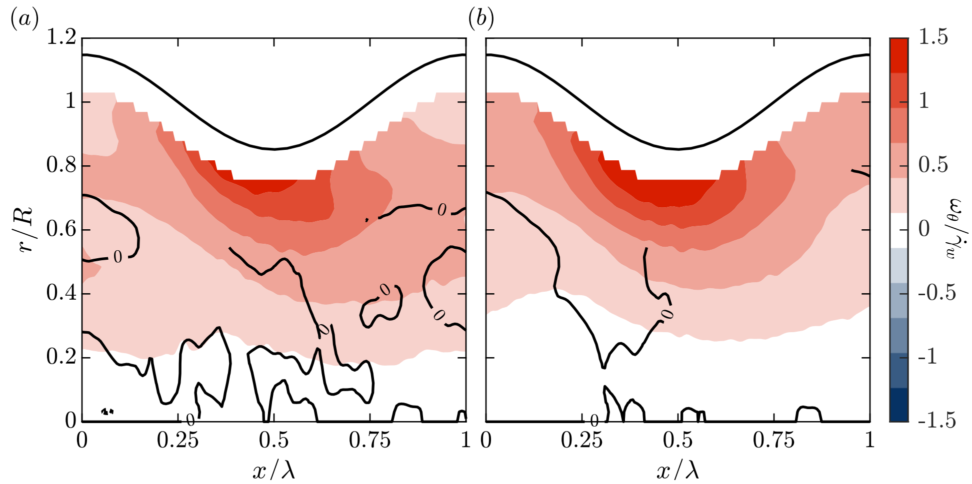

Figure 6.18: Contours of vorticity and the non-Newtonian torque for the flows of (*a*) of water with Re = 106, and (*b*) XG at c = 200ppm, Re = 71.7. Positive and zero contours are solid lines, while dashed lines are negative contours.

opposite can be observed within the PCT expansion ($0.5 < x/\lambda < 1$); the vorticity reduces with increasing x/λ, and hence $T_\theta/\dot{\gamma}_w^2$ is at its most negative. Similar observations can be made for the flow of PAM with c = 500ppm and Re = 35.5 in figure 6.19(*b*). Large values of $T_\theta/\dot{\gamma}_w^2$ are interspersed between positive and negative contours of $\omega_\theta/\dot{\gamma}_w$. In both cases, the Newtonian diffusion term (VSD) cannot account for the large spatial variations in $\omega_\theta/\dot{\gamma}_w$, implying that the non-Newtonian torque is needed to balance the vorticity equation.

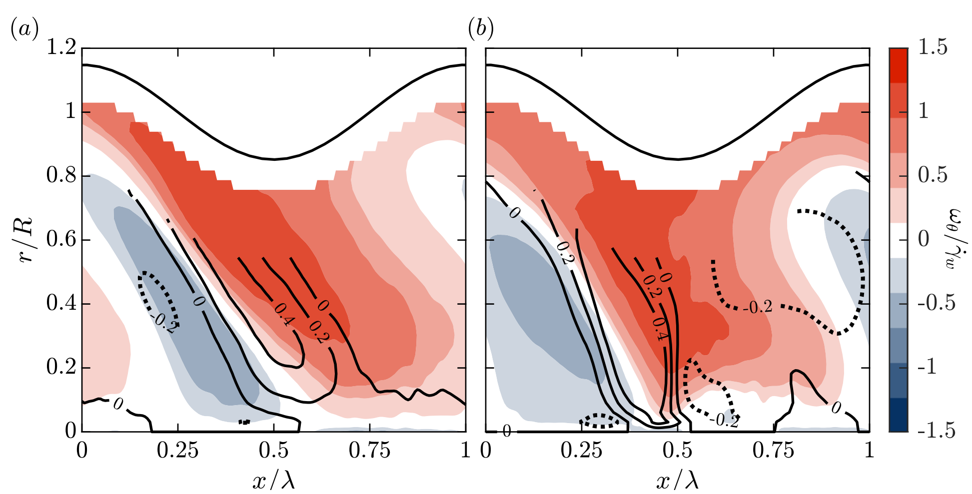

Figure 6.19: Contours of vorticity and the non-Newtonian torque for the flow of PAM solutions with (*a*) c = 300ppm, Re = 60.5, and (*b*) c = 500ppm, Re = 35.5. Positive and zero contours are solid lines, while dashed lines are negative contours.

Figure 6.20(*a*) demonstrates contours of $\omega_\theta/\dot{\gamma}_w$ and $T_\theta/\dot{\gamma}_w^2$ for C14 with c = 500ppm at Re = 119. Similar to the flows of PAM, C14 exhibits large values of $T_\theta/\dot{\gamma}_w^2$ intermittent between the regions of positive and negative $\omega_\theta/\dot{\gamma}_w$. The largest positive value of $T_\theta/\dot{\gamma}_w^2$ occurs within the contraction, where $\omega_\theta/\dot{\gamma}_w$

changes abruptly from negative to positive with increasing x/λ. The same can be observed for larger Re flows, such as C14 with c = 500ppm and Re = 254, seen in figure 6.20(b). As Re increases – comparing figure 6.20(a) to (b) – the large positive contour of $T_\theta/\dot{\gamma}_w^2 = 0.2$ within the PCT contraction moves closer towards the centreline. Overall, the large values of $T_\theta/\dot{\gamma}_w^2$ are coupled with the strong spatial variations in $\omega_\theta/\dot{\gamma}_w$. Distributions in $T_\theta/\dot{\gamma}_w^2$ are relatively consistent among solutions of flexible polymers and surfactants as the two solutions apply the same mechanism via non-Newtonian torque for disrupting $\omega_\theta/\dot{\gamma}_w$. This mechanism is potentially associated with a common rheological feature that produces the non-Newtonian torque.

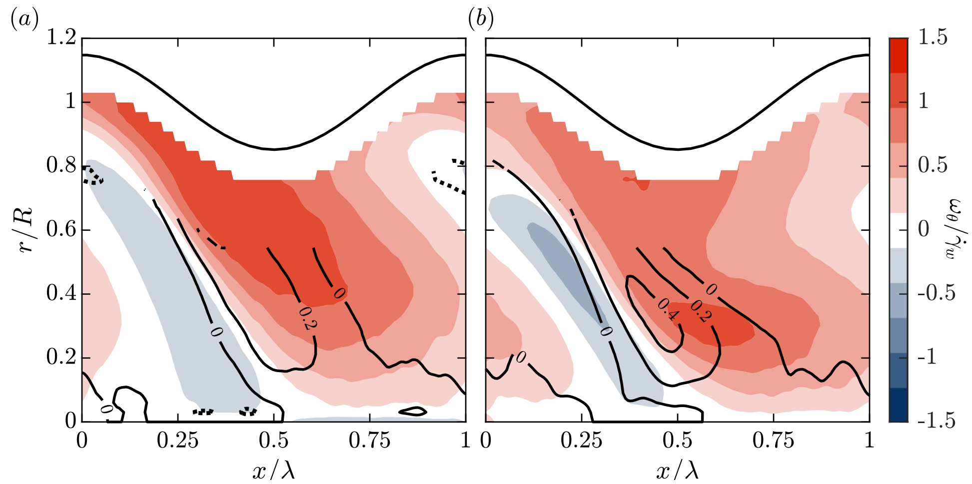

Figure 6.20: Contours of vorticity and the non-Newtonian torque for the flow of C14 solutions with (a) c = 500ppm, Re = 119, and (b) c = 500ppm, Re = 254. Positive and zero contours are solid lines, while dashed lines are negative contours.

6.5 Discussion

Rheometric measurements showed that PAM and XG have prevalent shear thinning and linear viscoelasticity, while C14 has a Newtonian and water-like shear viscosity, as shown in figures 5.1 and 5.2. On the other hand, high c and Re flows of PAM and C14 within the PCT demonstrate noticeably similar features. These features include the asymmetric half chevron velocity pattern, negative vorticity contours and non-Newtonian torque – all of which are not encountered in the flows of water or XG. This peculiar observation in the velocity and vorticity profiles of PAM and C14 can be explained by non-Newtonian qualities that do not exist for XG. Indeed, XG solutions do not exhibit elastocapillary thinning in DoS rheometry, unlike the PAM solutions shown in figure 5.3. It is plausible that the chevron-shaped velocity pattern for PAM in the PCT can be explained by a resistance to extensional flow. However, this does not explain the existence of the same chevron-shaped pattern observed for C14 flows within the PCT since the C14 solutions do not exhibit elastocapillary thinning. It is hypothesized that structures induced by shear, elongational or mixed kinematics are formed within the PCT flow of the surfactant solution when Re is sufficiently large. These structures behave similarly as flexible polymers. The remaining discussion interprets the results for PAM and C14 further in an attempt to reconcile the cause for their non-Newtonian velocity and vorticity patterns within the PCT.

In viscoelastic flows through gradual planar contractions, large near-wall velocity overshoots have been observed experimentally. Poole *et al.* (2005) were among the first to observe near-wall velocity overshoots in the flow of a PAM solution through a duct that gradually contracted along one Cartesian direction. Poole *et al.* (2005) coined the near-wall velocity overshoot as "cat's ears" due to their appearance. The canonical flow of Poole *et al.* (2005) was not axisymmetric, and later numerical investigations by Afonso & Pinho (2006) and Poole *et al.* (2007) demonstrated that the magnitude of the velocity overshoot was different depending on the Cartesian plane of interest. Subsequent investigations by Alves & Poole (2007) and Poole & Alves (2009) of viscoelastic flows through planar contractions concluded that the cat's ears and divergent streamlines were inherently elastic, and attributed to a large extensional viscosity and first normal stress differences along the centreline of the duct. Velocity statistics for PAM, seen in figure 6.10 and 6.11, reflect both cat's ears and divergent flow, implying the PAM solutions impose a large resistance to extensional flow along the centreline of the PCT – as per the conclusion of Alves & Poole (2007) and Poole & Alves (2009). Moreover, a complex interplay between elasticity and inertia within the PCT was alluded to, based on the trend in $\mathcal{R}(U_0)/\bar{U}_0$ with respect to Re and De for PAM. From figure 6.12 it was observed that $\mathcal{R}(U_0)/\bar{U}_0$ increased provided $De > 0.1$ and $Re < 35$. Using these threshold values to delineate the different flow regimes, a qualitative phase diagram shown in figure 6.21 was constructed. In figure 6.21, the De and Re of each PAM flow is shown with a colour that corresponds to their respective value of $\mathcal{R}(U_0)/\bar{U}_0$. Inset axes in figure 6.21 show samples of the vorticity field (from figure 6.13) within each flow regime. The different flow regimes are summarized as follows.

1. Inelastic: $De < 0.1$ and $Re < 35$. Velocity and vorticity are symmetric with respect to $x/\lambda = 0.5$, as shown in figures 6.10 and 6.13. Velocity contours are similar to water or shear thinning XG solutions. Vorticity is everywhere positive. As De approaches 0.1, $\mathcal{R}(U_0)/\bar{U}_0$ is marginally enhanced relative to water flows.

2. Inertial: $De < 0.1$ and $Re > 35$. Mainly distinguished by the decreasing trend in $\mathcal{R}(U_0)/\bar{U}_0$ with increasing Re that was similarly observed for water flows in the PCT – seen in table 6.1 and figures 6.8(a) and 6.12(a). Possibly a result of small recirculations or more stagnant flow within the PCT expansion (Deiber & Schowalter, 1981; Pilitsis *et al.*, 1991).

3. Elastic: $De > 0.1$ and $Re < 35$. Near-wall velocity overshoots are apparent, as shown by figure 6.11(a). The negative vorticity contours occupy a large region of the PCT contraction. Values of $\mathcal{R}(U_0)/\bar{U}_0$ are significantly augmented relative to water and increase further with growing De and Re.

4. Inertioelastic: $De > 0.1$ and $Re > 35$. Values of $\mathcal{R}(U_0)/\bar{U}_0$ decrease with increasing Re; however, near-wall velocity overshoots are present – see figure 6.12(a). The negative vorticity contour occupies a smaller region of the PCT contraction compared to the elastic flows.

Far more fundamentally interesting is the observation that C14 solutions also demonstrate cat's ears and divergent flow, as shown in figures 6.14 and 6.15, which hints at the their elastic features. Evidently, the PCT stimulates the viscoelastic properties of C14 through the formation of structures induced from

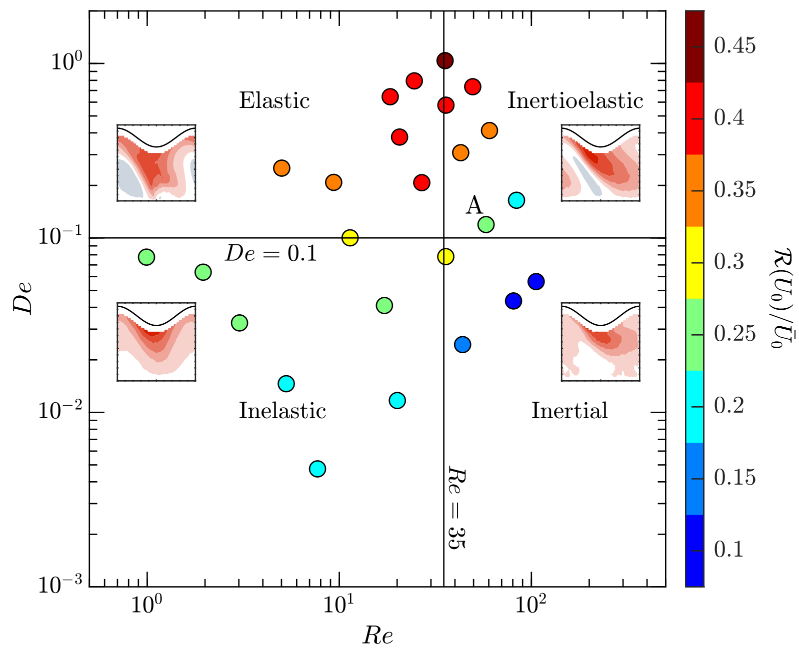

Figure 6.21: Phase diagram of the different PAM flows in De, Re space. The solid black lines separate the different flow regimes, which are labelled in each quadrant. The four inset axes show sample vorticity contours of flows within each regime. Data point colours correspond to the values of $\mathcal{R}(U_0)/\bar{U}_0$ identified from the colourbar.

shear, elongation or mixed deformation. The shape of the flow-induced structures are unknown, but they are conjectured to be groupings of micelles that can be conceived as polymer-like aggregates (Rothstein & Mohammadigoushki, 2020). The sudden jump in $\mathcal{R}(U_0)/\bar{U}_0$ with increasing Re, shown in figure 6.16, demonstrates that these flow-induced structures are formed when Re is greater than 100 within the PCT flows of C14. This corresponds to a value of $\dot{\gamma}_w$ of approximately 90 s^{-1}. From figure 5.1(d) no shear-induced structures (SISs) were observed in the shear rheograms of C14 near 90 s^{-1}; however, the PCT undergoes mixed deformations, both shear and extension. An explanation is that extension, or the combination of shear and extension, within the PCT is needed for the formation of these structures – similar to the so called "elongation-induced structures" alluded to by Sachsenheimer *et al.* (2014); Omidvar *et al.* (2018); Recktenwald *et al.* (2019). It was also observed that extensional DoS rheometry does not demonstrate EC thinning for C14, implying these elongation-induced structures are not formed within the filament necking process of the DoS rheometer. The reason extensional DoS rheometry does not reveal these elongation-induced structures for C14 is either a result of insufficient extensional deformation, or perhaps the lower surface tension of the surfactant solution, which in turn reduces the Rayleigh time t_R and Deborah number De of the necking process. If these structures are shear-induced, perhaps pre-shearing the samples before DoS could enable measurements of t_e, similar to prior works such as Wunderlich & James (1987); Vissmann & Bewersdorff (1990); Bhardwaj *et al.* (2007); Fukushima *et al.* (2022). Regardless of how the structures are formed within the PCT (shear, elongation, or mixed kinematics), they produce the same qualitative net-effect as PAM, revealed by the velocity contours of figure 6.14, and the vorticity and non-Newtonian torque contours of figure 6.17.

With reference to figure 6.21, the C14 flows that exhibit cat's ears fall within the inertioelastic regime, considering their Re is larger than 35. The similarity between the vorticity patterns for C14 and PAM, or more precisely the $\mathcal{R}(U_0)/\bar{U}_0$ value, can be used to estimate the relaxation time t_e of the C14 solutions. For example, the C14 solution shown in figure 6.17 with c = 500ppm and Re = 254 has a $\mathcal{R}(U_0)/\bar{U}_0$ value of 0.26, which is equal to the $\mathcal{R}(U_0)/\bar{U}_0$ value of the PAM flow with the label A shown in figure 6.21. Estimating the flow time scale t_f of the C14 flow based on $t_f = \lambda/\langle U_0 \rangle$ and extracting the $De = 0.12$ from figure 6.21, the relaxation time of this C14 solution is estimated to be approximately 4.1 ms. This example shows that measurements of $\mathcal{R}(U_0)/\bar{U}_0$ using the PCT along with a phase diagram similar to figure 6.21 can be used for estimating the relaxation time of the C14 solutions. However, figure 6.21 is currently too sparse to provide an accurate map of $\mathcal{R}(U_0)/\bar{U}_0$ values. It is envisaged that a larger and more dense matrix of $\mathcal{R}(U_0)/\bar{U}_0$ can be used to obtain an accurate phase diagram for extracting the De, and therefore the relaxation time of the C14 solutions. Ultimately, the PCT is able to uncover the non-Newtonian features of the dilute C14 solutions.

6.6 Summary

In §6, three non-Newtonian solutions, comprised of XG, PAM and C14 were experimentally investigated in a steady, laminar flow through a periodically constricted tube (PCT). The tube with undulating walls imposed a mixture of shear and extensional deformation, where shear rates were as large as 300 s^{-1} and extensional strain rates as large as 58 s^{-1}. The experimental campaign compared several concentrations of each non-Newtonian solution at five unique Reynolds numbers (Re) within the PCT.

Particle shadow velocimetry (PSV) was used to determine the streamwise and radial velocity within the PCT. The vorticity transport equation was used to derive the non-Newtonian contribution to the vorticity field, referred to as the "non-Newtonian torque." Our experimental investigation is the first to produce measurements of the non-Newtonian torque – providing another means for comparison with numerical investigations that can derive the non-Newtonian torque explicitly from constitutive models.

Shown previously in §5, the steady shear rheology of XG and PAM was shear thinning. PAM solutions were the only non-Newtonian fluids to exhibit elastocapillary thinning from extensional rheology. Within the PCT, solutions of XG demonstrated evidence of a plug-like flow, consistent with expectations for pipe flow of inelastic shear thinning solutions. PCT flows of PAM solutions exhibited different dynamics depending on the Deborah number (De) and Re. A phase diagram that delineated the different flow regimes in $De - Re$ space was constructed for the PAM solutions, based on the change in the amplitude of the centreline velocity along the streamwise direction of the PCT. Above a De of 0.1, PAM flows within the PCT exhibited "chevron" velocity contours, near-wall velocity overshoots and divergent streamlines with shape and curvature that departed dramatically from the sinusoidal wall profile. Within the contractions of the PCT were regions of negative vorticity and non-Newtonian torque. Despite having a shear viscosity that was identical to water and no elastocapillary extensional rheology, C14 exhibited similar non-Newtonian features as PAM within the PCT when Re exceeded 100. The C14 solutions that demonstrated a non-Newtonian response within the PCT, reflected qualitative similarities with inertioelastic PAM flows with $De > 0.1$ and $Re > 35$.

Part III

Turbulent channel flows

Chapter 7

Comparing drag-reduced channel flows of polymers and surfactants

The current investigation compares three drag-reducing additives in the channel flow facility detailed in §4.2. The different additives include the same additives from §§5 and 6, those being PAM, XG and C14. The additive solutions are prepared such that the solutions impose the same level of wall shear stress at the same mass flow rate, i.e. same drag reduction DR. Two scenarios of DR are considered: a DR of approximately 58% referred to as high drag reduction (HDR), and a MDR case with DR of approximately 70%. To measure all three components of the velocity field with a high spatial resolution, the novel technique of three-dimensional particle tracking velocimetry (3D-PTV) based on the "Shake-The-Box" (STB) algorithm is employed (Schanz *et al.*, 2013). In addition, the rheology of the drag-reduced solutions is evaluated using the torsional rheometer discussed in §4.1.1 and a CaBER, detailed in §4.1.3.

7.1 Assessment of drag reduction

Two methods are used to determine the wall shear stress, τ_w, and drag reduction percentage DR of the non-Newtonian fluids within the turbulent channel flow depicted in §4.2. The first method used measurements of the pressure drop, ΔP, where $\tau_{w,1} = h\Delta P/\Delta x$ similar to (3.5), and h is the half-channel height ($H/2$). Subscript, 1, is used to distinguish this first method and, going forward, will denote variables calculated based on ΔP. In the second method, $\tau_{w,2}$ characterized by the subscript 2, was determined using a wall-normal gradient of the mean velocity obtained from 3D-PTV measurements, which is equivalent to equation (3.7) and will be elaborated on further in §7.3. The drag-reduction percentage DR was assessed similarly to (3.14), although based on a comparison of τ_w of a drag-reduced flow and that of water at the same mass flow rate $\dot{m}$, according to,

$$DR = \left(1 - \frac{\tau_{w,A}}{\tau_{w,N}}\right) \times 100\% \tag{7.1}$$

where $\tau_{w,A}$ is the wall shear stress of the additive solution and $\tau_{w,N}$ is the wall shear stress of the Newtonian flow of water at the same $\dot{m}$. Additionally, DR can be derived from ΔP (and $\tau_{w,1}$) as DR_1, which is equivalent to $DR_1 = (1 - \Delta P_A/\Delta P_N) \times 100\%$. In this equation, ΔP_A is the streamwise pressure drop for an additive solution and ΔP_N is the streamwise pressure drop for the flow of water at the same $\dot{m}$. All experiments with drag-reducing additives were performed at a $\dot{m}$ of 3.294 kg s^{-1}, which corresponds to a bulk velocity, U_b, of 1.839 m s^{-1}. For the flow of water, this flow rate equates to a bulk Reynolds number Re_H, from (3.3) of 31 900 and friction Reynolds number Re_τ, from (3.12), of 793. Certain drag-reducing solutions have a viscosity that is larger than that of water (Escudier *et al.*, 2009). Such an increase in kinematic viscosity of the flow will result in a decrease in Re_H although $\dot{m}$ and ΔP are kept constant. It is challenging to maintain a constant Re_H for the drag-reduced flows, since Re_H is calculated using the viscosity of the fluid at the wall-shear-rate, which is unknown *a priori*. In addition, changing $\dot{m}$ will vary ΔP and therefore DR.

Additional measurements were also performed for water at lower $\dot{m}$ to match the Re_τ of the drag-reduced flows. Table 7.1 lists U_b, Re_H, ΔP and $\tau_{w,1}$ for each flow case of water. Table 7.1 also provides $\tau_{w,2}$, the friction velocity $u_\tau = (\tau_{w,2}/\rho)^{1/2}$, viscous lengthscale $\delta_v = \nu/u_\tau$, and Re_τ of each water flow experiment. Here ρ is the density of the fluid. The variables in the last four columns of table 7.1 are derived based on the estimated $\tau_{w,2}$ from 3D-PTV measurements. The method will be discussed and evaluated in §7.3.

U_b (m s^{-1})	Re_H	ΔP (Pa)	$\tau_{w,1}$ (Pa)	$\tau_{w,2}$ (Pa)	u_τ (mm s^{-1})	δ_v (µm)	Re_τ
0.613	10 630	290	1.330	1.248	35.42	24.42	307
0.736	12 770	385	1.766	1.739	41.81	20.69	363
0.859	14 890	496	2.275	2.394	49.05	17.63	425
0.981	17 020	695	2.821	2.749	52.57	16.45	456
1.103	19 140	748	3.431	3.458	58.95	14.67	511
1.839	31 900	1790	8.211	8.317	91.43	9.46	793

Table 7.1: Flow properties for channel flow experiments using water as the working fluid.

7.2 Drag-reducing additives

To prepare the additive solutions, drag-reducing powders were weighed using a digital scale (AB104-S, Mettler Toldeo) with a 0.1 mg resolution, and added to 15 l of tap water. The combination was then agitated for approximately 2 h using a stand mixer equipped with a three-blade impeller set to 100 revolutions per minute (Model 1750, Arrow Engineering Mixing Products) and left to rest for approximately 16 h (Abu-Rowin *et al.*, 2018). The master solution was then added to the reservoir labelled in figure 4.4. The pump effectively mixed and diluted the 15 l concentrated master solution with 120 l of tap water, to bring the fluid to the desired concentration, c.

Two different cases of DR were considered for the present experiments. The first was a comparison of additive solutions at a high level of drag reduction (HDR). This case evaluated three drag-reduced solutions at a similar DR_1, approximately equal to 57.7% ± 1.2%. Seeing as the DR_1 is greater than 40%, this comparison is in the "HDR" regime according to Warholic *et al.* (1999*b*). The HDR amount of 57.7% was selected based on the largest DR that could be obtained using the rigid polymer. The second scenario was a comparison of the flexible polymer and surfactant solutions at MDR, which occurs at DR_1 of approximately 70.3% ± 1.8% for the Re_H considered here.

When the concentration of PAM increased beyond 50 ppm, it was observed that DR_1 plateaued at approximately 68.5%, as demonstrated by figure 7.1(a). This suggested that 50 ppm of PAM could generate the required MDR state. To achieve the HDR case, with smaller DR_1, the rotational speed of the centrifugal pump was increased to reduce DR_1 to the desired value by using mechanical degradation. Figure 7.1(b) demonstrates how this procedure was executed on a 50 ppm PAM solution. Upon initially adding the master solution to the reservoir and letting the loop mix the solution for about 2 minutes at a low pump speed, DR_1 was 68.5% for a pump speed of 600 revolutions per minute (desired $\dot{m}$ of 3.294 kg s^{-1}). At this pump speed mechanical degradation is negligible and DR_1 remains constant. At t = 360 s, the pump speed was increased significantly to promote mechanical degradation. After approximately 720 s at a high pump speed, the pump speed was then returned to 600 revolutions per minute and the DR_1 became approximately equal to 58.0%. While lower levels of c for PAM could produce the same effect, mechanical degradation at lower values of c would have been greater, making flow measurements challenging (Virk & Wagger, 1990; Pereira *et al.*, 2013). Therefore, a degraded 50 ppm PAM solution was used instead of a lower concentration solution of PAM, for the case of HDR.

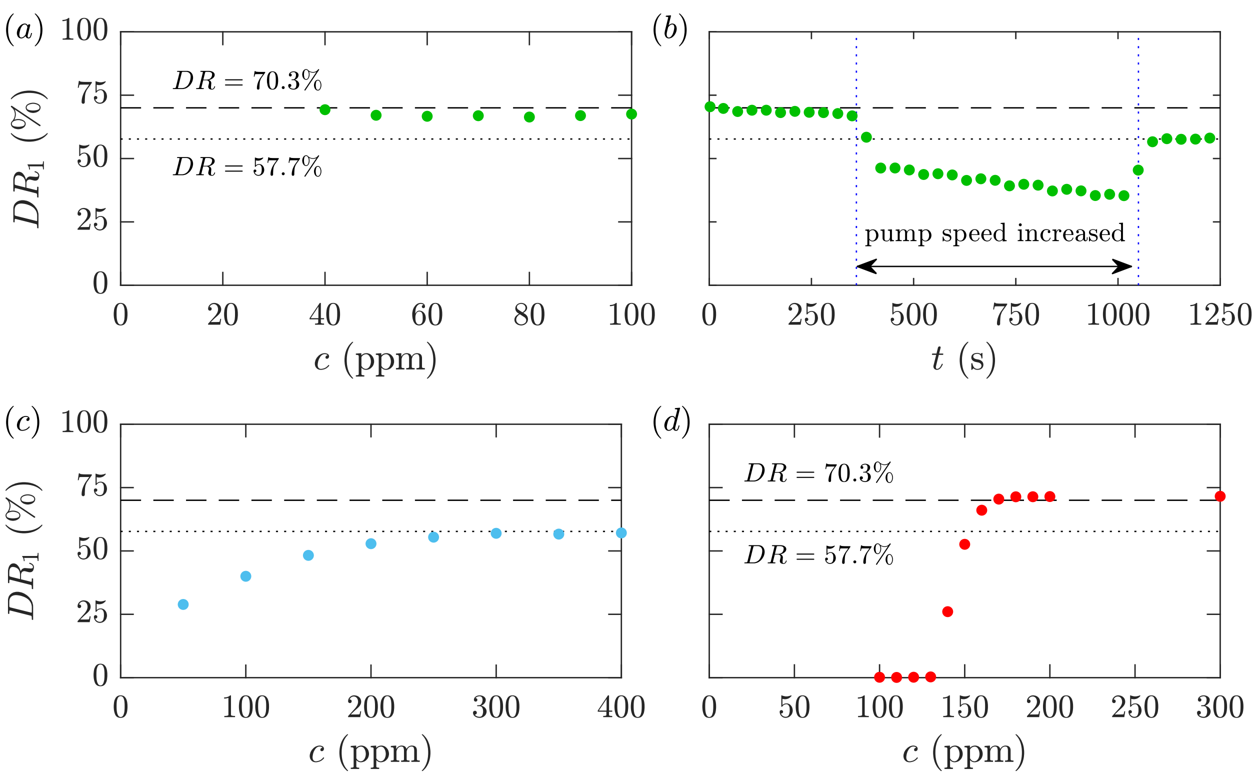

Figure 7.1: (a) Value of DR_1, as a function of c for PAM, (b) DR_1 of c = 50 ppm solution of PAM as a function of time, t, (c) DR_1 of XG as a function of c, (d) DR_1 of C14/NaSal (1:2 mM) as a function of c.

Figure 7.1(c) demonstrates that the largest DR_1 achieved was 58.5%, exhibited by 300 ppm of XG. The

XG solution showed negligible amounts of degradation, similar to the findings of Pereira *et al.* (2013). The largest DR_1 achieved using XG was chosen as the common HDR value. Due to the limited drag-reduction capability of XG, no MDR case was achieved.

Figure 7.1(d) shows that a 200 ppm (0.685 mM) solution of C14 produced DR_1 of 72.0%. No increase in DR_1 was observed if the c of C14 was increased further. Therefore, 200 ppm of C14 was perceived to produce MDR. Choosing a c equal to 150 ppm of C14 (0.521 mM), with the same 1:2 molar ratio of C14 to NaSal, produced DR_1 of 56.5% for HDR tests. The measurements of ΔP and DR_1 are listed in table 7.2 for each drag-reduced flow.

Fluid	c (ppm)	U_b (m s^{-1})	Re_H	$\tau_{w,1}$ (Pa)	DR_1 (%)
Water	–	0.613-1.839	10 6300-31 900	1.330-8.211	–
PAM solution	50*	1.839	25 550	3.445	58.0 (HDR)
PAM solution	50	1.839	25 260	2.578	68.5 (MDR)
XG solution	300	1.839	17 060	3.399	58.5 (HDR)
C14 solution	150	1.839	30 130	3.564	56.5 (HDR)
C14 solution	200	1.839	30 120	2.294	72.0 (MDR)

Table 7.2: Bulk flow measurements from Coriolis flow meter and pressure transducer. To reiterate, DR_1 is calculated based on ΔP. *Solution was subject to mechanical degradation.

The skin friction coefficient C_f derived from equation (3.8), as a function of Re_H, is demonstrated in figure 7.2 for flows of drag-reducing solutions and water. For drag-reduced flows, the kinematic viscosity, ν, that is used to calculate Re_H, corresponds to the measured shear viscosity at the wall shear rate. The procedure will be discussed in §7.4 and §7.5. The error bars shown in figure 7.2 propagate from random and systematic uncertainties in measurements of the flow rate, viscosity and streamwise pressure gradient. Figure 7.2 also presents two empirical correlations. The upper line in figure 7.2, corresponds to the equation (3.9) from Dean (1978) for a Newtonian turbulent channel flow that has a cross-section with W/H greater than 7. The measured C_f for the experimental data of water, shown by the blue markers in figure 7.2, are marginally lower than the Dean (1978) correlation equation. However, the results are in agreement with other turbulent channel flow experiments, several of which were used by Dean (1978) to obtain the correlation. The lower line in figure 7.2 corresponds to the MDR asymptote proposed by Virk *et al.* (1970) or (3.15). The original correlation was intended to be used for pipe flows. To adapt the equation to a channel flow, similar to Owolabi *et al.* (2017), the MDR asymptoteis plotted using a Reynolds number that is calculated based on the hydraulic diameter, $Re_b = U_b D_h/\nu$, where $D_h = 2HW/(H + W)$. The C_f of drag-reduced flows at MDR are about 15% greater than the C_f of the correlation. It should be noted that there is considerable ambiguity in the equation describing the MDR asymptote in channel flows. Escudier *et al.* (2009) applied a correction factor to the Reynolds number to account for potential secondary flows, while Ptasinski *et al.* (2003) simply used Re_H. The choice of the length scale in defining the Reynolds number will raise or lower the MDR asymptote along the vertical axis of the plot of C_f. Also, Virk *et al.* (1970) remarked that the C_f relationship was derived from an integration of the asymptotic mean velocity profile. White *et al.* (2012), among others, had cast doubt on the exactness of the mean velocity profile of drag-reduced flows at MDR. Therefore, the C_f distribution at MDR may also be erroneous and conditional on the canonical flow type, Reynolds number and additive type (White *et al.*, 2012).

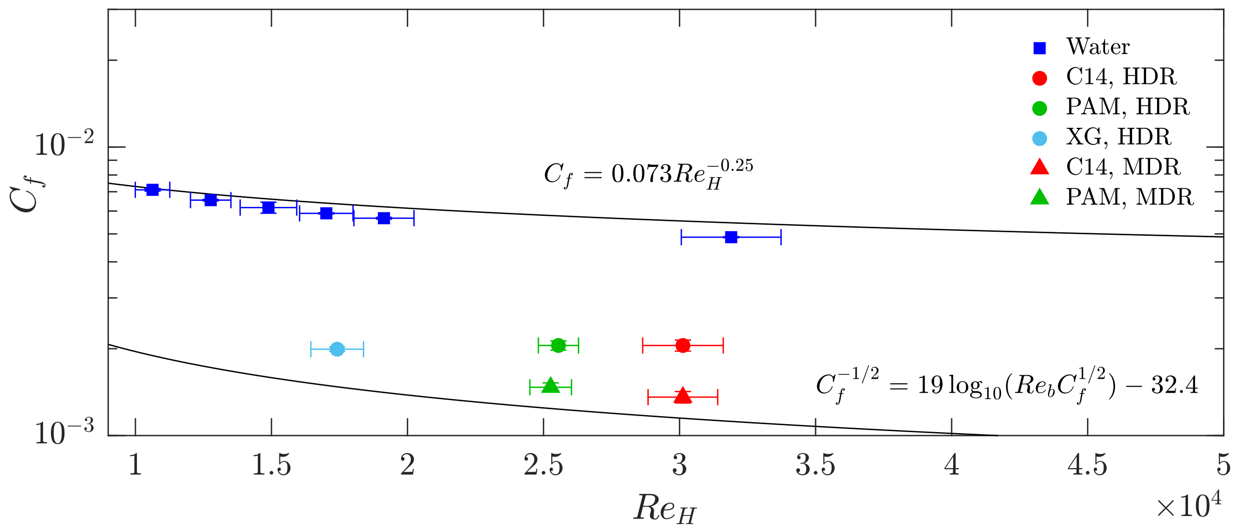

Figure 7.2: Skin friction coefficient as a function of bulk Reynolds number for drag-reduced flows and water. The upper equation shows the Dean (1978) correlation for Newtonian channel flows and the lower equation shows the MDR asymptote adapted for channel flows (Virk *et al.*, 1970).

Shear and extensional viscosity measurements were performed on samples of each drag-reducing solution. The samples were collected from the flow loop using an outlet valve at the corresponding DR and the rheology measurements were performed immediately afterwards. The shear viscosity μ as a function of shear rate $\dot{\gamma}$ for each additive solution and water, was determined using the torsional rheometer depicted in figure 4.1 equipped with the double gap cylinder geometry shown in figure 4.2(*b*). Shear viscosity measurements were performed three times for each sample listed in table 7.2 (including water) to establish the uncertainty of the measurements. The extensional relaxation time t_e was established using the CaBER apparatus detailed in §4.1.3.

7.3 Lagrangian 3D-PTV measurements

Flow measurements were carried out using 3D-PTV based on the state-of-the-art STB algorithm devised by Schanz *et al.* (2016). The STB algorithm predicts the three-dimensional particle position based on the established trajectories of previous time steps. The prediction is then corrected using an iterative particle reconstruction (Wieneke, 2012), where the particles are shifted ("shaked") in the volume ("box") until residual errors are minimized and a trajectory is established. The algorithm can analyse images with high seeding densities, allowing measurement of spatially resolved turbulent statistics and instantaneous flow structures. The efficacy of STB was exemplified by Schröder *et al.* (2015), where the turbulent Reynolds stresses were accurately measured for y^+ as low as 1.5.

The 3D-PTV system consisted of four high-speed cameras (v611, Phantom) and a high-repetition Nd:YLF laser (DM20-527 Photonoics Industries). Figure 7.3 provides a visual representation of the cameras and laser configuration. The laser emitted light with a wavelength of 532 nm and a maximum pulse energy of 20 mJ pulse^{-1}. As seen in figure 7.3, the circular laser beam was directed in the spanwise direction of the channel (negative z). A lens combination shaped and collimated the beam into an oval profile. The resulting oval profile was then cropped to form a rectangular cross-section with 5 mm thickness in the wall-normal direction, covering from $y = 0$ to 5 mm. The laser sheet was 16 mm in the streamwise direction, x. To increase the light intensity for the backward scattered camera, the laser sheet was also reflected back onto itself using a large mirror situated on the opposite side of the test section Ghaemi & Scarano (2010).

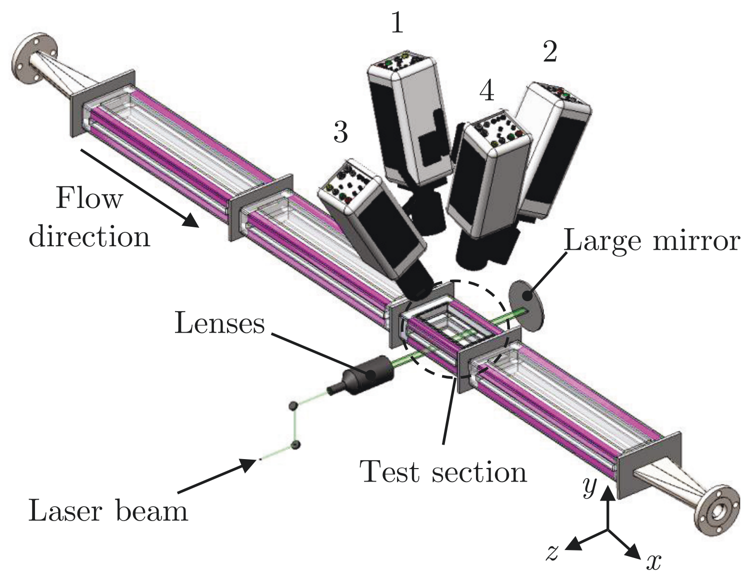

Figure 7.3: Three-dimensional rendering of high-speed laser and camera array for 3D-PTV.

The four Phantom v611 cameras had a 1280 × 800 pixel complementary metal oxide semiconductor sensor with pixel size of 20 × 20 µm^2 and 12 bit resolution. Scheimpflug adapters and Nikon lenses with a focal length of $f = 105$ mm were connected to the cameras. A reduced sensor resolution of 900 × 800 pixel was used to enable higher recording rates. The forward/backward scattering cameras (cameras 2 and 3 in figure 7.3) were placed along the z-direction and set to a lens aperture of $f/16$. The side scattering cameras (cameras 1 and 4) were placed along the streamwise x-direction with a lens aperture setting of $f/11$. The line of sight of cameras 2 and 3 had an angle of 60° with respect to each other, while the side scattering cameras were placed at 30° with respect to each other. The distance of the cameras to the measurement location was approximately 290 mm. This imaging configuration resulted in a magnification of approximately 0.56 and a resolution of 27.9 µm pixel^{-1}. The cameras and laser were synchronized using a programmable timing unit (PTU X, LaVision GmbH). Fluids were seeded with 10 µm silver coated hollow glass spheres (S-HGS-10, Dantec Dynamics). The density of the tracers in the images was approximately 0.05 particles per pixel. The fidelity for which the tracer particles can follow the fluid flow can be defined by two parameters, the Stokes number, St, and Froude number, Fr (Bewley *et al.*, 2008). The local values of St and Fr of the particles can be approximated as $St = t_p/t_f$ and $Fr = u_p/u_\tau$, and describe the significance of particle inertia and particle settling. The particle response time is $t_p = \rho_p d_p^2/18\mu$, and the settling velocity is $u_p = (\rho_p - \rho)d_p^2 g/18\mu$. Here ρ_p is the density of the particles and d_p the diameter. The characteristic fluid response time, t_f, was approximated as δ_ν/u_τ. The value of St was between 0.012 and 0.087 depending on the flow conditions. While the Fr for all flows was of the order of magnitude, 10^{-3} to 10^{-4}. Therefore, particle inertia and particle settling was considered inconsequential.

One time-resolved data set, for each drag-reduced and Newtonian flow, consisted of 6800 single-frame images captured at a frequency between 2.5 and 4.5 kHz. Therefore, one data set was between 1.5 and 2.7 s in duration. Depending on U_b of the flow being measured, the image capture rate was determined such that a maximum particle displacement of approximately 10 pixels across successive frames was maintained. After recording the images, the minimum intensity of each data set was computed and subtracted to remove any glare points caused by surface scratches and tracer particles stuck to the bottom wall. Images were further enhanced by applying a sliding minimum subtraction with kernel of 7 pixels and local intensity normalization over a kernel of 50 pixels.

Calibration of the imaging system was carried out by fitting a third-order polynomial mapping function onto images recorded from a dual-plane calibration target (058-5, LaVision GmbH). To improve the accuracy of the mapping function, volume self-calibration was employed (Wieneke, 2008), which brought the average disparity down to 0.02 pixels. An optical transfer function was generated for iterative particle reconstruction in STB (Schanz et al. 2013). The measurement volume was in the mid-span of the test section and had dimensions of $(\Delta x, \Delta y, \Delta z) = 670 \times 180 \times 670$ voxel $= 24 \times 5 \times 24$ mm^3. Additional image and volume cropping mitigated noise common along the borders of the volume. Lastly, the STB algorithm was performed in DaVis 8.4 (LaVision GmbH). The maximum triangulation error was constrained to 1 voxel. Particle displacement was limited to a maximum value of 15 voxels. In addition, particles with a change in velocity exceeding 2 pixels or 20% in successive image frames were discarded.

A moving second-order polynomial was fit on the particle trajectories in MATLAB. The length of the polynomial (kernel) was five time steps (1.11–2 ms) for obtaining first-order turbulence statistics. To mitigate noise in Reynolds stresses, a kernel with a length of 11 time steps (2.4–4.4 ms) was used. Trajectories less than the respective kernel length were removed from consideration. To obtain the velocity statistics, particle tracks were binned into slabs parallel with the wall, covering the entire measurement domain in the x and z directions. Each slab was 10 µm thick in the y direction for evaluating the mean velocity profiles ($\Delta y^+ = 0.4 - 0.7$) and 100 µm in the y direction for the Reynolds stresses ($\Delta y^+ = 4.0 - 6.7$). Both procedures incorporated a 75% overlap between neighbouring slabs in the y-direction. The statistics were obtained by averaging in time and the homogenous directions (x and z), and are indicated by angle brackets, $\langle \cdots \rangle$. To obtain instantaneous velocity fields in a Eulerian frame of reference, the particle tracks were binned into $24 \times 24 \times 24$ voxel cubes with 75% overlap in all three directions. The instantaneous velocities in x, y and z directions were denoted by U, V and W, respectively. The corresponding velocity fluctuations were represented by u, v, w.

As previously established, a superscript of + is indicative of inner normalization by friction velocity u_τ defined according to (3.10), and viscous length scale δ_v from (3.11). For the inner normalization, the wall shear stress is calculated as $\tau_{w,2} = \mu_w \partial\langle U\rangle/\partial y|_w$ according to (3.7), where $\partial\langle U\rangle/\partial y|_w$ is the mean velocity gradient at the wall. Drag-reducing solutions can exhibit shear thinning characteristics, where μ decreases with respect to $\dot{\gamma}$ (Warholic *et al.*, 1999*b*; Ptasinski *et al.*, 2001; Escudier *et al.*, 2009). Therefore, the shear viscosity measurements, discussed in §7.2, were used to estimate μ_w at the wall shear rate, i.e. at $\dot{\gamma} = \partial\langle U\rangle/\partial y|_w$. To determine $\partial\langle U\rangle/\partial y|_w$, a linear fit was applied on the mean velocity profile within $2 - 4 < y^+ < 5$ in the linear viscous sublayer. The lower bound varied depending on the flow Re_τ but it corresponded to $y \approx 60$ µm. The efficacy of this procedure is discussed in §7.5 by comparing the normalized mean velocity profile and Reynolds stresses for turbulent channel flow of water with results from direct numerical simulation (DNS) at a similar Re_τ. Such an estimate of τ_w using the near-wall gradient of the mean velocity profile is an approximation for the drag-reduced flows. Solutions that are shear thinning can exhibit instantaneous variations in $\partial\langle U\rangle/\partial y|_w$ and therefore variations in μ_w with time. To ensure $\tau_{w,2}$ of the drag-reduced flows was reasonable, results were validated by comparing the estimated DR_2 with the DR_1 that was obtained using measurements of ΔP.

Uncertainty in the normalized velocity and Reynolds stresses are quantified based on two sources of error. The first source propagates from the uncertainty in measurements of μ. This was estimated by repeating the measurements of μ, which will be shown in §7.4. The uncertainty in μ affects variables used for inner scaling, that is u_τ and δ_v, following a root-sum-of-squares propagation of uncertainty (Wheeler & Ganji, 2010). The second source of uncertainty is a random noise in the measured flow velocity associated with particle positioning in 3D-PTV. Using a spectral analysis of the particle tracks, Abu-Rowin & Ghaemi (2019) and Ebrahimian *et al.* (2019) showed that an error of 0.1, 0.2 and 0.1 pixel was present in particle displacements along the x, y and z directions, respectively. Combined, these two sources of uncertainty contribute to the total uncertainty in normalized mean velocity, Reynolds stresses and wall-normal location. The estimated uncertainty is shown as error bars in the figures demonstrated in §7.5 to §7.7.

7.4 Fluid rheology

The results of the shear viscosity measurements using the torsional rheometer are shown in figure 7.4(*a*). The demonstrated shear viscosities are the average of the thrice repeated measurements for each sample. Error bars are the range in the measurements at each $\dot{\gamma}$. Within the presented values of $\dot{\gamma}$, the measurements of μ show good repeatability and low random error; the range in the measurements are less than 5.7 %. Based on figure 7.4(*a*), the measured μ of domestic tap water at 25°C is 0.861 ± 0.049 mPa s. The results for water can be contrasted with shear viscosity measurements of Nagashima (1977) and Collings & Bajenov (1983). They measured the viscosity of distilled water at 25°C; finding it to be 0.891 mPa s. The discrepancy between the results of figure 7.4(*a*) for water and the measurements of Nagashima (1977) and Collings & Bajenov (1983) is within the estimated uncertainty based on the three repeated measurements, and is attributed to systematic uncertainties inherent with the torsional rheometer.

From visual inspection of figure 7.4(*a*), it is apparent that the XG solution is shear thinning. The

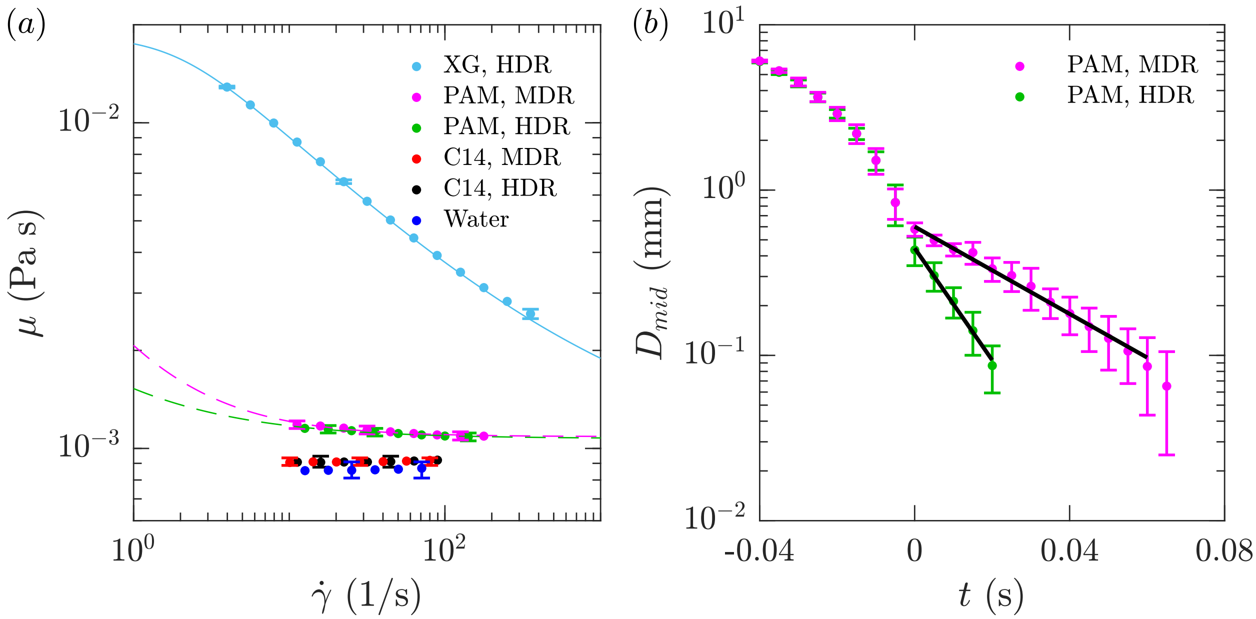

Figure 7.4: Rheology of aqueous solutions of drag-reduced additives including (*a*) shear viscosity as a function of shear rate, and (*b*) mid-point filament diameter with respect to time from uniaxial filament extension.

viscosity of the XG solution reduces by 80.4% between $\dot{\gamma}$ of 5 and 400 s^{-1}. For $\dot{\gamma}$ > 400 s^{-1}, Taylor instabilities produce a sudden increase in μ and the results were discarded. The values of $\partial\langle U\rangle/\partial y|_w$ for the drag-reduced, turbulent flows being investigated are beyond 2000 s^{-1}, much greater than the maximum achievable $\dot{\gamma}$ of 400 s^{-1} using this rheometer. Therefore, a predictive model is used to extrapolate the data and estimate μ_w of the drag-reduced turbulent flows. For the XG solution, the Carreau–Yasuda (CY) model (Carreau, 1972; Yasuda *et al.*, 1981) fit the measurements appropriately and is shown by the solid line in figure 7.4(*a*). The CY model is represented by the following equation,

$$\frac{\mu - \mu_\infty}{\mu_0 - \mu_\infty} = \frac{1}{(1 + (M\dot{\gamma})^a)^{k/a}} \tag{7.2}$$

where μ_0 is the zero-shear-rate viscosity, μ_∞ is the infinite-shear-rate viscosity, $M$is the consistency, k is the flow index and a is an additional fitting parameter introduced by Yasuda *et al.* (1981). For XG, μ_0 is 0.019 Pa s, μ_∞ is 0.937 mPa s, M is 0.517 s, k is 0.466 and a is 1.935. The uncertainty in the extrapolated shear viscosity for XG is taken to be the maximum range in the thrice-repeated measurements of μ. Using the above (7.2), the μ_w of XG at HDR, which corresponds to the value of $\dot{\gamma}$ that was equal to $\partial\langle U\rangle/\partial y|_w$, is 1.576 mPa s. Extrapolating the CY model may be subject to errors that can influence the variables derived for inner scaling, including $\tau_{w,2}$, u_τ and δ_v (Singh *et al.*, 2016). It will be demonstrated that the DR_2 derived using these rheology measurements is within 5% of the DR_1 determined from measurements of the streamwise pressure gradient. Propagation of uncertainty accounts for additional errors in the inner-scaling variables that can be seen by error bars in plots of the mean velocity profile and Reynolds stresses.

Solutions of PAM also demonstrate shear thinning qualities, but to a much lesser extent than XG. The viscosity of PAM at MDR reduced by 7.4% between $\dot{\gamma}$ of 10 and 180 s^{-1}. The viscosity of PAM at HDR reduces by 6.1% across the same range in $\dot{\gamma}$. Below $\dot{\gamma}$ of 10 s^{-1}, measurements of μ were noisy and ambiguous. In either scenario, measurements of μ are approximately constant for $\dot{\gamma} > 180$ s^{-1}, which is the maximum measurable $\dot{\gamma}$ of both PAM solutions (HDR and MDR) before Taylor instabilities impair the measurements. The Sisko (SI) model (Sisko, 1958) was used to represent μ of the PAM solutions at moderate and large values of $\dot{\gamma}$. This model is typically used when measurements close to the zero-shear-rate viscosity are lacking (Barnes *et al.*, 1989). The fitted SI model is shown in figure 7.4(*a*) using a dashed line and is represented by the following equation,

$$\mu = \mu_\infty + M\dot{\gamma}^{k-1} \tag{7.3}$$

where M and k are constants used to describe the power law decay in μ. The infinite-shear-rate viscosity, μ_∞, for PAM at HDR and MDR are estimated to be 1.072 and 1.087 mPa s, respectively. The fitting parameter k and M are 0.349 and 0.455 mPa s^k for PAM at HDR and 0.101 and 0.985 mPa s^k for PAM at MDR. Using the above (7.3), the μ_w of PAM at HDR and MDR is 1.074 and 1.088 mPa s respectively, not much greater than the corresponding values of μ_∞.

There is a negligible difference in measured values of μ for the 150 ppm C14 solution at HDR and the 200 ppm C14 solution at MDR. Unlike PAM and XG, solutions of C14 exhibit a Newtonian trend with constant μ for $10s^{-1} < \dot{\gamma} < 100s^{-1}$. Therefore, their viscosities were assumed constant for $\dot{\gamma} > 100$ s^{-1}. The estimated μ_w of C14 at HDR is 0.911 ± 0.036 mPa s and C14 at MDR is 0.912 ± 0.024 mPa s. No SISs are observed for C14; however, that does not rule out the possibility of their presence at higher values of $\dot{\gamma}$.

Using the CaBER system, it was not feasible to measure t_e of XG and C14 solutions, since the filament immediately ruptured upon moving the end plates. Similar findings for rigid polymer and surfactant solutions have been reported by previous investigations (Lin, 2000; Escudier *et al.*, 2009; Mohammadtabar *et al.*, 2020). The two PAM solutions were the only fluids that showed a measurable t_e using the CaBER apparatus. Figure 7.4(*b*) demonstrates the filament mid-point diameter, D_{mid}, as a function of time, t. Here $t = 0$ indicates the end of the top plate displacement. Similar to the shear viscosity measurements, the thrice-repeated measurements of $D_{mid}(t)$ were averaged for each sample and the error bars show the range of the measurements. The solid black line represents the exponential fit of $D_{mid}(t)$ usign (4.3). The resulting t_e for PAM at HDR and PAM at MDR were 4.3 and 11.0 ms, respectively. For the purposes of the current analysis, a comprehension that solutions of PAM have significantly larger extensional characteristics than those of XG and C14, will suffice.

Despite producing similar DR at HDR or MDR (see table 7.2), each drag-reducing solution exhibits a different shear viscosity and extensional characteristics. Of the additive solutions, XG has the largest overall μ and a strong shear thinning behaviour. PAM has the next largest distribution in μ; however, only approximately 20% larger than the average μ of water. C14, on the other hand, has a water-like distribution in μ. Although t_e could not be measured for C14 and XG using the CaBER system, the fact that t_e for PAM solutions could be measured implies that PAM has a larger t_e than C14 and XG. Rodd *et al.* (2005) specified that the operable range of the CaBER is constrained to fluids with t_e larger than approximately 1 ms when μ is smaller than 70 mPa s. Given the measured shear viscosities of XG and C14 are less than 70 mPa s, it is possible that their t_e are less than 1 ms. However, further measurements of the extensional rheology are needed to confirm this hypothesis, one possible method being the dripping-onto-substrate technique detailed in Dinic *et al.* (2017). Such a method was capable of measuring the pinch-off dynamics of fluids with μ less than 20 mPa s and t_e less than 1 ms, according to Dinic *et al.* (2017). Nonetheless, a correlation relating DR to t_e, similar to that proposed by Owolabi *et al.* (2017) for flexible polymers, may not apply to solutions of XG or C14. The above analysis using conventional torsional and extensional rheometers highlights that the drag-reduced solutions demonstrate different rheological characteristics.

Other authors have demonstrated that flows obtained from DNS and using the FENE-P (finitely extensible non-linear elastic spring, with a Peterlin approximation) model with large Weissenberg number, $Wi = t_e\, \partial\langle U\rangle/\partial y|_w$, have an effective viscosity that increases with distance from the wall (Procaccia *et al.*, 2008). A viscosity that increases monotonically with distance from the wall is achieved inherently by shear thinning fluids. It is intriguing that DR exists for both XG with relatively small t_e and large shear thinning behaviour, and PAM with large t_e and minimal shear thinning characteristics. This could suggest that polymers achieve DR using a viscosity that increases monotonically with y. Flexible polymers achieve this viscosity gradient using polymer elasticity (i.e. Wi), while rigid polymers are naturally shear thinning. Such a hypothesis is only speculative. Measurements connecting the role of shear thinning characteristics to DR are warranted.

7.5 Newtonian turbulent channel flow

The following section seeks to evaluate the 3D-PTV measurements for water by comparing them with DNS of Iwamoto *et al.* (2002) at $Re_\tau = 300$, Moser *et al.* (1999) at $Re_\tau = 395$, and Lee & Moser (2015) at $Re_\tau = 550$. The previously listed DNS data, in that order, are compared with the experimental water data at $Re_\tau = 307, 425$ and 511, respectively, in figures 7.5 and 7.6. The comparison involves an evaluation of $\langle U\rangle^+$ in figure 7.5 and the Reynolds stress distributions in figure 7.6. The error bars in figures 7.5 and 7.6 originate from a propagation of uncertainty stemming from errors in velocity and shear viscosity measurements. For clarity of the figures, the error bars are down sampled in figures 7.5 and figure 7.6.

As demonstrated in figure 7.5, the 3D-PTV measurements of mean velocity at the three Re_τ agree with the distributions established using DNS and the law of the wall. Rather remarkable is the spatial resolution at which these measurements can be attained. For the lowest velocity case of $Re_\tau = 307$, the spacing of data points along y^+ is $0.4\delta_\nu$ and the velocity measurements are obtained for y^+ as low as 2 (60 µm from the wall). The spatial resolution of the velocity measurements with respect to inner scaling decreases with increasing Re_τ. For $Re_\tau = 511$, the spatial resolution is $0.7\delta_\nu$ and a minimum y^+ of 4 (60 µm from the wall). The closest data point to the wall is limited by the size of the tracer particles and glare spots that formed due to a reflection of the laser sheet from imperfections on the surface (small scratches and particles stuck to the wall). As shown in figure 7.5, there is no observable noise in the velocity distributions obtained from 3D-PTV based on STB.

The 3D-PTV measurements of the Reynolds stress profiles are compared with those of DNS in figure 7.6. The results from 3D-PTV and DNS agree well with one another, although there are some minor deviations. The maximum discrepancy in the peak streamwise Reynolds stress, $\langle u^2\rangle^+$, shown in figure 7.6(*a*), is approximately $0.4u_\tau^2$. The maximum deviation in the y^+ location of the peak in $\langle u^2\rangle^+$ is $2.6\delta_\nu$. The wall-normal Reynolds stress profile, $\langle v^2\rangle^+$, overlaps well with DNS for Re_τ of 425 and 511, as shown

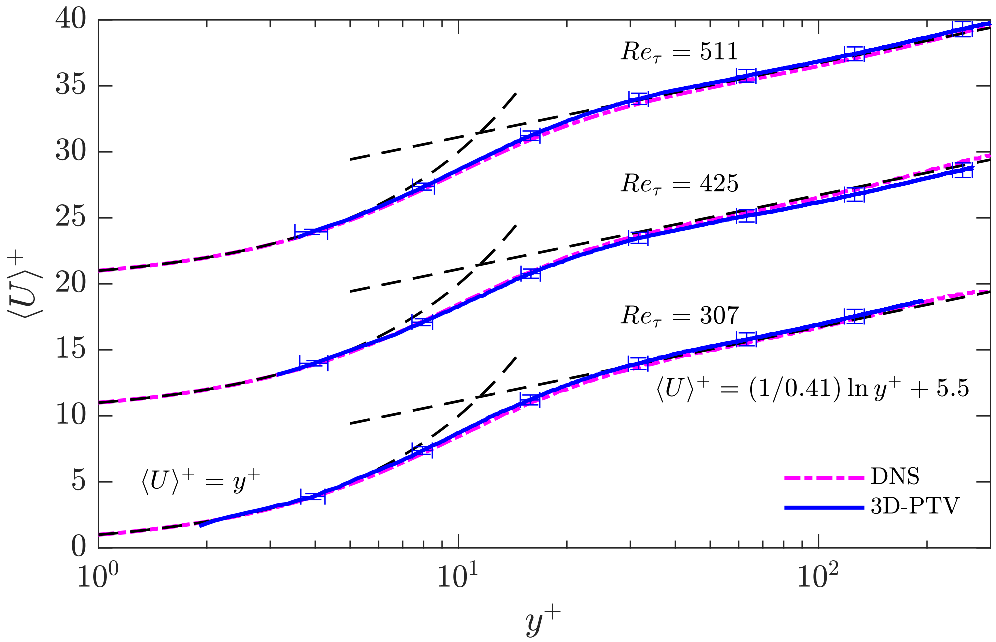

Figure 7.5: Inner-normalized mean streamwise velocity from 3D-PTV measurement for water in comparison with DNS and the law of the wall. The three profiles are shifted upward along the vertical axis by 10. 3D-PTV measurements at $Re_\tau = [307, 425, 511]$ are compared with DNS from Iwamoto *et al.* (2002) with $Re_\tau = 300$; MMoser *et al.* (1999) with $Re_\tau = 395$; and Lee & Moser (2015) with $Re_\tau = 550$.

in figure 7.6(b). The $\langle v^2\rangle^+$ profile for data with a Re_τ of 307 has a constant deviation, relative to the DNS profile, approximately equal to $0.1u_\tau^2$ for all y^+. Generally, the spanwise Reynolds stress distributions, $\langle w^2\rangle^+$, for all 3D-PTV results, are in good agreement with DNS, as seen in figure 7.6(c). The 3D-PTV results and DNS also show good agreement in their Reynolds shear stress profiles, $\langle uv\rangle^+$, shown in figure 7.6(d). One minor exception might be that the 3D-PTV profile of $\langle uv\rangle^+$ at Re_τ of 425 has a marginally larger peak by approximately $0.1u_\tau^2$ with respect to the DNS profile.

The profiles of $\langle v^2\rangle^+$ and $\langle uv\rangle^+$, shown in figure 7.6(b,d) both have visible low-amplitude noise. This is associated with the larger particle positioning error of 3D-PTV in the out-of-plane direction and the smaller flow motions in this direction (v component). The largest peak-to-peak noise oscillation in figure 7.6(b) is approximately $0.03u_\tau^2$, occurring between $y^+ = 230$ and 250 for the case of $Re_\tau = 425$. This peak-to-peak noise corresponds roughly to a pixel disparity of 0.1 pixel, given the digital resolution of 27.9 µm pixel^{-1} and the image acquisition rate of 2.9 kHz. Since 0.1 pixel is less than the assumed error of 0.2 pixel for v, the visible low-amplitude noise in figure 7.6(b,d) is within the assumed margin of uncertainty discussed in §7.3, and is captured by the error bars.

7.6 Mean velocity profile

The mean velocity profiles normalized using outer scaling are compared for drag-reduced flows at HDR and MDR in figures 7.7(a) and 7.7(b), respectively. Error bars are excluded from this figure, as the estimated 3D-PTV uncertainty is equivalent to the line thickness used here. In these figures, the mean velocity profile

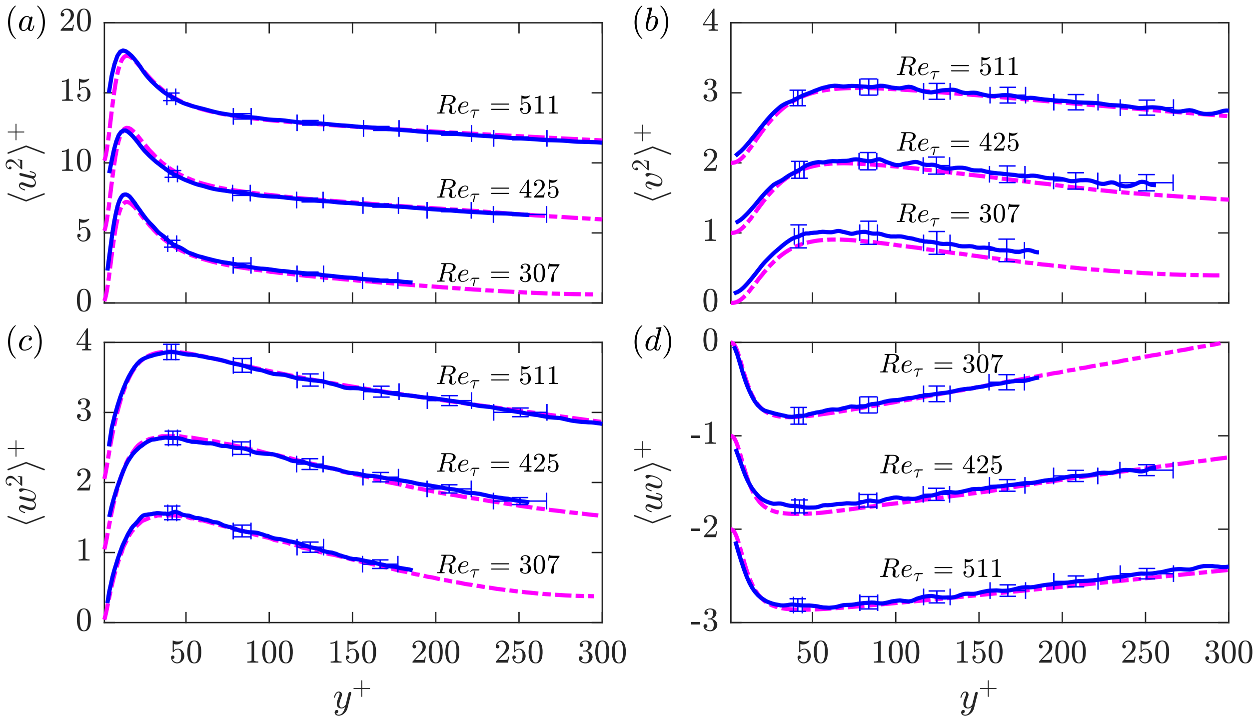

Figure 7.6: Reynolds stresses from 3D-PTV of water compared with DNS. (a) $\langle u^2 \rangle^+$, where each data set is shifted upward along the vertical axis by 5, (b) $\langle v^2 \rangle^+$ where each data set is shifted by 1, (c) $\langle w^2 \rangle^+$ where each data set is shifted by 1 and lastly (d) $\langle uv \rangle^+$ where each data set is shifted by -1. The legends are similar to figure 7.5. The 3D-PTV results with $Re_\tau = [307, 425, 511]$ are compared with DNS from Iwamoto *et al.* (2002) with $Re_\tau = 300$; MMoser *et al.* (1999) with $Re_\tau = 395$; and Lee & Moser (2015) with $Re_\tau = 550$.

for water at the same U_b as the drag-reduced flows is also presented. For water, this flow rate results in Re_τ of 793, which is larger than Re_τ of the drag-reduced flows. The magnitudes of mean velocity in the near-wall region for the drag-reduced solutions is smaller than mean velocity of water. Although not fully captured within the wall-normal extent of the 3D-PTV domain, farther away from the wall, mean velocity of the drag-reduced flows is expected to become larger than that of water to maintain a similar U_b.

Based on the shape of velocity profiles in figure 7.7(a), it can also be seen that the wall-normal gradient of mean velocity at the wall, $\partial\langle U\rangle/\partial y|_w$, for all three drag-reduced cases is smaller than $\partial\langle U\rangle/\partial y|_w$ of water. The profiles of C14 and PAM at HDR appear to approximately overlap in figure 7.7(a). The XG solution, on the other hand, starts with a lower $\partial\langle U\rangle/\partial y|_w$, and its $\langle U\rangle/U_b$ profile is smaller up until y/h of 0.42. The greater μ_w of XG compensates for its smaller $\partial\langle U\rangle/\partial y|_w$, resulting in a similar wall shear stress as PAM and C14. Within the region of $y/h < 0.4$ shown in figure 7.7(b), mean velocity for the two MDR cases of PAM and C14 are significantly lower than water. The profiles also demonstrate that $\partial\langle U\rangle/\partial y|_w$ of PAM and C14 are smaller than $\partial\langle U\rangle/\partial y|_w$ of water. PAM at MDR has a marginally lower velocity for $y/h < 0.5$ when compared to C14.

Figure 7.7 confirms that a similar DR does not ensure overlap of the mean velocity profile for different drag-reducing additives when the profiles are normalized using outer scaling. This was observed clearly for the XG solution in figure 7.7(a). The results also show that the difference in the mean velocity profiles of

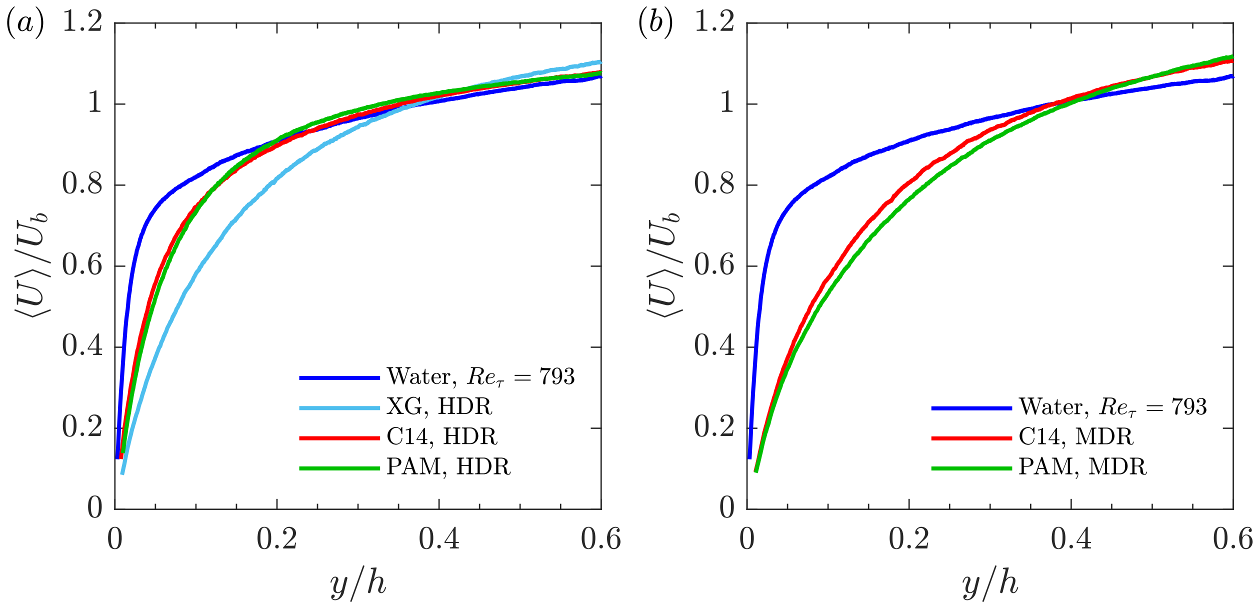

Figure 7.7: Outer-normalized mean streamwise velocity profile for drag-reduced flows at (*a*) HDR and (*b*) MDR.

different drag-reducing additives at a similar DR is not associated with the difference in their Re_H. In both figures 7.7(*a*) and 7.7(*b*), the mean velocity profiles of PAM and C14 solutions are similar while their Re_H is different (see table 7.2). The properties of the solutions suggest that their shear viscosity plays an important role in setting the outer-normalized mean velocity profiles. At a similar DR, drag-reduced solution with larger μ_w have a lower $\partial\langle U \rangle/\partial y|_w$ and $\langle U \rangle/U_b$ in the near-wall region. While solutions with a similar μ_w result in a similar $\mathrm{d}\partial\langle U \rangle/\partial y|_w$ and $\langle U \rangle/U_b$ in the near-wall region.

The inner-normalized mean velocity profile, $\langle U \rangle^+$, in the immediate wall vicinity at $y^+ < 15$ is demonstrated for all additives and for water in figure 7.8. The inner scales of the turbulent flows are estimated here by calculating $\partial\langle U \rangle/\partial y|_w$ using a linear fit of the data at $2 - 4 < y^+ < 5$. The lower wall-normal limit corresponds to the first valid data point from the 3D-PTV system which is determined to be at $y \approx 60$ µm. For consistency, the upper bound is chosen to be the maximum limit of the linear viscous sublayer for a Newtonian flow. Figure 7.8 shows the linear fit used to calculate $\partial\langle U \rangle/\partial y|_w$, and confirms the presence of a linear region for all the flows. The estimated $\partial\langle U \rangle/\partial y|_w$ values are presented in table 7.3 and are used to calculate the corresponding μ_w based on the shear viscosity models described in §7.3. This results in μ_w and the other inner-scaling variables for the drag-reduced flows that are presented in table 7.3. The comparison of the estimated DR_2 (based on $\partial\langle U \rangle/\partial y|_w$) in table 7.3 with the DR_1 (based on ΔP) in table 7.2 shows a reasonable agreement of the two methods. The difference between DR_1 and DR_2 is small and varies between 1.6% to 4.8%. The discrepancy is associated with several factors including the finite aspect ratio of the channel, deviation from the fully developed turbulence at the upstream pressure port, and the uncertainty in determining $\partial\langle U \rangle/\partial y|_w$.

The relatively good agreement amongst the wall statistics and DR using measurements of ΔP and 3D-PTV for XG, suggests the extrapolation of the CY model from §7.3 can reasonably estimate μ_w. A further

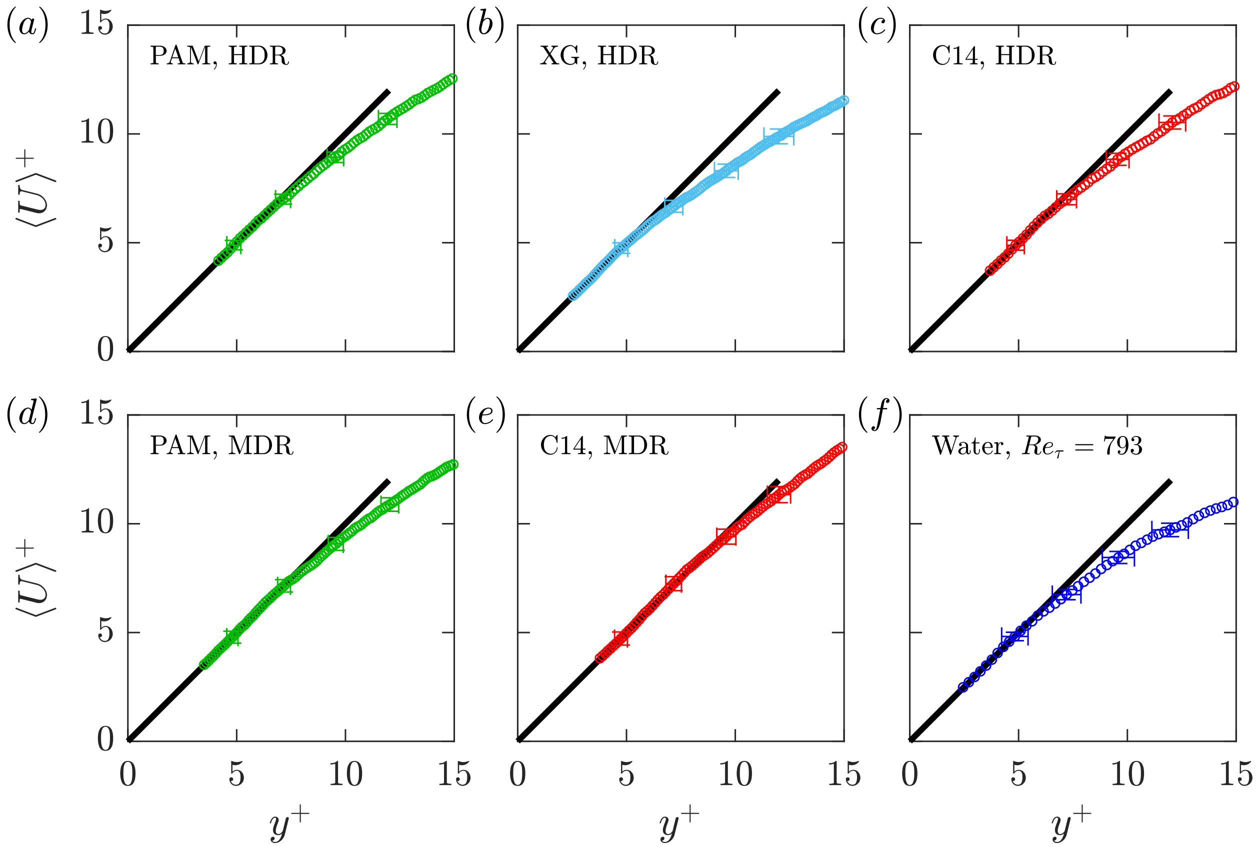

Figure 7.8: Mean streamwise velocity profile in the immediate near-wall region for (*a*) PAM at HDR, (*b*) XG at HDR, (*c*) C14 at HDR, (*d*) PAM at MDR, (*e*) C14 at MDR and (*f*) water.

means of communicating the agreement of these measurements is by determining μ_w using $\partial\langle U\rangle/\partial y|_w$ and $\tau_{w,1}$. Here, $\partial\langle U\rangle/\partial y|_w$ is obtained from 3D-PTV measurements, and $\tau_{w,1}$ is derived from measurements of ΔP. Such a validation has been done in experiments by Warholic *et al.* (1999*a*) and Ptasinski *et al.* (2001). If the the same analysis is performed, the viscosity of the XG solution at a shear rate of 2364 s^{-1} ($\partial\langle U\rangle/\partial y|_w$ from table 7.3) is 1.44 mPa s (using $\tau_{w,1}$ in table 7.1). This viscosity is approximately 0.14 mPa s lower than the μ_w listed in table 7.3, which is roughly 8%. The majority of this uncertainty is reflected in the error bars that propagate from a random error in repeated viscosity measurements and are shown in figures of mean velocity profile and Reynolds stresses to follow.

As alluded to earlier in §7.3, the method of multiplying $\partial\langle U\rangle/\partial y|_w$ and μ_w to establish $\tau_{w,2}$ for the non-Newtonian fluids is an approximation. Fluctuations in $\partial\langle U\rangle/\partial y|_w$ with respect to time can be significant and the instantaneous distribution of μ_w may not be simply determined by the mean shear rate. This is most significant for the XG solution, whose shear viscosity is described by the CY model. Gubian *et al.* (2019) demonstrated that τ_w can fluctuate by as much as 35% of the nominal value of τ_w for a Newtonian turbulent channel flow with a Re_τ of approximately 300. Assuming such a variance in τ_w is applicable to XG, an uncertainty in μ_w of approximately 0.06 mPa s is expected. Such a fluctuation in μ_w is captured by the error bars in the mean flow statistics demonstrated in the figures to follow.

In addition to demonstrating the fit of the linear viscous sublayer, figure 7.8 presents some insight into the

Solution	$\frac{\partial \langle U \rangle}{\partial y}\Big\vert_w$ (s^{-1})	μ_w (mPa s)	u_τ (mm s^{-1})	δ_v (µm)	Re_τ	DR_2 (%)
PAM, HDR	3458	1.074	61.10	17.67	424	55.3
PAM, MDR	2042	1.088	47.24	23.14	324	73.3
XG, HDR	2364	1.576	61.89	26.16	287	55.2
C14, HDR	4113	0.911	61.38	14.92	503	54.9
C14, MDR	2145	0.912	44.33	20.66	363	76.5

Table 7.3: The estimated inner scaling based on the wall-normal gradient of mean velocity at the wall for the drag-reduced flows.

thickness of the viscous sublayer for drag-reduced flows. The elastic sublayer model of Virk (1971) proposed that all drag-reduced flows have a viscous sublayer thickness of $y^+ = 11.6$ (corresponding to the tri-section point of the MDR asymptote, $y^+ = \langle U \rangle^+$, and the log law). However, figure 7.8 demonstrates that none of the drag-reduced flows, have a viscous sublayer thickness of $y^+ = 11.6$ (represented by the maximum extent of the black line). Nonetheless, there is still a considerable thickening of the linear viscous subregion relative to water for the drag-reduced flows. At $y^+ = 11.6$, HDR flows of XG, C14 and PAM solutions deviate from the linear fit by $1.98u_\tau$, $1.44u_\tau$ and $1.12u_\tau$, respectively. The largest deviation corresponds to the XG solution, which has the largest shear viscosity. Water has a deviation from the linear fit at $y^+ = 11.6$ of $1.97u_\tau$, which is equivalent to the deviation of XG. For MDR flows of C14 and PAM, the relative deviation from the linear profile at $y^+ = 11.6$ is smaller and equal to $0.6u_\tau$ and $1.0u_\tau$, respectively.

The results in figure 7.8 show that the thickness of the viscous sublayer is smaller for drag-reduced flows at HDR than MDR, suggesting that viscous sublayer thickens with increasing DR. It can also be seen that the thickness of the viscous sublayer depends on the additive type, i.e., the thickness varies for different solutions at a similar DR. The results also suggest that in general the thickness of the viscous sublayer in inner scaling reduces with increasing shear viscosity. The XG solution has the highest shear viscosity and has an almost identical viscous sublayer thickness as water, while other HDR flows with lower shear viscosity have a thicker viscous sublayer.

The velocity profiles normalized by inner scaling and presented in a log–linear format are shown in figure 7.9. The inner-normalized mean velocity profiles are compared with both the Newtonian law of the wall and the ultimate profile for drag-reduced flows at MDR, or equation (3.16) (Virk *et al.*, 1970). The results for flows at HDR in figure 7.9(*a*) are discussed first, followed by the results for MDR in figure 7.9(*b*).

The mean velocity profiles of the HDR flows in figure 7.9(*a*) are close to each other in the near-wall region. It can also observed that with increasing y^+, the HDR profiles of the three drag-reduced cases start to diverge and appear to have different slopes. Subject to the Virk (1971) elastic sublayer model for polymer flows at an intermediate DR, the $\langle U \rangle^+$ profile in the elastic sublayer (or buffer layer) is supposed to overlap with the ultimate profile, and for larger y^+ a Newtonian plug layer with a logarithmic profile with a similar slope as the Newtonian log layer should propagate. As shown in figure 7.9(*a*), none of the HDR profiles

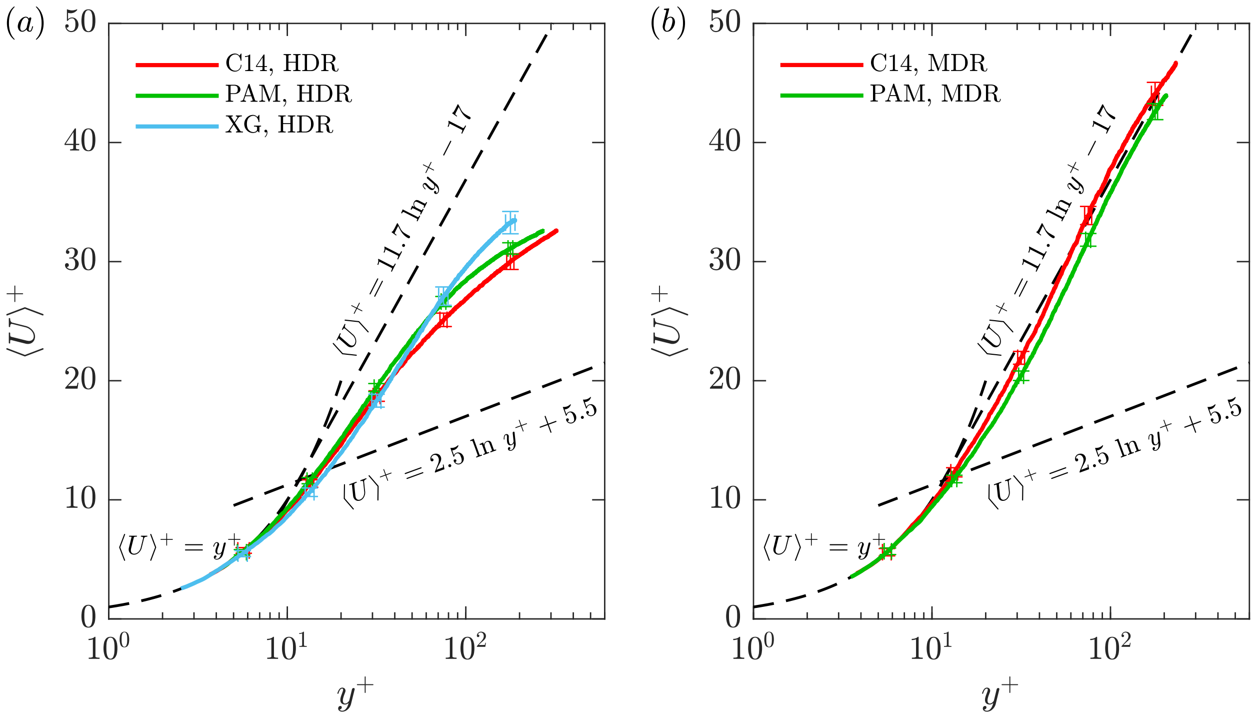

Figure 7.9: Inner-normalized mean streamwise velocity profile of drag-reduced flows at (*a*) HDR and (*b*) MDR.

overlap with the ultimate asymptote. Therefore, DR does not uniquely define the inner-normalized mean velocity profile since the type of additive plays a role in shaping the profile. In comparing the mean velocity profiles of different experiments, White *et al.* (2012) similarly observed variability in the outer layer of the mean velocity profile for polymer solutions with the same DR; albeit for cases of low DR, smaller than 40%. Due to the differences amongst the data sets, White *et al.* (2012) postulated that the velocity distribution in the outer layer depends on the Reynolds number, properties of the additive, and the canonical flow type. It is important to note that the results in figure 7.9(*a*) do not exclude the effect of Reynolds number. In other words, the variations can be partly attributed to differences in the Reynolds number of the drag-reduced flows.

The mean velocity profile of the two drag-reduced flows at MDR are shown in figure 7.9(*b*). The profile of C14 has a higher $\langle U\rangle^+$ than PAM outside the viscous sublayer, which is consistent with its slightly higher DR_2; 76.5% for C14 versus 73.3% for PAM solution. The C14 profile is also marginally greater than the MDR asymptote for $y^+ > 60$. Both previous experimental and numerical simulations have observed a small overshoot of the MDR asymptote for velocity profiles of polymer solutions (Escudier *et al.*, 2009; White *et al.*, 2012; Graham, 2014). Both profiles do not adhere to the MDR asymptote of (Virk *et al.*, 1970) and intersect with it at different y^+. In addition, the profile of C14 does not agree with the asymptote for drag-reducing surfactant solutions proposed by Zakin *et al.* (1996); $\langle U\rangle^+ = 23.4 \ln y^+ - 65$. This asymptote is not show in figure 7.9 for brevity. Considering the error bars and the slight difference in DR of C14 and PAM, the MDR asymptote seems to be unique and independent of the additive type and the Reynolds number. However, the drag-reduced flows of PAM and C14 at MDR do not follow the logarithmic trend proposed by

Virk *et al.* (1970); they share a similar S-shaped profile that straddles or at least intersects the asymptote of (Virk *et al.*, 1970). To further evaluate the logarithmic behaviour, the indicator function, $\zeta = y^+ \partial \langle U \rangle^+ / \partial y^+$, is investigated next in figure 7.10. Using the indicator function to evaluate logarithmic dependency, White *et al.* (2012) found that the inner-normalized mean velocity of polymer drag-reduced flows at MDR were not truly logarithmic functions of y^+.

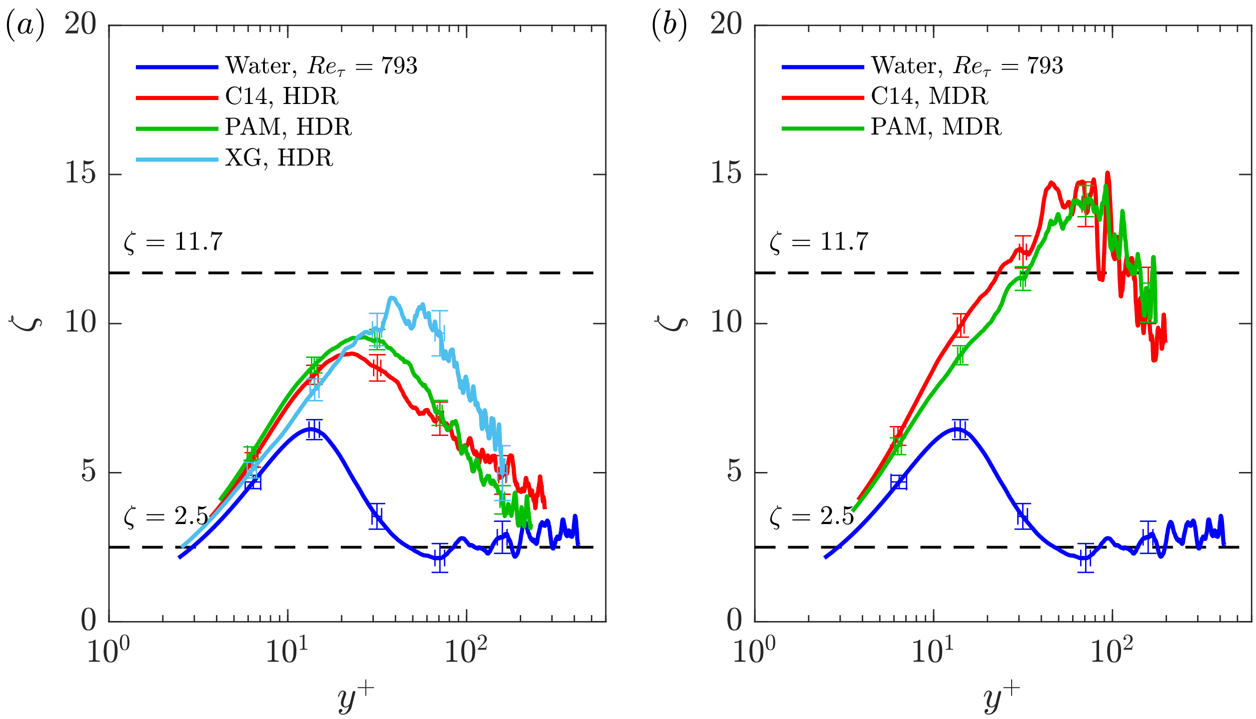

Figure 7.10: The indicator function for drag-reduced flows at (*a*) HDR and (*b*) MDR.

To establish $\partial \langle U \rangle^+ / \partial y^+$, and calculate ζ , a moving second-order polynomial filter, of length $10 - 15\delta_\nu$ (250 µm), was applied to the distribution of $\langle U \rangle^+$ as a function of y^+. The polynomials were then differentiated analytically. Figures 7.10(*a*) and 7.10(*b*) demonstrates ζ as a function of y^+ for HDR and MDR flows, respectively. A region of y^+ where ζ is constant is indicative of a layer where $\langle U \rangle^+$ varies logarithmically as a function of y^+. For example, the distribution of ζ for water, shown in both figures 7.10(*a*) and 7.10(*b*), is approximately constant and equal to 2.5 for $y^+ > 30$, which is indicative of a logarithmic layer for the Newtonian turbulent channel flows. White *et al.* (2012), Elbing *et al.* (2013) and White *et al.* (2018) proposed that for a polymer drag-reduced flow, the shape of the mean velocity profile, and similarly ζ, depends on the Reynolds number, polymeric properties and the canonical flow type. Figure 7.10(*a,b*) addresses the second postulate by comparing flows comprised of different additives at HDR and MDR.

Figure 7.10(*a*) shows that the HDR flows of C14 and PAM have similar distributions of ζ. White *et al.* (2012) stated that HDR flows are distinct in their lack of a Newtonian plug. By observation of figure 7.10(*a*) none of the HDR flows have a y^+ range where ζ appears constant and a Newtonian plug does not exist within the measurement domain. However, this does not rule out the possibility of a Newtonian plug existing at larger y^+. The profile of ζ for XG show relative similarity with the other HDR flows for $y^+ < 30$; however, the peak in its profile, though subject to experimental noise, appears to be marginally higher and located at larger y^+. The larger y^+ location of ζ peak for XG solution indicates that the centre of the elastic sublayer (buffer layer) is farther away for the wall. Therefore, the indicator function also provides further evidence that the shape of the velocity profile and the thickness of the sublayers is not uniquely defined by DR. Here, the thicker elastic sublayer of the XG solution is associated with its larger shear viscosity and lower Reynolds number. The y^+ location of the peak in the distribution of ζ, shows that the elastic sublayer is thinner for drag-reduced solution with higher Reynolds number (Re_H or Re_τ).

Figure 7.10(*b*) compares the plots of ζ for C14 and PAM at MDR. The two profiles appear similar for all y^+. The y^+ location and value in the peak of ζ is approximately (y^+, ζ) = (70, 14) for both drag-reduced flows. The peak is larger and farther away from the wall relative to the HDR cases, indicating a thicker elastic sublayer. Due to the lack of a region with constant ζ, White *et al.* (2012) concluded that the exact shape of the MDR profile was not logarithmic. Instead, MDR was achieved when the peak in ζ equals 11.7, corresponding to the slope in the MDR asymptote proposed by Virk *et al.* (1970). Figure 7.10(*b*) demonstrates that the peak exceeds this limit for both PAM and C14 solutions. In plotting ζ for experimental data from Escudier *et al.* (2009) collected for a rigid polymer solution at MDR with DR of 67%, White *et al.* (2012) demonstrated a similar overshoot of $\zeta = 11.7$. Elbing *et al.* (2013) also shows a peak in ζ greater than 11.7 for a flexible polymer solution with DR = 65%. Therefore, further doubt is cast on the exactness of the slope of the MDR profile of Virk *et al.* (1970). Figure 7.10(*b*) also appends the conclusion of White *et al.* (2012) to state that surfactant drag-reduced flows at MDR, in addition to polymer flows, also do not possess a logarithmic layer. Furthermore, while the shape of the two mean velocity profiles at MDR are not exactly logarithmic, they are similar. This implies that a universal distribution of $\langle U\rangle^+$, and ζ, for drag-reduced flows at MDR, that is irrespective of the additive type and the Reynolds number, may exist.

7.7 Reynolds stresses

The Reynolds stresses profiles for the HDR cases are compared in figure 7.11. In addition to the drag-reduced flows, the Reynolds stress profiles for water at four Re_τ that are similar to Re_τ of the drag-reduced cases are presented. For example, the Reynolds stress profiles of C14, PAM and XG, with Re_τ of 503, 424 and 287, are shown alongside those for water with a Re_τ of 511, 425 and 307. As expected, all of the Reynolds stress profiles of water show similar distributions, relative to one another, within the linear sublayer and buffer layer. Larger differences in the outer layer amplify with increasing y^+, as expected.

Figure 7.11(*a*) shows that all HDR flows possess a large peak value of $\langle u^2\rangle^+$ that is also shifted away from the wall, relative to water at a similar Re_τ. The $\langle u^2\rangle^+$ profiles of C14 and PAM appear similar for $y^+ < 70$ although the $\langle u^2\rangle^+$ peak is smaller for PAM. The two profiles deviate with further increase of y^+. Compared to C14 and PAM, XG has a smaller peak value of $\langle u^2\rangle^+$, which is displaced farther from the wall. Therefore, $\langle u^2\rangle^+$ peak is smaller and farther away from the wall for solutions with higher shear viscosity. In addition, the notion that drag-reduced flows of different additives at the same DR have a similar $\langle u^2\rangle^+$ peak appears to be invalid. The shift in the peak of $\langle u^2\rangle^+$ away from the wall is an indication of a thicker buffer layer that is consistent with previous observations.

Figure 7.11(*b,c*) demonstrates significant attenuation in the profile of $\langle v^2\rangle^+$ and $\langle w^2\rangle^+$ of the drag-reduced

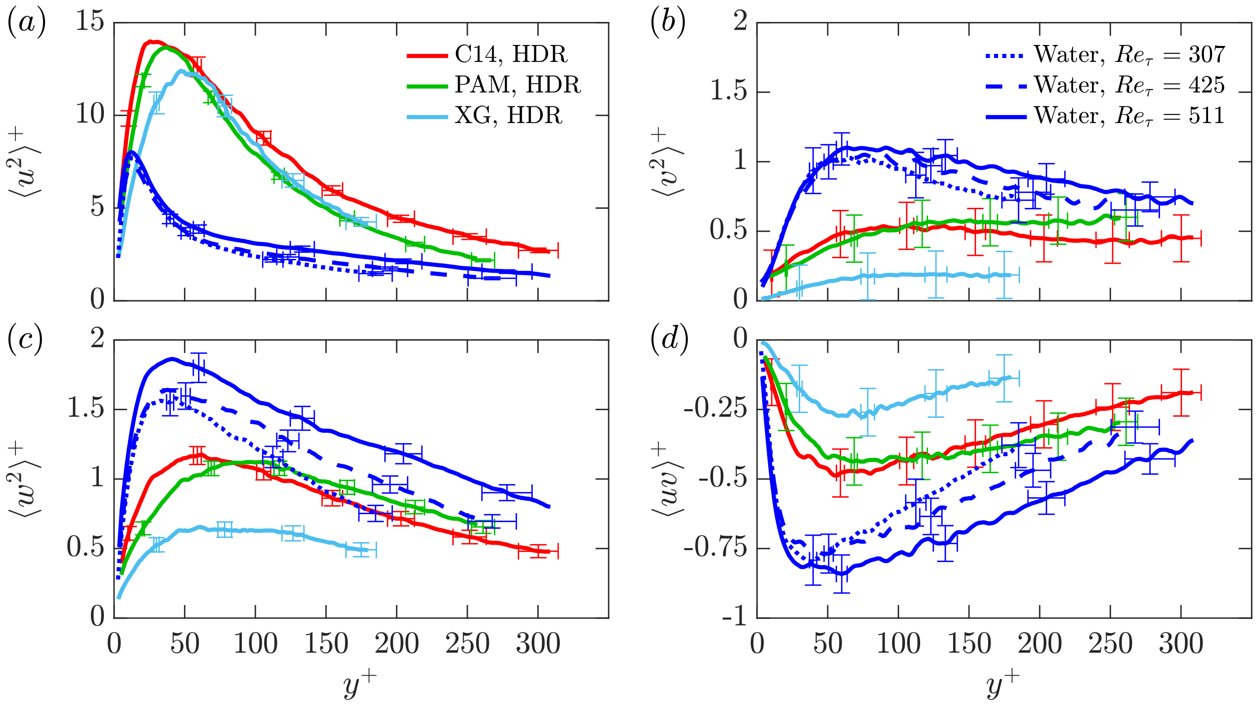

Figure 7.11: Inner-normalized mean Reynolds stress profiles of drag-reduced flows at HDR showing (*a*) streamwise Reynolds stress, (*b*) wall-normal Reynolds stress, (*c*) spanwise Reynolds stress profiles and (*d*) Reynolds shear stress.

flows relative to water. For $\langle v^2 \rangle^+$, this agrees with the observations of Escudier *et al.* (2009) for polymers and also WWarholic *et al.* (1999*a*) for surfactants. Attenuation in the profile of $\langle w^2 \rangle^+$ has been shown by White *et al.* (2004) for polymers. To the authors' knowledge, $\langle w^2 \rangle^+$ has never been demonstrated for surfactant drag-reduced flows. Similar to their $\langle u^2 \rangle^+$ profiles, C14 and PAM display rather similar profiles for $\langle v^2 \rangle^+$ and $\langle w^2 \rangle^+$ with subtle discrepancies. The $\langle v^2 \rangle^+$ and $\langle w^2 \rangle^+$ profiles for XG, on the other hand, are noticeably more attenuated than the other HDR flows. The peak value in the $\langle v^2 \rangle^+$ and $\langle w^2 \rangle^+$ distributions of XG are approximately 50% those of C14. Figure 7.11(*d*) demonstrates similar profiles in $\langle uv \rangle^+$ for C14 and PAM, but again a more attenuated distribution for XG. The larger attenuation in $\langle uv \rangle^+$ is likely attributed to a larger imposition of viscous stresses due to the larger overall shear viscosity of the XG solution. Therefore, different drag-reduced solutions at an identical DR do not exhibit identical distribution of Reynolds shear stresses, in particular when their shear viscosity is different. A lack of consistency in the shear viscosity of the drag-reduced solutions is also reflected by differences in the Reynolds number number of the solutions with similar DR (i.e. similar u_τ). Therefore, the discrepancy in the Reynolds stress distributions of the HDR flows can be similarly explained by differences in the Reynolds number of the drag-reduced solutions.

Figure 7.12 demonstrates the Reynolds stresses of C14 and PAM at MDR. Having observed that the Reynolds stresses of XG were much lower than the other HDR flows in figure 7.11, it was perceived to be prudent to include XG at HDR in the comparison with the MDR flows in figure 7.12. This was based on prior knowledge that the Reynolds stresses are more attenuated for flows with larger DR (Warholic *et al.*, 1999*b*; Ptasinski *et al.*, 2001; Escudier *et al.*, 2009). Similar to figure 7.11, figure 7.12 presents the Reynolds stresses of the drag-reduced flows alongside the distributions of water that share a similar Re_τ. C14 and PAM at MDR, alongside XG at HDR, with Re_τ of 363, 324 and 307, are presented together with the distributions of water with Re_τ of 363 and 307.

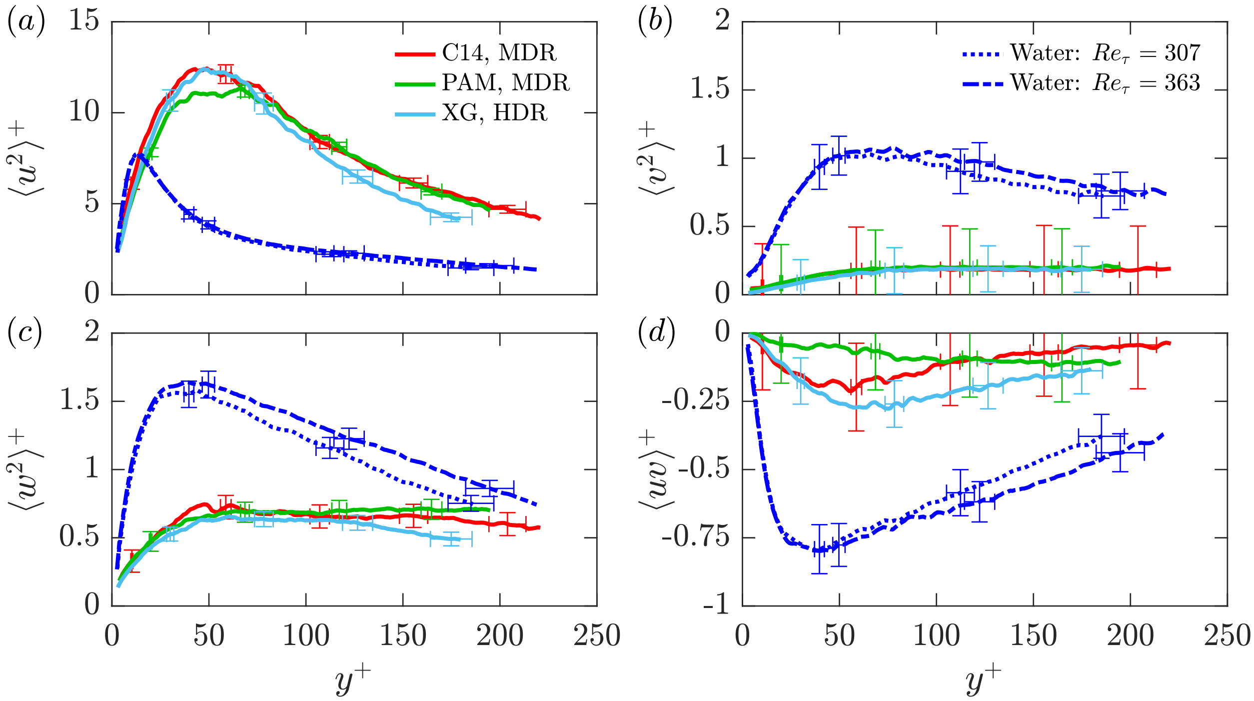

Figure 7.12: Inner-normalized mean Reynolds stress profiles of drag-reduced flows at MDR and XG at HDR; (*a*) streamwise Reynolds stress, (*b*) wall-normal Reynolds stress, (*c*) spanwise Reynolds stress profiles and (*d*) Reynolds shear stress.

In figure 7.12(*a*), there is relatively good overlap in the distributions of $\langle u^2 \rangle^+$ for the three solutions. Here the similarity in the XG profile with the other two profiles is striking, despite 18–21% difference in DR_2 of XG at HDR and the other two MDR flows. For polymer flows, Escudier *et al.* (2009) demonstrated that for $DR > 40\%$, $\langle u^2 \rangle^+$ decreases as a function of DR; albeit, results appeared mixed for other authors (Warholic *et al.*, 1999*b*). In the current investigation, the $\langle u^2 \rangle^+$ peak of C14 and PAM at MDR decreased relative to their corresponding HDR cases. However, the peaks did not decrease to a point where they are lower than the peak measured for water. While Li *et al.* (2005) and Warholic *et al.* (1999*a*) demonstrate a lower peak in $\langle u^2 \rangle^+$ for surfactant drag-reduced flows with large DR they have similarly shown that the peak in $\langle u^2 \rangle^+$ largely depends on the Re_τ of the flow. Warholic *et al.* (1999*a*) demonstrated this in their sweep of Reynolds number for different HDR flows, where the peak in $\langle u^2 \rangle^+$ was larger than water for surfactant drag-reduced flows with a large Reynolds number, but smaller than water for low Reynolds number. Thais *et al.* (2012) showed the peak in $\langle u^2 \rangle^+$ had a similar dependence on the Reynolds number based on DNS using the FENE-P model. Figure 7.12(*b,c*) demonstrates that the distributions of $\langle v^2 \rangle^+$ and $\langle w^2 \rangle^+$ for C14 and PAM at MDR, and XG at HDR, have nearly identical profiles that are also significantly suppressed relative to water. Li *et al.* (2005) and Warholic *et al.* (1999*a*) also observed significant attenuation in profiles of $\langle v^2 \rangle^+$ for surfactant drag-reduced flows near MDR. The overlap in $\langle u^2 \rangle^+$, $\langle v^2 \rangle^+$ and $\langle w^2 \rangle^+$ implies that the mean turbulent kinetic energy is the same for the three drag-reduced flows.

Lastly, figure 7.12(*d*) demonstrates that $\langle uv \rangle^+$ profiles of C14 and XG are slightly larger than the $\langle uv \rangle^+$ profile of PAM at $y^+ < 100$. However, for all three flows, the $\langle uv \rangle^+$ magnitudes are small and have the same order of magnitude as the error bars. Therefore, the values should be considered negligible and differences are Tamano *et al.* (2018) presented a finite $\langle uv \rangle^+$ distribution, while Warholic *et al.* (1999*a*) demonstrated a $\langle uv \rangle^+$ profile approximately equal to zero for flows of surfactant drag-reducing additives at MDR. The discrepancies in the small residual values of $\langle uv \rangle^+$ is potentially associated with measurement uncertainties as they are also present in the current measurements.

Considering PAM and C14 at MDR, the measurements presented in figure 7.12 show that Reynolds stress profiles of drag-reduced flows at MDR overlap. A perfect overlap can be seen for all components except Reynolds shear stress. For the latter component, there are subtle differences with the same magnitude as the measurement uncertainties. Therefore, it can be concluded, that at MDR the Reynolds stress profiles are not a function of additive type and Reynolds number. At MDR, the Reynolds stress profiles converge to a common set of distributions for polymer and surfactant drag-reduced flows with different Reynolds number.

The C_f values presented based on ΔP in figure 7.2, and mean velocity profiles of figure 7.9(*a*), suggest that XG is not at MDR. In contrast, the results of figure 7.12 demonstrate that Reynolds stress profiles of XG are similar to those of PAM and C14 at MDR. The measurements of DR_1 (based on ΔP) for XG in figure 7.1(*c*) also show that a higher level of DR was not achievable for XG with increasing its concentration; DR_1 plateaus to a constant 58.5% for c in excess of 300 ppm. Why XG has a lower asymptotic DR_1, relative to C14 and PAM at MDR, is likely attributed to the imposition of larger viscous stresses. To summarize, it is evident that the DR_1 of XG has attained an asymptotic state, according to figure 7.1(*c*). The Reynolds stresses also demonstrate that XG shares dynamical similarities with other MDR flows (see figure 7.12). Therefore, with respect to the turbulent flow and production of turbulent kinetic energy, XG is at an MDR state. The discrepancies in DR and mean velocity profile of XG with respect to the MDR state of the other drag-reduced flows is associated with larger inherent viscous stresses of this polymer solution.

7.8 Low- and high-speed streaks

The following analysis evaluates the length scale of the dominant flow structures at HDR and MDR using two-point correlation of streamwise velocity fluctuations. The spatial, two-point correlation is computed as

$$R_{uu}(\Delta z) = \frac{\langle u_{x_0,y_0,z_0} u_{x_0,y_0,z_0+\Delta z} \rangle}{\sqrt{\langle u^2_{x_0,y_0,z_0} \rangle} \sqrt{\langle u^2_{x_0,y_0,z_0+\Delta z} \rangle}} \tag{7.4}$$

Here, (x_0, y_0, z_0) is the coordinate of the reference point selected at $(0, 0.4h, 0)$, which is positioned within the logarithmic layer for Newtonian flows. The dominant coherent structures at this location are low and high-speed streaks that have also been observed in drag-reduced flows (White *et al.*, 2004; Mohammadtabar *et al.*, 2017). At higher Reynolds numbers and in Newtonian flows, these streaks form the very large-scale motions (Hutchins & Marusic, 2007). The incremental displacement along the spanwise direction is indicated as Δz, relative to the z_0 reference point. As a result, R_{uu} characterizes the spanwise scale of the low and high-speed streaks in the drag-reduced flows.

Figure 7.13(a) presents R_{uu} along $\Delta z/h$ for the HDR flows. The R_{uu} functions for water are shown alongside the drag-reduced flows. The overlap in the R_{uu} profiles indicate that the width of the streaks for the Newtonian cases are similar. The R_{uu} profiles for C14 and PAM at HDR are also approximately similar, indicating a similar streak spacing. This suggests that the R_{uu} distribution for drag-reduced flow may not be a strong function of the Reynolds number as PAM and C14 flows have different Re_H. The XG demonstrates a rather larger R_{uu} relative to C14 and PAM, which indicates even wider streaks. Therefore, the turbulent streaks of drag-reduced flows of PAM and C14 with similar shear viscosities appear to be more alike, while XG – a solution with a much larger overall shear viscosity – is distinct.

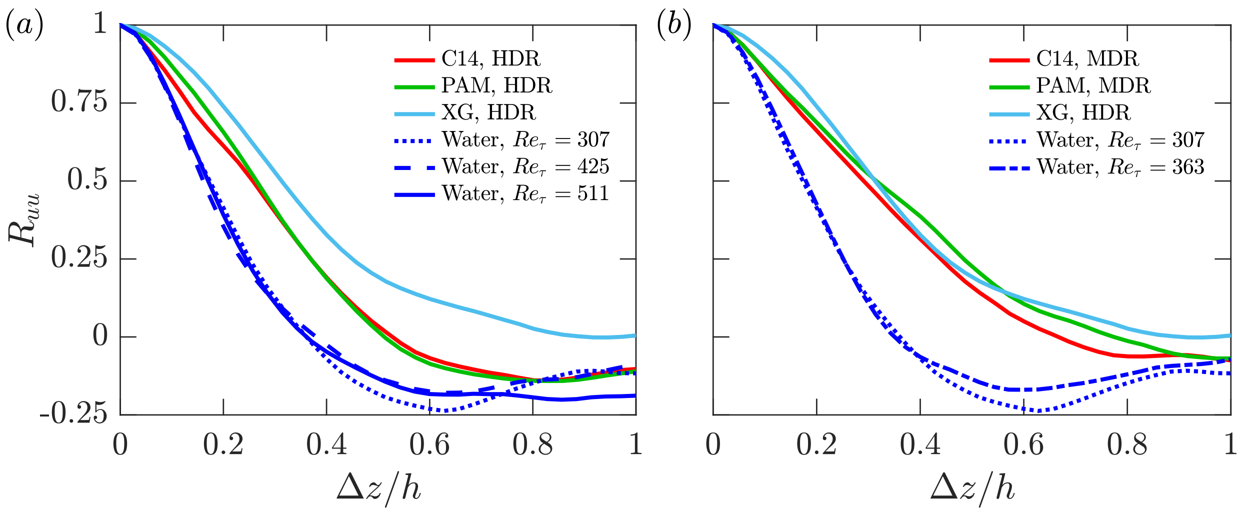

Figure 7.13: Two-point correlation of streamwise velocity fluctuations in the spanwise direction for drag-reduced flows at (a) HDR and (b) MDR. The reference location for the two-point correlations is at $(x_0, y_0, z_0) = (0, 0.4h, 0)$.

Figure 7.13(b) presents R_{uu} of drag-reduced flows of PAM and C14 at MDR, and XG at HDR. The profiles approximately overlap, and therefore streak spacing is expected to be similar for the three drag-reduced flows. Using a similar two-point correlation analysis, Li *et al.* (2006), White *et al.* (2004) and Tamano *et al.* (2018) demonstrated a monotonic increase in the spanwise width of the low- and high-speed streaks for polymer and surfactant drag-reduced flows with increasing DR. Comparing figure 7.13(a), with figure 7.13(b), both C14 and PAM exhibit growth in the average streak spacing with respect to DR. The XG profile appears to show more similarities in the width of its streaks with respect to solutions of C14 and PAM at MDR. This reinforces the notion that XG has attained a state of MDR regarding turbulent dynamics.

7.9 Summary

The main objective of this investigation was to compare the rheological features and turbulence statistics of three drag-reducing additives, PAM, XG and C14, in a turbulent channel flow. To ensure that the comparison of the additives is subject to similar conditions, the drag reducing solutions were prepared such that they all produced a similar level of drag reduction (DR) at a common mass flow rate. This is equivalent to maintaining a similar wall shear stress and mass flow rate. Two DR values were considered; the first being a high drag reduction (HDR) case with DR of 57.7% ± 1.2%, and the second being a maximum drag reduction (MDR) case with DR of 70.3% ± 1.8%. Based on measurements of the streamwise pressure gradient along the channel, solutions of PAM, XG, and C14 achieved the HDR condition, while only PAM and C14 could attain the larger MDR limit. Although the mass flow rate and DR were constant, the flows had different Reynolds numbers (Re_H) due to the difference in their shear viscosity.

Samples of each drag-reduced flow at HDR and MDR were collected for shear viscosity measurements in a torsional rheometer and measurements of their extensional relaxation time using a capillary breakup extensional rheometer (CaBER). Despite having the capability of generating similar levels of DR, none of the different types of additive solutions exhibited overlap in their apparent shear viscosity curves or similarities in their extensional relaxation times. Solutions of C14 exhibited low, and relatively constant shear viscosities that were almost identical to the shear viscosity of water. PAM solutions demonstrated only marginal shear thinning trends. The overall shear viscosity of PAM was approximately 20% larger than the shear viscosity of water. In contrast, the shear viscosity of the XG solution at low strain rates, was an order of magnitude larger than the other solutions, and had a pronounced shear thinning trend. Regarding the extensional relaxation time, CaBER measurements could only be performed for solutions of PAM. Solutions of XG and C14 failed to show considerable uniaxial filament stretching; the samples disintegrated rapidly upon a marginal imposition of strain from the CaBER system. Therefore, only solutions of PAM demonstrated measurable extensibility characteristics using CaBER, with a relaxation time of 4 to 11 ms. Although the current measurements, alongside previous experimental measurements from the literature, have not identified a common rheological trait for different drag reducing additives, the possibility of such a common feature existing cannot be ruled out. However, these results pose the question of how different drag-reducing solutions manipulate the wall turbulence. This question is addressed using detailed measurements of the turbulence statistics.

The turbulent channel flow of the drag-reduced additives and several Newtonian flows were characterized using three-dimensional particle tracking velocimetry. The drag-reduced solutions of PAM, XG, and C14 at the HDR state demonstrated different mean velocity profiles when normalized using outer and inner scaling. The indicator function showed inconsistencies in the inner-normalized mean velocity distributions and were a result of variations in the wall-normal thickness of the constituent sublayers of the three drag-reduced solutions. Drag-reduced solutions with a larger overall shear viscosity, and therefore a smaller Re_H, had a thinner linear viscous sublayer and a thicker elastic sublayer. At HDR, the Reynolds stress profiles of the PAM, XG, and C14 solutions did not overlap. In particular, the XG solution, which had the highest shear viscosity, had more attenuated Reynolds stresses. Two-point correlation of streamwise velocity also demonstrated larger spanwise streak spacing for the XG solution relative to the other HDR flows. However, similar to previous observations, the drag-reduced additives resulted in the same qualitative net-effect: that is, relative to a Newtonian turbulent wall flow, the buffer layer of all drag-reduced flows were thicker, the streamwise Reynolds stress profile was significantly larger, and the other Reynolds stress components were much smaller. The observations demonstrated that turbulent flows of different drag reducing additives generated mean velocity and Reynolds stresses profiles that were qualitatively similar, but quantitatively different. The discrepancy in the magnitude of flow statistics appeared to be mainly due to the difference in the flow Re_H.

In contrast to the HDR flows, the outer and inner-normalized mean velocity profiles of PAM and C14 at MDR approximately overlapped. The small deviation between the two profiles was associated with the marginal differences in their DR. The indicator function showed that the wall-normal spacing of the sublayers were similar for the two flows at MDR. Plots of the indicator function also demonstrated that a region where mean streamwise velocity varied logarithmically with distance from the wall, does not exist. That being said, the mean velocity profile at MDR was still asymptotic and independent of the type of additive and Re_H, despite not being precisely logarithmic in its distribution. The Reynolds stress profiles and two-point correlation of streamwise velocity fluctuations were also independent of additive type and Re_H as they converged to a common profile for PAM and C14 at MDR.

Although XG had a much lower DR, its Reynolds stress profile overlapped with the Reynolds stress distributions of PAM and C14 at MDR. The overlap in the Reynolds stresses indicated that the XG solution achieved a maximum level of attenuation in its turbulence, similar to PAM and C14 at MDR. In contrast, the DR and mean velocity profile of the XG solution at HDR was not consistent with those of PAM and C14 at MDR. The discrepancy was associated with the greater shear viscosity and therefore, lower Re_H of the XG solution. The large shear viscosity and lower Re_H of XG appeared to have hindered the solutions ability to produce a larger DR, and have its mean velocity profile intersect with the MDR asymptote. This observation refines the previous conclusions. It hints that the dependence of mean velocity profile and Reynolds stresses on the additive type was attributed to differences in the shear viscosity and Re_H, and not a rheological feature typically associated with drag reduction, such as the extensibility of the solution.

Chapter 8

Lubricating layer in drag-reduced channel flows of rigid polymers

The present investigation provides high-fidelity turbulence statistics of a drag-reduced channel flow of rigid polymers with varying Re_H. Few experiments of rigid polymers have explored the effect of Re_H on flow statistics. The existing measurements of rigid polymers in a turbulent channel flow have low spatial resolutions (Escudier *et al.*, 2009) or appear to be in an arguably transitional flow regime due to small Re_H (Mohammadtabar *et al.*, 2017). To alleviate this gap in the research, an experimental investigation is performed for a 170 ppm xanthan gum (XG) solution in a turbulent channel flow with a friction Reynolds number Re_τ between 170 and 700. The resulting levels of DR are between 27% and 33%, demonstrating little dependence on Re_H. Planar particle image velocimetry (PIV) measurements are used to measure the instantaneous velocity of the drag-reduced flows. Shear rheology is characterized using a double gap and a parallel plate geometry to capture the viscosity of the XG solution over a large range of shear rates. A mechanism for rigid polymer drag reduction is asserted from the perspective of lubricated flows. A thin layer of low-viscosity fluid near the wall is observed for the rigid polymer solution at all flow conditions, which is proposed to be essential for DR using rigid polymers.

8.1 Flow conditions

Experiments were performed in the same recirculating flow facility as shown in figure 4.4. For more information regarding the facility, refer to §4.2 or Warwaruk & Ghaemi (2021). The same right-hand orthonormal basis was used in the present experiments, with positions along the streamwise, wall-normal, and spanwise directions denoted by x, y, and z, respectively. The Cartesian coordinate system was placed at the midspan of the lower channel wall, as shown in figure 4.5. A shell and tube heat exchanger and a thermocouple were used to maintain a constant fluid temperature of 25°C ± 0.3°C. A differential pressure transducer (DP15, Validyne) with a 1 psi diaphragm was used to measure the streamwise gradient in the static pressure, i.e., $\Delta P/\Delta x$. Here the streamwise separation between the pressure ports was $\Delta x = 109H$, as detailed in §4.2.

Measurements were conducted for seven different conditions of bulk velocity $U_b = \dot{m}/\rho HW$, all of which are shown in Table 8.1 for water. In the case of water, the Reynolds number Re_H was between 9100 and 37 000. Recall that the symbol μ_w represents the dynamic viscosity of the fluid corresponding to the shear rate at the wall. While this is a variable for the polymer solutions, for a Newtonian fluid such as water, the dynamic viscosity is consistently 0.89 mPa s at 25°C (Nagashima, 1977; Collings & Bajenov, 1983). Therefore, the Re_H of the polymer solutions are calculated later in §8.3, when the wall shear rates and steady shear viscosity are obtained. The wall shear stress τ_w was established using measurements of the streamwise pressure gradient, i.e., (3.5) – equivalent to $\tau_{w,1}$ from the previous experiments detailed in §7.1 and Warwaruk & Ghaemi (2021). The friction velocity u_τ from (3.10), viscous lengthscale (3.11), and friction Reynolds number Re_τ (3.12) were then subsequently determined, the results for which are listed in Table 8.1 for the flow of water.

U_b (m s^{-1})	Re_H	ΔP (Pa)	τ_w (Pa)	u_τ (mm s^{-1})	δ_ν (µm)	Re_τ
0.542	9100	231	1.061	32.6	27.4	270
0.819	13 800	477	2.188	46.8	19.1	390
1.094	18 400	795	3.648	60.5	14.8	510
1.371	23 000	1179	5.407	73.6	12.1	620
1.647	27 700	1627	7.465	86.5	10.3	730
1.924	32 300	2139	9.814	99.2	9.0	830
2.197	37 000	2711	12.437	111.7	8.0	940

Table 8.1: Flow properties for channel flow of water.

8.2 Rigid polymer solution

The same rigid polymer, XG, used in §§6 and 7 was utilized for the present experimental investigation. Solid XG, in powder form, was weighed using a digital scale (AB104-S, Mettler Toledo) with a 0.1 mg resolution. The powder was then gradually added to 15 l of tap water and agitated using a stand mixer (Model 1750, Arrow Engineering Mixing Products). The concentrated 15 l master solution was then left to rest overnight for approximately 12 h. The following day, the master solution was added to 100 l of moving tap water within the flow loop. This diluted the master solution to the desired concentration of 170 ppm. A 170 ppm solution of XG produced a solution of good transparency for PIV measurements. To ensure the solution was homogeneous, the pump was operated at 1400 rpm (U_b = 4.380 m s^{-1}) for 1 h. Near the end of the 1 h duration, ΔP was marginally growing at a rate of approximately 10 Pa min^{-1}, about a 0.1% increase in ΔP every minute. This was considered sufficiently steady state. After the 1 h time mark, the pump speed was reduced to 800 rpm, corresponding to U_b = 2.197 m s^{-1}, for the first PIV measurement at the highest Re_H. The pump speed was then reduced in increments such that PIV measurements for each flow condition listed in Table 8.2 were taken. At all of the measured flow rates listed in Table 8.2, no variation in ΔP was observed during the PIV acquisition time. Therefore, any mechanical degradation or polymer deagglomeration was likely negligible after the 1 h mixing phase. Finally, fluid samples were collected for shear viscosity measurements using an access port along the flow loop.

U_b (m s^{-1})	Re_H	DR (%)	μ_w (mPa s)	u_τ (mm s^{-1})	δ_v (µm)	Re_τ
0.542	6200	27	1.285	29.2	44.1	170
0.819	10500	30	1.152	40.6	28.5	260
1.094	14800	31	1.087	51.4	21.2	350
1.371	19300	32	1.047	61.8	17.0	440
1.647	23800	33	1.021	72.1	14.2	530
1.924	28300	33	1.002	82.2	12.2	610
2.197	32800	33	0.988	92.3	10.7	700

Table 8.2: Flow properties for channel flow of 170 ppm XG solution.

8.3 Steady shear viscosity

Shear viscosity μ versus shear rate $\dot{\gamma}$ was measured for water and the 170 ppm XG solution using the torsional rheometer depicted in §4.1.1 and figure 4.1. Two geometries were used, the double-gap (DG) concentric cylinder shown in figure 4.2(*b*) for low to moderate $\dot{\gamma}$ and a parallel plate (PP) geometry shown in figure 4.2(*c*) for moderate to high $\dot{\gamma}$.

Figure 8.1(*a*) displays measurements of μ as a function of $\dot{\gamma}$ for the 170 ppm XG solution and water at 25 °C. The μ for water was measured between $\dot{\gamma}$ of 2 and 140 s^{-1} using the DG geometry and $\dot{\gamma}$ between 60 and 2000 s^{-1} using the PP geometry. For the rigid polymer solution, measurements of μ using the DG geometry are presented for 0.8 s^{-1} < $\dot{\gamma}$ < 180 s^{-1}. Results using the PP geometry were performed between $\dot{\gamma}$ of 10 and 2500 s^{-1} for the XG solution. The lower limit of $\dot{\gamma}$ for the viscosity measurements is a result of the low-torque limit of the rheometer (Ewoldt *et al.*, 2015). The upper limit is a result of secondary or inertial flow instabilities that produce an increase in the measured torque and hence tamper with the measurements of μ. In the DG geometry, the secondary instabilities are Taylor vortices, while for the PP geometry secondary instabilities are radial flows or turbulence (Ewoldt *et al.*, 2015). Davies & Stokes (2008) demonstrated that secondary flows tampered with the PP measurements when the Reynolds number $Re_{pp} = \rho \Omega R_{pp} h_{pp}/\mu$ was greater than 100. Here Ω is the angular velocity of the upper plate in radians per second. Therefore, measurements of μ using the PP geometry with $Re_{pp} > 100$ were disregarded. Measurements using the PP geometry at low h_{pp} can also be subjected to errors caused by gap offsets and surface tension (Davies & Stokes, 2008; Johnston & Ewoldt, 2013; Ewoldt *et al.*, 2015). Appendix A.2 critically evaluates the consistency in measurements of μ for different gap heights and with alterations in the surface tension of the fluid by adding a small amount of TWEEN 20 to the XG solution. The measurements of μ were consistent for different h_{pp}, the $Re_{pp} = 100$ conservatively predicted the onset of inertial instabilities for different h_{pp}, and TWEEN 20 had little influence on the measurements of μ. Based on the results presented in Appendix

A.2, it can be concluded that gap offset errors were minimal, the assumed inertial limitation from (Davies & Stokes, 2008) was valid, and surface tension did not corrupt the measurements of μ.

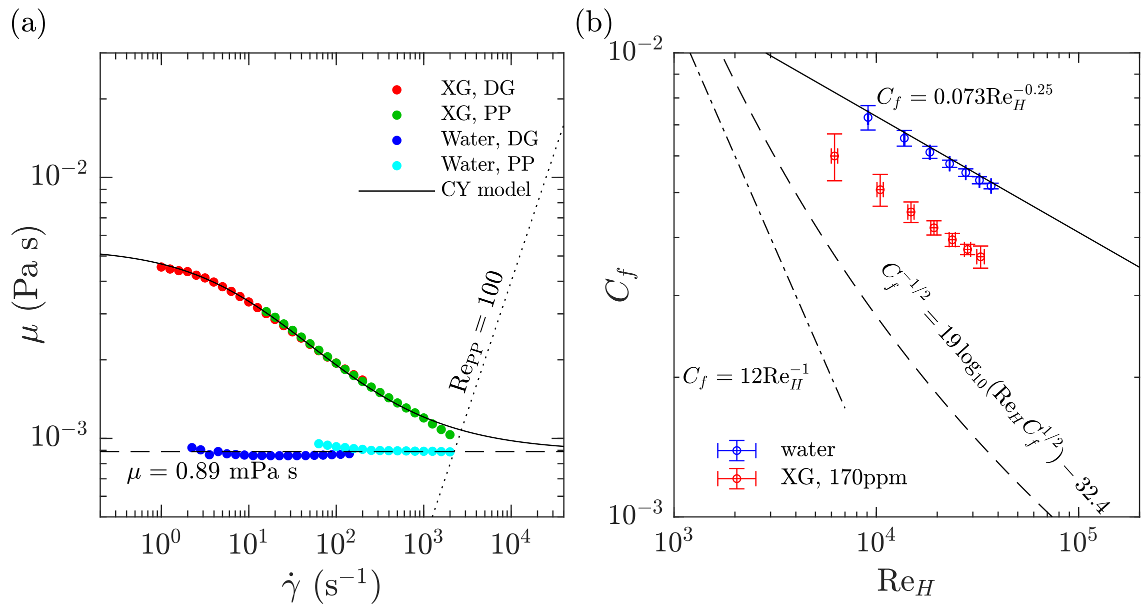

Figure 8.1: (*a*) Steady shear viscosity measurements of 170 ppm XG solution and water. (*b*) Skin friction coefficient as a function of Reynolds number for water and the 170 ppm XG solution.

The average and standard deviations in measurements of μ for water were 0.86 mPa s ± 3.2%. The average value of μ for water was approximately 3.5% different from the theoretical viscosity of water at 25 °C, i.e., 0.89 mPa s (Nagashima, 1977; Collings & Bajenov, 1983). Therefore, a 3.5% relative systematic uncertainty was assumed for all measurements of μ, including measurements of the XG solution. This uncertainty propagates to other variables, including those used for inner normalization of flow velocity. The trend in μ as a function of $\dot{\gamma}$ for the XG solution, shown in figure 8.1(*a*), was well approximated by the Carreau-Yasuda (CY) model, represented by equation (7.2) (Carreau, 1972; Yasuda *et al.*, 1981). A Levenberg-Marquardt nonlinear least-squares method was used to fit equation (7.2) to the measurements of μ as a function of $\dot{\gamma}$ in MATLAB. The resulting CY fit for the XG solution had a μ_0 of 5.4 mPa s, μ_∞ of 0.89 mPa s, M of 0.11 s, k of 0.55 s, and a of 0.67. Equation (7.2) with these values is shown for reference in figure 8.1(*a*) by the black solid line. The root mean square (rms) in the absolute deviation between the measurements and the CY model was 0.05 mPa s. The rms of the relative deviation was 2.1%. This was considered a relative random uncertainty in the measurements of μ for XG. Together with the 3.5% systematic uncertainty assumed from our viscosity measurements of water, the total relative uncertainty in our measurements of μ for XG was conservatively assumed to be 5.6%.

8.4 Skin friction coefficient and drag reduction

Plots of the skin friction coefficient C_f as a function of Re_H are shown for water and XG in figure 8.1(*b*). To determine C_f for the XG flows, the wall shear stress had to first be established. The τ_w of each rigid polymer flow condition was derived based on measurements of ΔP, i.e., (3.5). The near- wall shear rate $\dot{\gamma}_w$ was determined invoking the CY model coupled with pressure drop measurements by substituting $\mu_w = \tau_w/\dot{\gamma}_w$ into the left-hand side of equation (7.2) and using τ_w from (3.5), after which the values of $\mu_w = \tau_w/\dot{\gamma}_w$ of each XG flow were determined. Subsequently, the variables Re_H, u_τ, δ_v, and Re_τ were obtained, all of which are listed in table 8.2 for the rigid polymer flows. The resulting values of Re_H were then used in plots of C_f shown in figure 8.1(*b*). Error bars in the data points of C_f as a function of Re_H propagate from random errors in measurements of U_b and ΔP, as well as the assumed uncertainty in μ_w determined in the preceding section.

Measurements of C_f for water and XG show consistency with previous investigations. Equation (3.9), shown at the top of figure 8.1(*b*), is the empirical correlation relating C_f and Re_H for two-dimensional (2D) Newtonian turbulent channel flows prescribed by Dean (1978). The current measurements of C_f for water agree well with the equation derived by Dean (1978) and are within 5% of the C_f power-law equation. The lower equation shown in figure 8.1(*b*) is the Virk *et al.* (1970) MDR asymptote (3.15). The measurements of C_f for the XG flows are between the C_f correlations of Dean (1978) and Virk *et al.* (1970). Therefore, the XG flows do exhibit DR; however, none of the drag-reduced flows are at MDR. The C_f measurements for XG also reasonably agree with the expected trend for flows of type B drag-reducing additives with increasing Re_H. Virk & Wagger (1990) detailed that type B additives exhibit a ladder effect, where the trend in C_f as a function of Re_H would be lower but parallel to the Newtonian C_f correlation equation. In figure 8.1(*b*) a trend in C_f for XG that is approximately parallel to the Dean (1978) correlation with increasing Re_H can be observed. Drag-reduction was quantified by the attenuation in τ_w of the polymer solution relative to a turbulent Newtonian flow of a similar Re_H. The level of attenuation in C_f was described by the percent drag reduction DR, represented by equation (3.14). Values of DR were determined for each flow condition of XG, the values for which are listed in table 8.2.

8.5 Planar particle image velocimetry

Planar PIV was used to characterize the velocity of the Newtonian and non-Newtonian channel flows. Images were collected using a digital camera (Imager Intense, LaVision GmbH) with a 1376×1040 pixel^2 charged-coupled device sensor. Each pixel was 6.45×6.45 µm^2 in size with a digital resolution of 12 bits. A reduced sensor size of 1376×605 pixel^2 was used to enable a higher image acquisition rate and therefore a faster convergence in velocity statistics. A Sigma lens with a focal length f of 105 mm and an aperture size of $f/8$ was used to focus on the full height of the channel at its midspan. The resulting magnification was 0.55, the depth of field was 1.30 mm, and the scaling factor was 11.81 µm pixel^{-1}. Figure 8.2 illustrates the flow measurement setup relative to the test section. The camera was arranged in a portrait orientation such that the 1376 pixel dimension of the sensor was parallel to the height of the channel. Therefore, the field of view (FOV) of the images was $(\Delta x, \Delta y) = 12.28 \times 16.25$ mm^2. Along the x-direction, the center of the FOV was placed at the center of the glass test section, which is $107H$ downstream of the channel inlet. The illumination source for the planar PIV measurements was a 90 mJ pulse^{-1} Nd:YAG laser (Gemini PIV 30, New Wave Research Inc.). Two spherical lenses (one concave, the other convex) and one concave cylindrical lens expanded the 4.5 mm diam beam output from the laser head into a 20 mm wide (along the

x-direction) by 1-mm-thick (along the z-direction) laser sheet at the measurement location. Silver-coated hollow glass spheres, 2 µm in diameter, were used to seed the flows (SG02S40 Potters Industries). Das & Ghaemi (2021) demonstrated that these small silver-coated particles have strong side scattering and relatively consistent sizing. Synchronization between the camera and the laser was achieved using a programmable timing unit (PTU 9, LaVision GmbH) and DaVis 7.3 software (LaVision GmbH). One data set consisted of 9000 pairs of double-frame images, recorded at an acquisition rate of 7.4 Hz. The time delay Δt between image frames was 50–400 µs depending on the Re_H of the flow. The specific value of Δt was chosen such that the maximum particle displacement between image frames was approximately 12 pixels.

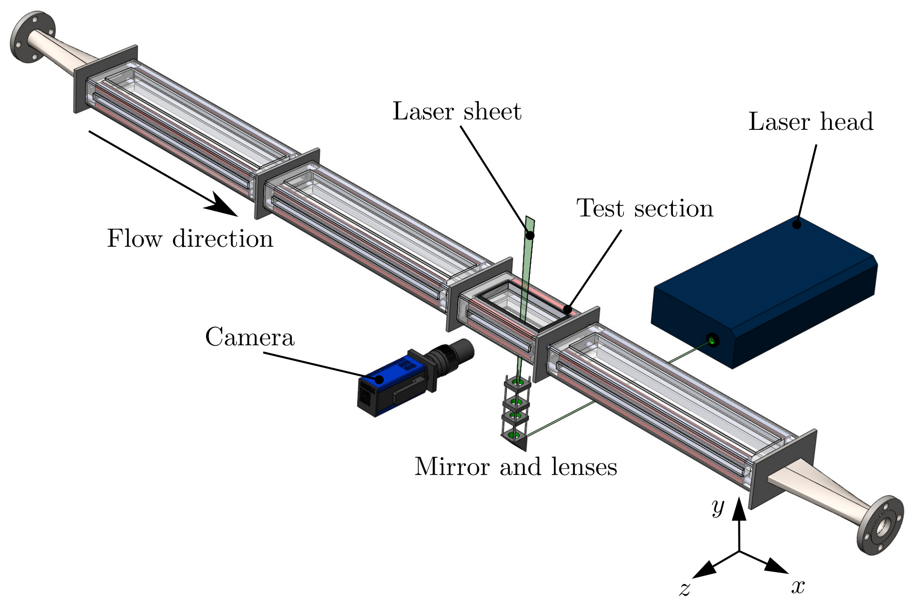

Figure 8.2: Isometric three-dimensional model of the planar PIV setup relative to the glass test section and channel section.

All PIV processing was performed using DaVis 8.4 software (LaVision GmbH). First, the minimum intensity of all images was subtracted from each image. Next, each data set was normalized with their respective average ensemble intensity. The instantaneous velocity vector was defined as U. Its components along the streamwise and wall-normal directions were defined as U and V, respectively. Angular brackets were used to denote the ensemble average of the variables over time and the x-direction. The latter averaging is applied due to the homogeneity of the fully developed turbulent channel flows in the streamwise direction. Fluctuations in the streamwise and wall-normal velocities were denoted by u and v, respectively. High spatial resolution profiles of mean streamwise velocity $\langle U \rangle$ were established using the ensemble-of-correlation method with a final interrogation window (IW) size of 6×6 pixel^2 (0.07×0.07 mm^2) and 83% overlap between neighboring IWs (Kähler *et al.*, 2012). The resulting profiles of $\langle U \rangle$ had a single pixel spatial resolution ($0.3\delta_\nu - 1.5\delta_\nu$, depending on Re_H). The lower limit of the measurements in $\langle U \rangle$ was y = 35 µm, which corresponds to $y^+ = 0.76 - 3.15$, depending on Re_H. The instantaneous velocities U and V were determined using a multipass cross-correlation algorithm with an initial IW size of 64×64 pixel^2

and a final IW size of 32×32 pixel^2 (0.38×0.38 mm^2), both with 75% overlap between adjacent IWs. The spatial resolution of instantaneous velocity measurements was 8 pixels or 0.09 mm ($2\delta_v - 12\delta_v$). Vector postprocessing using the universal outlier detection algorithm developed by Westerweel & Scarano (2005) was used to remove any spurious vectors in the measurements of U and V, after which the Reynolds normal stresses $\langle u^2 \rangle$ and $\langle v^2 \rangle$ and the Reynolds shear stress $\langle uv \rangle$ were determined. All first- and second-order velocity statistics attained reasonable statistical convergence with minimal random errors, as demonstrated in Appendix A.3.

The wall location was determined based on the local intensity maximum I_{max} that forms due to the glare line of the wall in the average intensity distribution of the PIV images. The uncertainty in the wall location was considered to be the extent of the high-intensity glare, which was assumed to be the Δy separating I_{max} and I_{max}/e^2 (Abu-Rowin *et al.*, 2017). The corresponding uncertainty in the wall location was estimated to be approximately 3 pixels or 35.4 µm ($0.8\delta_v - 4.4\delta_v$). Errors in the wall location were treated as an uncertainty in y and were a contributing factor to the error bars in wall-normal distributions of mean velocity and Reynolds stresses.

Variables scaled using inner normalization were identified with the superscript +. Velocity statistics were normalized with the friction velocity u_τ, positional coordinates were normalized with the wall units δ_v, and viscosity variables were normalized by the wall viscosity μ_w, as listed in tables 8.1 and 8.2. Error propagation was used to derive the uncertainties in u_τ and δ_v based on the assumed errors in μ (see §8.3) and random errors in ΔP. A conservative 0.1 pixel uncertainty in the PIV measurements of U and V was also assumed (Raffel *et al.*, 2018). Such uncertainties in the inner scaling variables and the velocity measurements were reflected by error bars in plots of $\langle U \rangle^+$, $\langle u^2 \rangle^+$, $\langle v^2 \rangle^+$, and $\langle uv \rangle^+$.

8.6 Flow field analysis

Assuming the present XG solution follows the shear thinning trend shown in figure 8.2(a), an approximation for the 2D instantaneous distribution of μ was obtained within the turbulent channel flow using the following procedure. First, a 2D version of the strain rate, $\dot{\gamma} = (2\mathbf{D} : \mathbf{D})^{1/2}$, was determined. Here $\mathbf{D} = (\nabla \boldsymbol{U} + \nabla \boldsymbol{U}^\dagger)/2$, is the rate of strain tensor, the dagger symbol, †, denotes a matrix transpose, and the colon operator represents the double dot product of the rank two tensors. Considering the PIV vectors were 2D, $\dot{\gamma}$ was determined using U and V alone, i.e. $\dot{\gamma} = [2((\partial U/\partial x)^2 + 1/2(\partial U/\partial y + \partial V/\partial x)^2 + (\partial V/\partial y)^2)]^{1/2}$. Therefore, our version of $\dot{\gamma}$ was an approximation that does not take into account spanwise velocity, W, or spatial gradients along the spanwise direction. A moving second-order polynomial plane with a size of 40×40 pixels, or 0.45×0.45 mm^2, was fit along instantaneous distributions of U and V. Each 2D polynomial function was differentiated to obtain the spatial gradients in the velocity, i.e. $\partial U/\partial x$, $\partial U/\partial y$, $\partial V/\partial x$, $\partial V/\partial y$. The 2D instantaneous distribution of μ was then established by substituting $\dot{\gamma}$ into the CY model or equation (7.2), that relates shear viscosity to shear rate for the XG solution. Time-averaging was performed on the instantaneous viscosity profile to obtain a mean viscosity, $\langle \mu \rangle$, and fluctuating viscosity, $\mu' = \mu - \langle \mu \rangle$, similar to those derived in DNS using GN constitutive models (Singh *et al.*, 2017, 2018; Arosemena *et al.*, 2020, 2021). After which, plots of the inner-normalized mean viscosity, $\langle \mu \rangle^+ = \langle \mu \rangle / \mu_w$, and the inner-normalized standard deviation of the viscosity, $\mathcal{R}(\mu)^+ = \sqrt{\langle \mu'^2 \rangle}/\mu_w$ were determined. A two-point correlation of μ'

was used to characterize the length scale of the viscosity fluctuations. The correlations coefficient, $R_{\mu'\mu'}$ can be represented by the following equation,

$$R_{\mu'\mu'}(\Delta x, \Delta y) = \frac{\langle \mu'_{x_0,y_0}\, \mu'_{x_0+\Delta x, y_0+\Delta y}\rangle}{\sqrt{\mu'^2_{x_0,y_0}}\,\sqrt{\mu'^2_{x_0+\Delta x, y_0+\Delta y}}}, \tag{8.1}$$

where (x_0, y_0) is the streamwise and wall-normal coordinate of the reference point and Δx, Δy represent the spatial shift along the *x*- and *y*-directions. Two reference points were considered, the first being (x_0, y_0) = (0.1h, 0.07h), and the second being (x_0, y_0) = (0.1h, 0.42h).

Assuming the GN constitutive model holds for XG, and the 2D approximation of $\dot{\gamma}$ is appropriate, the inner-normalized mean stress, τ^+, across the half channel can be determined based on,

$$\tau^+ = \tau_v^+ + \tau_v'^+ - \langle uv\rangle^+, \tag{8.2}$$

where $\tau_v^+ = \langle\mu\rangle^+\partial\langle U\rangle^+/\partial y^+$ is the mean viscous stress, and $\tau_v'^+ = 2\langle\mu'^+ d_{xy}^+\rangle$ is the turbulent viscous stress, named by Singh *et al.* (2017). Note that $\mathbf{d} = \mathbf{D} - \langle\mathbf{D}\rangle$, is the fluctuating component of the rate of deformation tensor, and $d_{xy} = (\partial u/\partial y + \partial v/\partial x)/2$. When normalized, $d_{xy}^+ = d_{xy}\delta_v/u_\tau = d_{xy}/\dot{\gamma}_w$. Alternatively, the mean shear stress can be equally represented as $\tau^+ = 1 - y^+/Re_\tau$. Previous investigations have denoted $\tau_v'^+$ as a "polymer stress", estimated from the deficit $\tau_v'^+ = \tau^+ - \tau_v^+ + \langle uv\rangle^+$ (Warholic *et al.*, 1999*b*; Ptasinski *et al.*, 2003). Given that all components listed in equation (8.2) can be explicitly determined, the CY shear thinning GN constitutive equation can be used to establish $\tau_v'^+$ and comment on its contribution to τ^+.

Another component of our analysis involved a spatial gradient in the mean velocity profile along y, i.e. $\partial\langle U\rangle/\partial y$. To remove high frequency experimental noise and to differentiate the profile, a moving second-order polynomial filter was applied to the distribution of $\langle U\rangle$ with respect to y. The length of the filter was 24 pixel or 283 µm ($6\delta_v$-$35\delta_v$, depending on Re). Coefficients of the fitted second-order polynomial were used to calculate $\partial\langle U\rangle/\partial y$, and then established the indicator function, $\zeta = y^+\partial\langle U\rangle/\partial y^+$. Calculating $\langle\mu\rangle$ near the wall is limited by the spatial resolution of measurements in U and V. Better spatial resolutions were achieved in $\langle U\rangle$ due to the utilization of the ensemble-of-correlation method. To approximate $\langle\mu\rangle$ near the wall it was assumed that the dominant component of $\dot{\gamma}$ very close to the wall was $\partial\langle U\rangle/\partial y$. The wall-normal gradient in the mean viscosity was then substituted into the CY model to obtain an approximation of $\langle\mu\rangle$ near the wall. This is an assumption; one that is rather bold for a turbulent flow. As such, these profiles were denoted a "pseudo-mean viscosity," and is indicated by $\tilde{\mu}$.

8.7 Newtonian turbulent channel flow

The following section begins by comparing measurements of the mean velocity profiles for water with the Newtonian law of the wall in figure 8.3. For brevity, only experimental data for water with a Re_τ less than or equal to 620 are plotted. These conditions of Re_τ were chosen because they are similar in magnitude to the Re_τ conditions of the XG flows listed in table 8.2. Following the plots of $\langle U\rangle^+$, measurements of the Reynolds stresses for water are shown in figure 8.4. Three experimental Reynolds stress profiles with Re_τ of 270, 390 and 510 are presented on the same axes as the Reynolds stresses derived from Newtonian channel

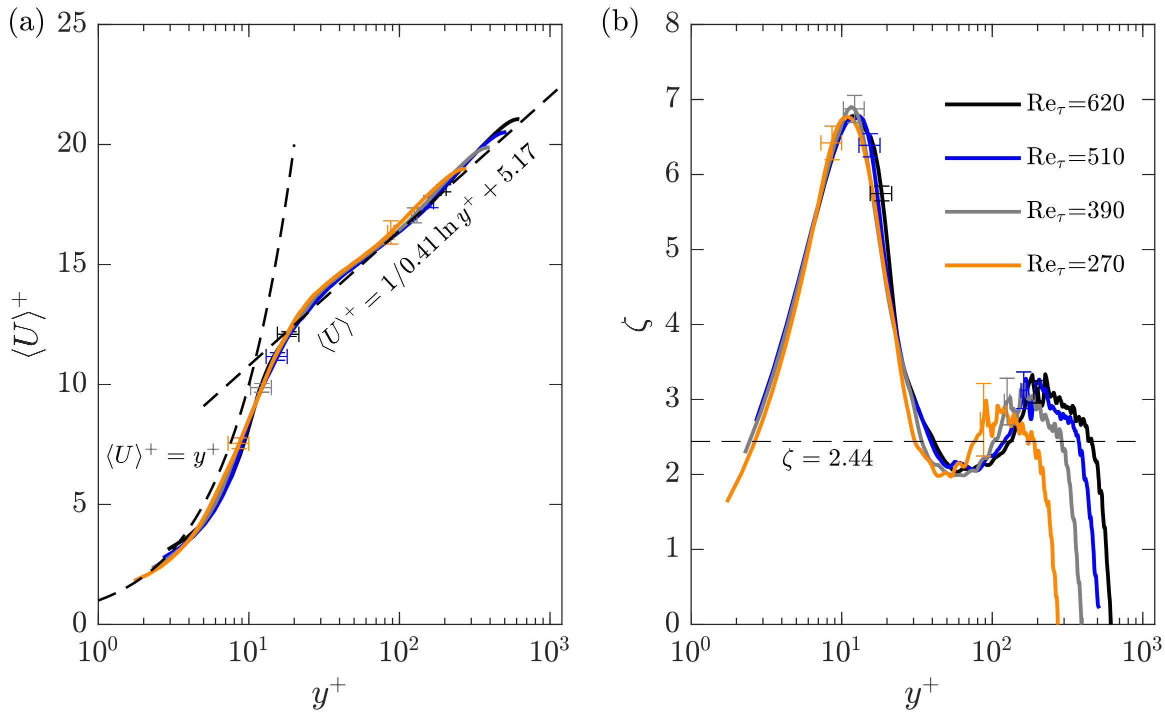

Figure 8.3: Inner-normalized distributions of (a) mean streamwise velocity and (b) the indicator function, for Newtonian flows.

flow DNS by Iwamoto *et al.* (2002) at $Re_\tau = 300$ and Lee & Moser (2015) at $Re_\tau = 550$. The error bars in figures 8.3 and 8.4 are a result of uncertainties propagating from μ, ΔP, U and y. For clarity, only two error bars are shown for each profile, one approximately in the buffer layer, the other within the outer layer.

Figure 8.3(a) demonstrates that all experimental profiles of water show good agreement with the law of the wall. The profiles were limited to $y > 35$ µm, which corresponds to $y^+ = 1.29$ to 2.89, for Re_τ between 270 and 620. For $y^+ < 5$ and greater than their respective lower limit, experimental measurements overlap with the profile of the linear viscous sublayer, $\langle U\rangle^+ = y^+$. Farther from the wall, all of the experimental distributions in figure 8.3(a) overlap with the log law, $\langle U\rangle^+ = 1/\kappa \ln y^+ + B$. A Von Kármán constant, κ, of 0.41 and intercept, B, of 5.17, as prescribed by Dean (1978) for 2D Newtonian channel flows, is shown for comparison. Distributions of ζ shown in figure 8.3(b) accentuate the logarithmic dependence of $\langle U\rangle^+$ with respect to y^+. The profiles of ζ imply that κ is larger than 0.41 in the logarithmic layer for all profiles of water. Comparing the experimental profiles of $\langle U\rangle^+$ for different Re_τ, all distributions appear to overlap with one another within the boundaries of measurement uncertainties. The DNS of a Newtonian channel flow by Lee & Moser (2015) demonstrated that profiles of $\langle U\rangle^+$ over a wider Re_τ range of 180 to 5000 also overlapped. The current experimental results for water also reflect universality in their distributions of $\langle U\rangle^+$ and ζ among different Re_τ.

Figure 8.4(a) presents experimental profiles of $\langle u^2\rangle^+$ relative to Newtonian channel flow DNS. For water with a $Re_\tau = 510$, instantaneous PIV measurements with IWs of 32×32 pixels and 75% overlap, translates to a spatial resolution of $7.8\delta_v$. As a result, the linear viscous sublayer and a portion of the buffer layer is missed in these measurements. However, for lower Re_τ the spatial resolution of the measurements improve. The scenario with $Re_\tau = 270$ has a spatial resolution of $3.5\delta_\nu$ and has measurements that extend to wall-normal locations as small as $y^+ = 9$. Within the logarithmic and outer layers, the experimental results overlap with their DNS counterparts at similar Re_τ. The moderate $Re_\tau = 390$ case demonstrates consistency, considering it lies between the two DNS and experimental profiles at lower and higher Re_τ. Figure 8.4(b) shows experimental and DNS profiles of $\langle v^2 \rangle^+$ and $\langle uv \rangle^+$. Similar to the distributions in $\langle u^2 \rangle^+$, experimental profiles in $\langle v^2 \rangle^+$ and $\langle uv \rangle^+$ agree well with the DNS results at similar Re_τ. However, there are some small discrepancies. For example, the experimental profile of $\langle v^2 \rangle^+$ at $Re_\tau = 510$ appears to be minutely larger than the DNS profile of $\langle v^2 \rangle^+$ at $Re_\tau = 550$ for $y^+ > 100$. Overall, the experimental mean velocity and Reynolds stress measurements show consistency and agreement with 2D Newtonian channel flow DNS. Therefore, subsequent results of the non-Newtonian solution can be presented with relatively good confidence in the validity of the measurements. It should also be noted that the spatial resolution of the measurements will improve with the addition of polymers, considering DR is coupled with a reduction in u_τ and an increase in δ_ν. This can be observed by comparing the larger values of δ_ν for XG flows with the δ_ν values of water in tables 8.1 and 8.2.

8.8 Non-Newtonian turbulent channel flow

The current section investigates the turbulent flow of the XG solution with varying Re_τ. The section is divided into three portions. The first subsection presents wall-normal distribution of the mean velocity profile, $\langle U \rangle^+$, indicator function, ζ, and pseudo-viscosity profile, $\tilde{\mu}$, obtained from the vector fields with high-spatial-resolution. The second subsection investigates spatial distributions of the viscosity derived from the 2D shear rate. Lastly, the final subsection delves into the Reynolds stresses and viscous stresses of non-Newtonian flows at different Re_τ.

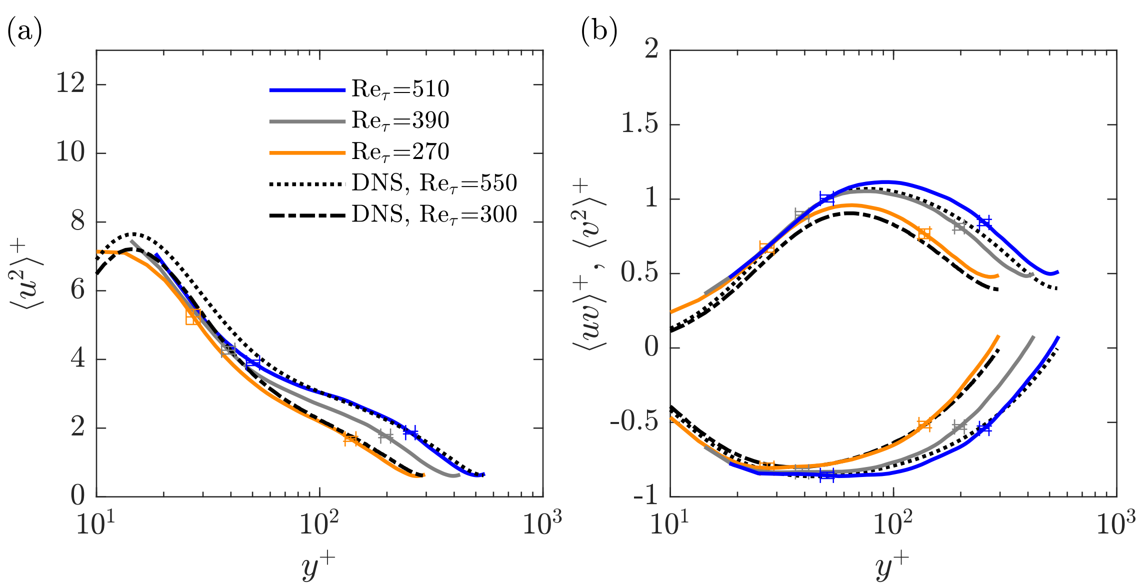

Figure 8.4: Inner normalized profiles of (a) streamwise Reynolds stress, (b) wall-normal and Reynolds shear stresses, for Newtonian flows.

8.8.1 Mean velocity profile

Profiles of $\langle U\rangle^+$ for the XG scenarios are shown in figure 8.5(a). Near the wall, experimental distributions of $\langle U\rangle^+$ conform well with the linear viscous sublayer profile, $y^+ = \langle U\rangle^+$, for all Re_τ under consideration. The upper limit of the linear viscous sublayer appears to grow relative to Newtonian wall turbulence. For a Newtonian turbulent channel flow, the linear approximation of the viscous sublayer is valid to within 10% at $y^+ = 5$ (Pope, 2000). If a 10% confidence interval from $y^+ = \langle U\rangle^+$ is used as a threshold, the size of the linear viscous sublayer for the non-Newtonian profiles shown in figure 8.5(a) can be approximated. The following table 8.3 lists the size of the linear viscous sublayer for the flows, both in inner- and outer-scaling. The size in inner-scaling is denoted, y_v^+, while the size in outer-normalization is y_v/h. All values of y_v^+ are between 8 and 12, demonstrating that the linear viscous sublayer is expanded relative to Newtonian wall turbulence, which has a y_v^+ between 3 and 5 (Pope, 2000). With increasing Re_τ, the non-Newtonian values of y_v^+ increase subtly, implying that the very near wall profiles might be slightly different, and potentially depend on the small increase in DR with increasing Re_τ, as shown in table 8.2. However, with error bars, these differences could be a result of uncertainty in the measurements. At the larger Re_τ, between 530 and 700, the linear sublayer appears to saturate and nearly approach the tri-section point, $(y^+, \langle U\rangle^+) = (11.6, 11.6)$, where the Virk MDR asymptote, equation (3.16), intersects with $y^+ = \langle U\rangle^+$ and the Newtonian log law. Values of the outer-scaled thicknesses, y_v/h, decrease with increasing Re_τ, mainly due to the large shrinkage in y_v caused by increasing Re_τ.

Farther from the wall at $y^+ > 30$, figure 8.5(a) demonstrates a larger $\langle U\rangle^+$ relative to the logarithmic

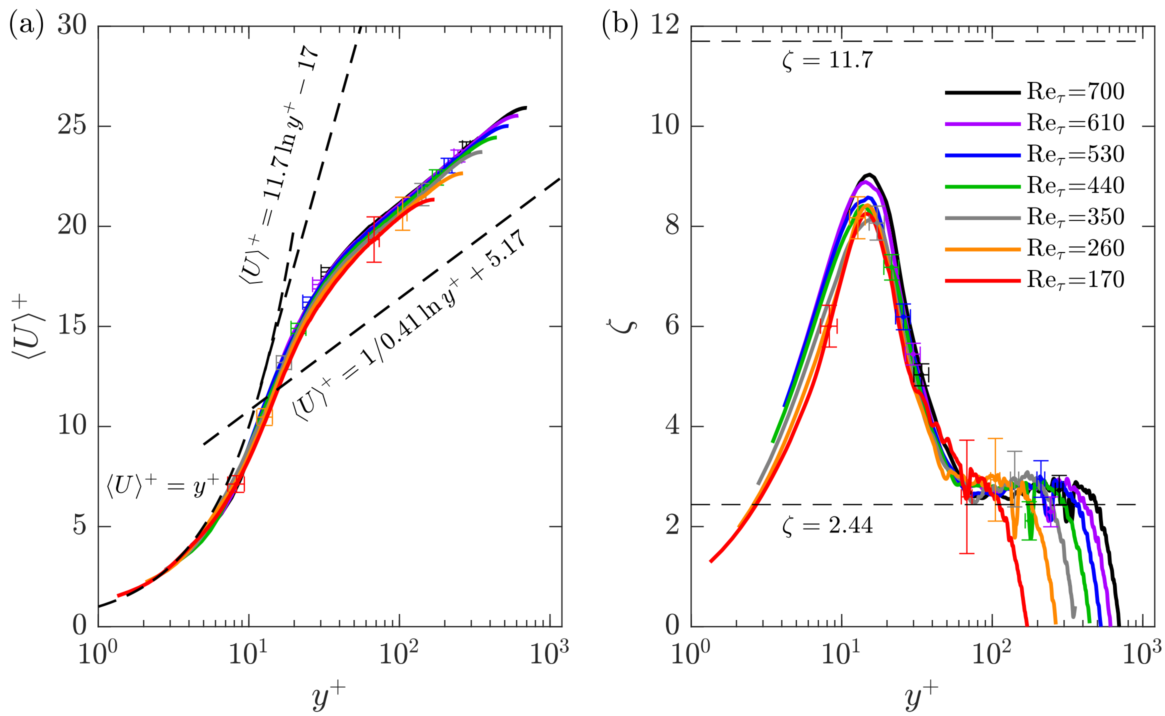

Figure 8.5: Inner-normalized distributions of (a) mean streamwise velocity and (b) the indicator function, for flows with 170ppm XG solution.

Re_τ	y_v^+	y_v/h
170	8.3	0.051
260	9.1	0.036
350	10.1	0.030
440	10.8	0.025
530	11.5	0.023
610	11.2	0.019
700	11.4	0.017

Table 8.3: Linear viscous sublayer sizes for non-Newtonian flows in inner- and outer-scaling.

law of the wall; an observation common for drag-reduced flows. Virk (1971), and later Warholic *et al.* (1999*b*), demonstrated that LDR flows form a Newtonian plug profile, which is observed as an increase in the log law intercept, B, but a similar κ, relative to the log law distribution of a Newtonian fluid. Virk (1971) detailed that the growth in B was proportional with DR. A larger DR would result in an increased buffer layer thickness (deemed the elastic sublayer) and hence an enhancement in B. Findings from Warholic *et al.* (1999*b*) showed that a Newtonian plug exists only for LDR flows with $DR < 35\%$. Given DR of the present XG flows are between 27-33% (see table 8.2), the current XG flows satisfy the criteria for LDR. Therefore, our measurements agree well with previous observations of $\langle U \rangle^+$ profiles for polymer drag-reduced LDR flows. Furthermore, figure 8.5(*a*) demonstrates that profiles of $\langle U \rangle^+$ for XG have little dependence on Re_τ. There is perhaps a subtle increase in B for $170 < Re_\tau < 440$; however, this could be attributed to the small growth in DR with increasing Re_τ. The uncertainty in the flow measurements, shown by the error bars, also captures the small variations in B.

White *et al.* (2012) re-evaluated the efficacy of the Virk (1971) elastic sublayer model using the indicator function, ζ, which highlights regions of strong logarithmic dependence. They compared mean velocity profiles from various experimental and numerical investigations of different DR, canonical flows and Re_H. For LDR flows, White *et al.* (2012) observed constant ζ (generally for $y^+ > 50$), which is indicative of a Newtonian plug. Profiles of ζ shown in figure 8.5(*b*) also demonstrate regions of constant ζ, providing further evidence of a Newtonian plug for rigid polymer solutions. For all Re_τ, these regions of constant ζ are observed for $y^+ > 60$. This lower limit of $y^+ = 60$ is larger than the lower limit of $y^+ = 30$ for the Newtonian log layer (Pope, 2000), demonstrating an expansion of the viscous sublayer. The peak values of ζ for XG at $y^+ = 15$ is greater than the peak values of ζ for water as seen in figure 8.3(*b*). The implication is that the slope of $\langle U \rangle^+$ within the buffer layer is larger for flows of XG relative to water. A larger slope in $\langle U \rangle^+$ is indicative of an “effective slip” in the buffer layer which, in turn, results in an increase in $\langle U \rangle^+$ within the logarithmic layer Lumley (1969); Virk (1971). Another observation is that the constant value of ζ for the XG flows in the Newtonian plug layer, are marginally larger than the values of ζ observed for water in the logarithmic layer shown in figure 8.3(*b*). White *et al.* (2012) similarly observed that κ was slightly larger than water in the

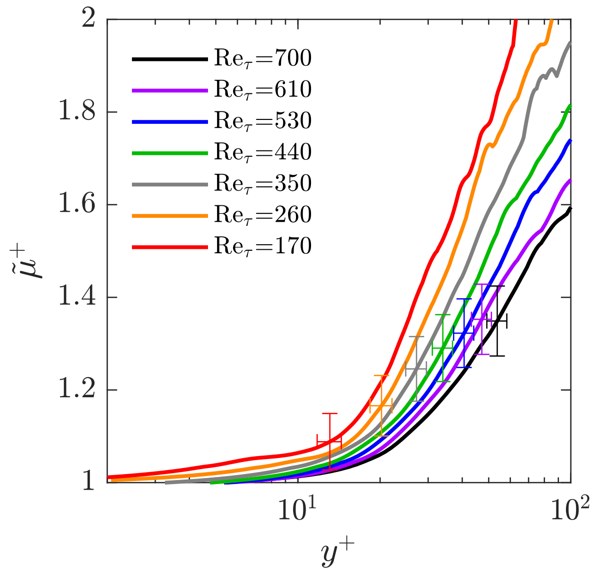

Figure 8.6: The pseudo-mean viscosity normalized by wall viscosity as a function of inner-normalized wall location.

Newtonian plug for LDR flows. White *et al.* (2012, 2018) broadly suggested that the inner-normalized mean velocity profile of a polymer drag-reduced flow depends on the Reynolds number, polymeric properties and the canonical flow. Therefore, if DR is constant distributions of the inner-normalized mean velocity profiles of a rigid polymer solution are relatively independent of Re_τ within the inner layer of the flow.

Figure 8.6 demonstrates distributions of the normalized pseudo-viscosity, $\tilde{\mu}^+$, with respect to y^+, for the XG flows of different Re_τ. The profiles of $\tilde{\mu}$ are an approximation of the mean viscosity in the near-wall region. Intuitively, the decreasing trend in $\tilde{\mu}^+$ with increasing Re_τ at a given y^+ is plausible. Flows of higher Re_τ have larger $\partial\langle U\rangle/\partial y$, hence $\tilde{\mu}$ should be correspondingly lower relative to a flow of smaller Re_τ. For $y^+ < 10$, all XG flows have distributions of $\tilde{\mu}^+$ that are approximately constant; only growing subtly by about 1% with increasing y^+. As y^+ increases beyond 10 all profiles experience a dramatic increase in the magnitude of $\tilde{\mu}^+$. The precise y^+ location where this inflection in $\tilde{\mu}/\mu_w$ occurs depends on the Re_τ being considered. The thickness of the near-wall region of approximately constant $\tilde{\mu}$ appears to conform well with the peak in profiles of ζ, shown in figure 8.5(b) and indicative of the central location of the buffer layer. The inner-normalized thickness of this region of constant $\tilde{\mu}$ grows with increasing Re_τ. However, the value of $\tilde{\mu}^+$, appears to monotonically decrease with increasing Re_τ at any chosen value of y^+. Flows of large Re_τ experience a less aggressive change in $\tilde{\mu}$ with respect to y^+, but the size of their near-wall region of low viscosity is larger. Generally, all flows experience a large and sudden change in $\tilde{\mu}$ for y^+ between of 10 and 30. For example, the XG flow with $Re_\tau = 170$ has a $\tilde{\mu}$ that is 50% larger than μ_w at $y^+ = 30$. A near wall region of constant mean viscosity that suddenly and dramatically increases with respect to y^+ has also been observed from numerical simulations using generalized Newtonian (GN) models (Singh *et al.*, 2017, 2018; Arosemena *et al.*, 2020, 2021). Our results appear to qualitatively agree with the results of DNS using inelastic shear thinning GN models near the wall (Singh *et al.*, 2017, 2018; Arosemena *et al.*, 2020). This is despite the approximation used to derive the pseudo-viscosity profile, $\tilde{\mu}$, based on 2D velocity data.

8.8.2 Turbulent shear viscosity

Figure 8.7(a) shows an instantaneous contour of u for XG with Re_τ of 170, while figure 8.7(b) shows a snapshot of μ. Contours (a) and (b) are extracted at the same time instance. In both figures 8.7(a), zones of low and high speed flow are observed. Figure 8.7(b) demonstrates that the viscosity near the wall is low and within 20% of μ_w for $y/h < 0.2$. Away from the wall, $y/h > 0.2$, most of the fluid has a μ between 1.5 to 3 times larger than μ_w. In general, the spatial distribution of μ shows large streamwise-elongated zones of low and high viscosity that contain small-scale viscosity fluctuations. For example a large, low viscosity slug can be found at around $y/h = 0.6$ and extending from $x/h = 0$ to 0.6 in the snapshot shown in figure 8.7(b). The location of this low viscosity slug appears to coincide roughly with the interface between the low and high speed zones, shown in figure 8.7(a). A second streamwise-elongated zone of low viscosity is observed extending from the wall at a shallow angle. Similarly, this low viscosity zone overlaps with the shear layer between low and high speed zones.

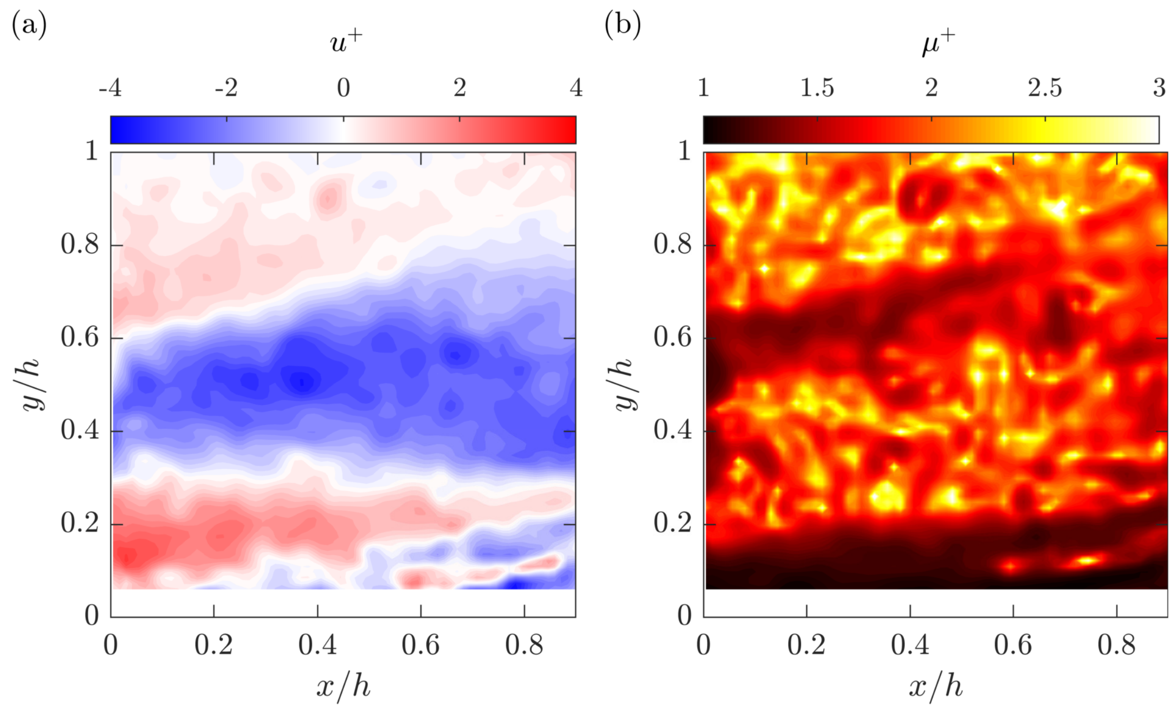

Figure 8.7: Instantaneous contour of (a) streamwise velocity fluctuations and (b) viscosity for XG at $Re_\tau = 170$.

Probability density functions (PDFs) of μ'^+ are shown in figure 8.8 for the XG flows at different Re_τ within the inner and outer layers of the flow. Figure 8.8(a) demonstrates the PDFs of μ' at y/h of 0.07. While figure 8.8(b) shows the PDFs at y/h of 0.42. Within both the inner and outer layers of the flow, PDFs of μ'^+ are positively skewed. Within the inner layer, flows with smaller Re_τ (e.g. $Re_\tau = 170$) tend to have a more narrow PDF than flows of larger Re_τ and demonstrate a smaller PDF peak. In contrast, figure 8.8(b) demonstrates that at $y/h = 0.42$, the peak PDF in μ'^+ is larger for flows of high Re_τ. This implies that viscosity fluctuations are likely larger for low Re_τ flows within the outer layer. Wall-normal profiles of $\langle\mu\rangle^+$

and rms$(\mu')^+$ better demonstrate these differences.

Figure 8.9 provides inner-normalized profiles of the mean viscosity, $\langle \mu \rangle^+$, and the rms of μ', for the non-Newtonian flows of different Re_τ. Figure 8.9(a) demonstrates that distributions of $\langle \mu \rangle^+$ appear to be logarithmic, consistent with DNS using GN constitutive models (Singh *et al.*, 2017, 2018; Arosemena *et al.*, 2020, 2021). The profiles of $\langle \mu \rangle^+$ for different Re_τ do not overlap; flows with lower Re_τ have larger $\langle \mu \rangle^+$ in the outer-layer of the flow. Figure 8.9(b) shows the inner-normalized rms profiles of μ', which also reflect a similar dependency as $\langle \mu \rangle^+$ with respect to Re_τ. Unlike the present findings of figure 8.9, Singh *et al.* (2018) observed that $\langle \mu \rangle^+$ and the rms$(\mu')^+$ overlapped for pipe flow DNS with a power law GN model. The overlap is suspected to be contingent on the choice of the rheological model, i.e. the power law model. The nominal wall viscosities listed in table 8.2, encroach on the second Newtonian regime of the CY model and are likely not well described by a power law equation. Therefore, it appears that μ_w is an insufficient scaling parameter. Nonetheless, distributions of $\langle \mu \rangle^+$ demonstrate a lower average viscosity near the surface and a substantially larger viscosity closer to the core, much like the implication of the $\tilde{\mu}^+$ profiles shown in figure 8.6.

To characterize the length scale of the viscous fluctuations, a two-point correlation of μ' using equation (8.1) was performed for each of the XG channel flows with different Re_τ. As mentioned in §8.6, two reference points were considered, the first being $(x_0,\ y_0) = (0.1h,\ 0.07h)$, and the second being $(x_0,\ y_0) = (0.1h,\ 0.42h)$. Therefore, the first point falls within the inner layer of the channel flow, while the second point is well into the outer layer of each flow ($y/h > 0.1$).

Figure 8.10(a) demonstrates distributions of the correlation coefficient, $R_{\mu'\mu'}$, along the streamwise direction, Δx, and at y/h of 0.07. Although, figure 8.10 does not observe the value of Δx at which $R_{\mu'\mu'}$ becomes zero, it can be reasonably inferred that the size of the viscosity fluctuations along the x-direction decrease in magnitude with increasing Re_τ. The same observation can be made in the outer layer based on

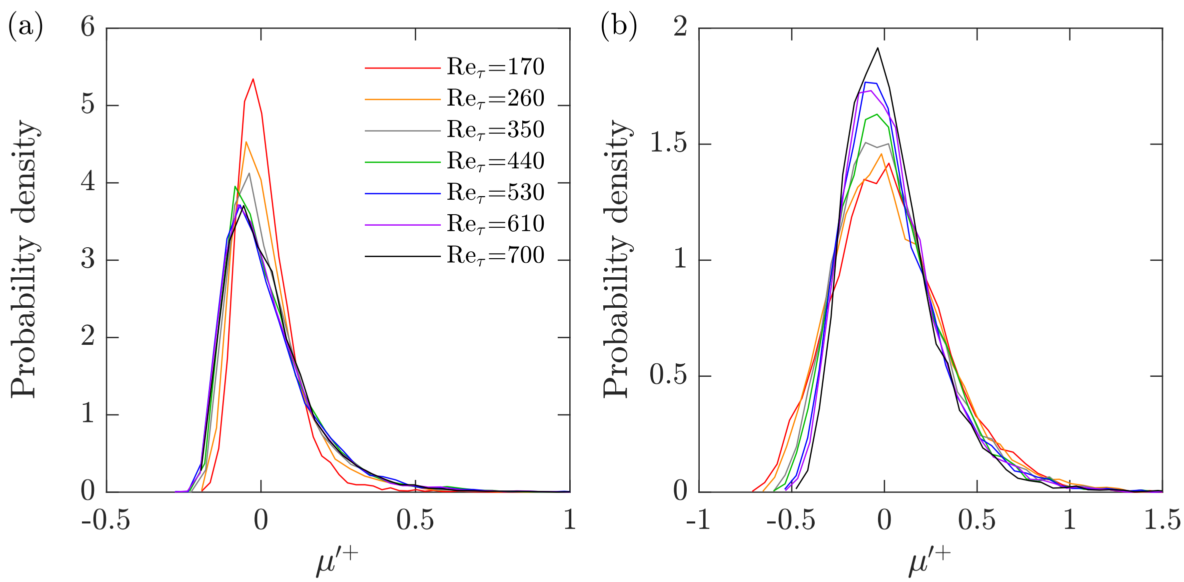

Figure 8.8: Probability density function of fluctuating viscosity taken at x of $0.1h$ and y of (a) $0.07h$, and (b) $0.42h$.

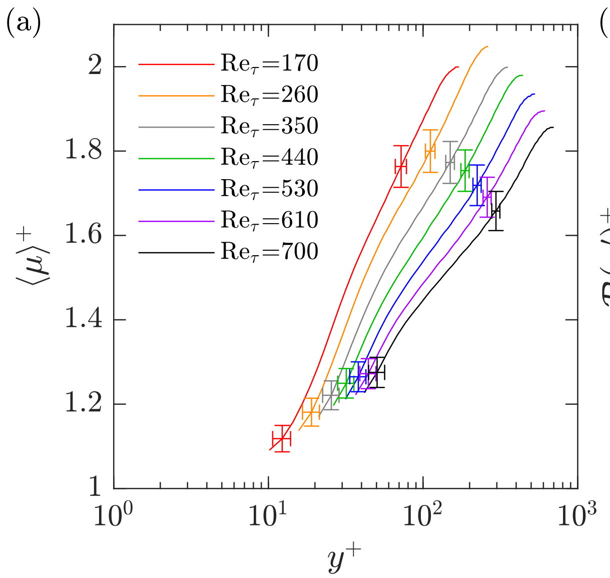

Figure 8.9: Wall-normal profiles of (*a*) mean viscosity, and (b) the root mean square of the fluctuating viscosity. Error bars are shown at y/h of 0.07 and 0.42.

plots of $R_{\mu'\mu'}$ as a function of Δx and at a constant y/h of 0.42, seen in figure 8.10(*b*). Figure 8.11 presents profiles of $R_{\mu'\mu'}$ at x/h of 0.1, and along the wall-normal direction, Δy. For all Re_τ, $R_{\mu'\mu'}$ decays to zero within $0.06h$ when y_0 is $0.07h$, as seen in figure 8.11(*a*). For lower Re_τ cases, (e.g. 170 and 260), there is a significant anti-correlation between $\Delta y/h$ of 0.06 and 0.2. The anti-correlation indicates a streaky pattern in the viscosity field, potentially generated by the shear layer structures between the streamwise elongated low and high-speed zones. It is suspected that this prevalent anti-correlation cannot be observed for large Re_τ

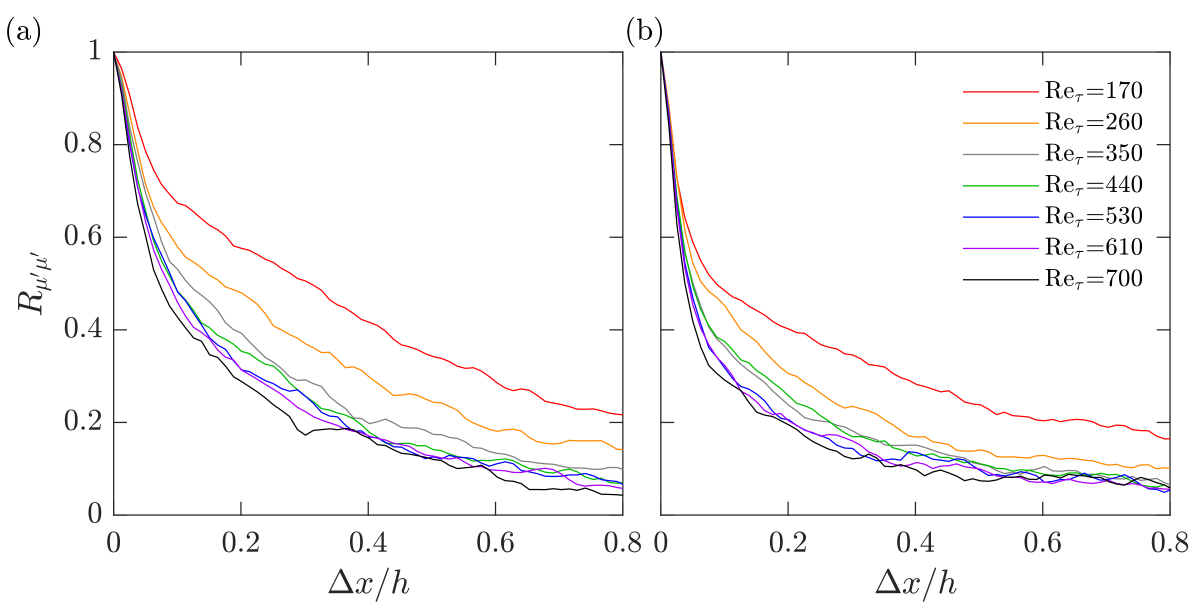

Figure 8.10: Two-point correlation of viscosity fluctuations along the streamwise direction at wall-normal locations of (*a* $y/h = 0.07$ and (*b*) $y/h = 0.42$.

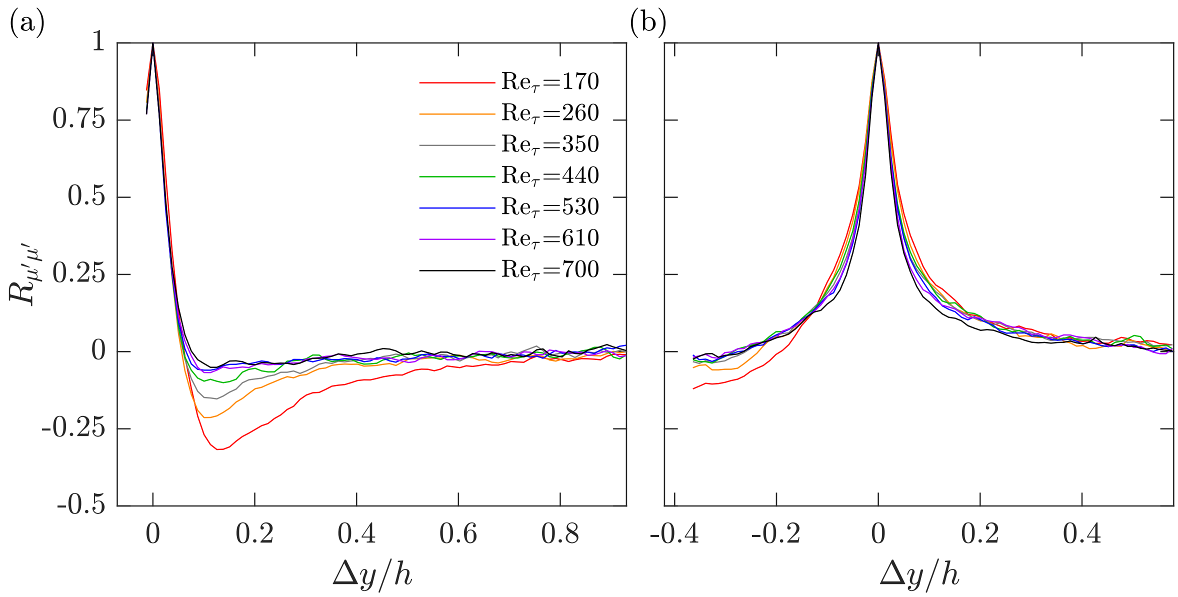

Figure 8.11: Two-point correlation of viscosity fluctuations along the wall-normal direction with a reference wall-normal location of (*a* $y_0 = 0.07h$ and (*b*) $y_0 = 0.42$.

due to the choice of y_0. For the case with the lowest Re_τ of 170, $y_0 = 0.07h$ is equivalent to a y^+ of 12, which lies near the centre of the buffer layer or the peak in ζ. For $Re_\tau = 700$, a y_0 of $0.07h$ corresponds to a y^+ of 49, which is close to the upper y^+ limit of the buffer layer. Therefore, μ' within the viscous sublayer appears to be opposite in sign convention to μ' within the log and outer regions of the flow. When y_0 is set to $0.42h$, profiles of $R_{\mu'\mu'}$ are generally the same for all Re_τ cases, seen in figure 8.11(*b*). The correlation coefficient attains a value of zero, or very close to zero (< 0.01), within Δy of $0.3h$. Based on figure 8.7(*d*), viscosity fluctuations are marginally more elongated along the x-direction relative to y. The size of the structures become more isotropic with growing distance from the wall.

8.8.3 Reynolds stresses and mean shear stress budget

Figure 8.12(*a*) presents plots of $\langle u^2\rangle^+$ for the XG flows alongside experimental data of water with $Re_\tau = 510$ and Newtonian channel flow DNS from Lee & Moser (2015) with $Re_\tau = 550$. Unlike the experimental results for water shown in figure 8.4(*a*), the peak in $\langle u^2\rangle^+$ could be resolved for at least the two lowest Re_τ scenarios, i.e. $Re_\tau = 170$ and 260. The use of XG makes resolving the peak in $\langle u^2\rangle^+$ easier, since drag-reducing additives have been shown to shift the peak in $\langle u^2\rangle^+$ farther from the wall relative to Newtonian fluids (Warholic *et al.*, 1999*b*; Escudier *et al.*, 2009). In general, the magnitude in $\langle u^2\rangle^+$ for all Re_τ scenarios is increased relative to the experimental profile for water shown in figure 8.12(*a*). The amount by which the XG profile of $\langle u^2\rangle^+$ increases depends on the Re_τ being considered. For example, comparing XG and water at similar Re_τ of 510, the XG profile of $\langle u^2\rangle^+$ is larger for nearly all y^+.

Profiles of $\langle v^2\rangle^+$ are the positive distributions shown in figure 8.12(*b*). Relative to Newtonian profiles of similar Re_τ, distributions of $\langle v^2\rangle^+$ for the XG solutions demonstrate significant attenuation along all values of y^+. This can easily be seen by comparing the plots of $\langle v^2\rangle^+$ for XG at $Re_\tau = 530$ with the experimental

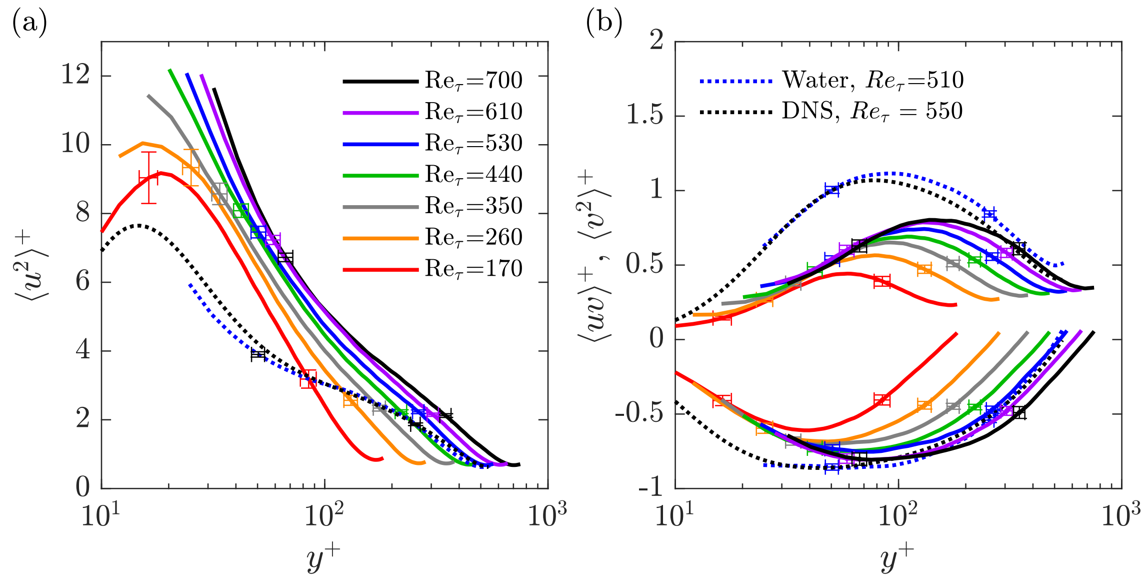

Figure 8.12: Inner normalized profiles of (a) streamwise Reynolds stress, (b) wall-normal and Reynolds shear stresses, for flows with 170ppm XG solution.

profile of water at $Re_\tau = 510$. Distributions of $\langle uv\rangle^+$ correspond to the negative profiles shown in figure 8.12(*b*). Unlike $\langle v^2\rangle^+$, profiles of $\langle uv\rangle^+$ are only strongly attenuated near the wall, relative to Newtonian distributions of comparable Re_τ. The values of $\langle uv\rangle^+$ are similar for $y^+ > 150$ when comparing XG and water at a Re_τ of 510. While for $y^+ < 150$, the XG solution shows a large reduction in the magnitude of $\langle uv\rangle^+$, when contrasted with the profile of water with a similar Re_τ of 510. Therefore, relative to Newtonian profiles of similar Re_τ, solutions of XG at LDR exhibit strong attenuation in $\langle v^2\rangle^+$ throughout the complete half-channel; however attenuation in $\langle uv\rangle^+$ is confined to a portion of the channel near the wall. Comparing the Reynolds stress profiles of XG with one another, all distributions for XG shown in figure 8.12 increase in magnitude monotonically with increasing Re_τ at a given y^+, similar to the trend in the Reynolds stresses for Newtonian fluids of increasing Re_τ.

Different components of the mean stress balance are presented in figure 8.13. For brevity and to avoid clutter, the mean stress balance is shown for only three of the seven Re_τ cases (170, 440 and 700) of XG. The XG flows exhibit a trade-off in the budget or contribution of τ_v^+ and $-\langle uv\rangle^+$ to the total mean stress, τ^+, depending on the y^+ location. Specifically, near the wall τ_v^+ contributes more to τ^+ than $-\langle uv\rangle^+$, while closer to the core of the channel, the opposite can be observed, i.e. $-\langle uv\rangle^+$ is larger than τ_v^+. For all XG flows, the turbulent viscous stress, $\tau_v'^+$, contributes little to τ^+, regardless of the y^+ location being considered. Distributions of τ^+, represented by the solid lines in figure 8.13 and determined from the summation of τ_v^+, $\tau_v'^+$ and $-\langle uv\rangle^+$ i.e., (8.2), agree well with $1 - y^+/Re_\tau$ within the margin of experimental uncertainty, represented by the down-sampled error bars. Therefore, it can be assumed that measurements of τ_v^+, $\langle uv\rangle^+$, and $\tau_v'^+$, are approximately valid. Arosemena *et al.* (2020, 2021) demonstrated that $\tau_v'^+$ accounted for less than 5% of τ^+ within the inner layer, based on DNS using a channel flow with a shear thinning GN constitutive model that had $DR \approx 10\%$. Although the present non-Newtonian flows have almost three times the DR as Arosemena et al. Arosemena *et al.* (2020, 2021), $\tau_v'^+$ also appears to be less than 5% for XG. Therefore, a drag-reduced turbulent flow of XG can largely be explained by Reynolds and viscous stresses, with very little influence from stresses imposed by the fluctuating non-Newtonian viscosity.

In summary, the rigid polymer solution demonstrates larger profiles in $\langle U \rangle^+$ within the logarithmic layer relative to water, conducive of a Newtonian plug. Non-Newtonian flows of different Re_τ and similar DR had overlapping profiles in $\langle U \rangle^+$, within the margin of measurement uncertainty. When compared to experiments of Newtonian turbulence at a similar Re_τ, XG exhibits larger profiles in $\langle u^2 \rangle^+$, and smaller profiles in $\langle v^2 \rangle^+$, for all y^+. Attenuation in $\langle uv \rangle^+$ is observable, but only near the wall. These findings share similarities with numerical investigations using inelastic models, such as the GN power-law or Carreau constitutive equations. Singh *et al.* (2018) used a power-law model to simulate an inelastic non-Newtonian turbulent pipe flow of Re_τ between 323 and 750. Constant material properties were maintained across their different cases of Re_τ to evaluate the effect of Re on the flow statistics, much like what is demonstrated in the present experimental investigation. Singh *et al.* (2018) observed a Newtonian plug for all flow conditions, profiles of $\langle U \rangle^+$ that overlapped across different Re_τ, an enhancement in $\langle u^2 \rangle^+$, attenuation in the radial and azimuthal Reynolds stresses, and a confined near wall attenuation in $\langle uv \rangle^+$, relative to a Newtonian flow of similar Re_τ. Contrasting this with experiments using flexible polymers or DNS using elastic models, such as FENE-P, the same observations can be made for mean velocity statistics of generally any LDR flow, including the current findings. Consistency in the mean velocity statistics of elastic and inelastic DR suggests that the net effect of DR using elastic or inelastic additives is the same, at least for flows at LDR. This is despite their dramatically different rheology and potentially unique mechanisms for mitigating drag.

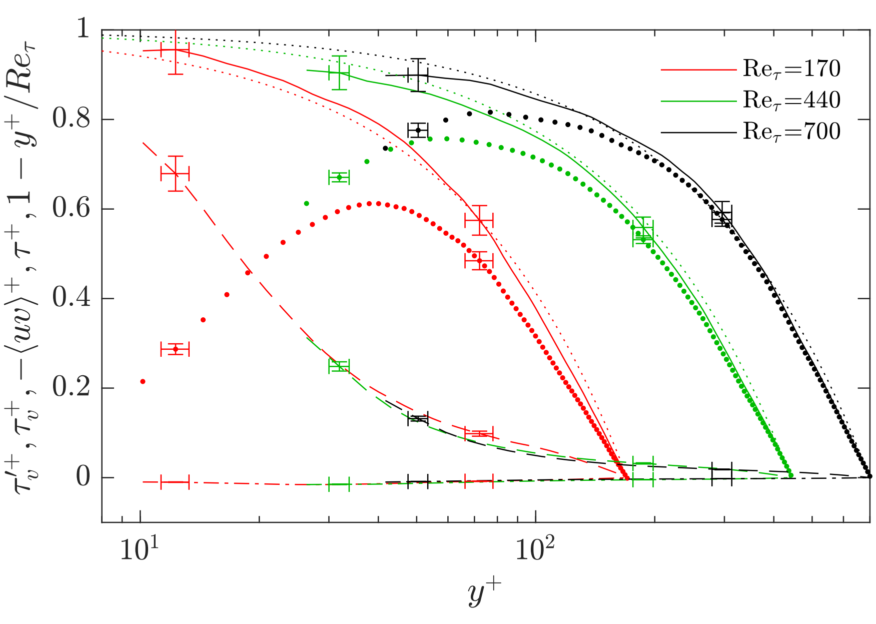

Figure 8.13: Inner-normalized mean stress balance of XG at three of the seven Re_τ conditions. The lines correspond to $\cdots$ $1 - y^+/Re_\tau$, —— τ^+, $\cdot$ $\langle uv \rangle^+$, — — τ_v^+, — $\cdot$ $\tau_v'^+$. Error bars are shown at y/h of 0.07 and 0.42.

8.9 Discussion - lubricating layer

The classical theories of polymer DR have insinuated that polymers interact with turbulence in a manner that quells regions of high strain and vorticity through either an enhanced extensional viscosity or elasticity (Lumley, 1973; de Gennes, 1990). Indeed, experiments with flexible polymers in isotropic homogeneous grid turbulence demonstrate suppression of the small scale turbulent eddies that correspond to regions of the flow with high extensional strain, and thus large extensional viscosities (Van Doorn *et al.*, 1999). However, shear thinning properties of rigid polymers work against these postulates, in that regions with large shear rates have lower viscosities, not enhanced. A comparison of isotropic turbulence using FENE-P versus inelastic shear thinning constitutive models could directly contrast the local instantaneous effect of flexible and rigid polymers on turbulence. Rather, it is argued that the phenomenon of DR for inelastic shear thinning fluids is primarily attributed to a wall-normal gradient in shear viscosity induced from the wall. Numerical investigations that employ inelastic shear thinning constitutive models seem to support this claim. Arosemena *et al.* (2021), performed channel flow DNS using an inelastic Carreau constitutive model and commented on the near wall turbulent structures within the flow. They demonstrated that forces arising from fluctuations in the viscosity do not necessarily act in opposition of turbulent structures, such as quasi-streamwise vortices and low/high-speed streaks. Instead, Arosemena *et al.* (2021) surmised that the local enhancement in the viscosity with increasing distance from the wall produces less energetic vortices and DR.

In the present experimental investigation, evidence of a striking demarcation in the viscosity, and the viscosity fluctuations, with growing distance from the wall are observed. For example, figure 8.6, 8.7(*b*) and 8.9(*a*) imply that the viscosity within the outer layer of the channel can be 20% to 300% larger than the nominal wall viscosity. Figures 8.10 and 8.11 demonstrate that the size of correlated viscosity fluctuations are thin ($\Delta y/h \approx 0.06$) and long ($\Delta x/h > 0.4$) within the buffer layer, but become more isotropic with increasing y. Moreover, spatial two-point correlations along the wall-normal direction show an anti-correlation between viscosity fluctuations within the near-wall region and the outer layer of the flow. It is apparent that the characteristics of the viscosity field are considerably different between the inner and outer layers of the flow. Furthermore, the mean stress balance, shown in figure 8.13, demonstrates that DR can largely be accounted for by a balance between viscous and Reynolds stresses alone, with little dependence on turbulent viscous stresses that arise from viscosity fluctuations. What is common among the present experimental investigation and DNS involving inelastic GN fluids (Singh *et al.*, 2017, 2018; Arosemena *et al.*, 2020, 2021), is a thin layer of nearly constant low viscosity fluid close to the wall followed by a sharp increase in the mean viscosity with increasing distance from the wall.

This thin near-wall layer of low viscosity is perhaps analogous to the low viscosity lubricating layer in the DNS of Roccon *et al.* (2019). In this numerical investigation, a thin layer of immiscible fluid with a different viscosity was introduced in the near wall region. When the near wall region had a viscosity comparable with that of the bulk fluid, Roccon *et al.* (2019) observed that the surface tension between the two fluids produced DR. However, for the cases where the near wall fluid had a lower viscosity, they commented that the near wall fluid acts as a lubricating layer that results in a smaller wall friction and consequently DR. In addition to this observation, there are some notable similarities with respect to the current investigation. In their DNS, Roccon *et al.* (2019) demonstrated that the average thickness of the lubricating layer was similar to the thickness of the expanded linear viscous sublayer, y_v/h, in the present experimental findings for XG. The DNS by Roccon *et al.* (2019) attained DR of 24% with a lubricating layer that was $0.038h$ in thickness; a value comparable to those of y_v/h for XG, which are between $0.017h$ and $0.051h$, as listed in table 8.3. However, it should be noted that the DR measured by Roccon *et al.* (2019) is based on a enhancement of volumetric flow rate considering they maintain a constant pressure gradient in their DNS – similar to most numerical investigations involving turbulent DR, including those of Arosemena *et al.* (2020, 2021) using GN constitutive models. In contrast, the present investigation considers a constant Re and evaluates the change in pressure gradient (a saving of "money" according to Frohnapfel *et al.* (2012)).

Turbulent DR using shear thinning liquids may also share commonalities with DR using superhydrophobic surfaces. Adding micro-scale roughness to a hydrophobic material produces a thin layer of air between the liquid and the solid boundary (Rothstein, 2010). The air layer causes the moving liquid to "slip", generally resulting in large quantities of DR (Ling *et al.*, 2016; Abu-Rowin & Ghaemi, 2019). This apparent slip of the liquid phase produces a mean velocity profile where values of $\langle U \rangle^+$ are larger for all y^+, but parallel to the Newtonian law of the wall – seemingly reminiscent of the Newtonian plug in polymer DR. Indeed, Lumley (1969) and Virk (1971) have regarded the Newtonian plug for polymer DR as being an "effective slip". The Newtonian plug is realized in a polymer drag-reduced flow when the log layer is displaced upwards to larger $\langle U \rangle^+$ (Virk, 1971). The Newtonian plug and the "effective slip" were alluded to in the results pertaining to profiles of $\langle U \rangle^+$, and was realized by the large peak in ζ. For rigid polymer solutions, slippage and the Newtonian plug are perhaps a manifestation of the fluids shear thinning rheology and the near-wall lubricating layer.

8.10 Summary

Solutions of xanthan gum (XG) polymer have historically demonstrated little viscoelastic and extensional properties; two rheological features often attributed to polymer drag-reduction (DR). Few existing experimental investigations have demonstrated the turbulence statistics of rigid polymers in a turbulent channel flow. The primary objective of the investigation in §8 was to scrutinize the effect of varying Reynolds number (Re_H) on the mean velocity and Reynolds stress profiles, independent of changes in DR. Our second objective was to evaluate the wall-normal gradient in the shear viscosity for drag-reduced flows of rigid polymers.

Inner-normalized mean velocity profiles for the XG flows of different Re_H approximately overlapped. Relative to the Newtonian law of the wall, the intercept of the log layer was considerably larger, and the slope demonstrated marginal growth (i.e., a Newtonian plug flow). Compared to Newtonian Reynolds stress profiles of similar Re_H, distributions for XG exhibited enhancement in streamwise Reynolds stresses and attenuation in wall-normal Reynolds stresses for all inner normalized wall-normal coordinates. Attenuation in the Reynolds shear stress was only observed near the wall. The effect of increasing Re in the non-Newtonian flows was the same as Newtonian, i.e., the Reynolds stresses increased in the logarithmic layer monotonically with increasing Re_H. The modification to the first- and second-order velocity statistics reflected consistency with results obtained from DNS using elastic and inelastic constitutive models and previous experiments with flexible polymers.

Instantaneous viscosity statistics were determined for each drag-reduced flow using the Carreau-Yasuda constitutive model and velocity gradients. The flows of XG possessed a thin near wall region with low mean viscosity. At wall-normal locations above the thin "lubricating layer", the fluid had a much larger mean viscosity. Fluctuations in the viscosity reflected different size and characteristics with increasing distance from the wall. That being said, these viscosity fluctuations have a negligible contribution to the mean stress balance of the flow. The lubricating layer consisted of the expanded linear viscous sublayer and portions of the buffer layer within the XG flows. It is hypothesized that rigid polymer DR is largely attributed to gradients in the mean velocity coupled with the solutions shear thinning rheology. The lubricating layer is a product of this interaction and a mechanism for generating an effective slip within the buffer layer.

Part IV

Turbulent boundary layer

Chapter 9

Local flow topology of a polymer-laden boundary layer

The invariants in the VGT of a Newtonian and polymer-laden turbulent boundary layer were experimentally analyzed using velocity vectors measured from 3D particle tracking velocimetry (3D-PTV) based on the shake-the-box (STB) algorithm developed by Schanz *et al.* (2016). Polymer-laden and Newtonian flows were compared at a similar friction Reynolds number Re_τ and momentum thickness Reynolds number Re_ϕ in a boundary layer formed on the floor of the water flume depicted in §4.3. Based on the VGT, the local flow topology is analyzed using the Δ-*criterion*, discussed in §3.3. Evidence is provided to test a hypothesis regarding the mechanism of polymer drag reduction. This hypothesis is inspired by the *viscous* theory of drag reduction mentioned in §1.3 – that being, the large extensional viscosity of polymer solutions strongly inhibits turbulent fluctuations just outside the viscous sublayer, causing the buffer layer to expand and wall friction to reduce (Lumley, 1973; White & Mungal, 2008). In a similar fashion, the work of Roy *et al.* (2006) proposed a mechanism by which polymers influence the nature of coherent structures that also pertains to the extensional viscosity of the polymer solution. In a channel flow simulation that utilized a simplified constitutive model of polymer stresses (the retarded-motion expansion), Roy *et al.* (2006) demonstrated that the non-Newtonian extensional viscosity opposed flow in both biaxial and uniaxial flow regions, which mitigated the strength and formation of quasi-streamwise vortices and reduced drag. Based on the findings of Roy *et al.* (2006), it is therefore, expected that changes in the topology will predominately occur in regions of strong uniaxial/biaxial extension. Uniaxial/biaxial flow regions are dissipative with $\Delta < 0$, and are strongly concentrated around the Vieillefosse tails in the JPDF of the VGT invariants discussed in §3.3 and shown in figure 3.5. They can also be identified from the invariants in the rate of deformation tensor or the symmetric component of the VGT, as demonstrated in §3.3 and figure 3.6. Details regarding the polymer solution and measurement apparatus are first presented, followed by an analysis of velocity statistics and flow topology based on the Δ-*criterion*.

9.1 Polymer solution preparation and characterization

The flexible polymer polyacrylamide (PAM) (6030S, SNF Floerger) with a molecular weight of 30-35 MDa, was chosen for the polymer-laden boundary layer experiments. A 3500 l homogeneous PAM solution (a polymer ocean) with a concentration c of 140 ppm was utilized. To prepare the polymer ocean, an 1140 l concentrated master solution (c = 430 ppm) was first mixed and then diluted to achieve the desired 140 ppm concentration within the flume. The master solution was mixed in two 570 l cylindrical vessels. Solid polymer powder was weighed using a scale with a 0.1 g resolution, and gently added to each container (245 g to each vessel) along with tap water. A stand mixer equipped with a 150 mm diameter impeller and set to a rotational speed of 50 rpm was used to mix the master solution in each vessel for 2 hours. The master solution was then slowly added to 2360 l of tap water that was contained within the flume. An air operated diaphragm pump was used to transfer the master solution from the mixing containers to the flume at a flow rate of 1 l s^{-1}. Upon adding the master solution to the flume, the 3500 l solution was then circulated for 30 min, where the rotational speed of the centrifugal pumps was set to 300 rpm. The 140 ppm solution was then left to rest for 12 h. The resulting fluid was visibly transparent and had no heterogeneous clumps of polymers.

Flow measurements were performed immediately after the PAM solution was left to rest for 12 h. The rotational speed of the pumps were set to 1000 rpm, which produced a U_∞ of 0.432 m s^{-1}. To avoid degradation of the PAM solution, the pumps were turned off intermittently between instances of image acquisition for 3D-PTV. For a single set of flow measurements, the pumps were turned on for 2 min. After which, the pumps were turned off for approximately 10 min to allow time for the 3D-PTV images to be saved. Eight sets of images were collected for 3D-PTV, therefore, this procedure of turning the pumps on for 2 min and off for 10 min was repeated eight times. Fluid samples were collected for rheology measurements immediately after each instance of image acquisition (eight fluid samples in total) while the pumps were turned off. Rheology measurements were necessary for characterizing the material properties of the fluid (i.e., shear viscosity and extensional relaxation time) and were also useful for diagnosing the effects of degradation.

Steady shear rheology was used to evaluate the viscous features of water and the 140 ppm PAM solution. Shear rheology measurements were performed using the torsional rheometer in §4.1.1 and figure 4.1. The double-gap concentric cylinder geometry of figure 4.2(b) was utilized for the measurements. Measurements of μ were performed over a logarithmic sweep of shear rate $\dot{\gamma}$ from 0.1 to 1000 s^{-1}, as shown in figure 9.1(a) for water and the 140 ppm PAM solution. Measurements of μ are limited by a minimum measurable torque T and the inception of Taylor vortices. The lower torque limit provided by TA instruments was 10 nN m §4.1.1; in practice, the lower limit was larger and equal to T = 600 nN m. Taylor instabilities occur at larger $\dot{\gamma}$ when the Taylor number Ta exceeds 1700 (Ewoldt *et al.*, 2015). The dashed lines labelled T = 600 nN m and Ta = 1700 in figure 9.1(a) represent the lower and upper limits of $\dot{\gamma}$, between which μ can be measured accurately.

Figure 9.1(a) demonstrates the average measurements of μ for water and PAM with c = 140 ppm. For water, μ was measured for three samples. The three measurements were then averaged at their respective values of $\dot{\gamma}$. The down-sampled error bars in figure 9.1(a) convey the range in the measurements of μ at each $\dot{\gamma}$. As expected for a Newtonian fluid, the values of μ are relatively constant with respect to $\dot{\gamma}$ for water. The average μ of water across all values of $\dot{\gamma}$ (with $T > 600$ nN m and $Ta < 1700$) was 0.98 cP – approximately 2.0% lower than the expected value according to Cheng (2008). This 2% deviation between the expected and

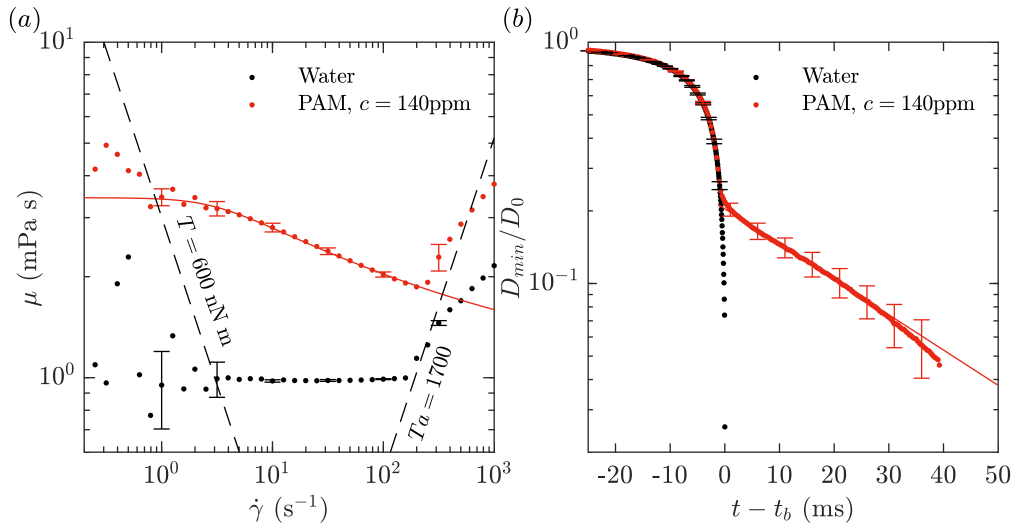

Figure 9.1: Rheology measurements of tap water and the 140 ppm PAM solution. Here (*a*) corresponds to measurements of steady shear viscosity as a function of shear rate and (*b*) demonstrates the diameter versus time of thinning droplet expelled from a needle. Black dashed lines in (*a*) represent the lower and upper shear rate limits of the torsional rheometer. The solid red line in (*a*) is the fitted line of (9.1) representative of the Carreau shear-thinning trend. The red solid line in (*b*) is the fitted line of (4.3) which describes elastocapillary thinning.

measured value of μ for water is assumed to be a systematic error in the shear viscosity. The measurements of μ for the 140 ppm PAM solution were taken for eight samples corresponding to different sets of 3D-PTV flow measurements. The data points in figure 9.1(*a*) are the average measurements of μ at each corresponding $\dot{\gamma}$ for the eight samples. Similar to water, the down-sampled error bars represent the range in the measurements of μ at each $\dot{\gamma}$. The error bars in μ are slightly larger for the PAM solution than water (for $T > 600$ nN m and $Ta < 1700$) and can be attributed to some degradation in the samples as the fluids are pumped within the flume. The largest relative error in μ is 4.9%; therefore, despite degradation being present, its influence on the measurements of μ are minimal. For a conservative estimate, it is assumed that the total uncertainty in measurements of μ is the root sum of the squared systematic uncertainty, determined from the measurements of μ for water, and the squared relative uncertainty of 4.9% caused by degradation. In other words, the total relative uncertainty in μ was assumed to be 5.3%.

The Carreau model was fit on the shear rheogram of the 140 ppm PAM solution to approximate the trend in μ as function of $\dot{\gamma}$ (Carreau, 1972). The model was of the form,

$$\frac{\mu - \mu_\infty}{\mu_0 - \mu_\infty} = \frac{1}{[1 + (M\dot{\gamma})^2]^{(1-k)/2}}, \tag{9.1}$$

where μ_0 is the viscosity at $\dot{\gamma} = 0$, μ_∞ is the viscosity at $\dot{\gamma} = \infty$, M is the consistency, and k is flow index. Nonlinear least square regression was used to fit (9.1) onto the average values of μ for the PAM solution between $\dot{\gamma}$ of 1 and 200 s^{-1}. The red solid line in figure 9.1 shows the Carreau model; the resulting fit of (9.1) agrees well with the experimental measurements for PAM. The values of μ_0, μ_∞, M, and k were 3.4 cP, 1.0 cP, 0.29 s and 0.76 respectively.

To evaluate the extensional rheology of water and the PAM solution, the deformation of a small droplet of fluid undergoing capillarly-driven thinning was measured, using the DoS apparatus depicted in §4.1.3. Three repeated measurements in the extensional rheometer were performed for water. Recall that eight samples of the PAM solution were collected immediately following 3D-PTV data collection. Three repeated measurements of the extensional rheology were performed for each sample of the PAM solution, resulting in 24 measurements in total. The minimum diameter D_{min} of the liquid bridge was established using MATLAB software (Mathworks Inc.).

Figure 9.1(b) demonstrates the evolution of D_{min}/D_0 with respect to time t. The markers in figure 9.1(b) represent the average values of the repeated measurements of D_{min} for each instance of t. The down sampled error bars indicate the range in the repeated measurements of D_{min} for each instance of t. For water, the liquid bridge ruptures quickly in t_b of 25 ms due to inertial and capillary forces and according to (4.2). The Ohnesorge number $Oh = t_v/t_R$ relates the time scale associated with viscous forces $t_v = \mu_0 D_0/2\sigma$ to that of surface tension and inertial forces, i.e., the Rayleigh time $t_R = (\rho D_0^3/8\sigma)^{1/2}$. Here σ is the surface tension, which for water and low concentration solutions of PAM is generally 72 mN m^{-1} (Miller *et al.*, 2009). For both water and PAM, Oh is less than 1, and the thinning process is dominated by inertial and capillary forces (Dinic *et al.*, 2017). However, for the PAM solution, elastic forces also contribute to the pinch-off dynamics. The Deborah number $De = t_e/t_R$ represents the ratio of elastic forces to inertiocapillary forces, where t_e is the elastic relaxation time of the fluid. When De is greater than 1, the droplet exhibits elastocapillary thinning described by (4.3). Nonlinear least square regression is used to fit (4.3) on the average measurements of D_{min}/D_0 for $t > t_b$ of the PAM solution. The solid red line in figure 9.1(b) demonstrates the fitted (4.3) with respect to the measurements of D_{min}/D_0. Using (4.3), t_e of the PAM solutions was determined to be 9.90 ms.

9.2 Flow measurements

Two types of flow measurements were used to characterize the Newtonian and non-Newtonian turbulent boundary layers. The first was 3D particle tracking velocimetry (3D-PTV) based on the shake-the-box (STB) algorithm (Schanz *et al.*, 2016), which was used primarily to measure the VGT. The second consisted of a two-camera planar particle image velocimetry (PIV) setup, that was used to obtain bulk properties of the flow, including U_∞, the momentum thickness ϕ and the boundary layer thickness δ. These measurements were done concurrently, after the pumps for the flume were turned on. Both systems are described in the following sections.

9.2.1 3D particle tracking velocimetry

To obtain 3D measurements of the velocity vector $\boldsymbol{U}$ within the Newtonian and non-Newtonian turbulent boundary layers, 3D-PTV using the STB algorithm was used (Schanz *et al.*, 2016). The 3D-PTV measurements produce Lagrangian trajectories representative of particles that travel through the discrete measurement domain. The STB algorithm enhances the 3D-PTV technique by allowing for large particle seeding densities and a significantly greater number of trajectories within the measurement volume (Wieneke, 2012; Schanz *et al.*, 2016). The velocities of the Lagrangian trajectories are then projected onto an Eulerian grid at each instance of time t. This effectively produces 3D time resolved measurements of $\boldsymbol{U}$.

An isometric view that illustrates the 3D-PTV measurement apparatus, with reference to a section of the water channel, is shown in figure 9.2(a). The 3D-PTV measurement apparatus consisted of four high-speed cameras (Phantom v611, Vision Research Inc.), each of which is labelled from 1 to 4 in figure 9.2. A high-repetition Nd:YLF laser (DM20-527, Photonics Industries), was used to illuminate the volume of interest (VOI). A zoomed in depiction of the VOI is shown in figure 9.2(b) with reference to the Cartesian coordinate system, where x, y and z are the streamwise, wall-normal and spanwise directions respectively. The beam that exited the head of the laser had a diameter of 5.8 mm, a wavelength of 532 nm and a maximum pulse energy of 20 mJ pulse^{-1}. The beam exited the laser head along the positive $z-$direction and underneath the water channel (i.e., negative y). One cylindrical lens was used to expand the beam along the $x-$direction. A mirror was then used to re-direct the resulting ovular beam along the positive $y-$direction. The beam then penetrated the channel from beneath the glass floor. Four knife edges secured to the underside of the glass floor of the water channel were used to crop the ovular laser beam, such that it captured the desired dimensions of the VOI along x and z shown on figure 9.2(b). The centre of the laser volume was positioned such that the VOI was at the channel mid-span ($W/2$) along z and 4.5 m downstream of the inlet to the water channel along x. The cropped laser volume was 3.5 mm thick along z and approximately 15 mm in width along x, and had a rather uniform intensity profile along those respective directions.

Each of the four high-speed cameras had a 1280×800 pixel complementary metal oxide semiconductor sensor. The pixels that comprised each sensor were 20×20 µm^2 in size and had a 12 bit digital resolution. To achieve larger acquisition times, the sensors on all cameras were cropped to 1280×304 pixel. The four cameras were arranged in a cross-like configuration, as depicted in figure 9.2(a). All cameras were placed in a portrait orientation such that the 1280 pixel dimension of each sensor was parallel to the $y-$direction. The three side-scattering cameras, i.e., cameras 1, 2 and 3, were placed along the same horizontal plane, which was parallel to the bottom wall of the channel (or the $xz-$plane). Cameras 1 and 3 had a viewing angle of $\pm 30°$ rotated about the positive $y-$axis and depicted in figure 9.2(c). Camera 2 directly imaged the $xy-$plane with no viewing angle. The forward-scattering camera, i.e., camera 4, was positioned directly above camera 2 and on the same plane parallel to yz – as shown in figure 9.2(d). Camera 4 had a viewing angle that was 20° rotated clockwise about the positive $x-$axis. Water-filled prisms helped mitigate image distortion caused by refraction for cameras 1, 3 and 4, which had large viewing angles. Each prism consisted of a 3D printed nylon frame with a glass viewing pane that was bonded to the exterior of the channel side wall and filled with distilled water. Sigma lenses with a focal length f of 105 mm and 2× teleconverters (Teleplus pro300, Kenko) were used to achieve a magnification of approximately 0.72 for all four of the cameras. All cameras had a lens aperture of $f/16$, with an approximated depth-of-focus of 7 mm. Schiempflug adapters were also used for cameras 1, 3 and 4 to ensure images of the VOI were in focus. The cameras and laser were synchronized using a programmable timing unit (PTU X, LaVision GmbH) and image acquisition was performed using DaVIS 8.4 software (LaVision GmbH). The fluids within the flume were seeded with 2 µm silver coated hollow glass spheres (SG02S40, Potters Industries). The density of tracers within the images was approximately 0.05 particles per pixels.

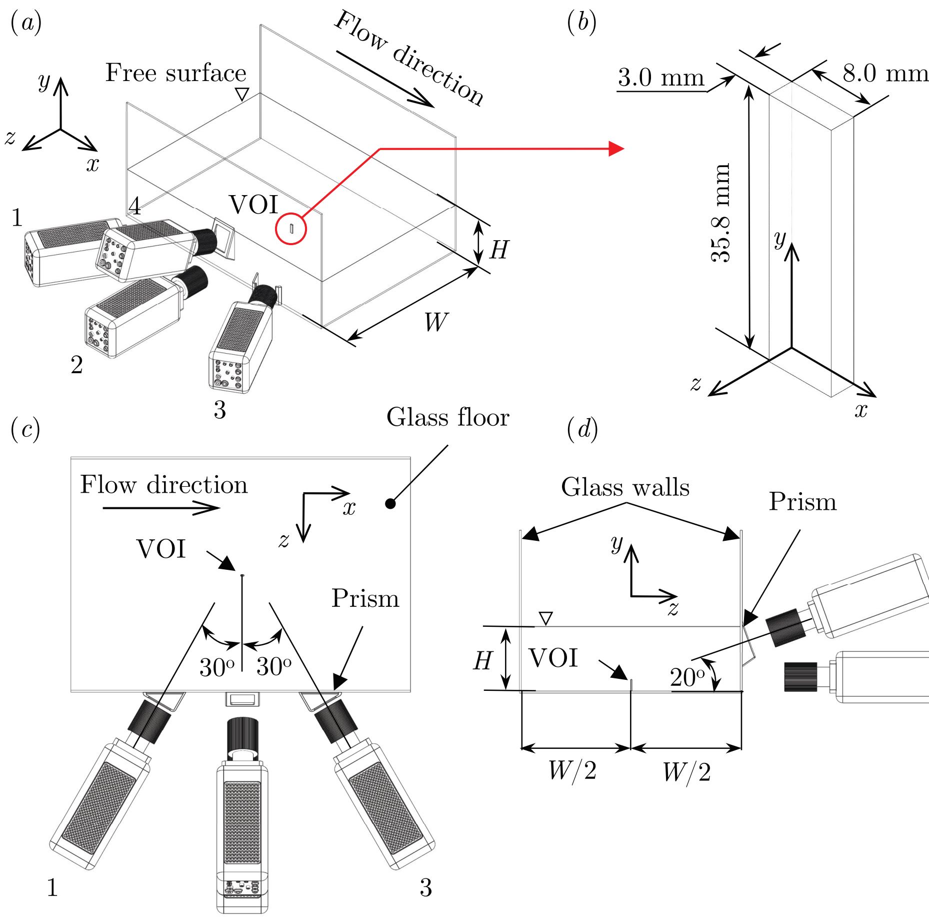

Figure 9.2: A schematic of the 3D-PTV flow measurement setup with reference to a section of the water channel. Here (a) shows an isometric view of the measurement apparatus and water channel, (b) provides an isometric view of the volume of interest (VOI) with reference to the Cartesian coordinate system, (c) demonstrates a top view of the 3D-PTV measurement setup, and (d) provides a front view of the measurement setup.

One time-resolved data set, for both measurements of the Newtonian and non-Newtonian turbulent boundary layers, consisted of 14354 single-frame images captured at a frequency between 0.52 kHz and 1.82 kHz. Therefore, one data set took between 7.9 s and 27.6 s or $36.2\mathcal{T}$ and $62.7\mathcal{T}$, where $\mathcal{T} = \delta/U_\infty$ is a representative advection time or large eddy turnover time and δ is the boundary layer thickness. The frequency was selected depending on U_∞, and such that a maximum particle displacement of 5 pixels across subsequent images was achieved. Image processing consisted of first determining the minimum intensity at each pixel and over the complete image ensemble, and then subtracting the minimum from all images in a data set. Second, the intensity signal at each pixel was normalized by the average intensity of the ensemble. Lastly, a sliding minimum subtraction with a kernel size of 5 pixels and local intensity normalization with a kernel size of 500 pixels were applied to every image. For the different Newtonian and non-Newtonian flows, eight data sets, equivalent to 114832 images, were collected to ensure sufficient convergence of the different ensemble statistics in the analysis. Therefore, the total duration of the eight data sets used for computing ensemble statistics was between $260\mathcal{T}$ to $500\mathcal{T}$ depending on the flow condition. The statistical convergence of the 3D-PTV measurements were evaluated in Appendix A.4. It is shown that all velocity statistics attain sufficient statistical convergence, with low random errors, within the last 5700 realizations.

Calibration of the imaging setup was achieved by fitting a third-order polynomial mapping function onto images of a dual-plane 3D calibration target (025-3.3, LaVision GmbH). Volume self-calibration was used to significantly improve the accuracy of the mapping function (Wieneke, 2008). Self-calibration reduced the average and maximum disparity vector magnitude, or error in the mapping function, to 0.02 and 0.06 pixels respectively. After self-calibration, an optical transfer function was generated to account for changes in the imaged particle patterns across the 3D volume (Schanz *et al.*, 2013). The resulting measurement volume or VOI had dimensions $(\Delta x, \Delta y, \Delta z) = 272, 1220, 102$ voxel $= 8.0, 35.8, 3.0$ mm^3, as shown in figure 9.2(*b*). Finally, the STB algorithm was performed using DaVIS 10.2 software (LaVision GmbH). The maximum triangulation error was set to 1 voxel, and particle displacements were limited to a maximum of 8 voxel. Particles with an acceleration that was larger than 2 pixels or 20% between subsequent image frames were discarded. The STB algorithm yielded approximately 6200 Lagrangian trajectories per time step within the VOI.

A moving first-order polynomial with a length of nine time steps was fit on the particle trajectories. Two types of binning were used to convert the Lagrangian trajectories into Eulerian vector components. The first involved averaging the trajectories into slabs that were parallel with the wall and covered the entire measurement domain along x and z. Each slab was 6 voxels or 0.18 mm thick in the $y-$direction. Neighbouring slabs along y, overlapped by 75%. This binning procedure was used exclusively for establishing the mean streamwise velocity $\langle U \rangle$ with high spatial resolution. Here, the angle brackets $\langle \cdots \rangle$ denote averaging in time and along the spatially homogeneous direction z. It was also assessed that $\langle U \rangle$ did not vary significantly along Δx within the VOI; hence, the statistics were also averaged along the $x-$direction within the VOI. The second binning procedure involved averaging particle tracks for each time step in $32 \times 32 \times 32$ voxel or $0.94 \times 0.94 \times 0.94$ mm^3 cubes to obtain the instantaneous velocity vector $\boldsymbol{U}$ within the domain. Neighbouring cubes had 75% overlap with one another along the three Cartesian directions. Therefore, adjacent vectors were separated by 8 voxels or 0.235 mm. In terms of viscous wall units δ_ν, the bins were between $6.9\delta_\nu \times 6.9\delta_\nu \times 6.9\delta_\nu$ and $9.3\delta_\nu \times 9.3\delta_\nu \times 9.3\delta_\nu$ depending on the flow considered. The streamwise, wall-normal and spanwise components of the instantaneous velocity $\boldsymbol{U}$ are denoted as U, V and W, respectively. Velocity fluctuations were represented using lower case symbols, i.e., u, v and w.

A moving first-order polynomial surface was fitted to the velocity components at each instance of time and then differentiated to obtain spatial gradients in velocity. The size of polynomial surface was three velocity vector components along each Cartesian direction, which equates to $24 \times 24 \times 24$ voxels or $0.704 \times 0.704 \times 0.704$ mm^3. Spatial velocity gradients were then used to analyze the topology of the Newtonian and non-Newtonian turbulent boundary layers according to §3.3.

The uncertainty in the 3D-PTV measurements is scrutinized in Appendix A.5. Uncertainty is primarily assessed based on how well the velocity vectors satisfy the divergence free condition, where $\nabla \cdot \boldsymbol{U} = 0$. Appendix A.5 demonstrates that the present measurements adequately satisfy the divergence-free condition compared to other investigations that have utilized experimental flow measurements to measure the VGT

(Tsinober *et al.*, 1992; Zhang *et al.*, 1997; Ganapathisubramani *et al.*, 2007; Gomes-Fernandes *et al.*, 2014).

The variables for inner scaling were established by fitting a linear function to the mean velocity profile $\langle U \rangle$ of each flow near the wall. The linear function was then differentiated in order to determine the near-wall shear rate $\dot{\gamma}_w$ of each flow. Here, $\dot{\gamma}_w$ is established by differentiating the mean velocity, i.e., $\partial \langle U \rangle / \partial y$, for $y > 0.2$ mm and $y^+ < 3$. The lower bound of the fit was the smallest measurable value of y with a slab that did not overlap with the wall. While the upper bound of the fit is within the theoretical limit of the linear viscous sublayer. The wall shear stress τ_w was then established according to $\tau_w = \mu(\dot{\gamma}_w)\dot{\gamma}_w$ (similar to 3.7), where $\mu(\dot{\gamma}_w)$ is the viscosity of the fluid evaluated at the near-wall shear rate $\dot{\gamma}_w$ using the Carreau model that was fitted to measured values of μ for PAM detailed §9.1. For the water flows, μ does not vary with shear rate, and was equal to 1.00 cP according to Cheng (2008) and measurements of μ for water in §9.1. After establishing τ_w, the friction velocity u_τ from (3.10) and viscous lengthscale δ_v from (3.11) were determined. Several other variables were also used to characterize the flows. For example the skin friction coefficient $C_f = 2\tau_w / \rho U_\infty$ was used to defined the local friction of the boundary layer. The friction Reynolds number Re_τ was determined according to (3.19). Lastly, the Weissenberg number $Wi = t_e \dot{\gamma}_w$ was used to the define the ratio between the elastic and viscous forces of the flow. The different variables of the flow are listed in table 9.1.

Fluid	U_∞ (m s^{-1})	ϕ (mm)	δ (mm)	u_τ (mm s^{-1})	δ_v (mm)	Re_ϕ	Re_τ	$C_f \times 10^3$
Water	0.186	9.77	81.87	7.60	0.132	1814	612	3.35
Water	0.247	9.15	77.94	9.90	0.101	2257	765	3.22
PAM	0.432	10.33	94.31	14.20	0.137	2290	687	2.16

Table 9.1: Inner and outer scaling variables of the Newtonian and non-Newtonian turbulent boundary layers.

9.2.2 Planar particle image velocimetry

For all of the flows considered, the VOI measured using 3D-PTV did not capture the complete boundary layer thickness along y. Therefore, a planar PIV setup was used to obtain measurements of $\langle U \rangle$ over a larger field of view ($0 < y < \delta$), in order to determine the bulk flow properties of the Newtonian and non-Newtonian turbulent boundary layers. These bulk properties include the momentum thickness ϕ from (3.18), boundary layer thickness δ and free-stream velocity U_∞, all of which are listed in table 9.1. The boundary layer thickness is assessed as the y location where $\langle U \rangle = 0.99U_\infty$. The measurement location of the planar PIV apparatus was situated at the centre of the water channel along z, and 200 mm upstream of the VOI along x.

The planar PIV setup consisted of two double-frame digital cameras (Imager Intense, LaVision GmbH), each of which had a 1376×1040 pixels charged-coupled device sensor. Each pixel in the sensor was 6.45×6.45 µm^2 in size and had a 12 bit digital resolution. The sensors were cropped to 1376×128 pixels to enable higher acquisition rates, where the 1376 pixel dimension was parallel to the $y-$direction. Double-frame images were acquired at a frequency of 14.3 Hz. The fields of view (FOVs) of both cameras were stacked along the wall-normal direction y, and covered a region with a size of $\Delta x = 7.0$ mm and $\Delta y = 143.1$ mm. The FOVs were placed at the centre of the channel along z and 200 mm upstream of the VOI for 3D-PTV, along x. Illumination was provided from a 15 mJ pulse^{-1} Nd:YAG laser (Solo I-15, New Wave Research Inc.), that was synchronized with the cameras using a programmable timing unit (PTU 9, LaVision GmbH) and DaVIS 7.3 software (LaVision GmbH). Two spherical lenses (one concave, the other convex) and one concave cylindrical lens expanded the laser beam into a 20-mm-wide (along x) and a 1-mm-thick (along z) laser sheet. One data set consisted of 800 pairs of double-frame images, which took 56 s to collect. The time delay Δt between subsequent frames was between 1.43 and 5.00 ms depending on U_∞. The value of Δt was chosen such that the maximum particle displacement between images frames was approximately 15 pixels. Recall from §9.1 that eight data sets were collected for the two cases of water (corresponding to different Re) and the one condition of PAM. Therefore, each flow scenario consisted of 6400 double frame images.

Image processing was performed using DaVIS 8.4 software (LaVision GmbH). First the minimum intensity in each pixel was determined in each data set and subtracted from every image in the ensemble. Second, the intensity signals in each pixel were normalized by the average intensity of the ensemble. Vector fields were then established using cross-correlation with an initial interrogation window (IW) size of 64×64 pixels and a final IW size of 24×24 pixels with 75% overlap between neighbouring IWs. The mean streamwise velocity $\langle U \rangle$ with respect to y was determined by averaging U over all instances of time t and along the $x-$direction. Profiles of $\langle U \rangle$ with respect to y were then used to establish the free-stream velocity U_∞, the boundary layer thickness δ and momentum thickness ϕ.

9.3 Velocity statistics

Figure 9.3(a) demonstrates inner-normalized mean streamwise velocity $\langle U \rangle^+$ with respect to y^+ for the experimentally measured turbulent boundary layers of water with different Re_ϕ and the 140ppm PAM solution. Experimental $\langle U \rangle^+$ profiles are shown alongside the mean velocity profile derived from Newtonian turbulent boundary layer DNS in Jiménez *et al.* (2010) at an Re_ϕ of 1968, and also the law of the wall. All flows, both water and PAM, closely follow the linear viscous sublayer $\langle U \rangle^+ = y^+$ for $y^+ < 3$. For $y^+ > 30$ the boundary layers of water with different Re_ϕ both overlap with a logarithmic profile $\langle U \rangle^+ = 1/\kappa \ln(y^+) + B$ that has a Von Kármán coefficient κ of 0.384 and an intercept B of 4.5 – similar to the values prescribed by Nagib & Chauhan (2008) for Newtonian turbulent boundary layers. The polymer-laden flow exhibits enhanced values of $\langle U \rangle^+$ relative to the Newtonian boundary layers for $y^+ > 30$, a feature common in drag-reduced flows of polymer solutions. The slope in the log layer B of the polymer-laden boundary layer is larger than B for water, and visually κ is approximately the same. Although $\langle U \rangle^+$ is enhanced within the outer layer of the polymer-laden flow, it does not overlap with the maximum drag reduction asymptote $\langle U \rangle^+ = 11.7 \ln(y^+) - 17.0$ of Virk *et al.* (1970).

Figure 9.3(b) demonstrates inner-normalized plots of the four non-zero components of the Reynolds stress tensor with respect to y^+. Listed in descending order of magnitude, $\langle u^2 \rangle^+$, $\langle w^2 \rangle^+$ and $\langle v^2 \rangle^+$ are the streamwise, spanwise and wall-normal Reynolds stresses respectively, and $\langle uv \rangle^+$ is the Reynolds shear stress.

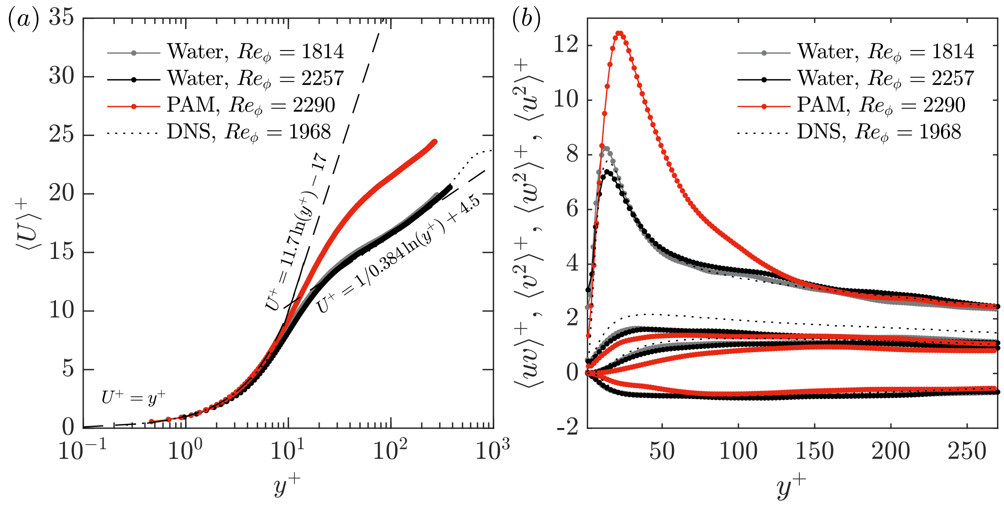

Figure 9.3: Plots of the (*a*) mean velocity, and (*b*) Reynolds stress profiles for the turbulent boundary layer flows of water and the 140 ppm PAM solution. The dotted lines are mean velocity and Reynolds stress profiles of Newtonian turbulent boundary layer DNS from Jiménez *et al.* (2010) at $Re_\phi = 1968$.

The experimentally measured profiles of $\langle u^2 \rangle^+$, $\langle v^2 \rangle^+$ and $\langle uv \rangle^+$ for water overlap well with the DNS of Jiménez *et al.* (2010) at a comparable Re_ϕ. That being said, the measured Reynolds stress profiles of $\langle w^2 \rangle^+$ for water are marginally less than that of the Newtonian DNS. That being said, profiles of $\langle w^2 \rangle^+$ for water with slightly different Re_ϕ show consistency with one another. Therefore, it is speculated that the lower than normal profile of $\langle w^2 \rangle^+$ is a unique condition of the present flow. Relative to the boundary layers of water, the polymer-laden boundary layer has augmented values of $\langle u^2 \rangle^+$ for $y^+ < 150$ and attenuated values of $\langle w^2 \rangle^+$, $\langle v^2 \rangle^+$ and $-\langle uv \rangle^+$ for $y^+ < 100$. The peak in $\langle u^2 \rangle^+$ is also shifted away from the wall for the PAM flow relative to water; for PAM, the peak in $\langle u^2 \rangle^+$ is at a y^+ of 21, while for both of the water flows, the peak in $\langle u^2 \rangle^+$ is at a y^+ of approximately 13.

Experimentally measured mean velocity and Reynolds stress profiles of PAM, shown in figure 9.3, reflect consistency with prior measurements of polymer drag-reduced flows with low drag reduction percentages (LDR) that are less than 38% (Warholic *et al.*, 1999*b*). LDR flows typically have an expanded buffer layer and a log layer with a larger B – often referred to as a Newtonian plug (Virk *et al.*, 1970; Warholic *et al.*, 1999*b*). The larger B is visually apparent in figure 9.3(*a*), and the expanded buffer layer is evident based on the shift in the peak of $\langle u^2 \rangle^+$ to larger y^+, seen in figure 9.3(*b*). Warholic *et al.* (1999*b*) similarly demonstrated that polymer drag-reduced channel flows at LDR consist of augmented $\langle u^2 \rangle^+$ values and attenuated $\langle w^2 \rangle^+$, $\langle v^2 \rangle^+$ and $-\langle uv \rangle^+$ values relative to water at a comparable Re_τ. Generally, the ensemble velocity statistics of PAM are in good agreement with the LDR flows depicted in Warholic *et al.* (1999*b*) and other investigations (Escudier *et al.*, 2009; Warwaruk & Ghaemi, 2022; Mitishita *et al.*, 2023).

Two-point correlation of the streamwise velocity fluctuations u is used to obtain a depiction of the integral length scale within the buffer layer of each flow. Moreover, it is the most common metric used in prior investigations of polymer drag-reduced flows for quantifying the size of large scale coherent motions. Therefore, it provides another good baseline comparison between the current and prior investigations of LDR flows. The spatial two-point correlation is calculated according to,

$$R_{uu}(\Delta x^+, \Delta y^+, \Delta z^+) = \frac{\langle u_{x_0^+, y_0^+, z_0^+} u_{x_0^+ + \Delta x^+, y_0^+ + \Delta y^+, z_0^+ + \Delta z^+} \rangle}{\sqrt{\langle u^2_{x_0^+, y_0^+, z_0^+} \rangle} \sqrt{\langle u^2_{x_0^+ + \Delta x^+, y_0^+ + \Delta y^+, z_0^+ + \Delta z^+} \rangle}}, \tag{9.2}$$

where (x_0^+, y_0^+, z_0^+) is the coordinate of a reference point, and $(\Delta x^+, \Delta y^+, \Delta z^+)$ are small displacements relative to the point of reference. Here, the point of reference is taken to be $(x_0^+, y_0^+, z_0^+) = 0, 20, 0$, which is at the border of the domain along x and z, and in the buffer layer of the flow along y.

Open contours of R_{uu} along the $xy-$plane and at $z^+ = 0$ are shown in figure 9.4(a). Contours are coloured according to the different flows and similar to that of figure 9.3. For the water flows at different Re_ϕ, contours of R_{uu} overlap, implying that the length of the large scale motions in viscous wall units are the same. Evidently, the VOI is not large enough along x to capture the complete integral length scale of each flow, or where R_{uu} becomes zero. That being said, it is clear that the PAM flow has a different distribution of R_{uu} than water. Compare, for example, R_{uu} with a value 0.95 or 0.85 in figure 9.4(b) for PAM to water. Values of $R_{uu} = 0.95$ for water extend to $(\Delta x^+, \Delta y^+) = 23.0, 4.8$ while for PAM, values of $R_{uu} = 0.95$ stretch to $(\Delta x^+, \Delta y^+) = 42.3, 2.8$. This demonstrates that the large scale motions within the buffer layer of the PAM boundary layer are double the length along x compared to those of water, and less angled upwards along y.

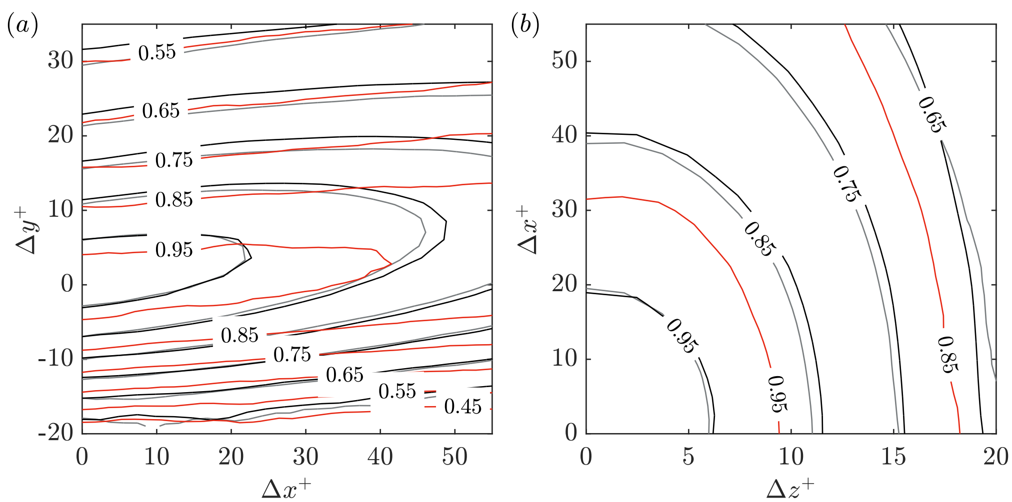

Figure 9.4: Two-point correlation R_{uu} of streamwise velocity fluctuations along the (a) $xy-$plane at $z^+ = 0$, and (b) along the $xz-$ plane at $y^+ = 20$. The reference point for the correlation is $(x_0^+, y_0^+, z_0^+) = 0, 20, 0$. The colours of the contours correspond to the same line colours and conditions of figure 9.3. Grey is water with $Re_\phi = 1814$, black is water with $Re_\phi = 2257$, and red is the 140 ppm PAM flow with $Re_\phi = 2290$.

Contours of R_{uu} along the $xz-$plane and at $y^+ = 20$ can be seen in figure 9.4(b). Similar to the $xy-$plane, contours of R_{uu} along the $xz-$plane overlap for the water flows with different Re_ϕ, implying that the width of the large scale motions in viscous wall units are the same. Based on figure 9.4(b), it is also apparent that the VOI is not wide enough along z to capture the complete width of the large scale motions where $R_{uu} = 0$. However, much like figure 9.4(a), there is an unambiguous difference in the contours of R_{uu} along the $xz-$plane among PAM and water. Contours of R_{uu} that are similar in value extend to larger Δ_z^+ for PAM compared to water. For example, when $\Delta_x^+ = 0$, values of R_{uu} equal to 0.85 extend to Δ_z^+ of 10.6 for water. For PAM, the contour of $R_{uu} = 0.85$ extends farther, to Δ_z^+ of 17.6, implying that the large scale motions in the flow of PAM are wider compared to water. An elongation and widening of high- and low-speed velocity streaks is a common feature of polymer drag-reduced flows (Warholic *et al.*, 1999*b*; White *et al.*, 2004; Farsiani *et al.*, 2020; Warwaruk & Ghaemi, 2021). The difference in R_{uu} among PAM and water observed in figure 9.4 implies the same augmentation to size of the large scale flow motions within the buffer layer.

Overall, the results of the current section demonstrates that the PAM boundary layer has one-point and two-point velocity statistics common for an LDR flow. It does not, however, provide a complete depiction of how, and why, the velocity statistics within the polymer-laden flow are different than a Newtonian turbulent boundary layer. For this, the distribution of fine scale motions and streamline patterns within the Newtonian and non-Newtonian boundary layers are scrutinized using the $\Delta-$*criterion*.

9.4 Flow topology

The topology of the Newtonian and non-Newtonian boundary layer is evaluated using the $\Delta-$*criterion* detailed in §3.3. Previous investigations of wall-bounded turbulence generally separate the topology of the flows into different regions of y^+, e.g., viscous sublayer, buffer layer, log layer, and wake region. Before separating the flow into these different wall-normal regions, the invariants in $\mathbf{L}$, $\mathbf{D}$, and $\mathbf{W}$ are evaluated for the complete spatial domain. Note, that all gradients are made dimensionless by multiplying the components of $\mathbf{L}$ by the large eddy turnover time $\mathcal{T} = \delta/U_\infty$ of each flow. Probability density functions (PDFs) are used to establish a histogram of the invariants P_L, Q_L, R_L, Q_D, Q_W and R_D, as well as the discriminant in (3.28) Δ and (3.31) Δ_D. Certain PDFs, such as P_L and Δ_D, also demonstrate the accuracy of the 3D-PTV flow measurements.

PDFs of P_L, Q_L and R_L are shown in figure 9.5(*a*) for the boundary layers of water at $Re_\phi = 1814$ and 2257, and PAM. For an incompressible fluid flow the first invariant in $\mathbf{L}$, P_L is equal to zero; however, the present experiments are subject to a divergence error ($P_L \neq 0$) caused by experimental noise and the limited spatial resolution involved with binning the Lagrangian trajectories produced from 3D-PTV. This error has been shown to have a significant impact on the measured topology of each flow using the $\Delta-$*criterion* (Ganapathisubramani *et al.*, 2007; Buxton *et al.*, 2011). Therefore, a stringent evaluation of the divergence error is made in Appendix A.5. It is shown in Appendix A.5 that the divergence errors are comparable or better than those of prior experimental investigations that have utilized multi-probe hot wire techniques, holographic PIV, dual-plane stereoscopic PIV, and stereoscopic PIV utilizing Taylor's hypothesis to measure the components of the VGT (Tsinober *et al.*, 1992; Zhang *et al.*, 1997; Ganapathisubramani *et al.*, 2007; Buxton *et al.*, 2011; Gomes-Fernandes *et al.*, 2014). Based on figure 9.5(*a*), it is also apparent that values of P_L are significantly smaller than other invariants, such as Q_L and R_L for all flow conditions. For the flows of water at different Re_ϕ, PDFs of Q_L and R_L overlap. Values of Q_L tend to be more positively skewed, while values of R_L are more negatively skewed. The PDF in R_L also cover a larger range of values than Q_L. Relative to water, the PAM flow has much fewer instances of non-zero values in both Q_L and R_L. Interestingly, PDFs of Q_L and R_L for PAM do not have a noticeable skeweness and reflect a similar range of values, unlike the PDFs for water.

Figure 9.5(*b*) demonstrates PDFs of Q_W, Q_D and R_D for the flows of water and PAM. As expected, all values of Q_D are negative, while all values of Q_W are positive. Similar to figure 9.5(*a*) PDFs of Q_W, Q_D

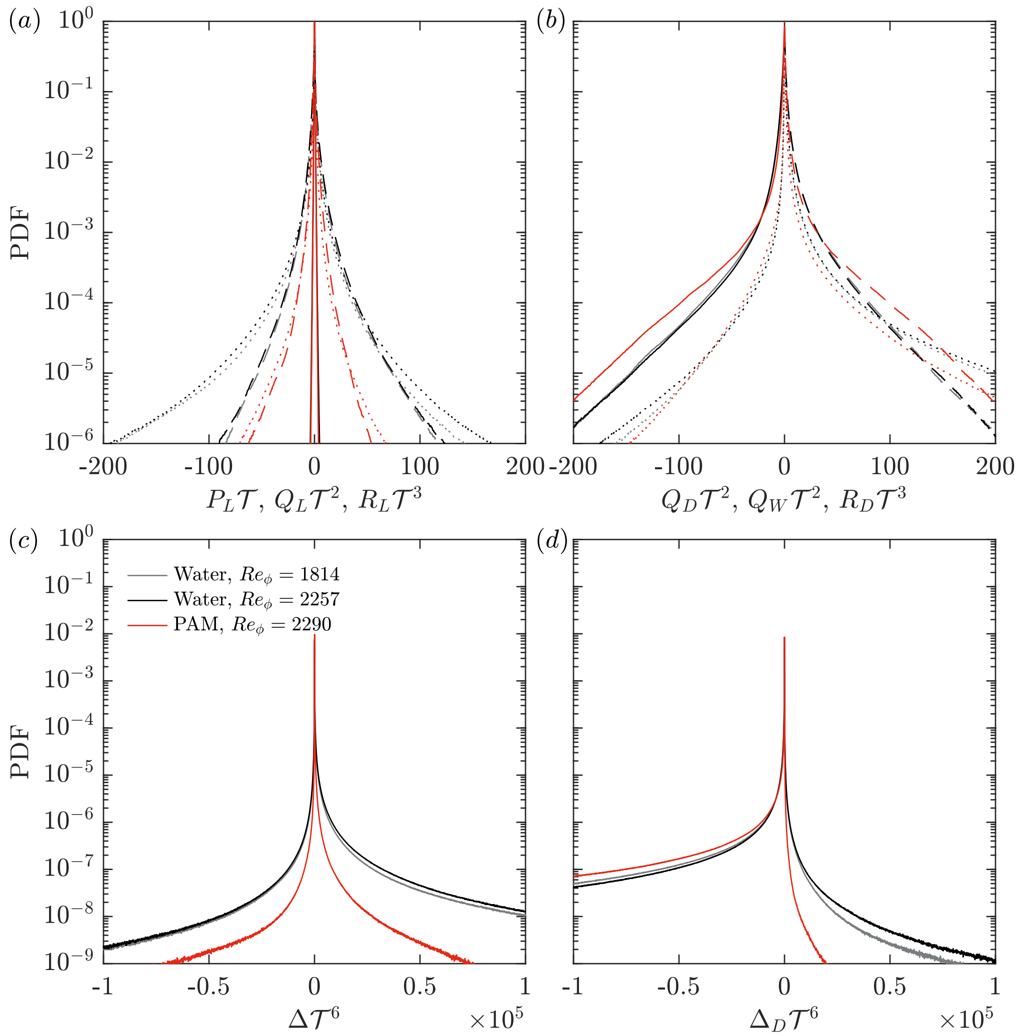

Figure 9.5: Probability density functions of (a) P_L, Q_L and R_L, (b) Q_D, Q_W and R_D, (c) Δ, and (d) Δ_D, for all measured y^+. In (a) PDFs of P_L are the solid lines, PDFs of Q_L are the dashed lines, and PDFs of R_L are the dotted lines. In (b) PDFs of Q_D are the solid lines, PDFs of Q_W are the dashed lines, and PDFs of R_D are the dotted lines. All flow gradients are made dimensionless by multiplying by the large eddy turnover time $\mathcal{T}$.

and R_D overlap for the flows of water at different Re_ϕ. The flow of PAM, on the other hand, has a higher likelihood of non-zero values of Q_W and Q_D compared to water – an opposite trend than the PDFs shown in figure 9.5(a). The PDF of R_D is similar for PAM and water for negative values of R_D; however, the probability of positive R_D values is lower for PAM compared to water.

Figure 9.5(c) shows PDFs of the discriminant Δ established using (3.28). PDFs of Δ are positively skewed and overlap for the two boundary layer flows of water. The boundary layer flow of PAM, on the other hand, has fewer instances of non-zero Δ. PDFs of Δ_D determined from (3.31) are provided in figure 9.5(d). Recall from §3.3 that the discriminant Δ_D is always less than 0. This is predicated on the assumption that $P_L = P_D = 0$ and (3.29) only consists of the invariants Q_D and R_D. Therefore, the positive values of Δ_D seen in the PDFs of figure 9.5(d) are a result of the divergence error or non-zero values of P_L. Despite the appearance that the PAM flow has fewer instances of $\Delta_D > 0$ in figure 9.5(*d*), the percentage of values with $\Delta_D > 0$ among all flows is similar and between 12-13%. Although this is not ideal, this discrepancy is not outside the norm for experimentally derived velocity vectors – see the comparable divergence error among the current measurements and previous experimental works in Appendix A.5.

Joint probability density functions (JPDFs) of the different invariants in $\mathbf{L}$, $\mathbf{D}$, and $\mathbf{W}$ are used to determine the distribution of fine scale motions within certain wall-normal bounds of each flow (§3.3). The wall-normal bounds include the buffer layer ($5 < y^+ < 30$), the log layer ($y^+ > 30$, $y/\delta < 0.3$), and the wake region ($y/\delta > 0.3$) (Pope, 2000). The JPDFs of Q_L and R_L (similar to figure 3.5), Q_D and R_D (figure 3.6), $-Q_D$ and Q_W (figure 3.7) are presented for each wall-normal region of the flow. The results for the boundary layers of water are first shown, followed by PAM. Figure 9.6 presents JPDFs of the different tensor invariants for water with an Re_ϕ of 1814 alongside the other flow of water with an Re_ϕ of 2257. Filled contours corresponds to the lower Re_ϕ case, while the open contours with black dashed lines are the higher Re_ϕ scenario.

The JPDF of Q_L and R_L within the buffer layer, log layer and wake region are presented in figures 9.6(*a, b, c*) respectively, for the different boundary layers of water. Within the buffer layer, i.e., figure 9.6(*a*), the $Q_L - R_L$ JPDF is skewed towards positive Q_L, but rather evenly distributed among positive and negative values of R_L. Overall, there is preference towards focal topologies with $\Delta > 0$. Moving farther away from the wall and into the log layer, the $Q_L - R_L$ JPDF in figure 9.6(*b*) continues to reflect a preference for topologies with $\Delta > 0$. As expected, the strength of the velocity gradients diminishes with increasing distance from the wall and the range of possible Q_L and R_L values decreases. Within the log layer, the shape of the $Q_L - R_L$ JPDF takes on a more well-defined tear-drop pattern with a clear point at the right-Vieillefosse tail ($\Delta = 0$, $R_L > 0$) compared to the JPDF of the buffer layer in figure 9.6(*a*). Moving into the wake region, figure 9.6(*c*) demonstrates that the range in possible values of Q_L and R_L continues to decrease with increasing y. That being said, the general shape of the $Q_L - R_L$ JPDF is similar to that of the log-layer in figure 9.6(*b*). A similar enhancement in the shape of the tea-drop pattern with increasing y was also observed in Newtonian DNS of channel flows by both Blackburn *et al.* (1996) ($Re_\tau = 395$) and Mortimer & Fairweather (2022) ($Re_\tau = 180$), and boundary layers by Chong *et al.* (1998), who used the boundary layer DNS of Spalart (1988) with an Re_ϕ of 670. When comparing the JPDFS of Q_L and R_L for water at different Re_ϕ, similar contour levels overlap within their respective wall-normal region of the flow, implying the flows at different Re_ϕ posses a similar distribution of fine scale motions.

The most notable difference between the $Q_L - R_L$ JPDFs of figure 9.6(*a, b, c*) and that of Newtonian wall-bounded DNS (Blackburn *et al.*, 1996; Chong *et al.*, 1998; Mortimer & Fairweather, 2022), is that DNS produces a more "pointed" ridge at the right Vieillefosse tail. Buxton *et al.* (2011) demonstrated that divergence errors, inherent in most experimentally derived velocity vectors, do not alter the general shape and limits of the $Q_L - R_L$ JPDF, with the exception that it erodes the tip of the $Q_L - R_L$ JPDF along the right-Vieillefosse tail, making it more rounded. Although the tip of the tear-drop pattern becomes more rounded from divergence errors, Buxton *et al.* (2011) demonstrated that it continues to remain centred on the right-Vieillefosse tail, i.e., $\Delta = 0$. Considering the present measurements have a comparable divergence error to that of prior experimental invesitgations of the VGT, as demonstrated in Appendix A.5, the JPDFs shown

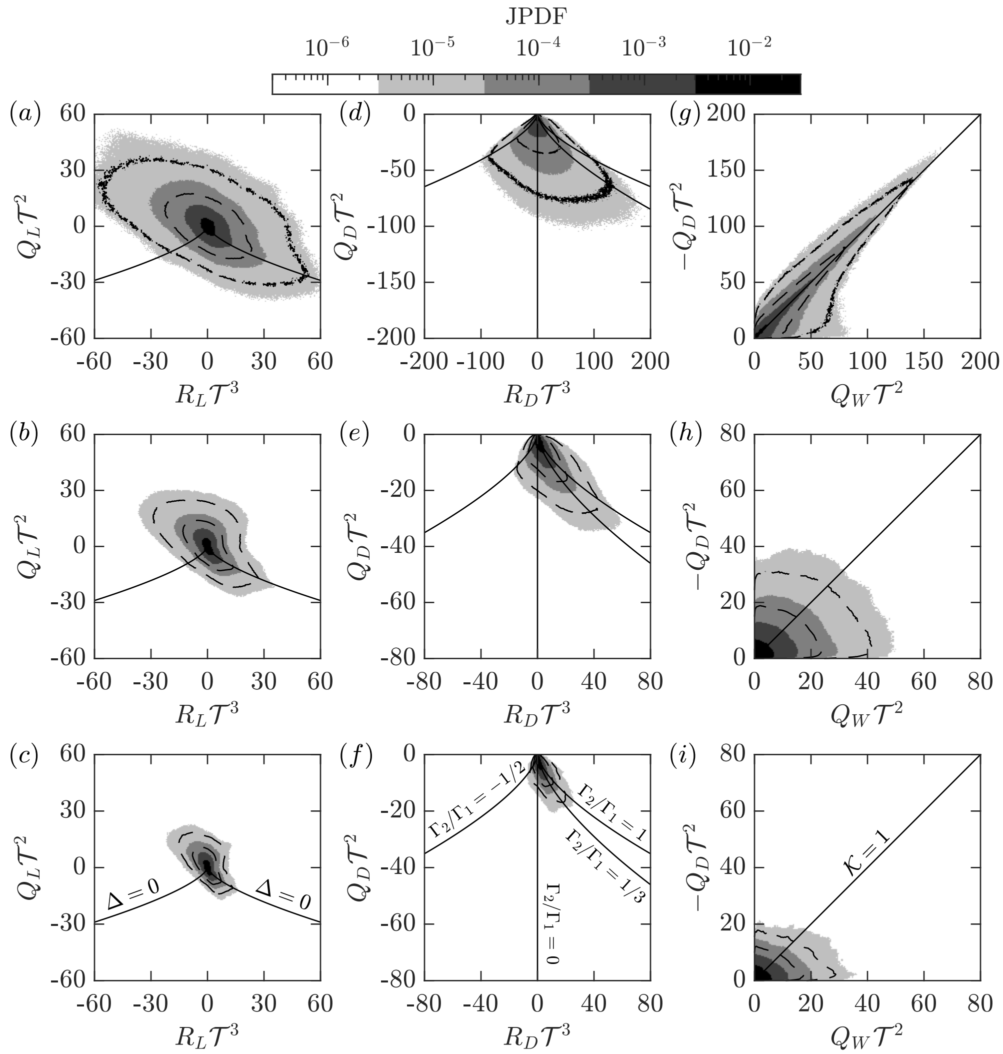

Figure 9.6: Joint probability density functions of the invariants in the VGT, rate of deformation tensor and rate of rotation tensor for boundary layers of water. Rows of figure correspond to different wall-normal locations: (*a, b, c*) buffer layer, (*d, e, f*) log layer, (*g, h, i*) wake region. Columns of figure correspond to JDFs of different invariants: (*a, d, g*) Q_L and R_L, (*b, e, h*) Q_D and R_D, (*c, f, i*) $-Q_D$ and Q_W. Filled contours are the JPDFs of water with $Re_\phi = 1814$, open contours with black dashed lines are the JDFs of water with $Re_\phi = 2257$ at 10^{-5} and 10^{-4}.

in figure 9.6(*a, b, c*) should provide a reasonable depiction of the distribution of fine scale motions within the Newtonian boundary layer. Moreover, the $Q_L - R_L$ JPDFs overlap for the different flows of water with unique Re_ϕ and spatial resolutions. Also, the JPDFs of Q_L and R_L take on a similar shape as those derived experimentally in a Newtonian turbulent boundary layer with approximately 5 times the spatial resolution of the present measurements and a presumably higher divergence error (Elsinga & Marusic, 2010).

Figure 9.6(*d, e, f*) demonstrates the JPDFs of the invariants in $\mathbf{D}$ for the water boundary layers with different Re_ϕ. JPDFs of Q_D and R_D are presented alongside lines of different eigenvalue ratios, namely Γ_2/Γ_1, similar to that shown in figure 3.6. Recall from §3.3 that $\Gamma_2/\Gamma_1 = 1$ corresponds to biaxial extension,

$\Gamma_2/\Gamma_1 = 0$ represents steady shear or planar extension, and $\Gamma_2/\Gamma_1 = -1/2$ is uniaxial extension. Ashurst *et al.* (1987) demonstrated that the most probable eigenvalue ratio was Γ_2/Γ_1 of 1/3 using DNS of Newtonian isotropic turbulence, hence $\Gamma_2/\Gamma_1 = 1/3$ is also shown on figure 9.6(*d, e, f*). Within the buffer layer, shown in figure 9.6(*d*), there is a higher preference towards unstable node-saddle-saddle flow events with $R_D > 0$ and Γ_2/Γ_1 between 0 and 1. Interestingly, a large ridge in the $Q_D - R_D$ JPDF within the buffer layer appears to align with the preferential eigenvalue ratio of $\Gamma_2/\Gamma_1 = 1/3$ for the Newtonian isotropic turbulence found by Ashurst *et al.* (1987). Moving away from the wall to the log layer and wake region shown in figure 9.6(*e, f*), the flow becomes increasingly skewed toward biaxial extensional flow events with $R_D > 0$ and $\Gamma_2/\Gamma_1 > 0$. Compared to the $Q_D - R_D$ JPDF of the buffer layer, shown in figure 9.6(*d*), the log layer and wake regions have more events with $\Delta_D > 0$, indicative of divergence errors. Based on Appendix A.5, and also shown in Ganapathisubramani *et al.* (2007) and Gomes-Fernandes *et al.* (2014), regions of the flow with lower velocity gradients are generally coupled with larger divergence errors. Therefore, it is expected that the log and wake layers, with overall smaller velocity gradients than the buffer layer, may exhibit higher divergence errors – an effect of this being a positive Δ_D. That being said, the JPDFs of Q_D and R_D are generally similar to those derived from Blackburn *et al.* (1996) and Chong *et al.* (1998) using DNS of a Newtonian channel flows ($Re_\tau = 395$) and boundary layers ($Re_\phi = 670$), where preference to $R_D > 0$ grows as y increases. Similar to the VGT invariants, $Q_D - R_D$ JPDFs of water at different Re_ϕ overlap, implying the straining motions within Newtonian flow are also similar among turbulent boundary layers at different Re_ϕ.

JPFs of the invariants $-Q_D$ and Q_W are presented for the water boundary layers at different Re_ϕ in figure 9.6(*g, h, i*), similar to that of figure 3.7. Much like the previously detailed JPDFs of $Q_L - R_L$ and $Q_D - R_D$, the JPDFs of $-Q_D$ and Q_W overlap for the water flows at different Re_ϕ. Within the buffer layer of the flow, shown in figure 9.6(*g*), there is a preference towards flow motions exhibiting conditions consistent with steady shear, with $\mathcal{K} = 1$. Soria *et al.* (1994) detailed that turbulent mixing layers with flow regions having $\mathcal{K} = 1$ consisted almost entirely of vortex sheets. Chong *et al.* (1998) demonstrated a similar preference to $\mathcal{K} = 1$ and vortex sheet topologies within the buffer layer of a turbulent boundary flow with an Re_ϕ of 670, that was derived from Newtonian DNS (Spalart, 1988). Although the JPDF of figure 9.6(*g*) is concentrated around $\mathcal{K} = 1$, there are deviations, particularly at smaller values of $-Q_D$ and Q_W. Chong *et al.* (1998) similarly observed subtle deviations from $\mathcal{K} = 1$ within the buffer layer near the origin of $-Q_D$ and Q_W in their analysis of Newtonian boundary flow DNS by Spalart (1988). Within the log and wake layers of the flow, shown in figure 9.6(*h, i*), a large spread between $\mathcal{K}$ of 0 and ∞ emerges. Therefore, fine scale motions within the log and wake layers take on a variety of patterns, ranging from extensional to rotational, and the topology is similar to isotropic turbulence seen in Ooi *et al.* (1999).

JPDFs of the invariants of $\mathbf{L}$, $\mathbf{D}$, and $\mathbf{W}$ are shown in figure 9.7 for the polymer-laden boundary layer at different wall-normal regions of the flow. The limits of the wall-normal regions are the same as those from figure 9.6. Open contours with black dashed lines in figure 9.7 are the JPDFs of water with an Re_ϕ of 2257. Figure 9.7(*a*) provides the JPDF of Q_L and R_L for $5 < y^+ < 30$. Compared to the flow of water at a similar Re_ϕ, the PAM boundary layer has attenuated values of Q_L and R_L. The range in possible R_L values narrows considerably compared to water – almost a two fold reduction in the largest magnitude of R_L. A narrower range in R_L was similarly observed by Mortimer & Fairweather (2022) for drag-reduced viscoelastic channel flows at an Re_τ of 180 and derived from DNS. This is a general indication that stretching and extensional motions within the flow are diminished. Moving away from the wall, figure 9.7(*b*) demonstrates the $Q_L - R_L$ JPDF for $y^+ > 30$ and $y/\delta < 0.3$. Evidently, a reduction in the magnitude of Q_L and R_L relative to water at a similar Re_ϕ is still present farther from the wall. The tear-drop pattern no longer exists in the $Q_L - R_L$ JPDF of PAM, and a well-defined tip does not appear along the right-Vieillefosse tail. The trend continues into the wake region of the flow; figure 9.7(*c*) demonstrates again how the range of possible Q_L and R_L values is diminished for PAM relative to water. This is despite the fact that the boundary layers of PAM and water have comparable velocity fluctuations within the outer layer of the flow, as seen in figure 9.3(*b*).

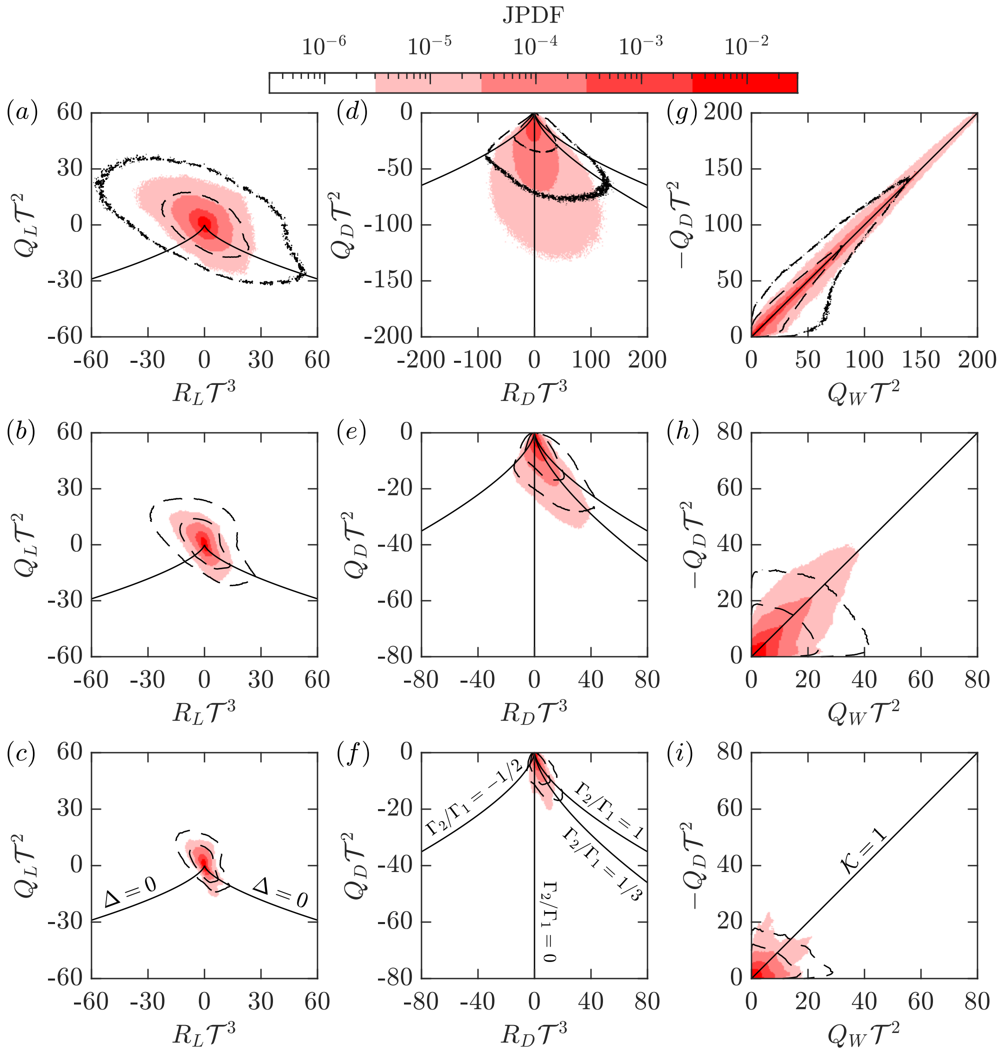

Figure 9.7: Joint probability density functions of the invariants in the VGT, rate of deformation tensor and rate of rotation tensor for boundary layers of water. Rows of figure correspond to different wall-normal locations: (*a, b, c*) buffer layer, (*d, e, f*) log layer, (*g, h, i*) wake region. Columns of figure correspond to JDFs of different invariants: (*a, d, g*) Q_L and R_L, (*b, e, h*) Q_D and R_D, (*c, f, i*) $-Q_D$ and Q_W. Filled contours are the JPDFs of the PAM boundary layer, open contours with black dashed lines are the JDFs of water with $Re_\phi = 2257$ at 10^{-5} and 10^{-4}.

Perhaps the most obvious difference between the topology of PAM and water are revealed in the JPDFs of Q_D and R_D. Figure 9.7(d) demonstrates the $Q_D - R_D$ JPDF for the polymer-laden boundary layer relative to water for $5 < y^+ < 30$. Although there is still a bias towards an unstable node-saddle-saddle flow type, the preference to $R_D > 0$ is greatly diminished relative to water at a similar Re_ϕ. Rather, the flow tends towards an eigenvalue ratio Γ_2/Γ_1 of 0, where the flow is more two-dimensional with conditions comparable to steady shear or planar extension. Farther from the wall for $y^+ > 30$, straining motions within the flow of PAM shown in figure 9.7(e, f) become more biased towards biaxial stretching, but do not show aa strong of a preference to $\Gamma_2/\Gamma_1 = 1$ as water.

JPDFs of $-Q_D$ and Q_W also demonstrate an unambiguous difference between fine scale motions within the polymer-laden and Newtonian boundary layers. Compared to water, the flow of PAM near the wall shown in figure 9.7(g) consists of $-Q_D$ and Q_W values that are almost always equivalent and concentrated on the line $\mathcal{K} = 1$. Together, with figure 9.7(d), this implies that the near-wall flow of PAM is primarily two-dimensional and shear-dominate, with sheet-like motions. Moving farther from the wall and into the range of $y^+ > 30$ and $y/\delta < 0.3$, the higher tendency for the PAM flow to exhibit features with $\mathcal{K} = 1$ continues. Compared to the flow of water at a similar Re_ϕ, the JPDF of $-Q_D$ and Q_W shown in figure 9.7(h) shows more of a preference towards shear-dominate flow with $\mathcal{K} = 1$, albeit less so than the PAM flow near the wall for $5 < y^+ < 30$. Within the wake region, figure 9.7(i) demonstrates a more scattered JPDF of $-Q_D$ and Q_W for the flow of PAM with no clear preference to a particular value of $\mathcal{K}$, but also no overlap with the JPDF of water at a similar Re_ϕ.

Based on the JPDFs of Q_D and R_D shown in figure 9.6(d, e, f) most straining motions within the Newtonian boundary layers were unstable node-saddle-saddle, with Γ_2/Γ_1 greater than 0. However, for the polymer-laden boundary layer, shown in figure 9.7(d, e, f), straining motions near the wall were more two-dimensional where $\Gamma_2/\Gamma_1 = 0$, and the local fine scale motions are akin to steady shear or planar extension. PDFs of Γ_2/Γ_1 are provided for the Newtonian and polymer-laden boundary layers within the buffer, log and wake regions in figure 9.8(a, b, c) respectively. The eigenvalues Γ_1 and Γ_2 are determined from locally solving (3.29) at every spatial coordinate and time instance. For the boundary layers of water, PDFs of Γ_2/Γ_1 overlap within the buffer layer, log layer and wake region. The probability of $\Gamma_2/\Gamma_1 > 0$ for the boundary layers of water are 58%, 70% and 70% for the buffer layer, log layer and wake region respectively, demonstrating the overall preference to an unstable node-saddle-saddle topology. Based on the near-wall PDF of Γ_2/Γ_1 for the PAM boundary layer, shown in figure 9.8(a), there is much higher probability of Γ_2/Γ_1 being zero compared to the flows of water. Moreover, the Γ_2/Γ_1 PDF of the near wall boundary layer of PAM, depicted in figure 9.8(a), has a probability of $\Gamma_2/\Gamma_1 > 0$ of 49%, which is 9% lower than water. Therefore, biaxial stretching events with $\Gamma_2/\Gamma_1 > 0$ are less abundant and two-dimensional shear or planar extensional flow features with $\Gamma_2/\Gamma_1 = 0$ are more common in the polymer-laden boundary layers for $y^+ < 30$. Despite the appearance of subtle difference in the JPDFs of Q_D and R_D in the log and wake regions among PAM and water in figure 9.7(e, f), the PDFs of Γ_2/Γ_1 shown in figure 9.8(b, c) demonstrate that the distribution of Γ_2/Γ_1 values is similar for the Newtonian and polymer-laden flows.

JPDFs of $-Q_D$ and Q_W for the Newtonian boundary layers, shown in figure 9.6(g), demonstrated that the flow near the wall consisted mostly of two-dimensional vortex sheets where $\mathcal{K} = 1$. However, in the log

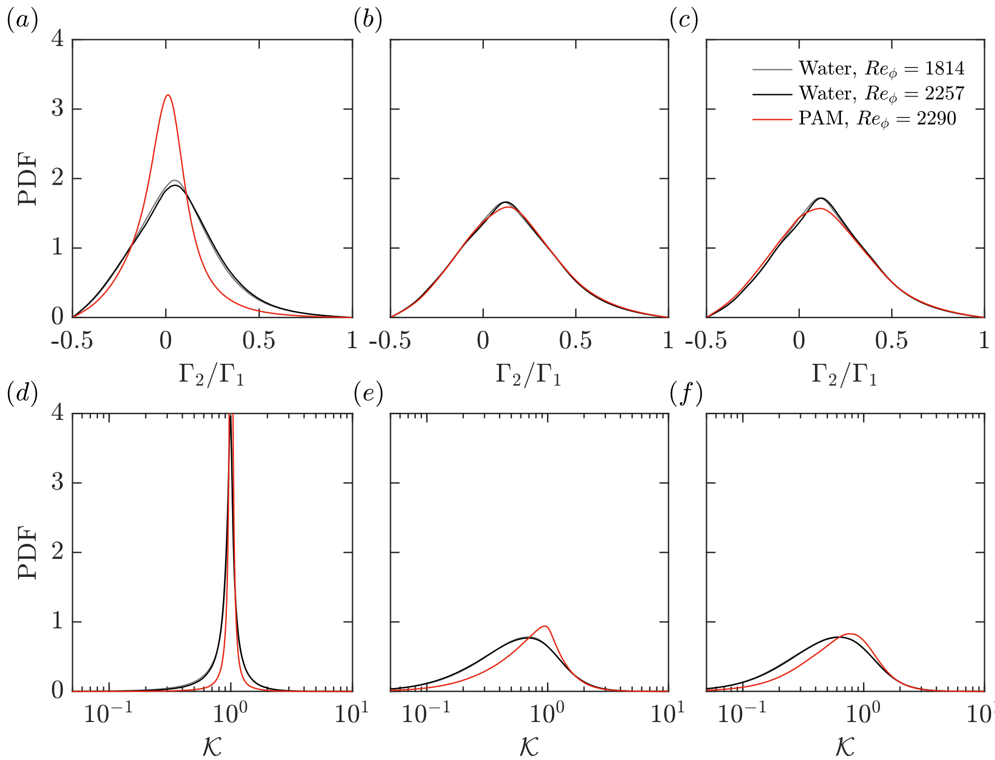

Figure 9.8: Probability density functions of (*a, b, c*) the ratio between the second and first eigenvalues of $\mathbf{D}$, and (*d, e, f*) the kinematical vorticity number $\mathcal{K}$ from (3.33). PDFs in (*a, b, c*) are conditioned to exclude $\Delta_D > 0$. PDFs (*a, d*) correspond to the buffer layer, (*b, e*) the log layer, and (*c, f*) the wak region.

and wake layers, shown in figure 9.6(*h, i*), the flow had a variety of dissipative and vortical motions with $\mathcal{K}$ between 0 and ∞, similar to isotropic turbulence (Ooi *et al.*, 1999). For the polymer-laden boundary layer, the flow was even more concentrated around $\mathcal{K} = 1$ within the buffer and log layers in figures 9.7(*g, h*) compared to water, while the topology within the wake region was scattered, with $\mathcal{K}$ between 0 and ∞. PDFs of $\mathcal{K}$ for the Newtonian and polymer-laden boundary layers are shown for the buffer, log and wake regions of the flows in figure 9.8(*d, e, f*). PDFs of $\mathcal{K}$ overlap for the flows of water at different Re_ϕ at all wall-normal regions. Within the buffer layer, figure 9.8(*e*) demonstrates visibly Gaussian PDFs of $\mathcal{K}$ where the average of $\mathcal{K}$ for water and the flow of PAM are both 1. However, the standard deviation in $\mathcal{K}$ for the polymer-laden flow is smaller and approximately equal to 0.15, compared to water where the standard deviation in $\mathcal{K}$ is 0.45. Within the log layer, water is slightly more biased towards $\mathcal{K} < 1$; the mode and median in the PDF of $\mathcal{K}$ for water shown in figure 9.8(*e*) is 0.685 and 0.910, respectively. For the polymer-laden boundary layer, the mode and median in the PDF of $\mathcal{K}$ within the log layer, shown in figure 9.8(*e*), is larger compared to water and equal to 0.945 and 0.975, respectively. Therefore, the polymer laden flow has less likelihood to exhibit dissipative topologies compared to water. In the wake region, the PDFs of water boundary layers shown in figure 9.8(*f*) are not significantly different than those of water in the log layer seen in figure 9.8(*e*). Also similar to the log layer, the wake region of the polymer-laden flow has a lower probability of exhibiting dissipative flow topologies and a higher preference towards $\mathcal{K}$ of 1.

9.5 Summary

The topology of a polymer-laden boundary layer was compared with two Newtonian turbulent boundary layers, one at a similar friction Reynolds number Re_τ of 687, and the other at a similar momentum thickness based Reynolds number Re_ϕ of 2290. Relative to the Newtonian boundary layer with a similar Re_ϕ, the polymeric flow had a 33% lower skin friction coefficient. Joint probability density functions (JPDFs) of the invariants in the velocity gradient tensor, the rate of deformation tensor and the rate of rotation tensor were used to establish a distribution of the different fine scale motions within the polymer-laden and Newtonian boundary layers, some of which include extensional- and vortical-type flow motions.

Unambiguous difference in the JPDFs of the invariants in the velocity gradient tensor, Q_L and R_L, were observed between the polymer-laden and Newtonian boundary layers. The JPDFs of Q_L and R_L for the Newtonian boundary layers overlapped with one another and exhibited the well-known tear-drop shaped pattern with a clear ridge at the right-Vieillefosse tail. Relative to the Newtonian flows, the polymer-laden boundary layer had attenuated values of Q_L and R_L; although values of R_L were diminished much more than Q_L. A narrowing of R_L provides evidence that uniaxial and biaxial stretching is less abundant within the polymer-laden flows.

Alterations to the invariants in the rate of deformation and rate of rotation tensor are more telling of the attenuation in the uniaxial and biaxial extension within the polymer-laden flow – particularly within the inner layer or $y/\delta < 0.3$. Here, the invariants of the rate of deformation tensor, Q_D and R_D, imply that straining motions of the polymeric flow are more two-dimensional and there is a higher preference for the second eigenvalue in the rate of deformation tensor to be zero compared to water. Moreover, JPDFs of Q_D and the invariant in the rate of rotation tensor Q_W, suggest that extensional flow motions (particularly biaxial extension) within the polymer-laden flow are less abundant and there is a larger bias towards shear-dominate flow and sheet-like motions. These sheet-like structures are similar to those seen in the viscous sublayer of Newtonian turbulence. However, in the polymer-laden flow these sheet-like motions are found at y^+ larger than the conventional limit of the viscous sublayer, implying that the viscous sublayer of the polymer-laden flow is thicker compared to water.

Part V

Closing

Chapter 10

Conclusions

The present thesis compared the rheology and turbulence of three different non-Newtonian solutions comprising drag-reducing additives (DRAs). The different drag-reducing solutions consisted of a flexible polymer polacrylamide (PAM), rigid polymer xanthan gum (XG) and a cationic surfactant referred to as C14. Conventional rheological measurements included steady shear, dynamic shear and extensional viscosity measurements. Nontrivial rheometry was evaluated by experimentally investigating the fluids in a steady, laminar flow through a periodically constricted tube (PCT). Lastly, the turbulence of the drag-reducing solutions were measured in a high Reynolds number channel flow and boundary layer. Particle image velocimetry and particle tracking velocimetry were used to measure the velocity statistics and coherent flow patterns within the wall-bounded turbulent flows of drag-reducing fluids.

10.1 Rheology of drag-reducing solutions

Chapter 5 documented the results of the conventional shear and extensional rheology measurements of the DRA solutions at concentrations between 100 ppm and 500 ppm. Steady shear rheology of XG and PAM demonstrated that both fluids exhibit shear thinning, while the C14 solutions had a viscosity similar to water for all concentrations. Dynamic shear rheology showed that large concentration solutions of PAM and XG were viscoelastic, but mostly viscous dominant with a loss modulus greater than gain modulus. Linear viscoelasticity measurements could not be performed for the C14 solutions; however, it is expected that the gain modulus for the C14 solutions is negligible considering their shear viscosity is comparable to water. PAM solutions were the only non-Newtonian fluids to exhibit elastocapillary thinning from extensional rheology. XG and C14 had no measurable extensional relaxation time, implying the extensional viscosity of XG and C14 is significantly smaller than PAM. Although shear and extensional rheological measurements were exclusively compared in §5, other investigations throughout this dissertation (including §§7, 8 and 9) reciprocated these findings.

In chapter 6, the velocity of the DRA solutions in a PCT were experimentally measured using particle shadow velocimetry. The PCT revealed that C14 solutions have similar non-Newtonian features as PAM solutions when the Reynolds number (Re) exceeded 100 in the PCT. Unlike PAM solutions, the non-Newtonian features of the C14 solutions were not detectable from conventional shear and extensional rheometric measurement techniques, as shown in §5,. Therefore, the measurements using the PCT proved to be a novel technique for uncovering the elastic features of dilute surfactant solutions. Extension or mixed kinematics within the PCT flows of C14 promoted the formation of flow-induced structures. It is hypothesized that these structures are long wormlike aggregates of micelles that are analogous to flexible polymers. These wormlike aggregates do not form in the conventional shear and extensional rheometric flows. C14 solutions that exhibited non-Newtonian features within the PCT, reflected qualitative similarities with inertioelastic PAM flows with Deborah number (De) greater than 0.1 and $Re > 35$. A preliminary estimate of the elastic relaxation time of the flow-induced structures was established based on comparisons with PAM flows. However, fine tuning this estimate of the relaxation time requires a denser sweep of Re and De for the PAM flows within the PCT.

10.2 Velocity statistics of drag-reduced channel flows

Chapter 7 measured the one-point and two-point velocity statistics of the different DRA solutions at a common drag reduction percentage (DR). The experimental investigation demonstrated that different DRAs generate drag-reduced channel flows with similar turbulence statistics, provided DR and Re are similar. Although the drag-reduced flows had similar velocity statistics, a common rheological feature that can be associated with drag reduction could not be identified. The extensional relaxation time, that has been shown to correlate with drag reduction for flexible polymers, does not seem to be pertinent for drag-reducing solutions of rigid polymers and surfactants. This ambiguity in our understanding can be explained two fold.

1. DRAs have a common rheological property that has yet to be identified from rheological measurements. This implies that the different additives reduce the turbulent drag via a common mechanism. This appears to be plausible for flexible polymers and surfactants, based on the observations of §6 and the similar response between PAM and C14 in the PCT.

2. The rheological feature responsible for drag reduction is different among the DRAs. This suggests that wall turbulence responds similarly to the different drag reduction mechanisms induced by fluids with unique rheology. Of the three DRAs, rigid polymers are the outlier. At a similar DR, solutions of XG are more shear thinning than the PAM solutions, but have no measurable extensional features. They also do not exhibit a chevron-pattern response in the PCT, like PAM and C14. Therefore, it is asserted that the XG solution reduces drag differently than the other DRAs, and primarily due to shear thinning. This notion was explored further in chapter 8

In chapter 8, the Carreau-Yasuda model and the spatial gradient in the velocity were used to approximate the instantaneous viscosity of different drag-reduced channel flows of XG. All XG flows possessed a near wall region that was thin and had a low mean viscosity. Fluid at wall-normal locations immediately above this region demonstrated dramatic growth in the mean viscosity. Viscosity fluctuations similarly reflected different size and characteristics with increasing distance from the wall. However, these viscosity fluctuations were shown to have a negligible contribution to the mean stress balance of the flow. Instead, drag reduction was primarily driven by a trade-off between viscous and turbulent Reynolds stresses in the budget of mean stress. The thin low viscosity layer is denoted as a “lubricating layer,” analogous to the wall-normal viscosity stratification observed in lubricated wall-bounded flows of immiscible fluids. This lubricating layer encapsulated the expanded linear viscous sublayer and portions of the buffer layer for flows of the XG solution. Its extent corresponded roughly to the peak in the indicator function, ζ. Unlike the classical theories of polymer drag reduction, it is hypothesized that rigid polymer drag reduction is largely attributed to gradients in the mean velocity coupled with the solutions shear thinning rheology. The lubricating layer is a product of this interaction and a mechanism for generating an effective slip within the buffer layer.

10.3 Local flow topology of polymer-laden boundary layer

Based on the viscous theory of drag reduction, the large extensional viscosity of flexible polymer solutions is believed to oppose regions of the flow exhibiting uniaxial and biaxial extension, and mitigate the strength and formation of counterrotating streamwise vortices (Lumley, 1973; Roy *et al.*, 2006). Chapter 9 sought to observe this effect by measuring the distribution of extensional and vortical motions within a polymer-laden boundary layer using three-dimensional particle tracking velocimetry and the Δ-*criterion* of Chong *et al.* (1990). The assertion that extensional flow motions are opposed within the polymer-laden boundary layer was shown to be plausible. It was demonstrated that extensional straining motions, predominately biaxial extension, are less pervasive within the inner layer of the polymeric flow compared to water at similar Re. Furthermore, strong vortical motions are also less abundant. Instead, the flow exhibits sheet-like structures similar to those found in the viscous sublayer of Newtonian turbulence, but at $y^+ > 5$, implying an expansion of the viscous sublayer. Each of these observations supports the assertions of Lumley (1973), and the simulations of Roy *et al.* (2006), that an attenuation of biaxial extensional flow motions inhibits vortical motions near the wall, expands the buffer layer and reduces skin friction.

10.4 Suggested future works

There are many research opportunities that can be explored to expand upon the findings of the current thesis. Three suggestions are provided.

Flow-induced structures of surfactants

At certain temperatures and concentrations, surfactants are known to form micelles of different shape (e.g., spherical, rodlike and wormlike micelles). Upon exposure to flow, it is hypothesized that these micelles group together to form higher-order structures or bundles of micelles called flow-induced structures. In §6 it was assumed that flow-induced structures were formed within the PCT; however, the shape of the micelles, let alone the flow-induced structures, were not determined. Measurements of the shape and conformation of these micelles and the resulting flow-induced structures (using for example, transmission electron microscopy, small angle neutron scattering and flow-induced birefringence) could provide better evidence of how these additives compare with polymers.

Simulations of generalized Newtonian models

Numerical simulations have commonly used viscoelastic constitutive equations, such as FENE-P, to model the flow of drag-reducing flexible polymer solutions. Although such simulations have observed drag reduction, it is unclear how the inputs to these simulations map to realistic flows and fluids. On the other hand, generalized Newtonian fluids use rheologically measured trends and constants to construct the constitutive model. The work in §8, along with the simulations of Owolabi *et al.* (2023), demonstrated that these models could be viable, although this requires further exploration. Direct comparisons between experiments and simulations using rheological measurements are needed.

Measuring in-situ elastic properties

The debate between the viability of the viscous versus elastic theory of drag reduction is ongoing. The present work of §9 drew inspiration from the viscous theory and provided some evidence in support of its applicability; however, this does not discredit the elastic theory. The elastic theory of de Gennes (1990), states that drag reduction occurs when the elastic energy becomes comparable to turbulent kinetic energy. While turbulent kinetic energy can be measured using flow measurements, elastic energy is more difficult to discern within a turbulent flow. Elasticity is a Lagrangian quality that depends on the initial configuration of the material. Kumar *et al.* (2022) provided a means for discerning elastic stresses using Lagrangian coherent structures, which can be measured. However, this has yet to be explored experimentally.

Bibliography

Abu-Rowin, W. & Ghaemi, S. 2019 Streamwise and spanwise slip over a superhydrophobic surface. *J. Fluid Mech.* **870**, 1127–1157.

Abu-Rowin, W., Hou, J. & Ghaemi, S. 2017 Inner and outer layer turbulence over a superhydrophobic surface with low roughness level at low reynolds number. *Phys. Fluids* **29**, 095106.

Abu-Rowin, W., Sanders, S. R. & Ghaemi, S. 2018 A recipe for optimum mixing of polymer drag reducers. *J. Fluids Engng* **140**, 1–10.

Adrian, R. J. 1984 Scattering particle characteristics and their effect on pulsed laser measurements of fluid flow: speckle velocimetry vs particle image velocimetry. *Appl. Opt.* **23** (11), 1690–1691.

Afonso, A. & Pinho, F. T. 2006 Numerical investigation of the velocity overshoots in the flow of viscoelastic fluids inside a smooth contraction. *J. Non-Newtonian Fluid Mech.* **139** (1-2), 1–20.

Ahrens, M., Yoo, Y. J. & Joseph, D. D. 1987 Hyperbolicity and change of type in the flow viscoelastic fluids through pipes. *J. Non-Newtonian Fluid Mech.* **24** (1), 67–83.

Alves, M. A., Oliveira, P. J. & Pinho, F. T. 2020 Numerical Methods for Viscoelastic Fluid Flows. *Annu. Rev. Fluid Mech.* **53**, 509–541.

Alves, M. A. & Poole, R. J. 2007 Divergent flow in contractions. *J. Non-Newtonian Fluid Mech.* **144** (2-3), 140–148.

Arosemena, A. A., Andersson, H. I. & Solsvik, J. 2020 Turbulent channel flow of generalized Newtonian fluids at a low Reynolds number. *J. Fluid Mech.* **908**, A43.

Arosemena, A. A., Andersson, R., Andersson, H. I. & Solsvik, J. 2021 Effects of shear-thinning rheology on near-wall turbulent structures. *J. Fluid Mech.* **925**, A37.

Ashurst, Wm. T., Kerstein, A. R., Kerr, R. M. & Gibson, C. H. 1987 Alignment of vorticity and scalar gradient with strain rate in simulated navier–stokes turbulence. *Phys. Fluids* **30** (8), 2343–2353.

Astarita, G. 1967 Two dimensionless groups relevant in analysis of steady flows of viscoelastic materials. *Ind. Eng. Chem.* **6** (2), 257–262.

Astarita, G. 1979 Objective and generally applicable criteria for flow classification. *J. Non-Newtonian Fluid Mech.* **6**, 69–76.

Bąk, A. & Podgórska, W. 2016 Interfacial and surface tensions of toluene/water and air/water systems with nonionic surfactants tween 20 and tween 80. *Colloids Surf. A* **504**, 414–425.

Barnes, H. A., Hutton, J. F. & Walters, K. 1989 *An introduction to rheology*. Elsevier Science B.W.

Bewersdorff, H. W. & Ohlendorf, D. 1988 The behaviour of drag-reducing cationic surfactant solutions. *Colloid Polym. Sci.* **266**, 941–953.

Bewley, G. P., Sreenivasan, K. R. & Lathrop, D. P. 2008 Particles for tracing turbulent liquid helium. *Exp. Fluids* **44**, 887–896.

Bhardwaj, A., Richter, D., Chellamuthu, M. & Rothstein, J. P. 2007 The effect of pre-shear on the extensional rheology of wormlike micelle solutions. *Rheol. Acta* **46** (6), 861–875.

Biancofiore, L., Brandt, L. & Zaki, T. A. 2017 Streak instability in viscoelastic couette flow. *Phys. Rev. Fluids* **2** (4), 043304.

Bird, R. B., Armstrong, R. C. & Hassager, O. 1987 *Dynamics of polymeric liquids. Vol. 1: Fluid mechanics*. John Wiley and Sons Inc., New York, NY.

Bird, R. B., Stewart, W. E. & Lightfoot, E. N. 2007 *Transport phenomena.*. J. Wiley.

Bird, R. B. & Wiest, J. M. 1995 Constitutive equations for polymeric liquids. *Annu. Rev. Fluid Mech.* **27**, 169–93.

Blackburn, H. M., Mansour, N. N. & Cantwell, B. J. 1996 Topology of fine-scale motions in turbulent channel flow. *J. Fluid Mech.* **310**, 269–292.

Burger, E. D., Chorn, L.G. & Perkins, T.K. 1980 Studies of drag reduction conducted over a broad range of pipeline conditions when flowing Prudhoe Bay crude oil. *J. Rheology* **24**, 603–626.

Buxton, O. R. H., Laizet, S. & Ganapathisubramani, B. 2011 The effects of resolution and noise on kinematic features of fine-scale turbulence. *Exp. Fluids* **51** (5), 1417–1437.

Cable, P. J. & Boger, D. V. 1978*a* A comprehensive experimental investigation of tubular entry flow of viscoelastic fluids: Part i. vortex characteristics in stable flow. *AIChE J.* **24** (5), 869–879.

Cable, P. J. & Boger, D. V. 1978*b* A comprehensive experimental investigation of tubular entry flow of viscoelastic fluids. part ii. the velocity field in stable flow. *AIChE J.* **24** (6), 992–999.

Cable, P. J. & Boger, D. V. 1979 A comprehensive experimental investigation of tubular entry flow of viscoelastic fluids: Part iii. unstable flow. *AIChE J.* **25** (1), 152–159.

Carreau, P. J. 1972 Rheological equations from molecular network theories. *Trans. Soci. Rheol.* **16**, 99–127.

Cattafesta III, L. N. & Sheplak, M. 2011 Actuators for active flow control. *Ann. Rev. Fluid Mech.* **43**, 247–272.

Cheng, N. S. 2008 Formula for the viscosity of a glycerol- water mixture. *Ind. Eng. Chem. Res.* **47** (9), 3285–3288.

Chong, M. S., Perry, A. E. & Cantwell, B. J. 1990 A general classification of three-dimensional flow fields. *Phys. Fluids A* **2** (5), 765–777.

Chong, M. S., Soria, J., Perry, A. E., Chacín, J., Cantwell, B. J. & Na, Y. 1998 Turbulence structures of wall-bounded shear flows found using dns data. *J. Fluid Mech.* **357**, 225–247.

Collings, A. F. & Bajenov, N. 1983 A high precision capillary viscometer and further relative results for the viscosity of water. *Metrologia* **19**, 61–66.

Das, P. & Ghaemi, S. 2021 Light-scattering of tracer particles for liquid flow measurements. *Meas. Sci. Technol.* **32**, 065302.

Davidson, P. A. 2015 *Turbulence: an introduction for scientists and engineers*. Oxford University Press.

Davies, G. A. & Stokes, J. R. 2008 Thin film and high shear rheology of multiphase complex fluids. *J. Non-Newtonian Fluid Mech.* **148**, 73–87.

de Gennes, P. G. 1990 *Introduction to polymer dynamics*. Cambridge University Press.

Dean, R. B. 1978 Reynolds number dependence of skin friction and other bulk flow variables in two-dimensional rectangular duct flow. *J. Fluids Engng* **100**, 215–223.

Deiber, J. A. & Schowalter, W. R. 1979 Flow through tubes with sinusoidal axial variations in diameter. *AIChE J.* **25** (4), 638–645.

DEIBER, J. A. & SCHOWALTER, W. R. 1981 Modeling the flow of viscoelastic fluids through porous media. *AIChE J.* **27** (6), 912–920.

DINIC, J., JIMENEZ, L. N. & SHARMA, V. 2017 Pinch-off dynamics and dripping-onto-substrate (dos) rheometry of complex fluids. *Lab on a Chip* **17**, 460–473.

DINIC, J., ZHANG, Y., JIMENEZ, L.N. & SHARMA, V. 2015 Extensional relaxation times of dilute, aqueous polymer solutions. *ACS Macro Lett.* **4** (7), 804–808.

EBRAHIMIAN, M., SANDERS, S. R. & GHAEMI, S. 2019 Dynamics and wall collision of inertial particles in a solid–liquid turbulent channel flow. *J. Fluid Mech.* **881**, 872–905.

EKANEM, E. M., BERG, S., DE, S., FADILI, A., BULTREYS, T., RÜCKER, M., SOUTHWICK, J., CRAWSHAW, J. & LUCKHAM, P. F. 2020 Signature of elastic turbulence of viscoelastic fluid flow in a single pore throat. *Phys. Rev. E* **101** (4), 042605.

ELBING, B. R., PERLIN, M., DOWLING, D. R. & CECCIO, S. L. 2013 Modification of the mean near-wall velocity profile of a high-reynolds number turbulent boundary layer with the injection of drag-reducing polymer solutions. *Phys. Fluids* **25**, 085103.

ELSINGA, G. E. & MARUSIC, I. 2010 Evolution and lifetimes of flow topology in a turbulent boundary layer. *Phys. Fluids* **22** (1).

ELSINGA, G. E., SCARANO, F., WIENEKE, B. & VAN OUDHEUSDEN, B. W. 2006 Tomographic particle image velocimetry. *Exp. Fluids* **41** (6), 933–947.

ESCUDIER, M. P., NICKSON, A. K. & POOLE, R. J. 2009 Turbulent flow of viscoelastic shear-thinning liquids through a rectangular duct: Quantification of turbulence anisotropy. *J. Non-Newtonian Fluid Mech.* **160**, 2–10.

ESCUDIER, M. P, PRESTI, F. & SMITH, S. 1999 Drag reduction in the turbulent pipe flow of polymers. *J. Non-Newtonian Fluid Mech.* **81**, 197–213.

ESTEVADEORDAL, J. & GOSS, L. P. 2006 Particle shadow velocimetry.

EWOLDT, R. H., JOHNSTON, M. T. & CARETTA, L. M. 2015 Experimental challenges of shear rheology: How to avoid bad data. In *Complex Fluids in Biological Systems* (ed. S.E. Spagnolie), pp. 207–241. Springer.

FARSIANI, Y., SAEED, Z., JAYARAMAN, B. & ELBING, B. R. 2020 Modification of turbulent boundary layer coherent structures with drag reducing polymer solution. *Phys. Fluids* **32**, 015107.

FROHNAPFEL, B., HASEGAWA, Y. & QUADRIO, M. 2012 Money versus time: evaluation of flow control in terms of energy consumption and convenience. *J. Fluid Mech* **700**, 406–418.

FUKUSHIMA, K., KISHI, H., SUZUKI, H. & HIDEMA, R. 2022 Modification of turbulence caused by cationic surfactant wormlike micellar structures in two-dimensional turbulent flow. *J. Fluid Mech.* **933**.

GANAPATHISUBRAMANI, B., LAKSHMINARASIMHAN, K. & CLEMENS, N. T. 2007 Determination of complete velocity gradient tensor by using cinematographic stereoscopic piv in a turbulent jet. *Exp. Fluids* **42** (6), 923–939.

GHAEMI, S. 2020 Passive and active control of turbulent flows. *Phys. Fluids* **32** (8), 080401.

GHAEMI, S. & SCARANO, F. 2010 Multi-pass light amplification for tomographic particle image velocimetry applications related content. *Meas. Sci. Technol.* **21**, 1–5.

GOMES-FERNANDES, R., GANAPATHISUBRAMANI, B. & VASSILICOS, J. C. 2014 Evolution of the velocity-gradient tensor in a spatially developing turbulent flow. *J. Fluid Mech.* **756**, 252–292.

GRAHAM, M. D. 2014 Drag reduction and the dynamics of turbulence in simple and complex fluids. *Phys. Fluids* **26**, 101301.

GRAHAM, M. D. & FLORYAN, D. 2021 Exact coherent states and the nonlinear dynamics of wall-bounded turbulent flows. *Ann. Rev. Fluid Mech.* **53**, 227–253.

Gubian, P. A., Stoker, J., Medvescek, J., Mydlarski, L. & Baliga, B. R. 2019 Evolution of wall shear stress with reynolds number in fully developed turbulent channel flow experiments. *Phys. Rev. Fluids* **4**, 074606.

Haward, S. J., McKinley, G. H. & Shen, A. Q. 2016 Elastic instabilities in planar elongational flow of monodisperse polymer solutions. *Sci. Rep.* **6** (1), 33029.

Haward, S. J, Page, J., Zaki, T. A. & Shen, A. Q. 2018*a* Inertioelastic poiseuille flow over a wavy surface. *Phys. Rev. Fluids* **3** (9), 091302.

Haward, S. J., Toda-Peters, K. & Shen, A. Q. 2018*b* Steady viscoelastic flow around high-aspect-ratio, low-blockage-ratio microfluidic cylinders. *J. Non-Newtonian Fluid Mech.* **254**, 23–35.

Hutchins, N. & Marusic, I. 2007 Evidence of very long meandering features in the logarithmic region of turbulent boundary layers. *J. Fluid Mech.* **579**, 1–28.

Iwamoto, K., Suzuki, Y. & Kasagi, N. 2002 Reynolds number effect on wall turbulence: toward effective feedback control. *Intl J. Heat Fluid Flow* **23**, 678–689.

James, D. F. 2009 Boger fluids. *Ann. Rev. Fluid Mech.* **41**, 129–142.

Jiménez, J., Hoyas, S., Simens, M. P. & Mizuno, Y. 2010 Turbulent boundary layers and channels at moderate reynolds numbers. *J. Fluid Mech.* **657**, 335–360.

Johnston, M. T. & Ewoldt, R. H. 2013 Precision rheometry: Surface tension effects on low-torque measurements in rotational rheometers. *J. Rheol.* **57**, 1515–1532.

Joseph, D.D. 1990 *Fluid dynamics of viscoelastic liquids*, , vol. 84. Springer-Verlag Berlin Heidelberg GmbH.

Kähler, C. J., Scharnowski, S. & Cierpka, C. 2012 On the resolution limit of digital particle image velocimetry. *Exp. Fluids* **52**, 1629–1639.

Khodaparast, S., Borhani, N., Tagliabue, G. & Thome, J. R. 2013 A micro particle shadow velocimetry (μpsv) technique to measure flows in microchannels. *Exp. fluids* **54** (2), 1–13.

Kim, K., Adrian, R. J., Balachandar, S. & Sureshkumar, R. 2008 Dynamics of hairpin vortices and polymer-induced turbulent drag reduction. *Phys. Rev. Lett.* **100** (13), 134504.

Kim, K., Li, C. F., Sureshkumar, R., Balachandar, S. & Adrian, R. J. 2007 Effects of polymer stresses on eddy structures in drag-reduced turbulent channel flow. *J. Fluid Mech.* **584**, 281–299.

Kim, K. & Sureshkumar, R. 2013 Spatiotemporal evolution of hairpin eddies, reynolds stress, and polymer torque in polymer drag-reduced turbulent channel flows. *Phys. Rev. E* **87** (6), 063002.

Kumar, M., Guasto, J. S. & Ardekani, A. M. 2022 Transport of complex and active fluids in porous media. *J. Rheol.* **66** (2), 375–397.

Läuger, J. & Stettin, H. 2016 Effects of instrument and fluid inertia in oscillatory shear in rotational rheometers. *J. Rheology* **60** (3), 393–406.

Lee, M. & Moser, R. D. 2015 Direct numerical simulation of turbulent channel flow up to. *J. Fluid Mech.* **774**, 395–415.

Lee, S. J. & Zaki, T. A. 2017 Simulations of natural transition in viscoelastic channel flow. *J. Fluid Mech.* **820**, 232–262.

Li, C. F., Sureshkumar, R. & Khomami, B. 2006 Influence of rheological parameters on polymer induced turbulent drag reduction. *J. Non-Newtonian Fluid Mech.* **140**, 23–40.

Li, F.C., Kawaguchi, Y., Segawa, T. & Hishida, K. 2005 Reynolds-number dependence of turbulence structures in a drag-reducing surfactant solution channel flow investigated by particle image velocimetry. *Phys. Fluids* **17**, 075104.

Lin, Z. 2000 The effect of chemical structures of cationic surfactants or counterions on solution drag reduction effectiveness, rheology and micellar microstructure. PhD thesis, The Ohio State University.

Ling, H., Srinivasan, S., Golovin, K., McKinley, G. H., Tuteja, A. & Katz, J. 2016 High-resolution velocity measurement in the inner part of turbulent boundary layers over super-hydrophobic surfaces. *J. Fluid Mech.* **801**, 670–703.

Lumley, J. L. 1969 Drag reduction by additives. *Annu. Rev. Fluid Mech.* **1**, 367–384.

Lumley, J. L. 1973 Drag reduction in turbulent flow by polymer additives. *J. Polym. Sci.* **7**, 263–290.

Macosko, C. W 1994 *Rheology Principles, Measurements and Applications*. New Tork: Wiley.

McKinley, G. H. & Tripathi, A. 2000 How to extract the newtonian viscosity from capillary breakup measurements in a filament rheometer. *J. Rheology* **44** (3), 653–670.

Meinhart, C. D., Wereley, S. T. & Santiago, J. G. 2000 A piv algorithm for estimating time-averaged velocity fields. *J. Fluids Eng.* **122** (2), 285–289.

Mezger, T. 2020 *The rheology handbook: for users of rotational and oscillatory rheometers*. European Coatings.

Miller, E., Clasen, C. & Rothstein, J. P. 2009 The effect of step-stretch parameters on capillary breakup extensional rheology (caber) measurements. *Rheol. Acta* **48**, 625–639.

Min, T., Choi, H. & Yoo, J. Y. 2003*a* Maximum drag reduction in a turbulent channel flow by polymer additives. *J. Fluid Mech.* **486**, 91–109.

Min, T., Yoo, J. Y., Choi, H. & Joseph, D. D. 2003*b* Drag reduction by polymer additives in a turbulent channel flow. *J. Fluid Mech.* **486**, 213–238.

Minor, G., Oshkai, P. & Djilali, N. 2007 Optical distortion correction for liquid droplet visualization using the ray tracing method: further considerations. *Meas. Sci. Technol.* **18** (11), L23.

Mitishita, R. S., Elfring, G. J. & Frigaard, I. A. 2023 Statistics and spectral analysis of turbulent duct flows with flexible and rigid polymer solutions. *J. Non-Newtonian Fluid Mech.* **311**, 104952.

Mohammadtabar, M., Sanders, R. S. & Ghaemi, S. 2017 Turbulent structures of non-newtonian solutions containing rigid polymers. *Phys. Fluids* **29**, 103101.

Mohammadtabar, M., Sanders, R. S. & Ghaemi, S. 2020 Viscoelastic properties of flexible and rigid polymers for turbulent drag reduction. *J. Non-Newtonian Fluid Mech.* **283**, 104347.

Mortimer, L. F. & Fairweather, M. 2022 Prediction of polymer extension, drag reduction, and vortex interaction in direct numerical simulation of turbulent channel flows. *Phys. Fluids* **34** (7), 073318.

Moser, R. D., Kim, J. & Mansour, N. N. 1999 Direct numerical simulation of turbulent channel flow up to $re_{\{\tau\}} = 590$. *Phys. Fluids* **11**, 943–945.

Mullin, J. A. & Dahm, Werner J. A. 2006 Dual-plane stereo particle image velocimetry measurements of velocity gradient tensor fields in turbulent shear flow. i. accuracy assessments. *Phys. Fluids* **18** (3), 035101.

Mysels, K.J. 1949 *Patent No. 2, 492, 173*. United States Patent Office.

Nagashima, A. 1977 Viscosity of water substance—new international formulation and its background. *J. Phys. Chem. Ref. Data* **6**, 1133–1166.

Nagib, H. M. & Chauhan, K. A. 2008 Variations of von kármán coefficient in canonical flows. *Phys. Fluids* **20** (10), 101518.

Ober, T. J., Haward, S. J., Pipe, C. J., Soulages, J. & McKinley, G. H. 2013 Microfluidic extensional rheometry using a hyperbolic contraction geometry. *Rheol. Acta* **52** (6), 529–546.

Omidvar, R., Dalili, A., Mir, A. & Mohammadigoushki, H. 2018 Exploring sensitivity of the extensional flow to wormlike micellar structure. *J. Non-Newtonian Fluid Mech.* **252**, 48–56.

Ooi, A., Martin, J., Soria, J. & Chong, M. S. 1999 A study of the evolution and characteristics of the invariants of the velocity-gradient tensor in isotropic turbulence. *J. Fluid Mech.* **381**, 141–174.

Orszag, Steven A 1971 Accurate solution of the orr–sommerfeld stability equation. *J. Fluid Mech.* **50** (4), 689–703.

Owolabi, B. E., Dennis, D. J. C. & Poole, R. J. 2017 Turbulent drag reduction by polymer additives in parallel-shear flows. *J. Fluid Mech.* **827**, 1–12.

Owolabi, B. E., Lin, C. A. & Poole, R. J. 2023 On the application of generalised newtonian fluids in the modelling of drag-reducing rigid polymers. *J. Non-Newtonian Fluid Mech.* **319**, 105089.

Page, J. & Zaki, T. A. 2015 The dynamics of spanwise vorticity perturbations in homogeneous viscoelastic shear flow. *J. Fluid Mech.* **777**, 327–363.

Page, J. & Zaki, T. A. 2016 Viscoelastic shear flow over a wavy surface. *J. Fluid Mech.* **801**, 392–429.

Pereira, A. S., Andrade, R. M. & Soares, E. J. 2013 Drag reduction induced by flexible and rigid molecules in a turbulent flow into a rotating cylindrical double gap device: Comparison between poly (ethylene oxide), polyacrylamide, and xanthan gum. *J. Non-Newtonian Fluid Mech.* **202**, 72–87.

Pilitsis, S., Souvaliotis, A. & Beris, A. N. 1991 Viscoelastic flow in a periodically constricted tube: The combined effect of inertia, shear thinning, and elasticity. *J. Rheology* **35** (4), 605–646.

Pipe, C. J., Majmudar, T. S. & McKinley, G. H. 2008 High shear rate viscometry. *Rheol. Acta* **47**, 621–642.

Poole, R. J. & Alves, M. A. 2009 Velocity overshoots in gradual contraction flows. *J. Non-Newtonian Fluid Mech.* **160** (1), 47–54.

Poole, R. J., Escudier, M. P., Afonso, A. & Pinho, F. T. 2007 Laminar flow of a viscoelastic shear-thinning liquid over a backward-facing step preceded by a gradual contraction. *Phys. Fluids* **19** (9), 093101.

Poole, R. J., Escudier, M. P. & Oliveira, P. J. 2005 Laminar flow of a viscoelastic shear-thinning liquid through a plane sudden expansion preceded by a gradual contraction. *Proc. R. Soc. A* **461** (2064), 3827–3845.

Pope, S.B. 2000 *Turbulent Flows*. Cambridge University Press.

Procaccia, I., L'vov, V. S. & Benzi, R. 2008 Colloquium: Theory of drag reduction by polymers in wall-bounded turbulence. *Rev. Mod. Phys.* **80**, 225–247.

Ptasinski, P. K., Boersma, B. J., Nieuwstadt, F. T. M., Hulsen, M. A., den Brule, H. A. A. Van & Hunt, J. C. R. 2003 Turbulent channel flow near maximum drag reduction: Simulations, experiments and mechanisms. *J. Fluid Mech.* **490**, 251–291.

Ptasinski, P. K., Nieuwstadt, F. T. M., Brule, H. A. A. Van Den & Hulsen, M. A. 2001 Experiments in turbulent pipe flow with polymer additives at maximum drag reduction. *Flow Turbul. Combust.* **66**, 159–182.

Qi, Y. & Zakin, J. L. 2002 Chemical and rheological characterization of drag-reducing cationic surfactant systems. *Ind. Engng Chem. Res.* **41**, 6326–6336.

Quintavalla, S. J., Angilella, A. J. & Smits, A. J. 2013 Drag reduction on grooved cylinders in the critical reynolds number regime. *Exp. Therm. Fluid Sci.* **48**, 15–18.

Raffel, M., Willert, C. E., Scarano, F. & Kähler, C. J. 2018 *Particle Image Velocimetry*. Springer.

Recktenwald, S. M., Haward, S. J., Shen, A. Q. & Willenbacher, N. 2019 Heterogeneous flow inside threads of low viscosity fluids leads to anomalous long filament lifetimes. *Sci. Rep.* **9** (1), 1–11.

Roccon, A., Zonta, F. & Soldati, A. 2019 Turbulent drag reduction by compliant lubricating layer. *J. Fluid Mech.* **863**, R1.

Rodd, L. E., Scott, T. P., Cooper-White, J. J. & McKinley, G. H. 2005 Capillary break-up rheometry of low-viscosity elastic fluids. *Appl. Rheol.* **15**, 12–27.

Rothstein, J.P. & Mohammadigoushki, H. 2020 Complex flows of viscoelastic wormlike micelle solutions. *J. Non-Newtonian Fluid Mech.* **285**, 104382.

Rothstein, J. P. 2010 Slip on superhydrophobic surfaces. *Ann. Rev. Fluid Mech.* **42**, 89–109.

Roy, A., Morozov, A., van Saarloos, W. & Larson, R. G. 2006 Mechanism of polymer drag reduction using a low-dimensional model. *Phys. Rev. Lett.* **97** (23), 234501.

Sachsenheimer, D., Oelschlaeger, C., Müller, S., Küstner, J., Bindgen, S. & Willenbacher, N. 2014 Elongational deformation of wormlike micellar solutions. *J. Rheology* **58** (6), 2017–2042.

Saeki, T. 2014 Application of a drag reduction phenomenon caused by surfactant solutions. *J. Chem. Eng. Japan* **47** (2), 175–179.

Santiago, J. G., Wereley, S. T., Meinhart, C. D., Beebe, D. J. & Adrian, R. J. 1998 A particle image velocimetry system for microfluidics. *Exp. fluids* **25** (4), 316–319.

Schanz, D., Gesemann, S. & Schröder, A. 2016 Shake-the-box: Lagrangian particle tracking at high particle image densities. *Exp. Fluids* **57**, 70.

Schanz, D., Gesemann, S., Schröder, A., Wieneke, B. & Novara, M. 2013 Non-uniform optical transfer functions in particle imaging: calibration and application to tomographic reconstruction. *Meas. Sci. Technol.* **24**, 024009.

Schröder, A., Schanz, D., Geisler, R., Gesemann, S. & Willert, C. 2015 Near-wall turbulence characterization using 4d-ptv shake-the-box. In *11th International Symposium on Particle Image Velocimetry - PIV15*.

Sepulveda, J., Montillet, A., Della Valle, D., Amiar, T., Ranchon, H., Loisel, C. & Riaublanc, A. 2021 Experimental determination and modeling of flow curves of xanthan gum solutions over a large range of shear rates. *Appl. Rheol.* **31**, 24–38.

da Silva, C. B. & Pereira, José C.F. 2008 Invariants of the velocity-gradient, rate-of-strain, and rate-of-rotation tensors across the turbulent/nonturbulent interface in jets. *P. fluids* **20** (5), 055101.

Singh, J., Rudman, M. & Blackburn, H. M. 2017 The influence of shear-dependent rheology on turbulent pipe flow. *J. Fluid Mech.* **822**, 848–879.

Singh, J., Rudman, M. & Blackburn, H. M. 2018 Reynolds number effects in pipe flow turbulence of generalized Newtonian fluids. *Phys. Rev. Fluids* **3**, 094607.

Singh, J., Rudman, M., Blackburn, H. M., Chryss, A., Pullum, L. & Graham, L. J. W. 2016 The importance of rheology characterization in predicting turbulent pipe flow of generalized newtonian fluids. *J. Non-Newtonian Fluid Mech.* **232**, 11–21.

Sisko, A.W. 1958 The flow of lubricating greases. *Ind. Engng Chem.* **50**, 1789–1792.

Soria, J., Sondergaard, R., Cantwell, B. J., Chong, M. S. & Perry, A. E. 1994 A study of the fine-scale motions of incompressible time-developing mixing layers. *Phys. Fluids* **6** (2), 871–884.

Spalart, P. R. 1988 Direct simulation of a turbulent boundary layer up to $re_\theta = 1410$. *J. Fluid Mech.* **187**, 61–98.

Tabor, M. & de Gennes, P. G. 1986 A cascade theory of drag reduction. *Europhys. Lett.* **2**, 519–522.

Tamano, S., Graham, M. D. & Morinishi, Y. 2011 Streamwise variation of turbulent dynamics in boundary layer flow of drag-reducing fluid. *J. Fluid Mech.* **686**, 352–377.

Tamano, S., Uchikawa, H., Ito, J. & Morinishi, Y. 2018 Streamwise variations of turbulence statistics up to maximum drag reduction state in turbulent boundary layer flow due to surfactant injection. *Phys. Fluids* **30**, 075103.

Thais, L., Gatski, T. B. & Mompean, G. 2012 Some dynamical features of the turbulent flow of a viscoelastic fluid for reduced drag. *J. Turbul.* **13**, 1–26.

Tirtaatmadja, V., McKinley, G. H. & Cooper-White, J. J. 2006 Drop formation and breakup of low viscosity elastic fluids: Effects of molecular weight and concentration. *Phys. fluids* **18** (4), 043101.

Toms, B. A. 1948 Some observations on the flow of linear polymer solutions through straight tubes at large reynolds numbers. *1st International Congress on Rheology* **2**, 135–141.

Truesdell, C. 1954 *The kinematics of vorticity.*. Indiana University Press.

Tsinober, A., Kit, E. & Dracos, T. 1992 Experimental investigation of the field of velocity gradients in turbulent flows. *J. Fluid Mech.* **242**, 169–192.

Van Doorn, E., White, C. M. & Sreenivasan, K. R. 1999 The decay of grid turbulence in polymer and surfactant solutions. *Phys. Fluids* **11**, 101301.

Virk, P. S. 1971 An elastic sublayer model for drag reduction by dilute solutions of linear macromolecules. *J. Fluid Mech.* **45**, 417–440.

Virk, P. S., Mickley, H. S. & Smith, K. A. 1970 The ultimate asymptote and mean flow structure in toms' phenomenon. *J. Appl. Mech. Trans. ASME* **37**, 488–493.

Virk, P. S. & Wagger, D. L. 1990 Aspects of mechanisms in type b drag reduction. In *Structure of Turbulence and Drag Reduction* (ed. A. Gyr), pp. 201–213. Springer.

Vissmann, K. & Bewersdorff, H. W. 1990 The influence of pre-shearing on the elongational behaviour of dilute polymer and surfactant solutions. *J. Non-Newtonian Fluid Mech.* **34** (3), 289–317.

Walkama, D. M., Waisbord, N. & Guasto, J. S. 2020 Disorder suppresses chaos in viscoelastic flows. *Phys. Rev. Lett.* **124** (16), 164501.

Warholic, M. D., Massah, H. & Hanratty, T. J. 1999*a* The influence of a drag-reducing surfactant on a turbulent velocity field. *J. Fluid Mech.* **388**, 1–20.

Warholic, M. D., Massah, H. & Hanratty, T. J. 1999*b* Influence of drag-reducing polymers on turbulence: effects of reynolds number, concentration and mixing. *Exp. Fluids* **27**, 461–472.

Warwaruk, L. & Ghaemi, S. 2021 A direct comparison of turbulence in drag-reduced flows of polymers and surfactants. *J. Fluid Mech.* **917**, A7.

Warwaruk, L. & Ghaemi, S. 2022 Near-wall lubricating layer in drag-reduced flows of rigid polymers. *Phys. Rev. Fluids* **7** (6), 064605.

Westerweel, J. & Scarano, F. 2005 Universal outlier detection for PIV data. *Exp. Fluids* **39**, 1096–1100.

Wheeler, A. J. & Ganji, R. J. 2010 *Introduction to engineering experimentation*, 3rd edn. Pearson Higher Education.

White, C. M., Dubief, Y. & Klewicki, J. 2012 Re-examining the logarithmic dependence of the mean velocity distribution in polymer drag reduced wall-bounded flow. *Phys. Fluids* **24**, 021701.

White, C. M., Dubief, Y. & Klewicki, J. 2018 Properties of the mean momentum balance in polymer drag-reduced channel flow. *J. Fluid Mech.* **834**, 409–433.

White, C. M. & Mungal, M. G. 2008 Mechanics and prediction of turbulent drag reduction with polymer additives. *Ann. Rev. Fluid Mech.* **40**, 235–256.

White, C. M., Somandepalli, V. S. R. & Mungal, M. G. 2004 The turbulence structure of drag-reduced boundary layer flow. *Exp. Fluids* **36**, 62–69.

Wieneke, B. 2008 Volume self-calibration for 3d particle image velocimetry. *Exp. Fluids* **45**, 549–556.

Wieneke, B. 2012 Iterative reconstruction of volumetric particle distribution. *Meas. Sci. Technol.* **24**, 024008.

Wunderlich, A. M. & James, D. F. 1987 Extensional flow resistance of dilute polyacrylamide and surfactant solutions. *Rheol. Acta* **26** (6), 522–531.

Xi, L. 2019 Turbulent drag reduction by polymer additives: Fundamentals and recent advances. *Phys. Fluids* **31**, 121302.

Yasuda, K., Armstrong, R. C. & Cohen, R. E. 1981 Shear flow properties of concentrated solutions of linear and star branched polystyrenes. *Rheo. Acta* **20**, 163–178.

Zakin, J. L., Myska, J. & Chara, Z. 1996 New limiting drag reduction and velocity profile asymptotes for nonpolymeric additives systems. *AIChE J.* **42**, 3544–3546.

Zhang, D. Y. & Calabrese, M. A. 2022 Temperature-controlled dripping-onto-substrate (dos) extensional rheometry of polymer micelle solutions. *Soft Matter* **18** (20), 3993–4008.

Zhang, J., Tao, B. & Katz, J. 1997 Turbulent flow measurement in a square duct with hybrid holographic piv. *Exp. Fluids* **23** (5), 373–381.

Zhang, Y., Schmidt, J., Talmon, Y. & Zakin, J. L. 2005 Co-solvent effects on drag reduction, rheological properties and micelle microstructures of cationic surfactants. *J. Colloid Interface Sci.* **286**, 696–709.

Appendices

A Uncertainty analysis

A.1 Errors in periodically constricted tube measurements

Sources of uncertainty in the PSV measurements were assumed to include (1) errors due to subpixel interpolation of the correlation function, (2) the finite DOF, and (3) optical distortion near the walls of the tube from radial curvature and differences in the refractive index. Each source of uncertainty was conservatively estimated, the details for which are listed below.

1. Errors from subpixel interpolation are conservatively estimated to be 0.1 pixels according to Raffel *et al.* (2018). A 0.1 pixel error in displacement translates to an error in velocity of 0.1 to 1.4 mm s^{-1} depending on Δt. If this error is normalized by the average centreline velocity, $\bar{U}_0$, the largest velocity error among all flow conditions was $0.012\bar{U}_0$.

2. Quantifying the uncertainties attributed to radial distortion and differences in the refractive index was challenging and would require ray tracing analysis (Minor *et al.*, 2007). Instead, errors from radial distortion were conservatively estimated based on how well the velocity within FOV1 could match the theoretical Poiseuille profile, as shown in figure A.1. The largest deviation from the parabolic velocity profile was $0.04\bar{U}_0$.

3. Slower moving particles within the DOF but outside the centre plane of the tube, will bias velocity vectors to lower values. If a parabolic velocity profile is assumed when the wall radius R_w is equal to R_i, a DOF that is $0.1R_i$ in thickness would produce a relative error in U_x of about $0.003\bar{U}_0$ near the centreline of the PCT and $0.1\bar{U}_0$ near the wall of the PCT. These errors reduce when considering regions of the PCT with a larger wall radius.

The total uncertainty in measurements of $\boldsymbol{U}$ from PSV was estimated to be the root sum squared value of the three previously listed sources of uncertainty. This was about $0.042\bar{U}_0$ near the PCT centreline and $0.108\bar{U}_0$ near the PCT walls, when considering regions of the PCT where $R_w = R_i$. In subsequent plots of velocity within the PCT, error bars are used to display the uncertainty in the velocity measurements from PSV.

Profiles of streamwise velocity U_x normalized by the centreline velocity U_0 for the flows of water at different Re_d within the entrance region (FOV1) are shown in figure A.1(a). Recall, that the tube walls have constant radius R_o in the entrance region, and U_0 does not vary with respect to x. Therefore, the Reynolds number is defined as $Re_d = 2U_0R_o/\mu_s$. Shown alongside the measurements of U_x/U_0 is the

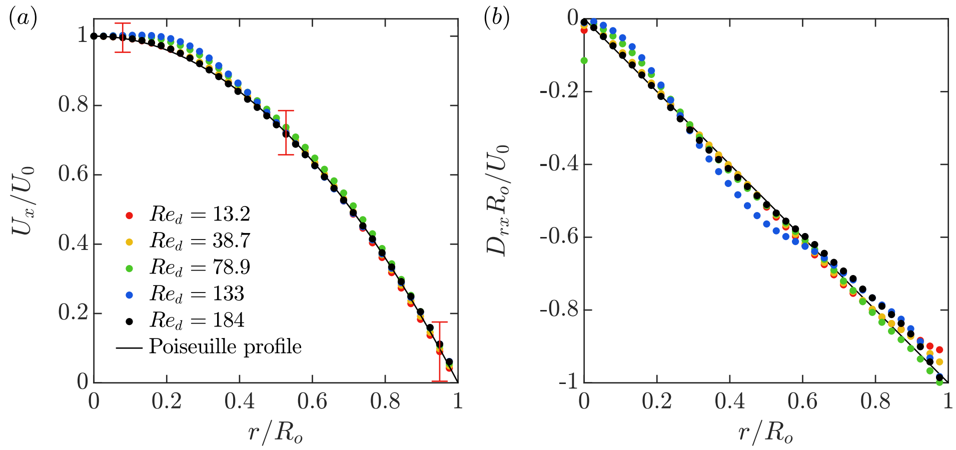

Figure A.1: Radial profiles of (*a*) streamwise velocity, and (*b*) the shear rate, at FOV1 for the flow of water at various Re_d. Error bars are shown for Re = 13.2 and correspond to the $0.042\langle U_0 \rangle$ uncertainty assumed from §6.2.

theoretical Poiseuille velocity profile for laminar pipe flow of a Newtonian fluid within a straight-walled pipe, $U_x/U_0 = 1 - r^2/R_o^2$. All measurements of U_x/U_0 are within 4% of the theoretical Poiseuille profile for different coordinates of r/R_o and agree well with theoretical expectations. Profiles of the shear component of the rate of deformation tensor D_{rx} are shown in figure A.1(*b*). When the Poiseuille profile for Newtonian pipe flow is differentiated, the relationship $\partial U_x/\partial r = 2D_{rx} = -2U_0 r/R_o^2$ is obtained. When simplified, it can be shown that $D_{rx}R_o/U_0 = -r/R_o$. Similar to the streamwise velocity profiles, measurements of $D_{rx}R_o/U_0$ agree well with the theoretical profile for all Re_d. In general, figure A.1 demonstrates that measurements within the entrance region reasonably satisfy the expectations for laminar fully-developed Newtonian pipe flow. We can proceed to measurements of the PCT knowing that the flow entering the PCT section is fully developed and the measurement technique is valid.

A.2 Influence of gap height and surface tension on parallel plate shear rheology

Steady shear viscosity measurements using a parallel plate (PP) geometry can be subjected to several sources of error, especially when dealing with small gap heights, h_{PP} (Ewoldt *et al.*, 2015; Davies & Stokes, 2008). Inertial flow instabilities, viscous heating, gap offsets and surface tension are some of the many factors that can corrupt the viscosity measurements. Techniques have been introduced to correct or account for these errors. For example, gap offset errors can be corrected by measuring μ, for different h_{PP} (Davies & Stokes, 2008). Measurements of μ at different h_{PP} are shown for the 170 ppm XG solution in figure A.2. In this figure, the upper shear rate threshold depended on the gap height and measurements were often terminated due to radial ejection of the fluid from the sides of the plates. Secondary flow instabilities are well demonstrated by the steep increase in μ at high $\dot{\gamma}$. The $Re_{PP} = 100$ threshold (Davies & Stokes, 2008), demonstrated by the colour coordinated dashed lines in figure A.2, conservatively estimated the critical $\dot{\gamma}$ at which the inertial instabilities corrupted the measurements of μ. At $\dot{\gamma}$ between 10 s^{-1} and 2500 s^{-1}, and ignoring viscosity measurement with $Re_{PP} > 100$, the measurements of μ for different h_{PP} are in good agreement; therefore, gap offset errors were considered negligible when $Re_{PP} < 100$.

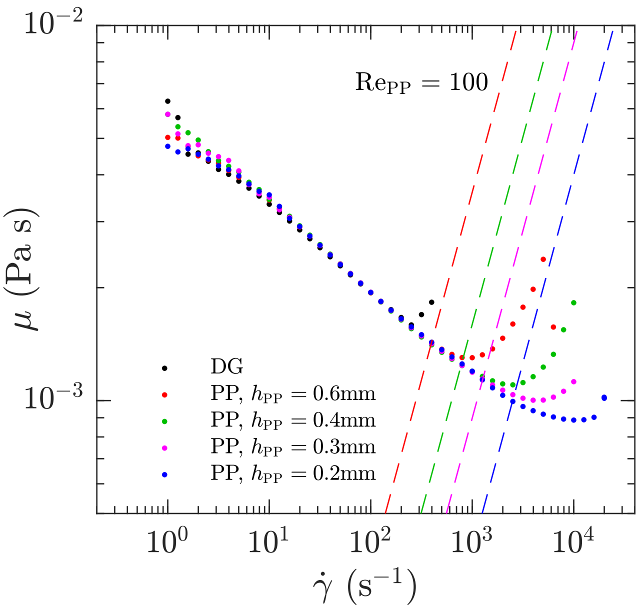

Figure A.2: Shear rheology of the 170 ppm XG solution measured for the PP geometry with different h_{PP}.

Surface tension can corrupt measurements of μ using the PP geometry when rotational symmetry is not maintained. The most likely scenario where this may occur is when the fluid sample is improperly added between the plates (sample underfilling or overfilling) (Johnston & Ewoldt, 2013). To identify if interfacial tension influenced the measurements of μ, we performed additional viscosity measurements that compared the 170 ppm XG solution with and without a small amount of TWEEN 20 (CAS 9005-64-5, Sigma Aldrich). Bąk & Podgórska (2016) performed interfacial tension measurements of various aqueous Tween 20 solutions. They observed that a TWEEN 20 concentration of 0.2 mM reduced the interfacial tension of water by about 30% and a concentration of 0.6 mM reduced the surface tension of water by 40%. The XG solution was given enough TWEEN 20 to achieve a concentration of 0.5 mM. Based on Bąk & Podgórska (2016), a TWEEN 20 concentration of 0.5 mM would have a significant influence on the surface tension of the solution. Figure A.3 demonstrates the measurements of the XG solution with and without TWEEN 20 at h_{PP} of 0.2 mm. There is good agreement among the measurements of μ using the DG geometry and the PP geometry with and without TWEEN 20. Therefore, we can confidently assume that the solution was loaded properly into the PP and surface tension has little influence on the shear viscosity measurements.

Although using the PP allowed us to obtain measurements of μ for much higher $\dot{\gamma}$ than we would have otherwise been able to achieve using just the DG geometry, there are more ideal measurement techniques for obtaining high shear rate viscometry. For example microfluidic channels or dedicated high shear rate rheometers can obtain viscosity measurements for $\dot{\gamma}$ on the order of 10^5 s^{-1}, with high accuracy and a low probability for human error. Pipe *et al.* (2008) were able to measure μ for $\dot{\gamma}$ up to 80000 s^{-1} using a microfabricated channel. Similarly, Sepulveda *et al.* (2021) measured the viscosity of various XG solutions using a microfluidic rheometer for $\dot{\gamma}$ up to 2×10^5 s^{-1}. Utilizing such measurement techniques could yield better quality of the CY fit and more certainty in the near wall scaling.

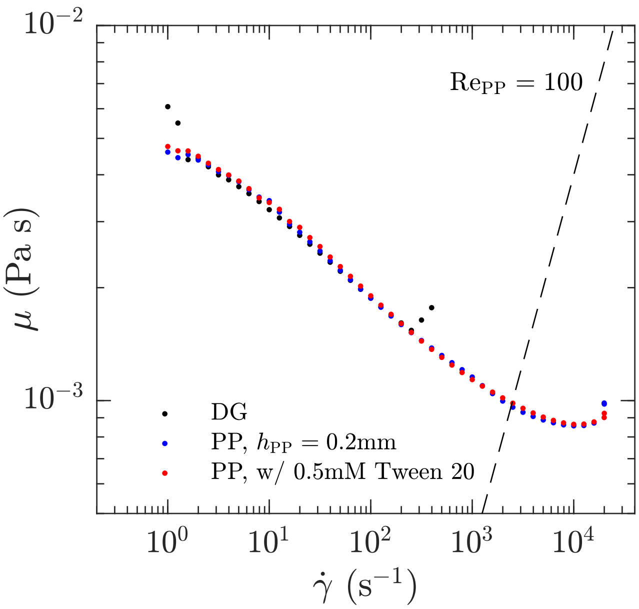

Figure A.3: Shear rheology of the 170 ppm XG solution measured for the PP geometry with and without TWEEN 20 and an h_{PP} of 0.2 mm.

A.3 Statistical convergence of planar PIV measurements of 170 ppm XG channel flows

The following figure A.4 demonstrates the convergence distributions of the first- and second-order statistics of velocity, as well as γ and μ, for XG with Re_τ of 170 and 700 and at a y^+ location of 100. The variable n denotes an instantaneous data point, while N is the total number of data points. Variables with a subscript of n, i.e. $\langle ... \rangle_n$, represent the average from the first data point to the n'th data point. Each convergence plot is normalized with their respective average over the complete ensemble of data points, $\langle ... \rangle_N$. All distributions converge to the ensemble average approximately within the last 20% of the data (from n/N = 0.8 to 1). A random error is calculated by determining the range (maximum subtracted from the minimum) in the convergence from n/N of 0.8 to 1, the results of which are shown in table A.1. The random errors for y^+ of 50 and 200 are also provided. Generally all random errors listed in table A.1 are less than 5%, implying good statistical convergence for all variables.

A.4 Statistical convergence of 3D-PTV measurements of 140 ppm PAM boundary layer

Figure A.5 demonstrate plots of the statistical convergence of the first- and second-order velocity statistics for the flows of water at different Re_ϕ and PAM at different wall-normal locations, namely y^+ of 20, 100, and y/δ of 0.4. Here N equals 114832, which is equivalent to eight datasets of 14354 vectors in time. All statistics in figure A.5 converge by n/N of 0.95, or within the last 5700 realizations. A random error is calculated from the range (maximum less minimum) of each convergence diagram from n/N of 0.95 to 1. The random errors of the velocity statistics are listed for each flow scenario and at y^+ of 20 in table A.2. Generally all random error listed in table A.2 are less than 5%, and the variables are considered adequately converged.

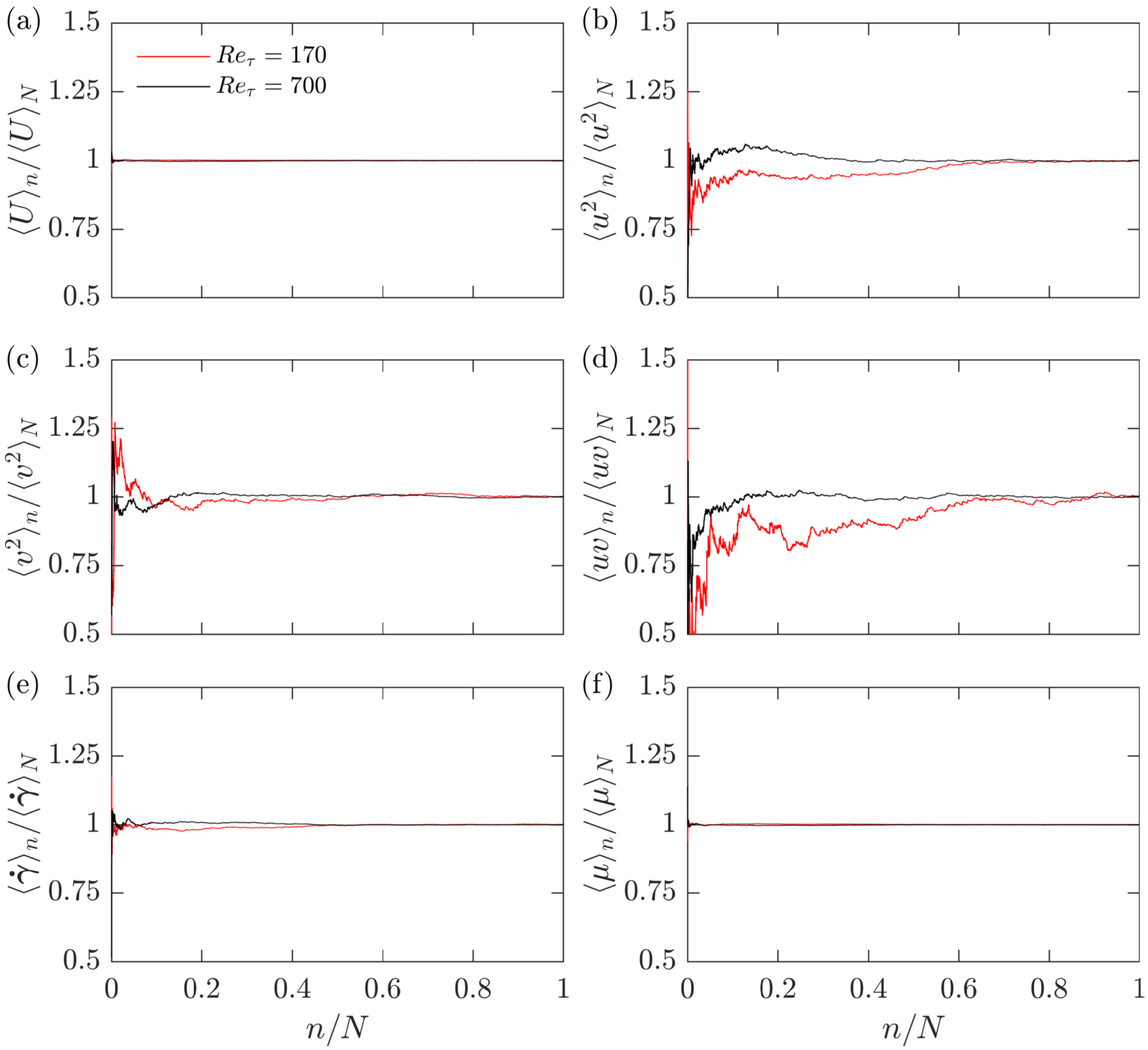

Figure A.4: Statistical convergence of (*a*) $\langle U \rangle$, (*b*) $\langle u^2 \rangle$, (*c*) $\langle v^2 \rangle$, (*d*) $\langle uv \rangle$, (*e*) $\langle \dot{\gamma} \rangle$, and (*f*) $\langle \mu \rangle$, for the flow of XG at its smallest and largest Re_τ cases of 170 and 700, and at a y^+ of 100.

A.5 Divergence errors in 3D-PTV measurements of 140 ppm PAM boundary layer

The accuracy of the velocity gradients, computed from the 3D-PTV measurements, is assessed by evaluating the divergence of the velocity, $\nabla \cdot \boldsymbol{U} = \mathrm{tr}(\mathbf{L}) = -P_L$. For an incompressible flow $\nabla \cdot \boldsymbol{U} = 0$. A similar assessment of the divergence-free condition is performed in other experimental investigations that utilize the Δ-*criterion* (Gomes-Fernandes *et al.*, 2014). Figure A.6(*a*) shows the JPDF of $\partial U/\partial x$ and $-(\partial V/\partial y + \partial W/\partial z)$ for the flows of water at different Re_ϕ and PAM. All velocity gradients are made dimensionless by multiplying them by the large eddy turnover time $\mathcal{T}$. Deviations from the diagonal dotted line in figure A.6(*a*), where $\partial U/\partial x = -(\partial V/\partial y + \partial W/\partial z)$, are indicative of divergence errors. JPDFs of $\partial U/\partial x$ and $-(\partial V/\partial y + \partial W/\partial z)$ agree reasonably well with the divergence-free line for all flows, compared to prior works that similarly

Re_τ	y^+	$\langle U \rangle$	$\langle u^2 \rangle$	$\langle v^2 \rangle$	$\langle uv \rangle$	$\langle \dot{\gamma} \rangle$	$\langle \mu \rangle$
170	50	0.13%	1.00%	0.69%	1.45%	0.37%	0.11%
170	100	0.05%	1.09%	1.24%	2.91%	0.49%	0.11%
170	200	0.03%	0.78%	0.65%	4.83%	0.21%	0.04%
700	50	0.07%	0.63%	1.47%	1.67%	0.25%	0.08%
700	100	0.08%	0.83%	0.55%	1.09%	0.22%	0.06%
700	200	0.03%	0.59%	0.62%	0.93%	0.37%	0.11%

Table A.1: Random error estimated from the range in the convergence of $n/N = 0.8$ to 1, for the velocity statistics of XG at its smallest and largest Re_τ cases of 170 and 700, and for y^+ of 50, 100 and 200.

Fluid	Re_ϕ	$\langle U \rangle$	$\langle u^2 \rangle$	$\langle v^2 \rangle$	$\langle w^2 \rangle$	$\langle uv \rangle$
Water	1814	0.30%	1.39%	1.03%	1.33%	1.84%
Water	2257	0.40%	1.87%	1.21%	1.00%	1.13%
PAM	2290	0.70%	2.14%	1.03%	1.12%	3.27%

Table A.2: Random errors estimated from the range in the convergence from $n/N = 0.95$ to 1, for the different flow conditions of water and PAM at y^+ of 20.

utilize the Δ-*crtierion* (Gomes-Fernandes *et al.*, 2014). The correlation coefficient between $\partial U/\partial x$ and $-(\partial V/\partial y + \partial W/\partial z)$ is 0.91, 0.94 and 0.84 for the flows of water at $Re_\phi = 1814$, water at $Re_\phi = 2257$ and PAM at $Re_\phi = 2290$, respectively. These are comparable or better than the correlation coefficients derived from Tsinober *et al.* (1992) (0.70) who used a multi-hot-wire probe technique, and Ganapathisubramani *et al.* (2007) (0.82) and Gomes-Fernandes *et al.* (2014) (0.5-0.6) who both used stereoscopic PIV with Taylor's hypothesis, to derive the VGT.

Another estimate for the divergence error is the ratio,

$$\xi = \frac{(\partial U/\partial x + \partial V/\partial y + \partial W/\partial z)^2}{(\partial U/\partial x)^2 + (\partial V/\partial y)^2 + (\partial W/\partial z)^2}, \tag{1}$$

developed by Zhang *et al.* (1997), who used holographic PIV to measure the turbulent flow of water in a square duct. The closer ξ is to 0, the better the divergence-free condition is satisfied. PDFs of ξ are shown in figure A.6(*b*) for the flows of water at different Re_ϕ and PAM. The mean value of ξ for water at an $Re_\phi = 1814$, water at $Re_\phi = 2257$, and PAM at an $Re_\phi = 2290$ is 0.16, 0.12 and 0.25 respectivly. These are comparable to the mean values of ξ from holographic PIV performed by Zhang *et al.* (1997) (0.74-0.12), as well as stereoscopic PIV performed by Ganapathisubramani *et al.* (2007) (0.18).

Mullin & Dahm (2006) assessed the divergence error of their dual-plane stereoscopic PIV measure-

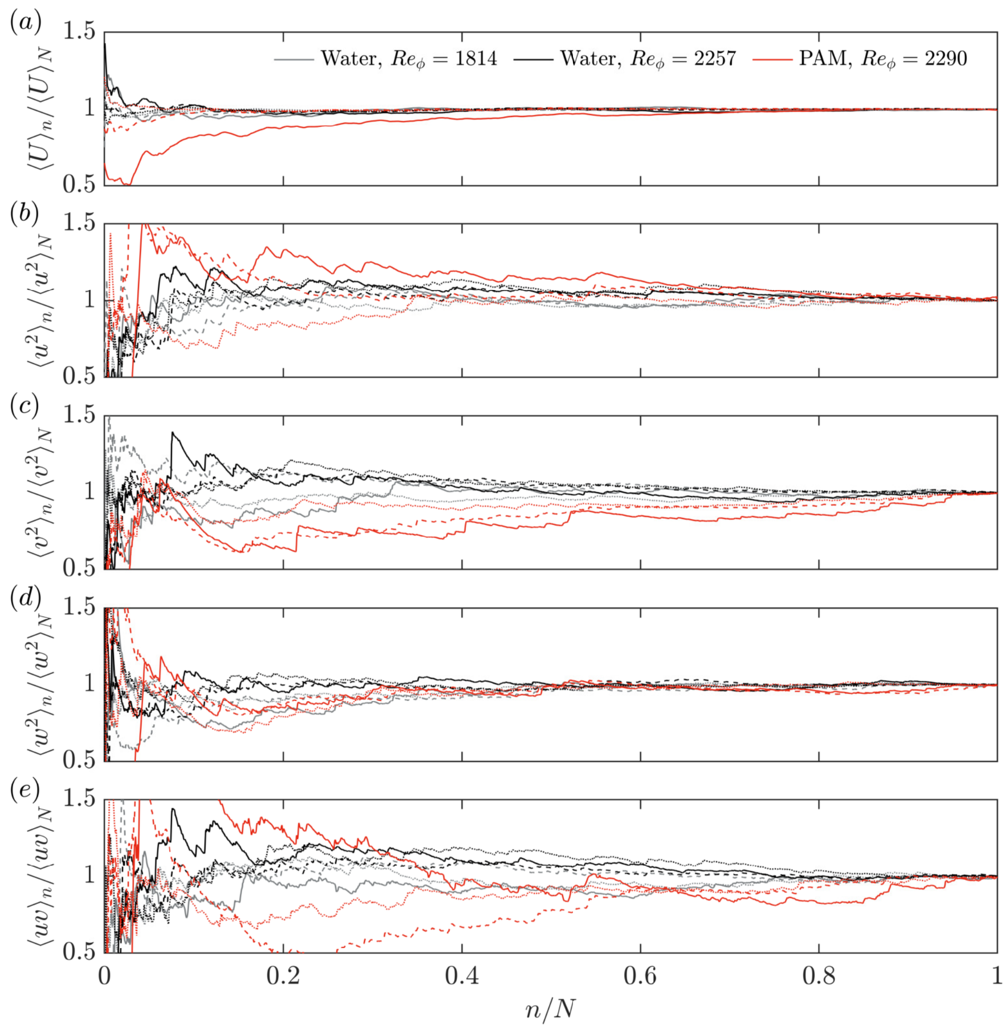

Figure A.5: Statistical convergence of (*a*) $\langle U\rangle$, (*b*) $\langle u^2\rangle$ (*c*) $\langle v^2\rangle$, (*d*) $\langle w^2\rangle$, and (*e*) $\langle uv\rangle$. The solid line is the convergence at y^+ of 20, the dashed line is the convergence at y^+ of 100 and the dotted line is the convergence at $y/\delta = 0.4$.

ments by calculating the divergence of the velocity vectors relative to the norm of the VGT. Figure A.7(*a*) demonstrates the PDFs of the diverence of velocity divided by the norm of the VGT. Here, the trace of the VGT or divergence in the velocity is written in index notation, i.e., $L_{ii} = \mathrm{tr}(\mathbf{L}) = \nabla \cdot \boldsymbol{U} = 0$, and the norm in the VGT is $(L_{jk}L_{jk})^{1/2}$. PDFs in $L_{ii}/(L_{jk}L_{jk})^{1/2}$ shown in figure A.7(*a*) are visibly Gaussian, with a mean that is approximately equal to 0 for all flow conditions considered. Mullin & Dahm (2006) assumed a divergence error equal to the root mean square (rms) in $L_{ii}/(L_{jk}L_{jk})^{1/2}$. The rms value of $L_{ii}/(L_{jk}L_{jk})^{1/2}$ for water at an $Re_\phi = 1814$, water at an $Re_\phi = 2257$, and PAM at an $Re_\phi = 2290$ is 0.119, 0.095 and 0.170 respectivly. These divergence errors are better than or comparable to the divergence error of the dual-plane steroscopic PIV measurements of Mullin & Dahm (2006) (0.35), and both the steroscopic PIV measurements of Ganapathisubramani *et al.* (2007) (0.25) and Gomes-Fernandes *et al.* (2014) (0.33-0.41).

Ganapathisubramani *et al.* (2007) demonstrated that divergence errors are strong functions of the magni-

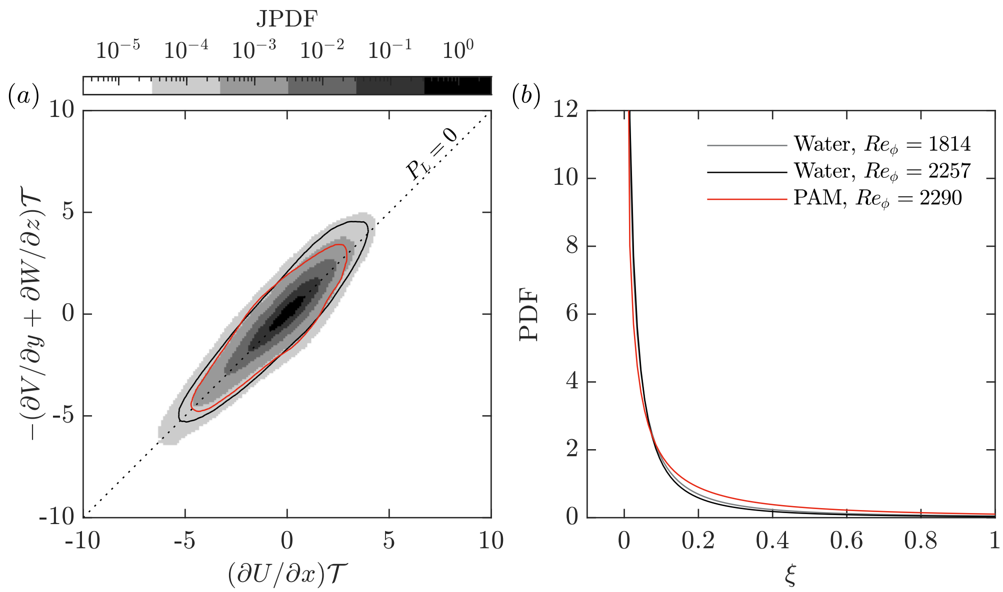

Figure A.6: (a) Joint probability density function of $\partial U/\partial x$ and $-(\partial V/\partial y + \partial W/\partial z)$. The open red contour in (a) is PAM with Re_ϕ = 2290 and a JPDF value of 10^{-4}. The open black contour in (a) is water with Re_ϕ = 2257 and a JPDF value of 10^{-4}. (b) Probability density function of local divergence error ratio ξ from Zhang *et al.* (1997).

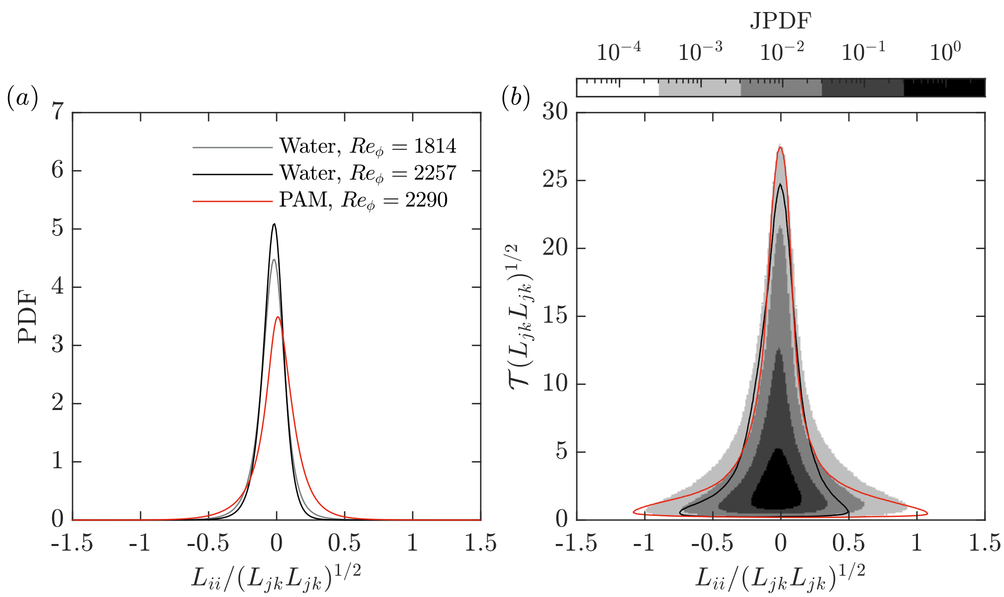

Figure A.7: (a) Probability density function of the velocity divergence L_{ii} normalized by the norm in the VGT $(L_{jk}L_{jk})^{1/2}$. (b) Joint robability density function of the norm in the VGT and velocity divergence normalized by the norm in the VGT. The open red contour in (b) is PAM with Re_ϕ = 2290 and a JPDF value of 10^{-3}. The open black contour in (b) is water with Re_ϕ = 2257 and a JPDF value of 10^{-3}.

tude of the VGT. JPDFs of $(L_{jk}L_{jk})^{1/2}\mathcal{T}$ and $L_{ii}/(L_{jk}L_{jk})^{1/2}$ are shown in figure A.7(b) for the boundary layers of water at different Re_ϕ and PAM, similar to those seen in Ganapathisubramani *et al.* (2007) and Gomes-Fernandes *et al.* (2014). The divergence error, characterized by the horizontal spread in the JPDF of figure A.7(b) along $L_{ii}/(L_{jk}L_{jk})^{1/2}$, is larger when $(L_{jk}L_{jk})^{1/2}\mathcal{T}$ is lower for all flow conditions. Therefore, it is expected that velocity gradients that are lower in magnitude are more corrupted by divergence error than those with a higher magnitude, similar to the conclusion of Ganapathisubramani *et al.* (2007) and Gomes-Fernandes *et al.* (2014).